QATAR UNIVERSITY

COLLEGE OF ENGINEERING

EXPERIMENTAL MEASUREMENTS AND TRANSIENT 3D SIMULATIONS OF TURBULENT PREMIXED FLAMES OF GAS-TO-LIQUIDS (GTL) FUEL IN A FAN-STIRRED COMBUSTION BOMB

BY

ABDELLATIF MOHAMMAD SADEQ

A Dissertation Submitted to

the College of Engineering

in Partial Fulfillment of the Requirements for the Degree of

Doctorate of Philosophy in Mechanical Engineering

June 2022

COMMITTEE PAGE

The members of the Committee approve the Dissertation of
Abdellatif Sadeq defended on 02/12/2021.

_____
Dr. Ahmad Sleiti
Thesis/Dissertation Supervisor

_____
Dr. Samer Ahmed
Thesis/Dissertation Co-Supervisor

_____
Dr. Fadwa ElJack
Committee Member

_____
Dr. Mohd Al-Khawaja
Committee Member

_____
Dr. Saud Ghani
Committee Member

Approved:

_____

Khalid Kamal Naji, Dean, College of Engineering

ABSTRACT

SADEQ, ABDELLATIF, MOHAMMAD, Doctorate: June: 2022, Doctorate of Philosophy in Mechanical Engineering

Title: Experimental Measurements and Transient 3D Simulations of Turbulent Premixed Flames of Gas-to-Liquids (GTL) Fuel in a Fan-Stirred Combustion Bomb

Supervisor of Dissertation: Ahmad, Khalaf, Sleiti.

Co-Supervisor of Dissertation: Samer, Fikry, Ahmed.

The rapid fluctuation in oil prices and the increased demand for alternative fuels to replace conventional fuels are challenging contemporary issues. One such alternative fuel that has gained significant interest recently is the Gas-to-Liquids (GTL) fuel, which is in the stage of replacing conventional diesel. However, detailed combustion characteristic investigations are required before using this alternative fuel broadly in engines. Therefore, the present dissertation is dedicated to experimentally investigate GTL (and its 50/50 by volume blend with diesel) turbulent flame speeds (S_t) under a wide range of thermodynamics and turbulence operating conditions using a cylindrical fan-stirred combustion bomb.

Turbulent premixed GTL flame is centrally ignited in an 81.7L cylindrical combustion bomb under atmospheric pressure at an initial temperature of 463K near Homogeneous and Isotropic Turbulence (HIT) conditions. The experiments are conducted under a wide range of equivalence ratios (Φ) between 0.7 to 1.3 and turbulence intensities ($u`$) that vary between 0.5m/s and 3.0m/s at an integral length

scale, L_t=20mm. The turbulent flame speed of the outwardly propagating GTL flame is measured using a pressure transducer, and the flame propagation is visualized by high-speed imaging. To extend and verify the experimental findings, Zimont Turbulent Flame Speed Closure (Zimont TFC) numerical model is adapted and implemented into ANSYS Fluent through a Reynolds Averaged Navier-Stokes (RANS) approach to study the influence of turbulence on GTL premixed combustion.

The results showed that: (i) rich diesel and lean GTL fuels are characterized by faster flame development and pressure rise rate (*dp/dt*) and thus, higher turbulent flame speeds; (ii) at the same elapsed time, turbulent Reynolds numbers (Re_T) and Damkohler numbers (*Da*) are higher for stoichiometric GTL fuel compared to diesel and 50/50 diesel-GTL blend, which indicates that the flame propagates towards the vessel's wall at a faster rate, and the chemistry has dominated turbulence in a shorter time, and (iii) at low turbulence intensity level ($u`$=0.5m/s), the flame morphology is defined by a wrinkled flamelet regime in Borghi diagram. However, at moderate and high turbulence levels ($u`$=1.5m/s and $u`$=3.0m/s, respectively), the corrugated flamelets regime defines the flame structure.

DEDICATION

This dissertation is dedicated to my family members, my respectful supervisors, and all the well-wishers and supporters.

ACKNOWLEDGMENTS

Firstly, I would like to thank Almighty God for giving me the dedication and strength to persevere through all the obstacles and difficult times throughout the different stages of my Ph.D. dissertation, as this project would have never finished without his support.

The present work has been accomplished at Qatar University, and I would like to sincerely acknowledge those who have assisted during the project period (about three years and a half).

I would like to gratefully thank my direct supervisor, Prof. Ahmad Sleiti, and my co-supervisor, Prof. Samer Ahmed, for their invaluable guidance, support, and advice throughout the whole project. Furthermore, I am grateful to all the committee members, Prof. Ibrahim Hassan, Prof. Saud Ghani, Prof. Mohammad Al-Khawaja, and Prof. Fadwa ElJack for their valuable comments, which have remarkably improved the final write-up of the dissertation.

In addition, I would like to send my warm gratitude to Eng. Yehia Darwish, Eng. Ahmad Saqr and Eng. Aboubaker Elbashir from the mechanical engineering department, who have spent much of their time preparing the test rig and conducting the experiments at the heat engine laboratory.

Last but not least, I would like to send my utmost gratitude to my parents, wife, friends, and all my well-wishers, who have wished me to always be there through the happy and challenging times.

TABLE OF CONTENTS

LIST OF TABLES

LIST OF FIGURES

CHAPTER 1. INTRODUCTION

The rapid fluctuations in oil prices and the increasing awareness about the harmful effect of greenhouse gases have directed the effort of researchers to find alternative energy resources that can substitute fossil fuels. Several research efforts have been taken in past decades to develop alternative fuels that can improve engine performance and minimize pollution emissions while remaining economical [1]–[4]. Gas to Liquids (GTL) fuel is one alternative fuel that has gained much interest, especially in Qatar, Russia, and the United States, in recent years due to its many advantages [5]. One of these advantages is the clean-burning nature of GTL that enhances the combustion properties compared to crude-oil-based diesel. Therefore, this fuel can reduce exhaust emissions to meet the local and international environmental regulations (The Paris Agreement, [6]). Moreover, GTL fuel is free of undesirable components such as metals, aromatics, and sulfur, making it less harmful to the environment with no toxicity. Furthermore, it is safer for storage and handling than diesel fuel and does not have an unpleasant smell [7]. According to Shell Company, GTL fuel can reduce Nitric Oxides (NO_x) emission by 25% and particulate matters (PM) emission by about 38% in comparison to diesel fuel [8]. Another research has also confirmed this conclusion [9], which has further demonstrated that GTL fuel produces lower in-cylinder peak pressure and less Brake Specific Fuel Consumption (BSFC). Due to these favorable GTL specifications and advantages, systematic research needs to be conducted on the optimum combustion characteristics

of GTL fuel at different operating conditions to determine its suitability for use in internal combustion engines. Detailed investigations for GTL combustion characteristics have not been performed yet, and it is essentially required before using this alternative fuel widely in engines.

Remarkable progress has been reported in appropriately investigating laminar flame speed (S_l) under various operating conditions for a variety of fuels and fuel blends, including GTL fuel [10]. S_l is a combustible mixture's property that is entirely dependent on the initial pressure (p_i), temperature (T_i) and the mixture equivalence ratio (Φ). In contrast to S_l,, turbulent flame speeds (S_t) cannot be precisely measured and consistently unified for all test rig configurations [11]. Flame speed influences knocking incidences in spark ignition (SI) engines and affects Ignition Delay (ID) time in diesel engines. In addition, both laminar and turbulent flame speeds must be studied to design more efficient engines and model predictive computational modelling techniques [12].

One of the experimental configurations that has been widely used to investigate the relationship between flame propagation and turbulent eddies is the fan-stirred combustion bomb [9], [13]. With a broad range of turbulence intensity levels (u') that can be obtained and precisely controlled, these vessels conveniently investigate the rates of flame propagation under different turbulent conditions. When compared to a burner-type configuration, this feature is highly desirable because the latter demands an additional increment in axial flow velocities to raise the turbulence intensity level [14]. When the flow rate is high, stabilizing techniques such as recirculation zones, pilot flames, or the bluff body must be utilized to prevent flashback. Nonetheless, the

design of fan-stirred vessels is cost-effective and does not allow for the flexible use of laser-based planar measurements [15].

Axis-symmetric mixing fans installed on the vessel's internal surface create homogeneous and isotropic turbulence inside the vessel. This arrangement may be used in various turbulence and thermodynamic conditions, including high temperatures, pressures, equivalence ratios, and turbulence intensities, which are relative to industrial applications [16]. The turbulent burning velocity and the overall wrinkling rate of the flame surface are significantly dependent on the existing turbulence features, such as the turbulent length scale (L_t) and the turbulence intensity (u'). When compared to the integral length scale, the initial flame kernel size is much smaller. As a result, during the early stages of flame development after ignition, it is not exposed to the whole spectrum of turbulence and remains laminar. As the flame grows, the surface of the flame is wrinkled by larger energy-containing eddies resulting in more energy and mass transfer and a thickening in the flame surface. Consequently, deep characterization of the turbulent flow is considered a prerequisite to understanding and analyzing the flame-turbulence interaction within this setup [9]. Although many researchers have experimentally used this setup to study the turbulent flow field, for example [11], [15], [17]–[23] , the velocities of the flow can only be measured in a two- dimensional plane with limited resolutions and ranges, so that the spatial and temporal fluctuations of small-scale motions cannot be properly captured [24]. Hence, well verified and validated 3D numerical simulations can bridge this gap.

Several combustion models found in the literature are used primarily for modelling reactive flow behavior. One of these widely-used computational models for studying

premixed turbulent combustion at high Reynolds numbers (Re_T) is the Zimont Turbulent Flame Speed Closure (TFC) model available in ANSYS Fluent and implemented using the pressure-based solver algorithm [25], [26]. The combustion process is defined in this model by a single transport equation (C- equation) for the reaction progress variable (C); turbulent closure for the progress variable's source term is determined by a model parameter utilized for turbulent flame speed computation. The turbulent flow field primarily results in wrinkling, thickening, and straining of the flame front, resulting in a closed-form expression of the turbulent flame speed that includes a critical gradient of the laminar flame thickness and speed, fluctuation intensity, and the local turbulent length scales. This method of closure is elegant and effective. It only requires one additional transport equation compared to non-reacting flows, and it excludes any costly chemical source term assessment or integration over probability density functions [27].

The past studies have investigated the turbulent flame speeds of several hydrocarbon gaseous fuels such as hydrogen, natural gas and different alkanes [14], [31], [32]. However, none of them has considered the investigation of turbulent flame speeds of heavy hydrocarbon liquid fuels such as diesel and GTL. Liquid fuels are characterized by a higher energy density compared to gaseous fuels, safer for storage and transportation, and are more economical for use [33]. Natural gas is converted into liquids through the Fisher-Tropsch process, starting from the partial oxidation of natural gas to form synthetic gas, then using a catalyst to convert the gas into liquids, and eventually, isomerization (cutting the molecules chains into shorter lengths) that produces GTL fuel in the final stage [8]. The clean-burning nature of GTL can

enhance the combustion properties compared to crude-oil-based diesel to increase the engine performance and lower the exhaust emissions. Moreover, GTL fuel is free of undesirable components such as metals, aromatics, and sulfur, in addition of being safer for storage and handling with no toxicity [8], [11], [18]. Therefore, the present dissertation aims to conduct a fundamental study of turbulent flame speeds of GTL fuel using the fan-stirred combustion bomb under different turbulence intensities ($0.5\text{m/s} < u` < 3.0\text{m/s}$) and equivalence ratios ($0.7 < \Phi < 1.3$). In this context, the significance of the dissertation outcomes can be addressed in the following points:

(i) The determination of the optimum operating conditions of GTL fuel assesses its suitability for replacing conventional diesel fuel as an alternative fuel.

(ii) The outcomes of this dissertation can benefit researches who are working in the field of premixed turbulent combustion and willing to conduct studies about chemical kinetics mechanisms, flame ignition mechanisms, ignition delay time, and flame extinction and diffusion.

(iii) Oil and gas industries, chemical refinements and renewable energy sectors can benefit from the dissertation outcomes by establishing well-planned production strategies to widen the use of GTL fuel in Qatar, and around the world.

(iv) Due to a lack of fundamental thermochemical, physical, and kinetic data for fuel components, studying flame speed is critical for predicting engine performance and emission rates.

(v) Bridge the gap for more comprehensive researches about similar topics, however, implementing other measurement techniques and numerical simulation models.

In order to verify and extend the experimental findings, Zimont Turbulent Flame Speed Closure (Zimont TFC) numerical model is adapted and implemented into ANSYS Fluent through a Reynolds Averaged Navier-Stokes (RANS) approach to study the influence of turbulence on GTL premixed combustion. This can assist in bridging the missing research gap in the literature by:

(vi) Investigating the existence of HIT condition in the combustion bomb by conducting a mean turbulent kinetic energy balance study.

(vii) Studying the premixed turbulent combustion of the three tested fuels at a broad range of turbulence intensities ($u`$), equivalence ratios (Φ), Reynolds numbers (Re_T) and Damkohler numbers (Da), which have not been studied before.

The main objectives of the present study are:

1) Experimentally investigate the turbulent flame speeds (S_t) of GTL fuel (and its 50/50 blend with diesel) over a wide range of turbulence intensities ($0.5\text{m/s} < u` < 3.0\text{m/s}$) and equivalence ratios ($0.7 < \Phi < 1.3$).
2) Use high-speed imaging to visually track the stoichiometric GTL flame propagation through its different growth stages.
3) Verify and extend the experimental findings by using Zimont TFC numerical model to study the influence of turbulence on GTL premixed combustion.

This dissertation is divided into seven chapters as follows. Chapter 1 introduces and addresses the present work's objectives, motivations, challenges, and experimental conditions. Chapter 2 provides a brief background about the various definitions and parameters that are commonly encountered when studying premixed turbulent flames. Chapter 3 overviews literatures pertaining to turbulent flame speed measurements, modelling, and visualization under different operating conditions. In Chapter 4, a detailed description of the test rig, measurement devices, fuel blends, and experimental procedures is provided, while chapter 5 describes the numerical simulation approach followed for turbulent flame speeds (S_t) computation. In Chapter 6, the experimental and numerical results are presented and discussed. Finally, Chapter 7 summarizes the main findings and outlines the suggested recommendations for future work improvements. At the end of the dissertation in the appendices, the laminar and turbulent flame speeds results are summarized in tables and attached. In addition, the calibration certificates of the measuring devices and instruments can be viewed.

CHAPTER 2. BACKGROUND

This chapter aims to provide a brief background about the different concepts and definitions commonly encountered when studying premixed turbulent flames such as laminar flames, turbulent flame brush, reaction progress variable, and others.

2.1 Laminar Flames

Laminar Premixed Flame (LPF) is a localized, self-sustaining combustion zone that moves at subsonic velocity. The laminar flame is localized because it only occupies a finite region in the space separating burned combustion products and unburned reactant species. To fully understand the concepts behind premixed flames, prior knowledge of chemical kinetics, mass, and heat transfer, in addition to thermodynamics, is required [34]. Studying the fundamentals of laminar premixed flames is essential for understanding turbulent premixed flames. Moreover, studying LPF is also necessary to track flame ignition behavior and extinction. Finally, the measurement of LPF is highly requested to develop the fundamentals of chemical kinetics mechanisms.

A laminar flame can be used as a reference frame to characterize the velocity of unburned reactants because it freely propagates ($S^o{}_{L,u}$). The superscript "L" indicates for laminar, and "u" stands for an unburned mixture. In addition, the superscript "o" stands for a non-stretched flame. Gases that leave the flame are burned gases moving with a velocity $S^o{}_{L,b}$, where "b" indicates the burned status of gases. Typically, a flame front can be represented in Figure 1 [35].

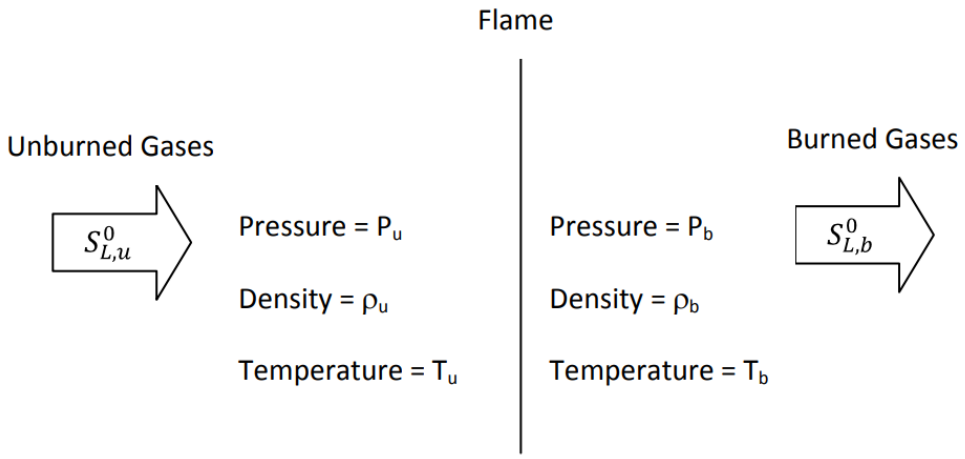

Figure 1. Flame sheet separating burned and unburned gases [35]

As the flame is traveling subsonically in the space, the pressures P_b and P_u have to be equal. In addition, the flame surface area remains the same (A=constant). However, the flame density ρ decreases from ρ_u to ρ_b due to combustion [36]. As a result, unburned and burned flame speeds can be related using the continuity equation [14]:

$$S^o{}_{L,u} A\, \rho_u = S^o{}_{L,b}\, A\, \rho_b \quad (1)$$

$$\frac{S^o{}_{L,b}}{S^o{}_{L,u}} = \frac{\rho_u}{\rho_b} = \sigma \quad (2)$$

where ρ_u and ρ_b represent the unburned and burned species densities, respectively. The ratio between the two densities is represented by σ .

One of the common experimental configurations used to track laminar flame propagation rates is the spherical/cylindrical combustion bomb. A spherical chamber or a closed cylinder with a central spark-ignition source is used in this experimental configuration [18]. As combustion begins, the flame propagates spherically with a

constant pressure wave, followed by a high and sudden increment in the pressure (approximated at around ten times the magnitude of initial pressure). To investigate flame propagation rates, the flame radius evolution can be optically tracked. In addition, a thermodynamic model can also be used to trace dynamic pressure variation across the combustion zone to track flame propagation rates [37].

In flame bombs, two types of velocities can be identified. The speed at which the flame front propagates into an unburned mixture is the first type and known as engulfment (entrainment) velocity or displacement speed. It is typically used to determine the consumption rate of unburned gases [19]. The other type is called the laminar burning velocity [14]. The rate of burned gas production can be calculated using a dynamic pressure transducer to track the pressure variation in the combustion bomb by multiplying the laminar burning velocity by the burned-gas density. Engulfment velocity is particularly interesting for engine designers who investigate the traveled distance by the flame after ignition.

On the other hand, laminar burning velocity has some safety applications, such as estimating the pressure increment after combustion. In addition, it is essential to notice that these two types of velocities are equal to planar flames. The laminar flame thickness (δ_L) is defined as [38]:

$$\delta_L = \frac{T_b - T_u}{|\nabla T|_{max}} \tag{3}$$

The temperatures of the burned and unburned gases are T_b and T_u, respectively. In addition, $|\nabla T|_{max}$ represents the largest temperature gradient that exists within the

flame. A laminar premixed flame is typically subdivided into three distinct zones: (i) the preheat zone, where no reaction occurs (only convection and diffusion);(ii) the reaction zone, where the majority of the heat is released due to the combustion of fuel; and (iii) the oxidation layer, where slow rates of oxidation occur for the formation of products (conversion of Carbon monoxide, CO to Carbon dioxide CO_2), as shown in Figure 2 [38].

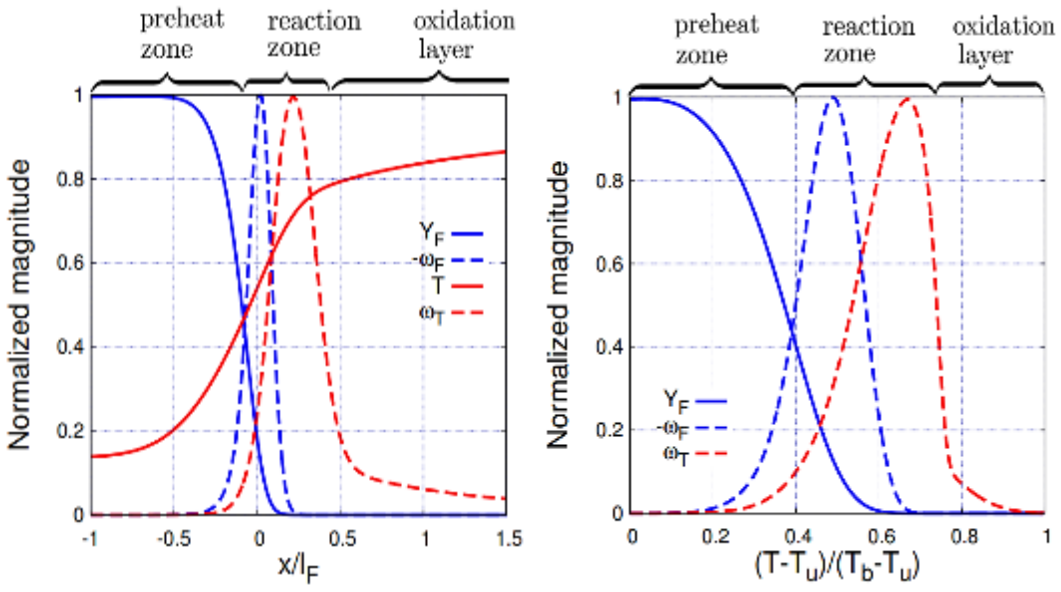

a) physical space b) temperature space

Figure 2. Representation of n-heptane/air flame profiles in physical and temperature spaces at atmospheric pressure (Φ=0.9, T_u =298 K). $\dot{\omega}_F$ is the chemical consumption rate, Y_F is the fuel mass fraction, and $\dot{\omega}_T$ is the heat release rate. Each quantity is normalized by its maximum value within the flame [38]

Some studies have investigated S_L using Schlieren Imaging [39], [40], while others have used optical techniques for measuring S_L [41], [42]. Furthermore, some numerical models have employed pressure data for establishing an equation that can be used to find S_L. One unique equation that is commonly used to find S_L is that one proposed by Lewis and Von Elbe [11]. This equation has proved its success when used to find S_L for Jojoba Methyl Ester (JME) , and it is written as the following [11]:

$$S_L = \left(\frac{dr_i}{d_t}\right)\left(\frac{r_i}{r_b}\right)^2\left(\frac{p_i}{p}\right)^{\left(\frac{1}{\gamma_u}\right)} \tag{4}$$

where,

$$\left(\frac{dr_i}{d_t}\right) = \left(\frac{R}{3(p_e - p_i)}\right)\left(\frac{d_p}{d_t}\right)\left[\frac{(p - p_i)}{(p_e - p_i)}\right]^{\left(\frac{2}{3}\right)} \tag{5}$$

$$r_i = R\left[\frac{(p - p_i)}{(p_e - p_i)}\right]^{\left(\frac{1}{3}\right)} \tag{6}$$

$$r_b = R\left[1 - \left(\frac{p_i}{p}\right)\left(\frac{T_u}{T_i}\right)\frac{(p_e - p)}{(p_e - p_i)}\right] \tag{7}$$

$$\left(\frac{T_u}{T_i}\right) = \left(\frac{p}{p_i}\right)^{\left(\frac{1}{\gamma_u}\right)} \tag{8}$$

where,

p_i, p and p_e are the initial, peak, and equilibrium pressure, respectively

γ_u is the specific heat ratio of unburned reactants

R is the radius of the cylindrical combustion bomb (R =20cm)

2.2 Turbulent Flame Brush (δ_t)

The laminar flame front (leading edge) is a thin wave, a high-temperature zone that propagates at laminar flame speed into a flammable mixture. δ_t is considerably thicker than a laminar flame front [29]. The thickness level in the flame front increases as the level of turbulence intensity becomes higher. The combustion zone, where unburned and burned gases exist on the boundaries, is known as a turbulent flame brush [37]. There are two categories in the formation of turbulent flame brush: (a) growing or developing flame brush, (b) fully developed turbulent flame brush [11]. Category (a) involves fan-stirred combustion bombs, V-flames, and Bunsen burners. In contrast, stagnation flows, low-swirl flames, and twin-counter flow flames fall under category (b). The classification of different flame types is shown in Figure 3 [11].

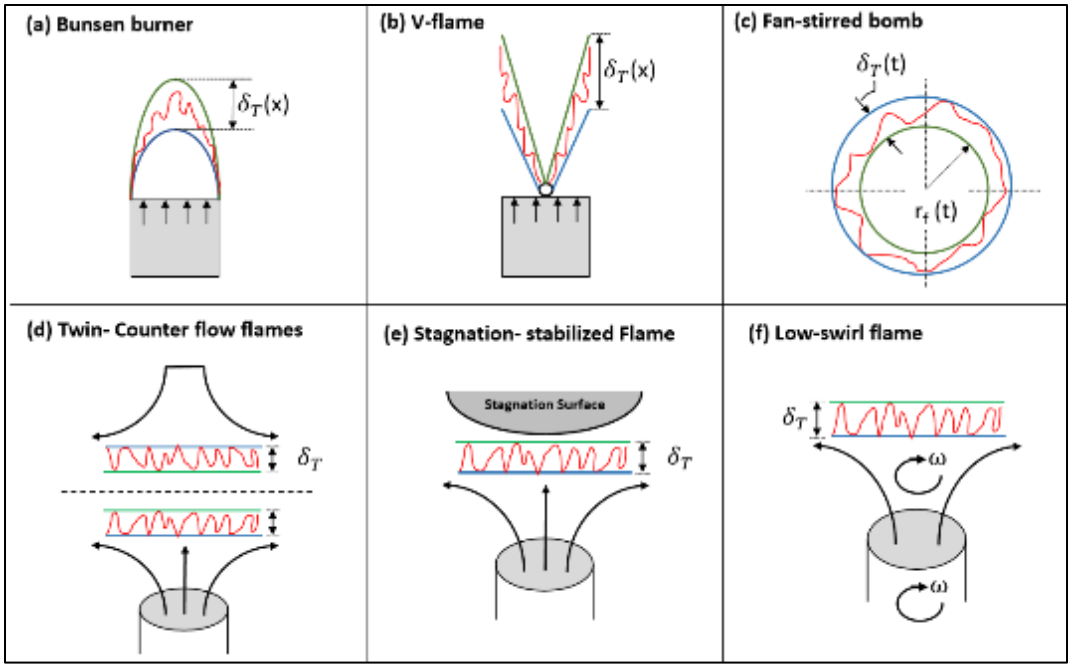

Figure 3. Developing flame brush: (a) Bunsen burner setup, (b) V-flames configuration, (c) fan-stirred combustion bomb. The configurations characterized by a fully developed turbulent flame brush are: (d) twin-counter flow setup(e) stagnation flow configuration (f) low-swirl burner [11]

As the flame propagates away from the holder, the Bunsen flame boundary layer changes spatially and becomes stable only at the rim of the burner. The conical V-flame results when a rod is placed at the middle of the burner outlet, which becomes stable behind the rod through recirculation zones. In these two configurations, the flame brush thickness expands axially away from the outlet of the burner. For spherically expanding flame, the brush thickness develops gradually with time (temporally) as the flame propagates outwardly in the combustion bomb [38]. This development of flame thickness is attributed to the random advection that turbulent

eddies cause on the surface of the flame brush. Taylor's law can explain such type of flame brush for turbulent diffusion, where this law governs the mixing layer growth as the following [39]:

$$\delta_t = \sqrt{2\pi}\, L'_o \left\{2t' \left[1 - \frac{1}{t'}\left(1 - e^{-t'}\right)\right]\right\}^{\left(\frac{1}{2}\right)} \tag{9}$$

where,

$$L'_o = \frac{L_T}{\left(1 + \frac{S_L^o}{2u'}\right)} \tag{10}$$

$$\tau' = \frac{L'_o}{u'} \tag{11}$$

$$t' = \frac{t}{\tau'_T} \tag{12}$$

δ_t represents the turbulent flame brush thickness, L_T the integral length scale, $u`$ the turbulence intensity, and t is time. In addition to the previous cases, a statistically stable flame that remains stationary with space and time can be achieved. The mean thickness of the flame brush is found to become constant after ignition incidence for low-swirl flames, twin-counter flows, and stagnation flames [40]. Nevertheless, those types of flames are governed by a different brush-growth principle. As the flow becomes farther from the burner outlet, the mean flow starts to decelerate. For instance, for the stagnation flame case, the velocity field can be modeled by the following, $u_r = a_t r/2$ and $u_x = U - a_t x$ for the radial velocity and axial velocity, respectively [11]; (where *r* and *x* are the distances away from the outlet of the burner, *U* is the spatially mean velocity, and a_t is the acceleration). The surface of the flame is advected by turbulent eddies, however the strong mean flow (strain rate) acts

against it as the flow propagates more from the burner rim. As a result, the flame brush becomes fully developed after the instant of initial- ignition transient [38].

The same principle applied for stagnation flames can be passed to low-swirl flames and twin-counter flow flames described by their divergence in mean flow (They decelerate as they move away from the outlet of the burner). This class of premixed flames is considered convenient for studying fully developed turbulent flame brushes. However, actual flames in the industry (gas turbines and IC engines) are developing naturally, and they consume some time to become fully developed ($\sim\tau_T\ {S_L}^2$) [15].

2.3 Reaction Progress Variable

A scalar known as the reaction progress variable $\langle c \rangle$ is used to identify each isosurface inside the turbulent flame brush. The percentage of combustion completion determined at each isosurface is represented by this variable. [41]. It can be defined using the normalized density, temperatures, or other species fractions (Ex. oxygen or fuel mass fraction). $\langle c \rangle$ value ranges between 0 to indicate an unburned gas to 1, which indicates that the gas is completely burned within the flame brush.

It's worth noting that the chemical enthalpy falls as the fuel mass fraction decreases. Furthermore, as the temperature rises, the sensible enthalpy values increases [11]:

$$\langle c \rangle = \frac{\bar{T} - T_u}{T_{b-}\ T_u} = \frac{\bar{\rho} - \rho_u}{\rho_{b-}\ \rho_u} \tag{13}$$

where $\bar{T}$ and $\bar{\rho}$ represent the mean temperature and density of the gases insides the turbulent flame brush up to one specific surface.

For all distinct turbulent flame geometries, the value of $\langle c \rangle$ can be estimated. When using a Bunsen burner configuration, $\langle c \rangle$ is found to steadily increase from 0 to 1 as moving away from the flame chemiluminescence, with $\langle c \rangle$=0.5 coincides with the highest turbulent intensity ($u`$). Different flame reaction zones can be identified and binarized as either unburned or burned gas utilizing laser-sheet imaging (such as OH-PLIF technique). The average of those values can be obtained by assembling multiple images at each pixel to find the mean value of $\langle c \rangle$ [42].

The surface of the flame that corresponds to a specific $\langle c \rangle$ value is represented by pixels that are positioned at a surface of $\langle c \rangle$=constant. Several $\langle c \rangle$ contours are recognized at horizontal isosurfaces assigned in an axial direction for twin-counter flow, low-swirl burners, and stagnation flows [43]. Because the $\langle c \rangle$ =constant varies over different flame surfaces within the flame brush, turbulent flame speeds (S_t) vary as well. S_t depends extensively on the surface at which it is measured. In a V-flame setup, for example, $\langle c \rangle$ gradually increases away from the burner hole, resulting in varied values for S_t [11].

The values of $\langle c \rangle$ in fan-stirred combustion bombs are determined by optical diagnosis techniques. Other techniques such as indirect methods (pressure-trace) and Schlieren imaging can also be used. According to Bradley et al. [15], the value of $\langle c \rangle$ identified by the two methods was different at the mean flam surface. The Schlieren tip correlates statistically with a propagating flame surface of roughly $\langle c \rangle$=0.1, and this study has also found that the flame surface with $\langle c \rangle$ = 0.6 also coincides with the same radii using the dynamic pressure trace.

2.4 Definition Dependency of Turbulent Propagation Rates

The displacement speed ($S_{T,c}$) and the global consumption speed ($U_{T,c}$) are two commonly used definitions for turbulent burning rates in the literature [15]. $U_{T,c}$ is calculated by dividing the ratio of mass burning rate to mean area of the flame surface by the product of unburned gas density and flame surface area ($U_{T,c}$). In contrast, displacement speeds ($S_{T,c}$) (known as engulfment or entrainment speeds) are the difference between the unburned gas velocity and the observed wave speed when it is normal to the surface of the flame. The global consumption speed ($U_{T,c}$) is assessed at $\langle c \rangle = 0.5$ in the middle of the flame brush, but the displacement speed ($S_{T,c}$) is estimated at $\langle c \rangle \approx 0.05{-}0.1$ at the flame front. When the net rate of formation (consumption) of products (reactants) is required, $U_{T,c}$ is investigated. $S_{T,c}$, on the other hand, is used to determine the speed of the flame front (for example, within an engine) [11]. As a result, these two speeds cannot be directly compared. Within each category, however, flame speeds can be compared for various flame geometries.

A simple example of the difference between the two definitions is a growing flame brush for a planar flame. Within the flame brush, various $\langle c \rangle$ isosurfaces are observed, each with a different surface area (A) and moving at a different speed. For burner premixed flames which are stabilized at the holder of the flame, the difference in speeds for the surfaces defined with $\langle c \rangle$ approaches zero ($\langle c \rangle \rightarrow 0$) and $\langle c \rangle$ approaches one ($\langle c \rangle \rightarrow 1$) is proportional to $U\frac{d\delta T}{dx}$, and $\frac{d\delta T}{dt}$ for spherical flames (where T is the isosurface temperature, x is the axial distance away from the flame holder, and U is the mean flow velocity) [44]. The displacement speed ($S_{T,c}$) of each isosurface can

then be used to identify it. As a result, in the planar turbulent flame example, it is not feasible to define a single displacement speed because each isosurface has a different speed. However, $U_{T,c}$ is the same at each isosurface (single value) and can be calculated by dividing the total burning rate by the product of unburned gas density and the flame surface area [11].

In practical applications, flames are curved and developing. Hence, it is not feasible to determine a single value for the displacement speed due to the curved topology of the flame. Moreover, the global consumption speed also depends on the isosurface used for estimating it, as the area of each isosurface is different in this case due to flame curvature [44]. Different flame geometries result in different global consumption speeds and displacement speeds. In the case of using Bunsen burner flames, the flow typically diverges, which decreases $U_{T,c}$ below $S_{T,c}$. However, in fan-stirred bombs or low-swirl burners, the flow is convergent, which decreases $S_{T,c}$ below $U_{T,c}$ [15].

2.5 Turbulence in Combustion

Turbulence is an essential phenomenon that is almost encountered in all practical flows in engineering applications. Thus, it is necessary to acquire adequate knowledge about turbulence concepts and how it affects combustion as turbulence alters the dynamics of the flame and its structure. Both the laminar and turbulent flows are common in being viscous fluid flows. The streamlines in the laminar flow slide past each other smoothly and orderly, mixing results due to molecular diffusion [45]. On the other hand, turbulent flows occur at high Reynolds numbers (Re_T) when

the inertial forces overcome the viscous forces, which cause the laminar flow to become chaotic and unstable. The fluid motion becomes unsteady and three-dimensional, causing rapid pressure and velocity fluctuations [45].

Turbulent flows are unsteady and random. Eddies move randomly within the fluid layers, and the fluid velocity fields change significantly in both time and position [46], [47]. Consequently, this makes the turbulent flow analysis difficult, and statistical techniques must be followed to find a solution [48]. Diffusivity is one of the intrinsic properties of turbulence. In this process, rapid mixing causes mass, heat, and momentum transfer to be enhanced as mixing takes place at high rates [49].

Eddies are used in the discussion of turbulence physics to visualize a turbulent flow across a spectrum of scales. An eddy is defined as a localized swirling motion with a characteristic dimension that provides a local turbulence scale [49]. Although the smallest eddy size is minimal, it is still larger than the scale of the molecules [50]. Eddies of various sizes overlap in the turbulence domain, and larger eddies carry out smaller eddies; as discussed in Section 2.7.

Turbulence follows a cascade mechanism that transfers kinetic energy from larger to smaller eddies. The large eddies are of L_t size, and they break down into smaller eddies and become unstable in the flow. Due to the effect of molecular viscosity, the kinetic energy transmitted to the smaller eddies is eventually dissipated as heat [50]. The dissipation of kinetic energy, denoted by ε, is a basic feature for studying the behavior of turbulent flows. The kinetic energy dissipation rate (ε), is commonly

estimated by the rate of energy transfer from larger eddies to smaller ones, as follows [11]:

$$\varepsilon \sim \frac{u'^3}{l_t} \tag{14}$$

where ε is the dissipation rate, and l_t the integral length scale. Unlike large eddies, which are directional and anisotropic, small-scale eddies move with a universal isotropic form as proposed by Kolmogorov [11]. The motion of small-scale eddies (Kolmogorov scale) can be uniquely described using a velocity (u_η) and dissipation (ε). Time (τ_η), length (η_η), and velocity (u_η) scales can be obtained for small eddies using dimensional analysis such that [11]:

$$\tau_\eta = \left(\frac{\nu}{\varepsilon}\right)^{\frac{1}{2}} \tag{15}$$

$$\eta_\eta = \left(\frac{\nu^3}{\varepsilon}\right)^{\frac{1}{4}} \tag{16}$$

$$u_\eta = (\nu\,\varepsilon)^{1/4} \tag{17}$$

where ν represents the kinematic viscosity.

The behavior of turbulence is complex, and Reynolds proposed a statistical method to analyze this behavior involving averaging [49]. The averaged equations are known as Reynolds averaged equations, and they are commonly used for unsteady flows. In this form of averaging, each term is expressed as a sum of an averaged value and a fluctuation about the mean. Thus, the instantaneous velocity can be written as the following [11]:

$$u_i\,(x,t) = \overline{u_i\,(x,t)} + u_i'(x,t) \tag{18}$$

where $\overline{u_i\,(x,t)}$ is the mean velocity, and $u_i'(x,t)$ is the fluctuating part. Ensemble averaging for the case of the mean velocity can be calculated as [11]:

$$\overline{u_i\,(x,t)} = \lim_{N \to \infty} \frac{1}{N} \sum_{n=1}^{N} u_{i,n}\,(x,t) \tag{19}$$

where $u_{i,n}$ is the value of u_i at the nth repetition out of N independent realizations. Using this averaging in the conservation of mass (continuity) equation and momentum (excluding the body forces) arises the following equations (noting that the density is considered to be constant herein) [49]:

- Conservation of mass

$$\rho\,\frac{\partial\,\overline{u_i}}{\partial\,x_i} = 0 \tag{20}$$

- Conservation of momentum

$$\rho\,\frac{\partial\,\overline{u_i}}{\partial\,t} + \rho\,\frac{\partial}{\partial\,x_j}\left(\overline{u_i}\,\overline{u_j} + \overline{u_i'u_j'}\right) = -\frac{\partial\,\overline{p}}{\partial\,x_i} + \frac{\partial}{\partial\,x_j}\left(\overline{\mathrm{T}}_{ij}\right) \tag{21}$$

where ρ, $\overline{p}$, $\overline{\mathrm{T}}_{ij}$ represent the fluid density, the pressure (normal stress), and viscous stresses, respectively. The unclosed terms u_i', u_j' appear in the equation due to averaging, and they are known as the Reynolds stress tensors.

Four variables are unknowns for a typical three-dimensional flow: the pressure and the three velocity components [51]. When modelling turbulence statistically, the number of unknowns is raised to ten as there are six Reynolds stress components, which are also unknown. Consequently, these equations are considered anonymous. There should be some suitable models for estimating the unknown Reynolds stresses

to find a solution for these equations. The simplest one is the Eddy Viscosity Model (EVM) introduced by Boussinesq [52], and it is based upon turbulence viscosity approximation. Based on this assumption, the Reynolds stresses are proportional to the mean strain rate and are written as [52]:

$$\overline{\rho}\,\widetilde{u_i'' u_j''} = -\mu_t \left(\frac{\partial \widetilde{u_i}}{\partial x_j} + \frac{\partial \widetilde{u_j}}{\partial x_i} - \frac{2}{3}\,\delta_{ij}\,\frac{\partial \widetilde{u_k}}{\partial x_k} \right) + \frac{2}{3}\,\overline{\rho}\widetilde{k}\delta_{ij} \tag{22}$$

where μ_t represents the eddy viscosity, $\widetilde{u_i'' u_j''}$ are the Reynold stresses, δ_{ij} is the mean strain rate, and $\widetilde{k}$ is the turbulence kinetic energy, which is expressed as [52]:

$$\widetilde{k} = \frac{\widetilde{u_i'' u_i''}}{2} \tag{23}$$

The eddy viscosity is a product of a velocity scale and a mixing length and represents the ratio of the Reynold stresses (turbulent quantities) to mean shear (mean flow quantities). In addition, it is essential to note that μ_t depends on the geometry of the flow and the turbulent eddies that exist in the flow, and it is not a fluid property. Several methods are suitable for defining the eddy viscosity, and different models can characterize it. Some of these models are the zero, one, and two equations models [49], which will be discussed in Section 3.3.

2.6 Dimensionless Numbers for Turbulent Combustion

An arbitrary size for a given eddy l ($\eta < l < L_T$) in the inertial subrange of a turbulent spectrum can be related to its corresponding velocity $u'(l)$ as [11]:

$$\frac{u'(l)^3}{l} = \varepsilon \tag{24}$$

where η is the Kolmogorov length scale, L_T the integral length scale, ε is turbulence dissipation rate

The turnover time (τ_l) of this eddy is expressed as [11]:

$$\tau_l = \frac{l}{u'(l)} = \varepsilon^{-\frac{1}{3}} l^{\frac{2}{3}} \tag{25}$$

A laminar flame propagates into eddies of different sizes within a turbulent flow domain. The characteristic chemical time scale defined as [11]:

$$\tau_c = \frac{\delta}{S_{L,u}^0} \tag{26}$$

where,

$S_{L,u}^0$: the unstretched, unburned laminar flame speed

$\delta = \frac{\nu}{S_{L,u}^0}$: Zeldovich flame thickness and ν the kinematic viscosity

Damkohler number (Da)

A ratio between the characteristic eddy timescale (τ_T) and chemical time scale (τ_c). It is commonly used with the integral length scale (the largest eddy) [11]:

$$Da = \frac{\tau_T}{\tau_c} = \left(\frac{u'}{S_L}\right)^{-1} \left(\frac{L_T}{\delta}\right) \tag{27}$$

Karlovitz number (ka)

Relates the laminar flame thickness (δ) to the Kolmogorov turbulent scale (η) [11]:

$$ka = \left(\frac{\delta}{\eta}\right)^2 \left(\frac{u'}{S_L}\right)^{\frac{3}{2}} \left(\frac{L_T}{S_L}\right)^{-\frac{1}{2}} \tag{28}$$

Turbulent Reynolds number (Re_T)

Based on the integral length scale (L_T), the turbulent Reynolds number is defined as [11]:

$$Re_T = \frac{u` L_T}{\nu} = \left(\frac{u`}{S_L}\right)\left(\frac{L_T}{\delta_L}\right) = (Da\ ka)^2 \quad (29)$$

Lewis number (Le)

It is a dimensionless number that relates the species thermal diffusivity (α) to their mass diffusivity (D) [11]:

$$Le = \frac{\alpha}{D} \quad (30)$$

Markstein number (Ma)

Characterizes the effect of the propagating flame's local heat release on the topology and curvature of the flame surface [48]:

$$Ma = \frac{\text{L}}{\delta_L} \quad (31)$$

where,

L: Markstein length

δ_L: the characteristic laminar flame thickness

2.7 Energy Cascade

Within a turbulent flow, most of the turbulent kinetic energy (k) is carried out by eddies of the order of the integral length scale L_T, such that [49]:

$$k = \frac{1}{2}\left(\overline{u_i` u_i`}\right) \tag{32}$$

For a homogeneous and isotropic turbulent field, k becomes [49]:

$$k = \frac{3\overline{u_i`^2}}{2} \tag{33}$$

where i indicates for the x, y, or z direction.

Eddies of large sizes tend to break up into smaller eddies continuously, and therefore eddies of different sizes exist within a turbulent flow. Energy is transferred from larger to smaller eddies until viscous forces become dominant and the smallest eddies are dissipated. To compensate for the kinetic energy losses and maintain the turbulent flow, an external energy source is required. In the absence of an external energy source, the turbulent flow is characterized by a decreasing trend in turbulent kinetic energy. The energy cascade, depicted in Figure 4, describes the energy transfer from large-scale eddies to smaller ones [49]. The region between the integral (largest) and the Kolmogorov (smallest) length scales is known as the inertial subrange, and it is characterized by a constant energy transfer rate of a slope -5/3 [49].

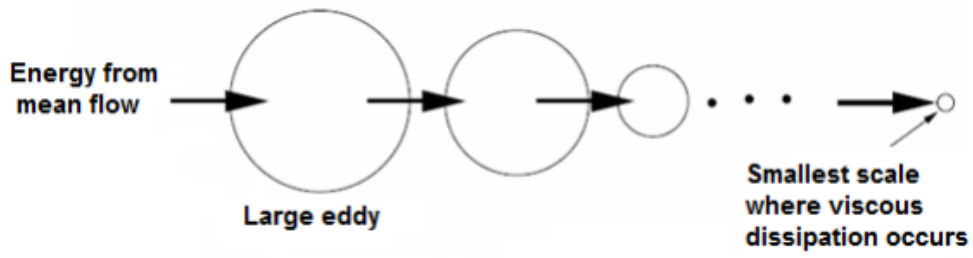

Figure 4. Schematic diagram for energy cascade [49]

2.8 Turbulent Combustion Regime (Borghi) Diagram

According to Damkohler, the propagation of turbulent flames can be divided into two distinct regimes: (i) small-scale and (ii) large-scale turbulence [53]. The interaction between the turbulent flow field and the wrinkled flame front in the latter phase is entirely kinematics and is independent of length scales. Damkohler obtained an expression that quantifies the ratio between the turbulent and laminar burning velocity in terms of laminar flame speed (S_L) and turbulence intensity (u') by equating the flame front's turbulent flame speed with the unburned gas mass flux ($\frac{D_T}{D}$) of a wrinkled flame surface moving at S_L [53]:

- For large-scale turbulence

$$\frac{S_T}{S_L} = \left(1 + C \left(\frac{u'}{S_L} \right)^n \right)^{1/n} \quad (34)$$

- For small-scale turbulence

$$\frac{S_T}{S_L} = \left(\frac{D_T}{D}\right)^{\frac{1}{2}} = \left(\frac{u`}{S_L}\,\frac{L_T}{\delta}\right)^{\frac{1}{2}} \tag{35}$$

where *n* and *C* are constants =1

In small-scale regimes, this ratio is dependent on the proportion between turbulence and molecular diffusivity. Turbulent eddies alter the unburned reactants and the reaction zone structure in this case. Regardless of the turbulent regime, S_T is always greater than S_L [50].

Different phases of turbulent combustion regimes have been observed and classified into the Borghi diagram since classical Damkohler theories (Figure 5) [11]. Reynolds (Re_T), Damkohler (*Da*) and Karlovitz (Ka) numbers are used to establish several boundaries in the Borghi diagram that represents a log-log plot of the normalized turbulence intensity (u' / S_L) and the turbulence integral length scale normalized by the laminar flame thickness (L_T / δ).

Laminar flame propagation can be viewed in the zone below Re_T =1 in this diagram. Furthermore, a weak turbulent sub-regime is bounded in the zone where 1 < Re_T <100, where the classical Kolmogorov-scaling is not followed. Re_T >>1 characterizes the majority of the turbulent combustion regimes discussed here. Chemical timescales dominate the turbulent time scale in a well-stirred reactor combustion regime, corresponding to Da < 1 [11].

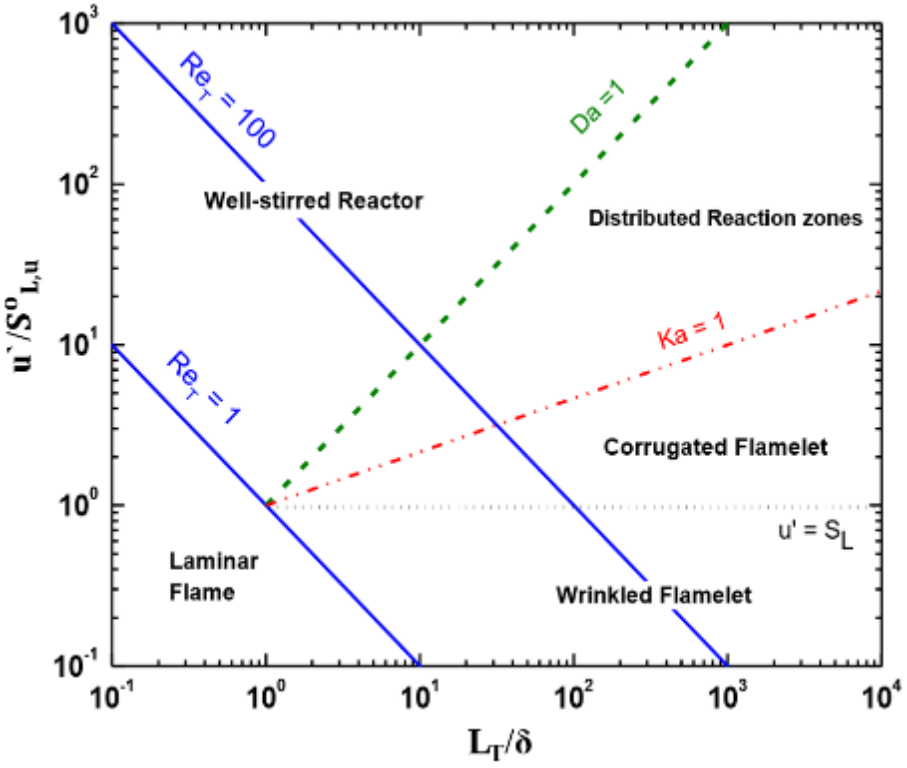

Figure 5. Classical Borghi diagram [11]

The flamelet mode exists when *ka* is less than one, and *Da* is more than one. In this regime, turbulent eddies have no effect on the laminar flame structure that comprises the preheat and reaction phases. The flame front continues to propagate until the imposed turbulent field wrinkles the laminar flamelets. In this mode, the laminar flame thickness exceeds the size of the smallest eddy within the turbulent field. Two competing processes determine the turbulent burning rate: I.) flame front self-propagation destructs the flame surface area, and II.) wrinkling of the flame surface by turbulent eddies, with the latter dominating the former [54]. The wrinkled mode and the corrugated flamelet combustion regime (weak and moderate turbulence levels, respectively) can be classified into the flamelet regime, with the $u'/S_L = 1$

borderline separating these two regimes. The Klimov-Williams limit (Ka =1) line marks the transition between the flamelet and the distributed reaction zone regime (Da > 1 and ka > 1).

Borghi's combustion regimes diagram was later modified by Peter [52] based on the Ka to include thin-reaction zones (where 1< Ka <100: when Ka=100, Ka_δ= 1, where $Ka_\delta = \delta^2 * Ka$; δ =0.1 (δ is the thickness of the laminar flame) of several hydrocarbon flames. The smallest eddy in this situation is smaller in size than the preheat zone, allowing it to penetrate it and transfer heat and mass (radical transport). The thickness of the reaction zone, on the other hand, is unaffected as its size is less than the size of the smallest eddy within the turbulence field. In the zone where $Ka \geq 100$, thickened flames or broken-reaction zones appear, in which turbulent eddies penetrate both the preheat and reaction zones, completely disrupting the laminar flame structure. Due to a considerable quantity of heat loss, the temperature in the preheat zone continues to drop in the broken reaction zone, followed by a loss of radicals and, eventually, flame extinction [11].

Furthermore, time scales and mixing lengths can be calculated to aid in the understanding of flame-turbulence interactions in the thin reaction zone and corrugated flamelet regimes. The flame and turbulent eddies interact in a pure kinematic form in the corrugated flamelet regime. As a result, the velocity of the local laminar flame (S_L) must be equal to the velocity of the eddy that will wrinkle its advancing front for ka < 1 and Re_T >> 1. As a result, the Gibson length scale (L_G) is introduced, with the following definition [11]:

$$L_G = \frac{{S_L}^3}{\varepsilon} \tag{36}$$

where ε represents turbulence dissipation rate

Eddies smaller than L_G cannot wrinkle the advancing flame front because this action is only restricted to eddies of size L_G, whilst the flame front is wrinkled by eddies larger than L_G. The boundary between the corrugated and wrinkled regimes is formed by $L_G = L_T$ when the macro-turbulent intensity level equals S_L. This situation is referred to as the lower cut-off scale for the scalar energy spectrum function. Kolmogorov and Gibson's scales are similar when Kolmogorov velocity equals S_L (Obukhov-Corrsin scale) [11], [52].

CHAPTER 3. LITERATURE REVIEW

One of the experimental configurations used for studying premixed turbulent combustion is the fan-stirred combustion bomb. These vessels allow investigating the rates of flame propagation under turbulent operating conditions, where a wide range of turbulence intensity levels (u') can be obtained and controlled conveniently. This literature review is divided into three sections. In Section 3.1, the effect of varying the fan speed and geometry is discussed first. After that, the different turbulent flame speed measurement techniques are described. Finally, the effect of varying the fuel type on the combustion characteristics is handled in the last subsection. Section 3.2 overviews literatures pertaining to using diesel and gasoline optical engines for flame visualization and diagnosing the combustion characteristics. In Section 3.3, the three commonly used approaches for modelling premixed turbulent combustion are described, and the different numerical models used in the simulation of premixed turbulent combustion through a RANS approach are discussed.

3.1 Fan-stirred Combustion Bomb

The first use of fan-stirred vessels to measure turbulent flame speed S_T (in literature, both S_T and S_t symbols are used for turbulent flame speed) is referred to Semenov [55]. Later, many researchers have considered the fan-stirred vessels to conduct their experiments. In the spherical combustion vessel, the flame initiates at the vessel's center, and it propagates radially outward in all directions with uniform turbulence. Three of the most often used ways to diagnose the flame propagation rate include

laser tomography, Schlieren imaging, and pressure trace measurements. [56]. With the use of this configuration, several advantages can be offered in comparison with the burner type, where the intensity level has to be achieved with a high mean velocity, in addition to some difficulties in stabilizing high laminar flame speeds S_L at the top of the burner surface [57]. The use of fan-stirred vessels overcomes all of these disadvantages, which are correlated with the system. It allows for the measurement of flame speeds in near homogeneous and isotropic turbulence (HIT) conditions using high values of u'.

On the other hand, the spherical combustion chamber suffers from some deficiencies as it is extremely challenging to develop them, and it is prohibitive to build them besides being very expensive. Furthermore, the absence of a well-defined surface that can be used as a reference for the measured burning velocity complicates the investigation of the time-varying flame propagation [58], [59]. Nevertheless, some previous studies claimed that these difficulties could be counteracted by making appropriate assumptions [60], [61]. For premixed turbulent combustion, the two major parameters used to characterize such flow fields are: (i) the integral length scale (L_T) and (ii) the level of turbulence intensity (u'). The largest eddy within the flow is defined as the integral length scale, whereas turbulence intensity is utilized to characterize the intensity of turbulence. The following subsections discuss the correlation between the fan speed and geometry with the turbulent flame speed. In addition, a particular focus is given for the discussion of using different turbulent flame speed measurement techniques to track the flame propagation and investigate

the flame speed. Finally, the effect of using various fuel types on the combustion characteristics is handled in the last subsection.

3.1.1 Fan Speed and Design Variation

a) Fan Speed

There is a clear contribution to the variation of turbulence intensity u' on the turbulence flame speed S_T. In the beginning, S_T starts to increase with u' until it reaches a maximum level; after that, it drops down until the flame quenching occurs. When the turbulence intensity level u' is lower than S_L ($u' < S_L$), the flame wrinkling that results from turbulence is dominated by flame propagation. This regime is not considered relevant to any industrial system. On the other hand, at higher turbulent intensity levels ($u' > S_L$), there is a significant increment in the flame speed due to the enhanced mass and heat transfer rates that result in the turbulent diffusion. Most of the apparatus used to study the turbulent flame speed in the combustion vessels emphasizes a uniform distribution of velocity fields in the vessel's center. However, two studies have revoked these two observations [62], [63] and indicated that a non-linear distribution of velocity fields exists in the spherical combustion bomb. The observation of these anomalies can refer to some specificities of the measurement setup; Nonetheless, maintaining HIT conditions within a spherical combustion bomb with a radius that equals the maximum size of the spherical flame is critical.

Birouk et al. [63] have studied the effect of fan speed variation on u' and L_T under HIT conditions. They have observed a gradual increase in u' when increasing the fan speed and turbulent kinetic energy (k) from 0.1 to 1.45 m^2/s^2. The Probability

Density Function (PDF) of the instantaneous velocity had a zero skewness (a measure of the symmetry of the probability distribution for a random variable about its mean) and a kurtosis (a measure of whether the data are light-tailed or heavy-tailed to a normal distribution) of value three at all fan speeds, which further confirms that HIT conditions have been successfully achieved inside the chamber. In addition, the isotropy and homogeneity ratios have been computed and found to be within ±5% of the ideal value required to maintain a perfect HIT condition. Integrating the longitudinal spatial correlation coefficient curve yielded the integral length scale (which was determined to be 8.6 mm), and contrary to turbulence intensity, L_T was found to be constant across all fan speeds. In a similar Plexiglas enclosure and under HIT conditions, eight continuous-wave pulsed jet actuation-controlled mechanisms have replaced the fans by Hwang and Eaton [64]. The fans were precisely controlled to achieve the desired isotropy and homogeneity. A spatial map inside an area of 1600 mm^2 in the middle of the chamber was generated. It was found that the isotropy ratio varies between 0.88 and 1.24, and the homogeneity ratio had a fluctuation of ±10% of their spatially averaged value. The turbulent kinetic energy dissipation rate has been estimated using a large eddy simulation (LES) technique. Thus, other turbulence parameters such as Kolmogorov, Euler, and Taylor scales could be evaluated [65]. Due to errors in assessing the velocity derivatives, significant variance in earlier turbulence statistical data was recorded. In addition, it was observed that the integral length scale, however, remains the same and spatially distributed in the space at all fan speeds.

b) Fan Geometry

The pitch angle of the impeller was varied by Kwon et al. [66] from 45 degrees (fixed earlier to 30degrees by Fansler and Groff [67]). They found a 50% reduction in L_T while keeping the turbulence intensity level (u′) the same in both cases. It was determined that the impeller geometry influences the magnitude of turbulent eddies, affecting the L_T scale; nevertheless, HIT criteria were not met due to impeller misalignment. The misalignment of the impeller inside the combustion vessel was verified and fixed in a later study [59], resulting in a mean flow reduction from 0.3–0.6u′ to 0.1u′, which is considered a negligible mean flow. Leisenheimer and Leukel [60] employed two different vessels radiuses (r= 25cm and r= 65cm, where r is the vessel radius). They concluded that L_T is mainly determined by the vessel's dimensions rather than the impeller's shape. Shy et al. [68] proposed placing a perforated plate ahead of the fans to prevent big vortices from forming in the flow and promote rapid mixing. In a wind tunnel, Liu [69] evaluated the effect of such plates on the downstream turbulent field flow. It was deduced that the orifice size and the solidity ratio (the ratio between the area fractions of the plate's solid parts) can be changed independently to vary both L_T and u′.

In another study [11], four high-speed central-symmetric fans were installed inside a spherical combustion bomb. Three different fan designs with a radial shape instead of an axial one were used to find the optimum impeller design to generate isotropic and homogeneous turbulence inside the combustion bomb [11]. It was noticed that there is no remarkable variation in the intensity level when using different impeller

designs, and the velocity probability density function for the three models was found to follow a Gaussian profile. The homogeneity of the flow field was found to be slightly dependent on the geometry of the impeller. However, the isotropy was observed to be insensitive to the fan geometry. As the number of blades increases (six blades instead of four), a higher deviation is observed from the isotropic turbulence. As was discussed by Kwon et al. [66], the variation in blade pitch angle affects the integral length scale. However, this variation in L_T can occur while maintaining the near HIT conditions within the combustion vessel.

3.1.2 Measurement Techniques

Different techniques can be used to measure the laminar or turbulent flame speeds of the spherically propagating flame in fan-stirred combustion bombs. These techniques vary in their setup, resolution, cost, and accuracy. In addition, each method proposes some assumptions for measuring flame speed, and different advantages and drawbacks are associated with the use of each of them. The three commonly used techniques for measuring laminar or turbulent flame speed are Schlieren imaging, pressure trace, and optical techniques. In this dissertation, the turbulent flame speed of the outwardly propagating GTL flame is measured using a pressure transducer, and the flame propagation is visualized by high-speed imaging. The present subsection aims to discuss and describe the features of these commonly used flame speed measurement techniques.

a) Schlieren Imaging

Schlieren imaging is one of the most common techniques used for S_L measurement and can conduct premixed turbulent combustion studies. In the laminar flame case, the flame starts to propagate outwardly after ignition in the radial direction. Consequently, the flame can be assumed to propagate in one direction. Despite being considered an integrated line of sight measurement technique, Schlieren imaging can be applied for configurations of such geometry. In the turbulent case, flame wrinkling results in a high anisotropy even in a well-controlled HIT environment, such as in the spherical combustion chamber. Thus, the propagation speed in the axial (out-of-plane) and the radial (in-plane) directions is not the same for any planar kernel. Nonetheless, Bradley et al. [58] demonstrated that based on the flame surface area found within the Schlieren silhouette; the average radius corresponds to a progress variable $\langle c \rangle \approx 0.1$ (where $\langle c \rangle$ is an isotherm that indicates for the percentage of combustion completion determined at the surface). Different configurations of the Schlieren setup can be used depending on various factors such as the available space, the experimental setup, and the objective behind the imaging technique [70]. However, most past research has considered using Z-type Schlieren setup [11], [47], [71]. This setup typically consists of two aluminized mirrors of spherical shape, a high-speed camera, a sharp blade knife-edge, and a single Light-Emitting Diode (LED) spotlight. The LED light beam is typically emitted from the light source and directed into the first mirror in the same line as the LED source in this configuration. The reflected beam then flows through the spherical chamber and onto the second spherical mirror, where it converges at the second mirror focal point until it reaches

the knife edge, where the dark background light white is cut off, and the remainder of the light continues to the high-speed camera. The schematic diagram for the Z-type Schlieren system is shown in Figure 6.

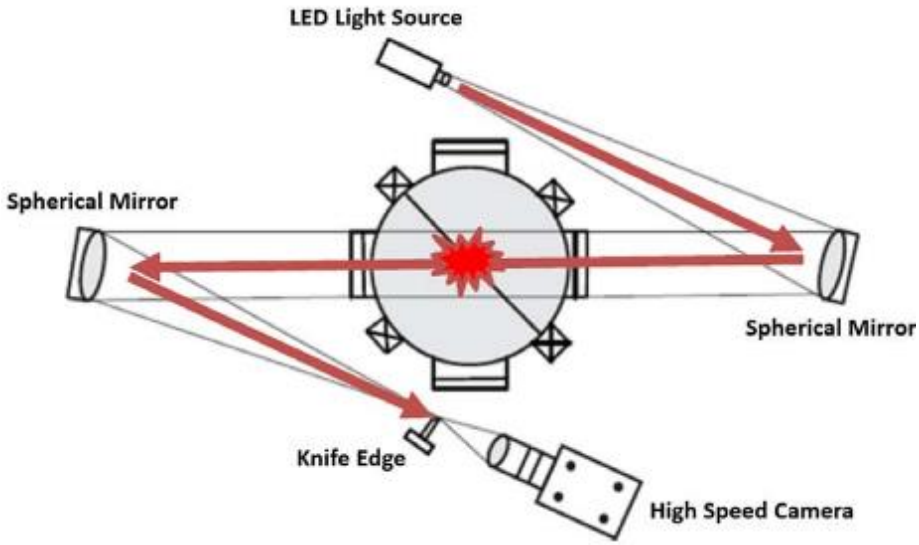

Figure 6. Schematic diagram for Z-type Schlieren setup [50]

b) Pressure Trace

The second most widely used diagnostic technique for flame speed measurement is the use of dynamic pressure trace of high frequency [50]. This technique is low-cost and does not require any optical ports to view flame propagation.

For a specific period, the pressure inside the constant-volume vessel remains constant. The unburned gases are then compressed isentropically before the flame ignites, causing a pressure increment. On the other hand, the significant pressure rise does not occur until the flame has developed spherically to a relatively large diameter. Although this system has its benefits, some drawbacks are associated with

its use [58]. Due to the confinement effects of the chamber, it is difficult to maintain the spherical shape at large flame radii. Second, at high radii, the consistency of turbulent conditions can no longer be maintained (close to the fans). Third, the isentropic compression of the unburned gas results in a significant increment in the temperature and pressure; thus, flame speeds are not captured at the initial unburned premixed conditions.

Moreover, flame visualization is not available when using this technique, making it an unattractive measurement technique. This technique was employed by Samim [10] to measure GTL laminar flame speeds in a cylindrical combustion bomb, which has been designed at Qatar University. Although the vessel was designed for high-speed imaging through the quartz glass, only a normal video camera that captures 60 frames per second was used.

Using Lewis and Von Elbe correlation, the pressure data from the pressure sensor was utilized to calculate the laminar flame speed [10]. Using a cylindrical combustion bomb and pressure transducer signals, the proposed model was also employed in another comparable study to compare the flame speed of Jojoba methyl ester with diesel fuel [71]. In addition, this technique has been employed by Ruelas et al. [72] to investigate S_L for natural gas/hydrogen fuel blends and by Bradley et al. [15] to measure the turbulent burning velocity of ethanol-air at elevated pressures.

c) Laser Tomography

The instantaneous flame surfaces can also be determined using 2D planar, single-sheet laser imaging to measure burning velocity [73], [74]. Nevertheless, there are many drawbacks associated with their use [11], [75]. There is still uncertainty about the assumption that turbulent flames have similar in-plane and out-of-plane propagation rates, and this subject is still open to debate. Additionally, huge eddies disperse the spark that originates in the vessel's center, causing a kernel dislocation away from the laser-sheet observation path. Subsequently, the location of the kernel relative to the laser sheet path cannot be identified accurately. Schlieren photography is more preferred than laser-sheet techniques because they almost give the same accuracy for flame propagation rates and are less expensive and require less equipment [74].

One of the standard techniques used in laser tomography to measure particles' velocity inside the combustion vessel is the Laser Doppler Velocimetry (LDV). In this technique, two laser beams are directed and focused on one point according to the desired velocity magnitude [76]. The two laser beams share the same wavelength, and their intersection creates a volume of interference called the probe volume [50]. This technique was employed by References [77]–[79] to compare the particle image velocimetry (PIV) measurements with those of LDV in a spherical combustion vessel, where the interrogation area in the LDV system is expanded into a 3D volume. Figure 7 shows a schematic diagram for the LDV setup.

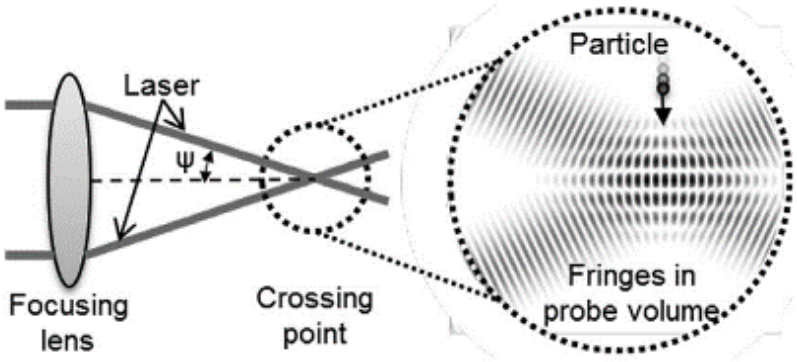

Figure 7. Schematic diagram for the LDV setup [77]

3.1.3 Fuel Type

As the fuel characteristics (reactivity, diffusivity, and exothermicity) play a significant role in determining the fuel-air combustion characteristics [78], it is of high importance to study the effect of using different types of fuels on the flame propagation rates. Several experiments were conducted in literature utilizing the spherical/cylindrical combustion bomb to match this demand. In this context, the role of this subsection comes to look at the most recent researches that have investigated the effect of different fuel properties on the mixture combustion characteristics.

a) Alkanes (C_1-C_3)

Ravi [11] studied turbulent flame displacement speeds ($S_{T,0.1}$) of alkanes, specifically methane (C_1), ethane (C_2), and propane (C_3), across a wide range of equivalence ratios ($0.7 < \Phi < 1.3$). Dimensionless Lewis number, *Le* (non-dimensional number that represents the ratio of thermal to species mass diffusivity), was found to significantly affect the displacement speeds for the mixtures

characterized by Le <1 compared to those with Le >1 at the same equivalence ratio. When methane (C_1 alkane) was used in lean conditions, it was characterized by a faster turbulent flame speed than ethane (C_2 alkane) or propane (C_3 alkane). On the other hand, rich methane had a slower turbulent flame speed than rich ethane and propane. As a result, it was concluded that for mixtures with *Le* <1, the flamelet surface area and the local burning rate increase the displacement speeds. Figure 8 depicts the change in turbulent flame speed for methane and ethane against the effective turbulence intensity ($u_k^{`}$).

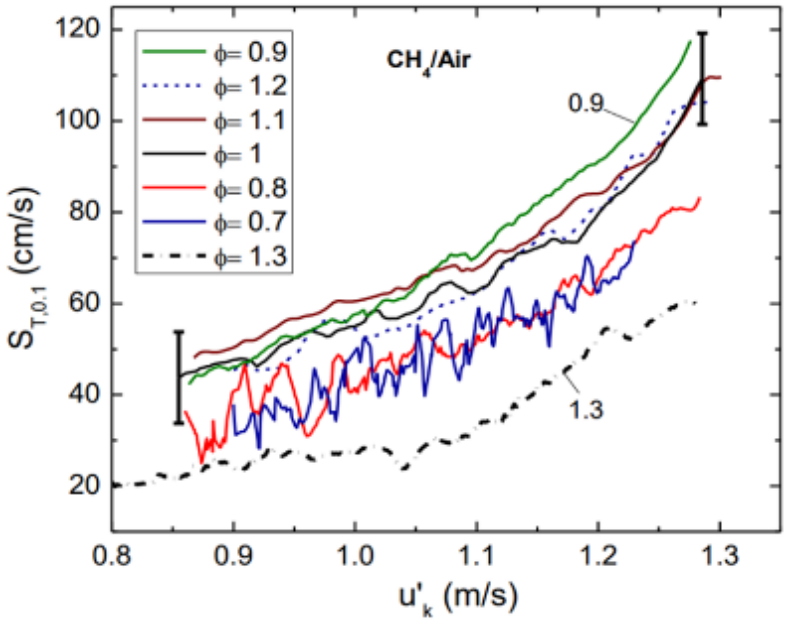

(a)

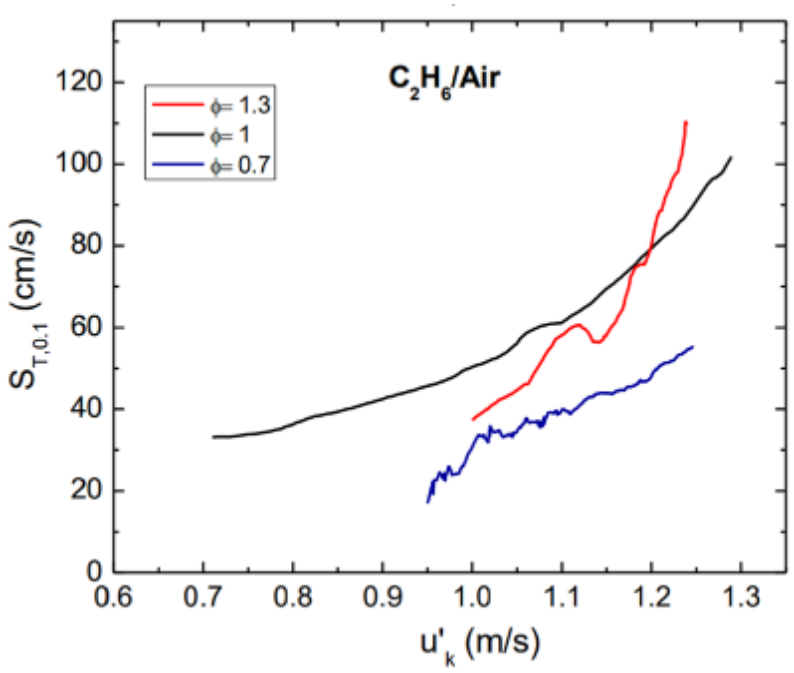

(b)

Figure 8. Flame speeds versus effective turbulence intensity ($\boldsymbol{u_k}$`) for: (a) methane-air mixture, (b) ethane-air mixture. The individual curves for each condition are the spline averages of three repeats. The estimated average scattering in flame speed is 10 centimeters per second. [11]

b) Natural Gas and Natural Gas–Hydrogen Blends

Turbulent displacement speed for a Natural Gas (NG_2) surrogate (NG_2: 1.25% n-C_5H_{12} + 2.5% C_4H_{10} + 5% C_3H_8 + 10% C_2H_6 + 81.25% CH_4) has been investigated by Ravi [11] at Φ = 0.7. $S_{T,0.1}$ for the three alkanes and NG_2 were compared using the same combustion vessel, and the results are shown in Figure 9.

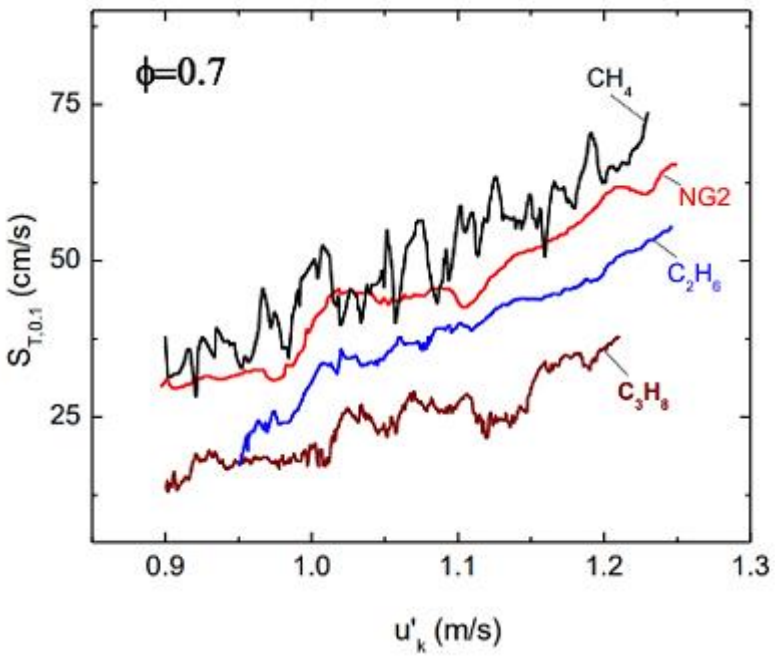

Figure 9. Alkanes and NG_2 displacement speeds at Φ = 0.7 [11]

When Φ = 0.7, the displacement speeds for methane were the highest, followed by ethane and propane. NG_2 has a very close trend to CH_4 at this condition, as NG_2 is predominantly methane. On the other hand, rich methane is characterized by lower displacement speeds than rich ethane and propane.

These trends can be explained by the Lewis number's (*Le*) effect on turbulent flame displacement speed. The local burning velocity reduces (enhances) when *Le* > 1 (*Le* < 1) due to an increase (reduction) heat release in positively curved flamelets [80]. Because the flame leading edge's mean curvature and mean strain rate are both positive, the propensity of finding positively strained and curved flamelets (convex into the direction of unburned gases) becomes higher within a reacting premixed turbulent flow [79]. In this situation, turbulent eddies cause the laminar flamelets to

stretch considerably, resulting in a significant difference between the unstretched flame speed and the local burning rate. Following that, for mixtures with $Le < 1$, an enhanced local burning rate causes the flamelet surface area, and thus the displacement speeds to increase. These effects explain why rich ethane and propane (or lean methane), which have $Le < 1$, have faster flame propagation rates. Other studies have previously documented similar observations [63], [81].

For gas-turbine combustor designers, blending hydrocarbon fuels with hydrogen is essential. This is because ultra-lean conditions allow for increased laminar flame speeds than the lean-flammability limit found in hydrocarbons. Due to the increased flame propagation rates, the propensity to flashback or auto-ignite increases as the fraction of hydrocarbons in the mixture increases. The primary mechanism for increasing laminar flame speed, which is essentially a kinematic effect, is the increase of the hydrogen radical's concentration in the combustible mixture. Ravi [11] investigated unstretched laminar flame speeds ($S_{L,u}$) and turbulent displacement speeds ($S_{T,0.1}$) for two different compositions (25% to 75% and 50% to 50% (by volume) blends of H_2 and NG_2) at various equivalence ratios (Φ) and hydrogen levels. It was observed that a large hydrogen concentration (50% H_2) caused a slight variation in laminar flame speeds between CH_4 and NG_2. Moreover, the addition of hydrogen has increased the turbulent flame displacement speed ($S_{T,0.1}$) remarkably for both fuels, and it was following the same trend as the laminar flame speeds.

c) Isooctane

Brequigny et al. [75] have experimentally investigated turbulent flame speeds for

isooctane–air mixture. Figure 10 [75] illustrates the corrected turbulent flame speed as a function of the corrected equivalent radius. As can be noticed, the flame speed increases gradually while the flame radius increases, and this can be referred to the wrinkling ratio. The increase in turbulence intensity causes a rise in wrinkling and, thus, the turbulent flame speed. Typically, the increase in wrinkling ratio is provoked by a decrease in small, turbulent scales, as was shown by Galmiche et al. [76] on the same combustion vessel.

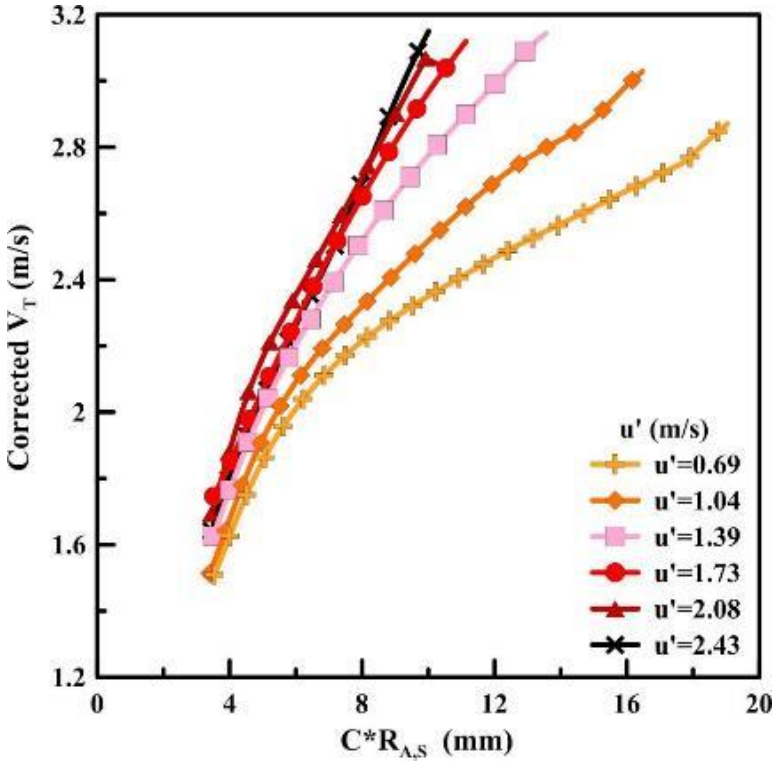

Figure 10. Corrected flame speed as a function of flame radius for different turbulent intensities obtained from the corrected Schlieren data: P = 0.1 MPa, T = 423 K, and Φ = 1.0 [75]

d) Biogas

Turbulent flame speeds for three different biogas surrogates have been experimentally investigated by Ayache [50]. It was observed that when adding more CH_4 into the mixture, the peak value shifts from the nearly lean equivalence ratio side to the stoichiometric value (Figure 11). In addition, it can be noticed that all the curves are "bell-shaped" where the maximum burning velocity occurs at a certain equivalence ratio and diminishes at the higher and lower ones [50]. The slowest burning velocity among all the surrogate's mixtures was observed when using the 50% CH_4 biogas flame, with a peak burning velocity of 27.5 cm/s at $\Phi = 0.9$. The addition of more CH_4 to the mixture has caused the peak to shift slightly toward the stoichiometric equivalence ratio, where the peak was noticed at 39 cm/s at $\Phi = 0.98$ for 70% CH_4. For the mixture (70% CH_4 and 30% CO_2), the rich and lean turbulent flame speeds were faster than those of 60% and 50% by 5 cm/s.

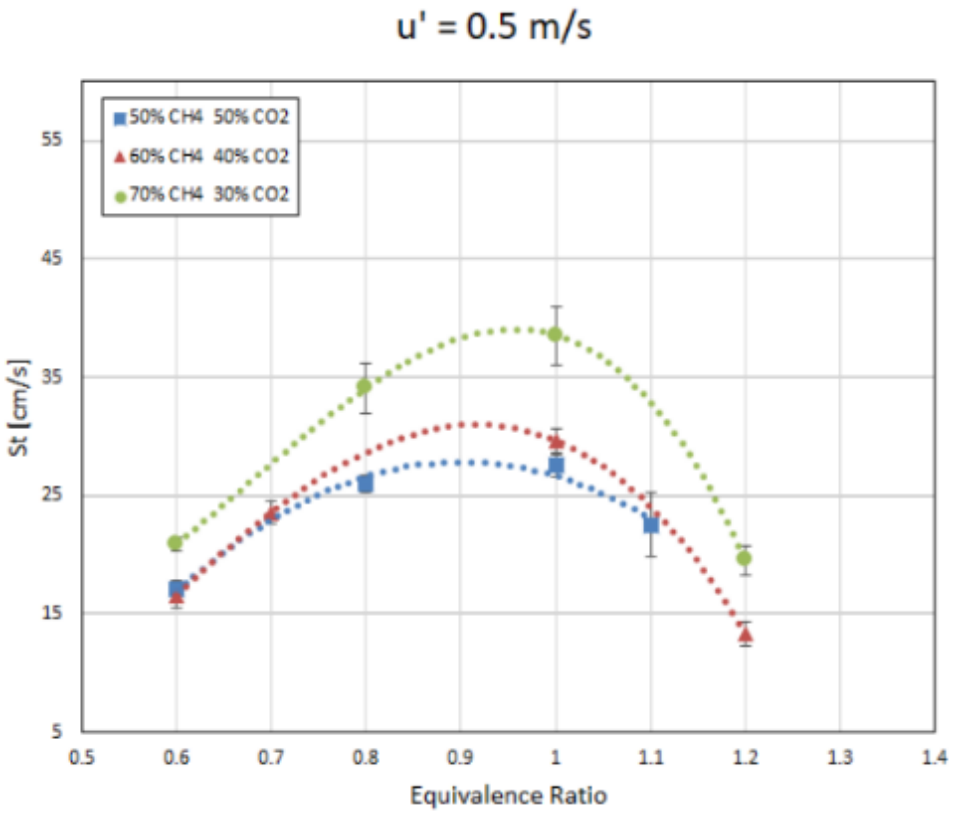

Figure 11. The turbulent burning velocity for three different biogas compositions at u`=0.5m/s [50]

e) Diesel

Laminar flame speeds for diesel fuel have been investigated by Samim [10] using a cylindrical bomb test rig that has been designed at Qatar University. It was observed that the flame speed is slightly low at lean conditions (Φ = 0.7–0.9), which further increases and peaks near stoichiometric conditions (Φ = 1.0–1.1). When the mixture becomes rich (Φ = 1.2–1.3), the flame speed starts to decrease slightly below the maximum laminar flame speed (S_L = 83 cm/s), as indicated in Figure 12. At low equivalence ratios, the excessive air causes flame quenching, and the flame becomes

unstable. As a result, the laminar flame speed is found to be low. On the other hand, using an excessive amount of fuel in the air-fuel mixture causes the combustion to be incomplete, which causes the flames speed to decrease.

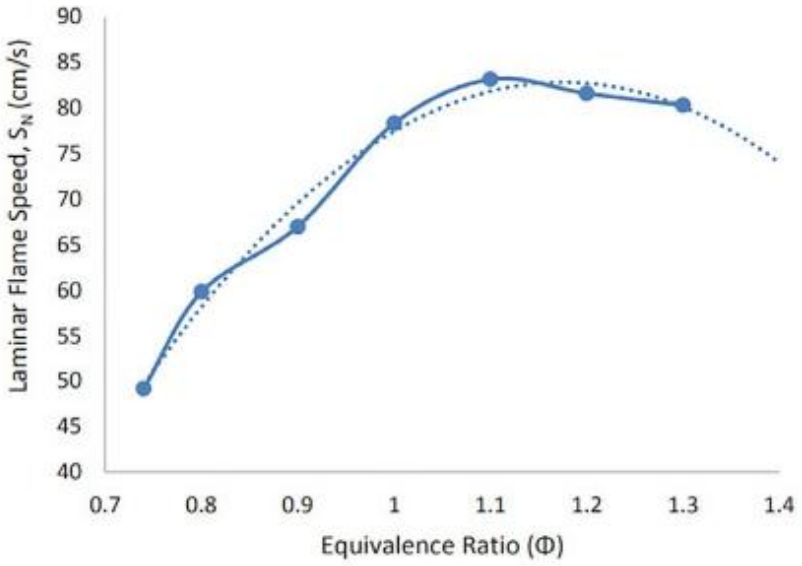

Figure 12. Laminar flame speeds of diesel fuel at different equivalence ratios [10]

f) Gas-to-Liquids (GTL) Fuel Blends

Samim has investigated the laminar flame speeds of GTL, diesel, and 50/50 diesel-GTL fuel blends over a wide range of equivalence ratios [10], as shown in Figure 13.

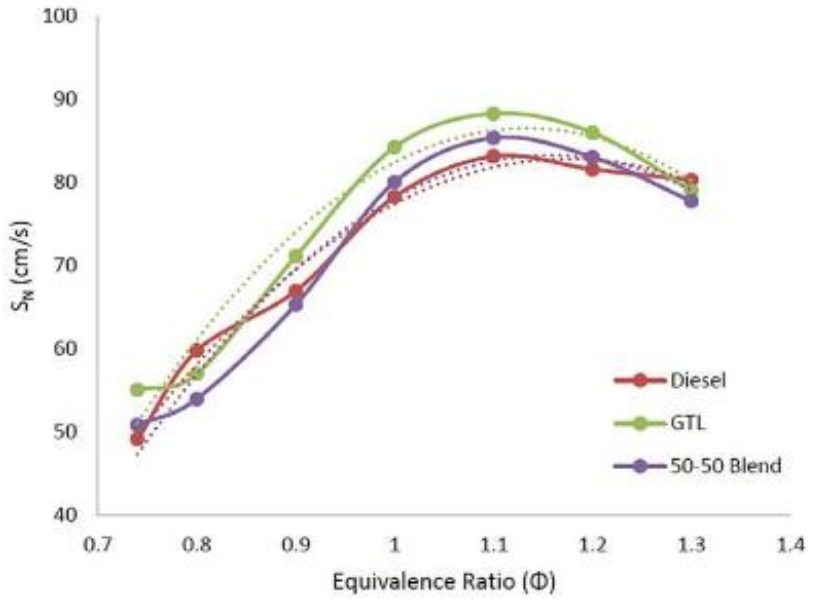

Figure 13. Conventional diesel, GTL, and 50–50 blend (laminar flame speed, S_N versus Φ) [10]

The highest laminar flame speed was observed around stoichiometry (Φ =1.0) using GTL fuel, which could be attributed to its highest calorific value. The flame speed of GTL is slightly lower than pure diesel at rich operating conditions. As a result, it can be deduced that GTL fuel can replace diesel fuel in applications where the operating conditions are close to stoichiometry, resulting in a faster laminar flame speed.

The 50/50 blend starts with the lowest laminar flame speed at the low equivalence ratios (Φ = 0.7–0.9) and maintains this behavior until it equalizes the readings of conventional diesel at Φ = 1.0. When Φ = 1.1, the flame speed for the 50/50 blend is only higher than the conventional diesel by 2–3 cm/s. After that, S_N starts to decrease lower than other fuels. Away from the stoichiometric condition, it can be

observed that the 50/50 blend has lower flame speeds than both pure fuels. However, at near stoichiometric conditions, the readings for the 50/50 blend are very close to those of diesel fuel, which indicates that this blend can replace diesel fuel in the industry to reduce exhaust emissions and keeps the environment cleaner. For the three tested fuels, the readings for the laminar flame speed at the lean conditions (e.g., excess air) are observed to be low due to flame quenching. On the other hand, excessive fuel use at rich conditions causes the combustion to be incomplete, resulting in a lower flame speed.

Discussions

Laminar flame speed S_L defines the propagation velocity of the flame front into a premixed unburned gas mixture. It was clearly noticed that using different types of fuels results in a remarkable variation in the flame speed (e.g., GTL has a higher S_L than diesel fuel at a broad range of equivalence ratios). In addition, it was observed that the laminar flame speed reaches its maximum value near stoichiometric conditions for hydrocarbon fuels such as diesel, GTL, and 50/50 diesel-GTL fuel blend. Furthermore, the laminar flame speed depends on other factors such as the temperature and pressure inside the combustion vessel.

Turbulence causes flame propagation to be promoted, causing the flame speed to be considerably higher than the laminar one. The impact of turbulence intensity on the flame speed depends on the stoichiometry and the fuel type. The effect of using different types of fuels is often explained by the impact of molecular and thermal diffusivity for the fuel on the evolution of corrugated flamelets, which can be interpreted by Lewis number, *Le* (a ratio between thermal diffusivity and molecular diffusivity). For example, it has been noticed how methane and natural gas are characterized by a higher turbulent flame speed than ethane and propane when running at lean conditions (Figure 9). However, rich methane had a lower displacement speed than ethane and propane. Also, it was observed how the mixtures of higher hydrogen content are characterized by a higher turbulent flame speed. This can be referred to the lower *Le* number of hydrogen when compared with other hydrocarbons. Moreover, it was noticed how the increase in turbulence intensity causes the flame speed to be augmented due to the rise in the wrinkling

ratio, which results in more turbulence within the mixture (Figure 10).

In an internal combustion engine, the flame speed is one of the fuel properties which determines its ability to be combusted without detonation. Subsequently, a high-flame speed combustion process should reflect in higher engine efficiencies and lower emissions due to the enhanced flame diffusivity and stability, which can thus result in a more complete combustion. The speed at which premixed flames propagate is a fundamental parameter used in several practical applications, such as combustion engines and gas turbines, to validate relevant kinetic mechanisms, which characterize the fuel's combustion behavior [73], [74].

An accurate description of the combustion phenomena is highly requested to assess the engine performance using a particular fuel type. Besides, this can positively assist in the development of advanced engine concepts for alternative fuels and petroleum-derived. Diesel, gasoline, and jet fuels are composed of several chemical compounds, and thus, making detailed predictions and modelling of fuels combustion characteristics is complex. In addition, the lack of fundamental thermochemical, physical, and kinetic data for the fuel compounds makes the study of flame speed very essential to predict engine performance and emission rates [50].

Summary

Table 1 summarizes literature studies of vessel shape and geometry, measurement techniques, fan details, turbulent characterization techniques, and fuel type.

Table 1. Summary of Literature Survey on Spherical and Cylindrical Combustion Bombs

Ref.	**Fansler et al.** [67]	**Kwon et al.** [66]	**Leisenheimer et al.** [61]	**Weib et al.** [62]	**Bradley et al.** [58]	**Ravi** [11]
Vessel Shape	Cylindrical	Cylindrical	Spherical	Cuboid with a spherical cavity at center	Spherical	Cylindrical
ID (cm)	26	26	Vessel 1(V_1): D =50	11.8	38	30.5
IL (cm)	26	26	Vessel 2(V_2): D= 130	11.8	38	35.6
No. Optical Ports	2	2+2 laser ports	2	4	3	2

Ref.	Fansler et al. [67]	Kwon et al. [66]	Leisenheimer et al. [61]	Weib et al. [62]	Bradley et al. [58]	Ravi [11]
Port Size (cm)	9.2	9.2; 10mm	Not provided	10	15	12.7
Meas. Techniques	Schlieren imaging	Schlieren imaging & Laser tomography	Pressure trace	Pressure trace	Schlieren imaging & Pressure trace	Schlieren imaging & Pressure trace
No. of Fans	4	4	V_1: 2,4,8; V_2: 4	8	4	4
Fan Diameter (cm)	13.5	13.5	V_1: 25; V_2:42	4.5	Not provided	7.62
Fan Blades	8		Not provided	6	8	3
Pitch Angle (Degrees)	45	30	Not provided	22.5	Not provided	20
Fan Width (cm)	2.3		Not provided	0.6	Not provided	3.8
Turb. Char. Tech.	LDV	LDV	five- hole pitot probe & HWA	LDV/PIV	LDV	PIV

Ref.	**Fansler et al.** [67]	**Kwon et al.** [66]	**Leisenheimer et al.** [61]	**Weib et al.** [62]	**Bradley et al.** [58]	**Ravi** [11]
Max u' (m/s)	2		V_1: 1.54 m/s; V_2:2.4 m/s	~3.7	12	3.5
Longitudinal L_T (mm)	25mm w/ u′; 40mm using 3D Gaussian u′	12.5; 19.15mm and 3D Gaussian u′ profile	V_1: 9 ±1mm; V_2: 24 ±2mm	3.9	20	50
Fuel	Not provided	Hydrogen +Air+Nitrogen	Not provided	Methane-Air & Propane-air & Hydrogen	Ethanol-Air & Propane-Air	Alkanes (C_1-C_3) & Natural gas & Natural gas-Hydrogen blends

As apparent from Table 1, the vessel geometry among these studies is different in terms of the Internal Length (IL) and the Internal Diameter (ID), and the measurement techniques used for investigating the turbulent flame speed are not the same. The most three common techniques are Schlieren imaging, the pressure trace and the optical techniques such as the LDV and PIV. Also, it can be figured out that the number, the geometry of fans and the number of fan's blades are also other

factors that are different among these studies. Due to that, it is expected that the turbulence intensity ($u`$) and the turbulence integral length scales (L_t) are found to be affected and different. Finally, it can be noticed in the last row that the flame speed and combustion characteristics of several hydrocarbon fuels have been the topic of these different studies such as hydrogen, natural gas and several alkanes.

The major findings of this literature survey are:

(1) The turbulent flame speed was noticed to increase roughly linearly with the turbulence intensity up to a certain level, and then passes through a bending region and finally exposed to quenching at very high intensities.

(2) The integral length scale (L_t), was noticed to be affected by the vessel geometry and the pitch angle of the fan blades rather than the level of turbulence intensity.

(3) The effect of varying the fan blades shape on $u`$ was investigated by Ravi [14], and it was found that there is no remarkable variation in $u`$ when using different blades shapes.

(4) The magnitude of the turbulent flame speed depends mainly on the physico-chemical and combustion properties of the air-fuel mixture and on the level of turbulence intensity.

The missing research gap in the literature that this dissertation is targeting is the investigation of the premixed turbulent combustion of heavy hydrocarbon liquid fuels such as diesel and GTL (and their 50/50 blend), which are characterized by different physico-chemical and combustion properties compared to those in the literature.

3.2 Optical Engine

Thermodynamics Single Cylinder Engines (TSCE) in Research and Development applications provides a versatile environment for testing engine operation's primary process and modules. Optical Single Cylinder Engines (OSCE) have less sophisticated diagnostic instrumentation than Multi-Cylinder Engines (MCE), and the simpler mechanical structure allows for more freedom in applying refined diagnostic access [82]. Figure 14 shows a schematic diagram for the major components of the single-cylinder optical engine [83].

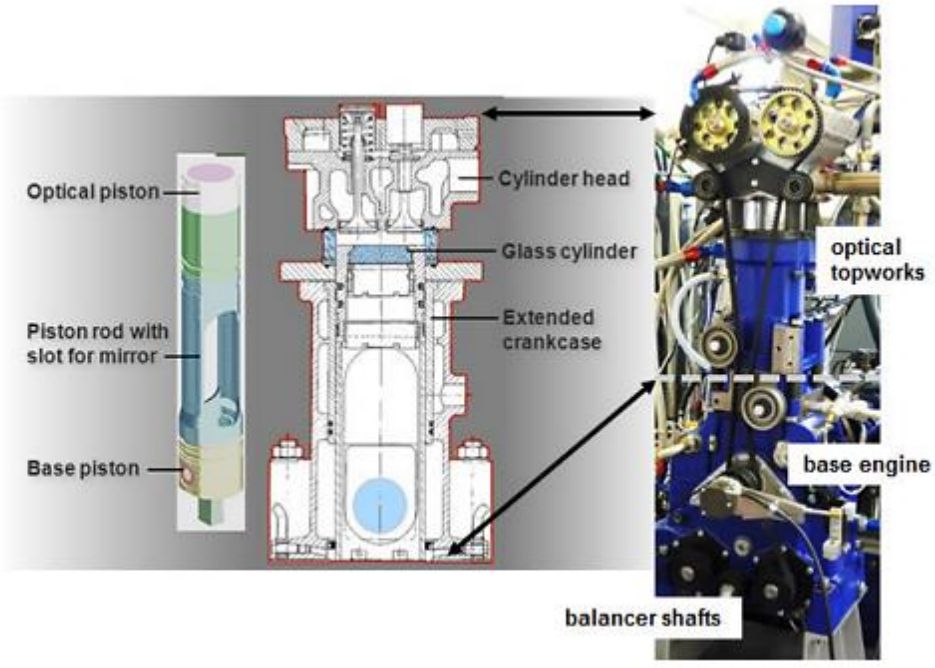

Figure 14. The complete assembly of an OSCE [83]

The extended crankcase design is employed to access the combustion chamber from the bottom side using a 45-degree mirror. Besides, it allows for separating the base engine's lube oil from the "dry" zone of the combustion chamber [83]. In general, optical engines are known to have high flexibility in their operation due to the separation of many peripheral modules like the coolant pumps, heat exchangers, fuel supply systems in addition to the lube oil from the engine[83]. Optical pistons, consisting of the piston rod, base piston, and piston crown, are occupied with a flat window entry [84]. The piston crown is designed to vary according to GDI applications [85]. In addition, the gasket rings are installed on the piston crown's lower end and slide on the liner part of the metal only. As a result, the compression ratio of the engine is substantially reduced [86]. Piston rings are located in the lower position rather than the normal position in OSCE. Using this low ring position and 0.5mm clearance between the cylinder and linear reduces the compression ratio of about two units [87].

Thus, it is clear how OSCE can highly enhance many features in engine combustion and emission, and its contribution to other research and development applications is essential. Complex thermodynamics, optical, or emission diagnostic techniques may be used in OSCE measurement instrumentation. The efficient use of these complex systems can be simplified by the proper usage of the diagnostic methods and with the adaption of different modular arrangements in that platform.

3.2.1 Diesel Optical Engine

Diesel engines that are widely used as power generators, mechanical engines, or mobile drives find extensive use in construction equipment, automobiles, locomotives, and countless industrial applications. Their realm involves almost all industries and can be observed daily at several applications [88]. Due to this importance, many research types are continuously developing to study their performance characteristics and lower emission rates. One of the most reliable research tools to match this demand is Optical Single Cylinder Engine (OSCE), which has different visualization and measurement capabilities. This subsection aims to lay a literature review on the most recent research utilizing diesel optical engines to conduct experimental studies in different aspects (ignition delay time, in-cylinder pressure, heat release rate, and flame luminosity).

a) Ignition Delay Time

Ahmad et al. [86] studied the combustion characteristics of diesel-methane Dual Fuel (DF), more specifically, the Ignition Delay Time (IDT) and the combustion duration (CD) as a function of methane equivalence ratio (ϕ_{CH4}). It was found that the increasing impact of the inhibiting methane on the ignition of pilot diesel causes IDT to increase as CH_4 increases [89], [90]. In the same principle, the Combustion Duration (CD) increases when ϕ_{CH4} increases in the mixture. However, when ϕ_{CH4} = 0.85, the CD begins to drop, which can be explained by the presence of local fuel-rich zones in the advanced (second and third) combustion stages. Due to pilot diesel-rich zones, the combustion chamber is expanded, causing the premixed methane-air combination to

begin burning fast at the end of the second stage and during the high-intensity third stage. Cheng et al. [89] evaluated the Cycle-to-Cycle Variation (CCVs) using an optically accessible heavy-duty diesel engine fuelled with methane (primary fuel) and diesel (pilot fuel). It was observed that decreasing λ_{CH4} in the fuel mixture results in a monotonic decrease in the global intensity. The addition of CH_4 has an increasingly high effect on high and low-temperature reactions in the CH_4-diesel-air mixture, resulting in more luminous soot formation and a longer Ignition Delay Time (IDT).

b) In-cylinder Pressure

Lee et al. [90] investigated the effect of varying the injection timing on the in-cylinder pressure rise using a diesel optical single-cylinder engine. In addition, a comparison between the experimental and simulation results was conducted. It was found that the maximum in-cylinder pressure decreases more when the injection timing is retarded, and the simulation results have approved well the same. Cheng et al. [89] evaluated the cylinder pressure as a function of λ_{CH4} using an optically accessible heavy-duty diesel engine fuelled with methane (primary fuel) and diesel (pilot fuel). It was observed that CH_4 plays as an inhibiting factor for combustion in the mixture. As a result, adding more CH_4 into the mixture causes the peak pressure to be higher. In addition, Li et al. [91] have used OSCE to measure the cylinder's mechanical deformation of a diesel optical single-cylinder engine at two different intake pressures (1.1 and 2.7 bar) that correspond to two different Top Dead Centre (TDC) cylinder pressures (31 and 80 bar), respectively. It was deduced that as the in-cylinder pressure rises, the mechanical deformation becomes more significant [92].

c) Heat Release Rate

Dual-fuel combustion, according to Ahmad et al. [86], is a complex process to analyze. The chemical and physical features of pilot-fuel sprays and the concentration of each gas in the premixed mixture all influence the combustion process. Pilot diesel is injected during the compression stroke near TDC in diesel-methane DF combustion, providing sufficient energy for the premixed mixture to ignite. As a result, heat is released with complex chemical and physical interactions. According to several studies, the DF combustion process varies depending on combustion modes and phases, necessitating more research [92], [93]. Heat Release Rate (HRR) profiles were observed to have multiple peaks (M-shaped), varying in magnitude depending on the amount of CH_4 in the fuel mixture. HRR profiles such as those are observed in many studies [94], [95]. Cheng et al. [89] have evaluated the HRR as a function of λ_{CH4} using an optically accessible heavy-duty diesel engine fuel with methane (primary fuel) and diesel (pilot fuel). The inhibiting effect for the addition of CH_4 was clearly observed in HRR. This can be referred to the weak flammability of the air-CH_4 mixture for the ultra-lean CH_4 condition. There is an unstable combustion and a slow flame speed, which results in a lower HRR.

d) Flame Natural Luminosity

Lee et al. [90] used the visualization kit between cylinder head and blocks to perform visualization experiments. It was found that the flame luminosity increases more when the injection timing is advanced. Figure 15 illustrates the variation of flame luminosity (NL) as a function of the crank angle at five different injection timing

(including the baseline case). In addition, Flame NL images were captured by Ahmad et al. [86] and others [95], [96] using OSCE.

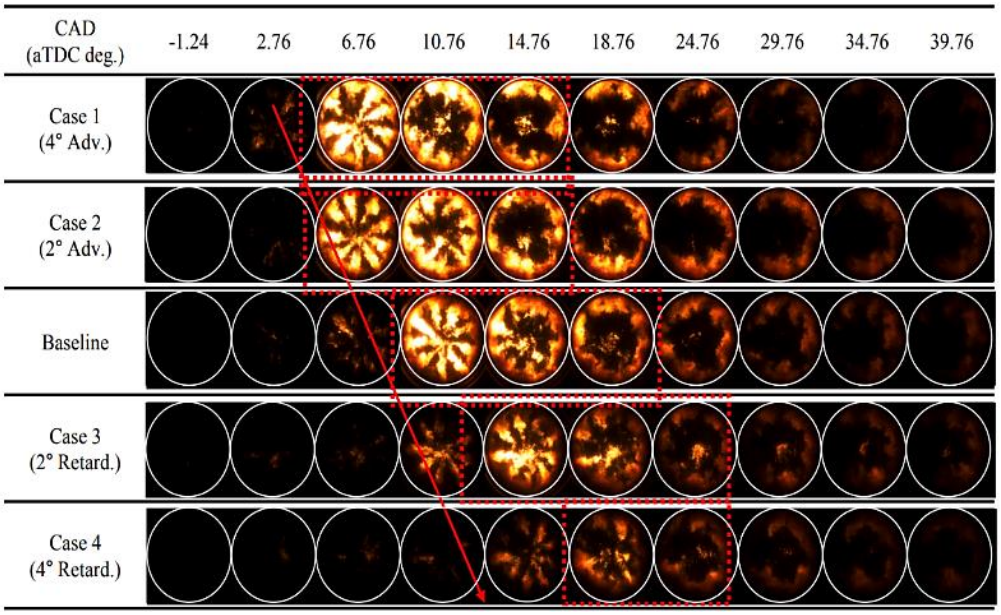

Figure 15. Flame luminosity as a function of injection timing sweep for five different cases [90]

Summary

A summary of studies using diesel optical engines is provided in Table 2 for the reader's convenience.

Table 2. Summary of Literature Survey on Diesel Optical Engine

Reference	**Ahmad et al., 2019** [86]	**Cheng et al., 2019** [89]	**Lee et al., 2019** [90]	**Li et al. 2018** [91]
Fuel	Diesel /methane	Diesel / methane	Diesel / Air / EGR Air	Diesel
Equivalence Ratio	0.57, 0.63, 0.72, 0.85	0.50, 0.56, 0.625	-	1.0
Engine Temperature (K)	353	298, 318, 328	-	323
Engine Speed (rpm)	1400	1400	1500	1200
Compression Ratio	13.5:1	17.9:1	16.0:1	13.7:1
Intake Air Pressure (bar)	1.0	1.1	-	1.1, 1.5, 1.9, 2.2, 2.7
IMEP (bar)	9 to 10	10	6	-
Swirl Ratio	2.7	2.7	2.4	-
Optical Access	Bowditch-designed optical access	Bowditch-designed optical access	Bowditch-designed optical access	Bowditch-designed optical access
Pressure Sensor Type	Kistler type 6125C	Kistler type 6125C	Kistler type 6125C	Kistler 4603B10
Camera Type	Photron Fastcam APX-RS 250 K	Photron Fastcam APX-RS)	Photron AX-100,	Photron SA-X2

Reference	**Ahmad et al., 2019** [86]	**Cheng et al., 2019** [89]	**Lee et al., 2019** [90]	**Li et al. 2018** [91]
Frame rate (fps)	9000	9000	100	21000
Main Measurements	Natural luminosity Ignition delay time Combustion duration Heat release rate	Heat release rate In-cylinder pressure Global intensity Pressure-based COV	Heat release rate Ignition Delay Time Combustion duration In-cylinder pressure	Heat release rate In-cylinder pressure In-cylinder volume Piston displacement
CAD at Injection	356 ATDC	-15 ATDC	-22.24 ATDC	-
CAD at Exhaust	150 ATDC	-	126 ATDC	-
No. of Averaged Cycles	150	150	-	50

It can be deduced from this summary in Table 2 that diesel optical engines are used as advanced research tools in the field of premixed turbulent combustion and they have different visualization and measurement capabilities. They have less sophisticated diagnostic instrumentation than Multi-Cylinder Engines (MCE), and the simpler mechanical structure allows for more freedom in applying refined diagnostic access [86]. The operating conditions can be varied conveniently to match the actual operating conditions in terms of engine temperature, engine speed and the intake air pressure. Also, they are equipped with advanced visualization technique. The standard Bowditch-designed optical access is used with the Photron Fastcam for high-

speed imaging and flame visualizing through its different growth stages. The main measurements that can be obtained from these advanced setups are: flame natural luminosity, ignition delay time, combustion duration, the heat release rate, the global intensity and the in-cylinder pressure.

3.2.2 Gasoline Optical Engine

Gasoline optical engines behave as a representative tool in researching and developing new concepts for combustion in spark ignition (SI) engines. This is due to their capabilities in applying quantitative and qualitative diagnostic techniques, which can be used to study combustion and emissions, mixing, and in-cylinder flow characteristics [97]. Such experimental measurements are essential for validating the computational model; however, they can also be processed to provide detailed information about the physical processes inside the cylinders. Subsequently, they help develop new combustion strategies as the Gasoline Direct Injection (GDI) engines [98]. In this context, the role of this section comes to give a glance at the past researches, which have utilized gasoline optical single-cylinder engine as a research tool to perform combustion studies.

a) In-cylinder Pressure

Boggio et al. [99] used an accessible optical single-cylinder spark-ignition engine to carry out measurements that show the effect of adding low levels of hydrogen to methane (5%, 10%, 20% volumetric basis) on the in-cylinder pressure under lean-burn and stoichiometric conditions. Thermodynamic results illustrated an increase in the maximum in-cylinder pressure as more hydrogen is added to methane fuel. This effect becomes more evident while operating the engine in the leanest condition. Donadio et al. [96] have also studied the combustion characteristics using thermodynamic (heat release) depicted from in-cylinder pressure measurements. Three different fuels were used in the optically accessible single-cylinder gasoline

engine: pure gasoline (G100), pure ethanol (E100), and 50% ethanol/gasoline blend (B50). As expected, the use of pure ethanol has resulted in the highest maximum in-cylinder pressure at both operating conditions, while the lowest belongs to pure gasoline. In addition, it was observed that the time at which the peak in-cylinder pressure is reached is in advance for pure ethanol when compared with other tested fuels. Consequently, it can be deduced that faster combustion than other fuels characterize ethanol. In addition, Martinez et al. [97] investigated the combustion characteristics of gasoline fuel at five different air-fuel ratios utilizing an optically accessible Direct Injection Spark Ignition (DISI) single-cylinder engine.

b) Flame Propagation Rate

Yang et al. [98] designed two tumble deflectors with two different Tumble Ratios (TR=1.5 and 2.2) using computational fluid dynamics and computer-aided design. Afterward, they were 3D printed and then installed on the optical engine intake ports, and then the firing tests were performed. The tumble deflectors were used to direct the flow into the intake ports so that changing the deflector thickness causes a variation in the level of the tumble. The use of the first (TR=1.5) and second (TR=2.2) tumble deflectors has resulted in a 13.9% and 34.5% increment in the flame propagation rate. This can be interpreted by the increase in TKE, which facilitates the mass-heat transfer between the unburned and burned zones, which results in a shorter combustion duration and an earlier heat release. Besides, a delayed and less appearance of yellow flame was originated, which indicates a reduced soot formation.

Boggio et al. [99] also investigated the flame growth speed and flame development for ethanol and gasoline. It was observed that ethanol fuel is characterized by a faster combustion when compared to gasoline. Moreover, the flame growth speed was obtained for both fuels by deriving the interpolating curves, which further confirmed the rapid development of ethanol flame upon ignition.

c) Indicated Mean Effective Pressure

Chen et al. [100] investigated the effect of using different spark plug types and spark ignition energy on the optical engine Indicated Mean Effective Pressure (IMEP) that operates with natural gas. The highest IMEP was observed at a specific crank angle for each spark plug configuration. The single-claw spark plug achieves its maximum IMEP of 5.87 bar at a spark timing of 20 °CA, whereas the multi-claw spark plug achieves its maximum IMEP (IMEP = 6.32) at a spark timing of -14 °CA. Therefore, it is suggested that when the engine is run under 50 mJ ignition energy, the engine's thermal efficiency can be enhanced by using a multi-claw spark plug since it improves combustion stability and thus optimizes the combustion phase. Yang et al. [98] also considered the effect of using the three different tumble deflectors on the optical engine IMEP from 100 consecutive cycles. It was noticed that the average IMPE of TR = 0.5 was about 2.59 bar, and with the use of the tumble deflectors, it increased to 2.81 bar and 3.02 for the TR=1.5 and TR=2.2 deflectors, respectively. This can be referred to the increased TKE and flow velocity found in the same work. Besides, this can also be explained by the faster flame propagation using the tumble deflectors. Martinez al. [97] found that as the air-fuel ratio was augmented, the IMEP

decreased as the amount of fuel injected was reduced compared to the stoichiometric case

d) UHC & NO_x Emission

Boggio et al. [99] have considered the analysis of exhaust gases, namely, UHC and NO_x, as they provide valuable information about combustion chemistry. UHC emissions are reduced when more hydrogen is added to the blend at the same air-to-fuel ratio, as reported in another study [101]. The can be explained by the reduction in the volume composition of methane in the air-fuel mixture. The highest value for NO_x was reported when operating with the stoichiometric combustion condition, which could be referred to the thermal effect of gases [102]. When operating with lean mixtures, two competing factors (low-burned gas temperature and high concentration of oxygen) possess different weights, considering that temperature has a more dominating effect resulting in less NO_x formation. NO_x concentration was reduced by 95% when operating at the leanest case, and this value is very close to the efficiency of a three-way catalytic converter [103]. Thus, it is highly emphasized to run the engine with a lean operation to reduce emissions and increase efficiency while paying attention to the use of catalytic converter in reducing HC and CO when operating at this condition [101].

Summary

A summary of studies using gasoline optical engines is provided in Table 3 for the reader's convenience.

Table 3. Summary of Literature Survey on Gasoline Optical Engine

Reference	**Boggio et al., 2018** [99]	**Yang et al., 2019** [98]	**Chen et al., 2019** [100]	**Martinez al., 2017** [97]
Fuel	Methane / Hydrogen blends	Gasoline	Methane	Gasoline
Equivalence Ratio	1.0, 0.71	1.0, 0.71	1.0	1, 0.77, 0.71, 0.67, 0.625
Engine Temperature (K)	330-335	298	368	330-335
Engine Speed (rpm)	900	1200	800	1000
Compression Ratio	-	11:1	13:1	10:1
Optical Access	Bowditch-designed optical access	Bowditch-designed optical access	Bowditch-designed optical access	Bowditch-designed optical access
Pressure Sensor Type	Quartz pressure transducer	Kistler type 6125C	Kistler type 6125C	-
Camera Type	PCO Dimax S1	High-speed color NAC CMOS	Photron SA-Z	Optronis CamRecord 5000
Frame rate (fps)	5400	-	5000	5000
CAD at Spark	-14 ATDC	15 BTDC	-18 ATDC	10,15,20,25,30 BTDC

Reference	**Boggio et al., 2018** [99]	**Yang et al., 2019** [98]	**Chen et al., 2019** [100]	**Martinez al., 2017** [97]
No. of Averaged Cycles	200	100	150	200
Main Measurements	In-cylinder pressure	Tumble ratio	In-cylinder pressure	Fuel conversion efficiency
	UHC, CO, and NO_x emission	Turbulent kinetic energy	Mass fraction burned	In-cylinder pressure
	Flame propagation rate	Swirl ratio	Flame development	Heat release rate
	Maximum flame penetration	Indicated mean effective pressure	Indicated mean effective pressure	Indicated mean effective pressure

Gasoline optical engines behave as a representative tool in researching and developing new concepts for combustion in spark ignition (SI) engines. This is due to their capabilities in applying quantitative and qualitative diagnostic techniques, which can be used to study combustion and emissions, mixing, and in-cylinder flow characteristics [101], as shown in Table 3. They feature less sophisticated diagnostic equipment than Multi-Cylinder Engines (MCE), and their mechanical construction provides for more flexibility in applying refined diagnostic access [86]. In terms of engine temperature, engine speed, equivalence ratio, and intake air pressure, the operating conditions can be easily changed to fit the actual operating conditions. They are also equipped with cutting-edge visualization techniques. The high-speed imaging

at a fast rate of about 5000fps allows for advanced flame visualization through its different growth stages. Flame propagation rates, maximum flame penetration, turbulent kinetic energy, tumble and swirl ratios, fuel conversion efficiency, the heat release rate, in-cylinder pressure, IMEP and different engines emission rates are the main measurements that may be derived from these advanced setups.

3.3 Modelling of Premixed Turbulent Combustion

This section describes the three commonly used approaches for modelling premixed turbulent combustion: Direct Numerical Simulation (DNS), Reynolds-averaged Navier-Stokes (RANS), and Large Eddy Simulations (LES) approach. This is followed by an introduction to the different numerical models used in the simulation of premixed turbulent combustion based on several past studies. Finally, a summary of these numerical models is presented, which aims to compare the features and drawbacks associated with the use of each of them.

3.3.1 Computational Modelling Approaches

Numerical solutions for turbulent premixed combustion applications can be achieved through one of these three computational approaches: Direct Numerical Simulation (DNS), Large Eddy Simulations (LES), and Reynolds-averaged Navier-Stokes (RANS) approach. These three approaches can describe the reaction flow behavior by providing a solution for the continuity (Equation 37), momentum (Equation 38), and reactive scalar (Equation 39) equations [49], which are rather difficult to be achieved analytically.

- **Continuity Equation**

$$\frac{\partial \rho}{\partial t} + \frac{\partial (\rho u_i)}{\partial x_i} = 0 \qquad (37)$$

- **Momentum Equation**

$$\frac{\partial(\rho u_i)}{\partial t} + \frac{\partial\left(\rho u_i u_j\right)}{\partial x_i} = \frac{\partial\left(\rho \tau_{ij}\right)}{\partial x_j} - \frac{\partial p}{\partial x_i} + \rho f_i \tag{38}$$

where,

p is the normal stress or pressure

τ_{ij} are the viscous stresses

f_i are the external body forces

- **Reactive Scalar Equation**

$$\frac{\partial(\rho Q)}{\partial t} + \frac{\partial(\rho Q u_i)}{\partial x_i} = \frac{\partial}{\partial x_i}\left(\rho \alpha \frac{\partial Q}{\partial x_i}\right) + \dot{S_Q} \tag{39}$$

Equation 39 is used to properly characterize a chemical reactive flow, in addition to the continuity and momentum equations. It is used to describe the transport of an arbitrary scalar Q (mass fraction or reaction progress variable in premixed combustion), and it is typically written in this form. The scalar temporal variations and convective transport are described by the two LHS terms, while the two terms can describe the molecular diffusion of the scalar Q on the RHS, where α is the diffusivity and $\dot{S_Q}$ is a source term describing the destruction or production of the scalar Q [104].

The flow characteristics and geometry, the required accuracy, the purpose of simulation, and the computational power are all factors that justify the selection of a suitable approach. In DNS, all the turbulent scales are determined explicitly, and the simulation captures their effect on the combustion process. However, DNS is

computationally very expensive and thus can only be applied to flows under low to moderate Re_T of simple geometries. On the other hand, the use of RANS is computationally very cheap and thus found to be used in many industrial applications [105]. The RANS approach provides a solution for the flow's mean quantities (Favre or Reynolds averaged quantities). As a result, the averaged equations require a closure model, such as a turbulence model to close the turbulent stress terms and a turbulent combustion model to close the heat release rate [106]. The LES approach explicitly calculates turbulence large eddy scale sizes, whereas the small eddy scale sizes are modeled using a sub-grid closure. LES instantaneous balance equations are filtered to obtain the balance equations. This approach is computationally more expensive than RANS [107].

I) Direct Numerical Simulation (DNS)

DNS approach is claimed to describe the turbulent flow behavior accurately and completely, as it resolves the whole range of turbulence time and length scales from the largest to smallest Kolmogorov scale. Therefore, this eliminates the need for modelling [108]. DNS is used to validate the predicted outcomes obtained from RANS or LES approaches when the experimental results are obtained. However, studying a turbulent flow in practical systems requires a large amount of resources and computational time. To reduce the numerical errors that stem from the estimation of the model governing equations, schemes of high order discretization are demanded for use. In addition, the identification of a suitable boundary layer requires considerable attention. Despite the rapid increase and development in computational

techniques, the DNS approach can only be applied to flows under low to moderate Re_T of simple geometries [49].

II) Reynolds Averaged Navier-Stokes (RANS)

RANS approach is the most widely used modelling technique in industrial applications. In contrast to DNS, all the turbulent scales of the energy spectrum are modeled. However, the grid size is significantly larger than the ones found in the DNS approach, thus providing cheaper and faster numerical results [105]. Unlike DNS, only average flow fields are obtained as a solution. All the flow variables are decomposed into mean and fluctuating components in the governing equations, using the Reynolds decomposition method, and the time averaging is applied to each term over a sufficiently long time interval $\Delta t = t_2 - t_1$. Time averaging for any flow variable q is expressed as [49]:

$$\bar{q} = \lim_{\Delta t \to \infty} \frac{1}{\Delta t} \int_{t_1}^{t_2} q(t)dt \; ; q(t) = \bar{q} + q'(t) \tag{40}$$

The averaging methods have to be reformulated as ensemble averages for transient cases to consider mean quantities' dependence on time. Applying the Reynolds-averaging method (expressed in Equation 40) to a reactive flow leads to variation in the density. Thus the correlations of velocity fluctuations and density are formed, requiring additional modelling [104]. To avoid these complications, Favre-averaging (density-weighted averaging) is applied to each flow property q in the reactive flow [49]:

$$\breve{q} = \frac{\overline{\rho q}}{\bar{\rho}} \; ; q(t) = \; \breve{q} + q'(t); \;\; \widetilde{q}^{``} = 0; \;\; \breve{\breve{q}} = \breve{q} \tag{41}$$

Substituting Equation 41 into mass, momentum, species, and energy equations yields the so-called Favre-averaged Navier Stokes equations as follows [49]:

- **Mass Equation**

$$\frac{\partial \bar{\rho}}{\partial t} + \frac{\partial (\bar{\rho}\, \widetilde{u_i})}{\partial x_i} = 0 \tag{42}$$

- **Momentum Equation**

$$\frac{\partial (\bar{\rho} \widetilde{u_i})}{\partial t} + \frac{\partial (\bar{\rho} \breve{u}_i \breve{u}_j)}{\partial x_j} = \frac{\partial (\widetilde{\tau_{ij}} - \bar{\rho} \widetilde{u_i^{``} u_j^{``}})}{\partial x_j} - \frac{\partial \bar{p}}{\partial x_i} + \overline{\rho f_i} \tag{43}$$

- **Species Equation**

$$\frac{\partial (\bar{\rho} \widetilde{Y_k})}{\partial t} + \frac{\partial (\bar{\rho} \breve{u}_i \breve{Y}_k)}{\partial x_i} = - \frac{\partial \overline{J_i^k}}{\partial x_i} - \frac{\partial \left(\bar{\rho} \widetilde{u_i^{``} Y_k^{``}} \right)}{\partial x_i} + \overline{\dot{\omega}_k} \tag{44}$$

- **Energy Equation**

$$\frac{\partial (\bar{\rho} \widetilde{h})}{\partial t} + \frac{\partial (\bar{\rho} \breve{u}_i \breve{h})}{\partial x_i} = \frac{\overline{Dp}}{Dt} - \frac{\partial \left(\bar{\rho} \widetilde{u_i^{``} h^{``}} \right)}{\partial x_i} - \overline{\tau_{ij} \frac{\partial u_i}{\partial x_j}} + \overline{\rho u_i f_i} + \bar{\dot{Q}} \tag{45}$$

where $\widetilde{u_i^{``} u_j^{``}}$ represents the unknown Reynold stresses, Y_k mass fraction of species, $\dot{\omega}_k$ the rate of chemical reaction, h the enthalpy, τ_{ij} the viscous stresses, f the external body forces and $\dot{Q}$ is the heat release rate. Two major consequences arise from this averaging process. First, the fine flow details are eliminated, and second, new terms in the time-averaged equations appear, which do not present in the initial time-dependent governing equations. One such example is the appearance of the additional

term $\widetilde{u_i}\widetilde{u_j}$ in the momentum equation (Equation 43), and these represent Reynolds stresses or turbulent stresses. These stresses and other unknown terms that appear in the time-averaged governing equations can be approximated through a method known as the closure problem. These turbulent stresses can be closed by introducing the eddy viscosity concept proposed by Boussinesq [52] or by solving the turbulent stresses transport equation. The latter method allows solving more unknown terms in the closure problem and is thus considered numerically more demanding. The zero, one, and two-equation models are all based on the Boussinesq approximation method, which offers the modelling of turbulent eddy viscosity. Prandtl's mixing length hypothesis [109] is the foundation for the zero-equation model. Fluid density, characteristic turbulent velocity, and a length scale known as the mixing length are used to characterize eddy viscosity. In the one-equation model, an additional transport equation for turbulent kinetic energy is solved. In contrast, the two-equation model provides a solution for combining either k and ε, or k and ω. The turbulence energy and scales are determined using the variables k and ϵ (turbulence dissipation) or k and ω (specific dissipation). The two-equation model is the most commonly used among these three models types. The $k-\varepsilon$ and *SST* $k-\omega$ turbulence models are the two most used equations [49].

The $k-\varepsilon$ model characterizes the properties of the turbulent flow by solving additionally two transport equations for k and ε. Different formulations are available for this model, such as the ones proposed by Chou [110] and Launder and Sharma [111]. The latter formulation is commonly referred to as the standard $k-\varepsilon$ model and

is the most widely used formulation [111]. It has shown satisfactory performance in many industrial relevant applications, particularly for thin shear layer flows accompanied by small pressure gradients. In addition, it has demonstrated its success in problems where there is a dominance of Reynolds shear stresses, such as in confined flows. Moreover, the model has shown moderate agreement in flows of free turbulence such as in free jet flows, wake, or mixing layers.

Nevertheless, the standard $k-\varepsilon$ model suffers from some drawbacks. First, it does not show good performance in low Re_T flows, adverse pressure gradient flows, and high spatial gradients flows. Second, unsatisfactory performance in regions of large strains, recirculation, or stress anisotropy. The $k-\omega$ model eliminates most of the problems mentioned above, accompanied by the $k-\varepsilon$ model, as it is suitable for use in near-wall regions, excluding the need to use any wall-damping functions in applications of low Re_T [112]. The $k-\omega$ model, on the other hand, has one critical limitation: its performance is dependent on the parameters of free-stream turbulence. As a result, the *SST* $k-\omega$ model, a hybrid model that combines the best features of the $k-\omega$ and $k-\varepsilon$ models, was developed. The standard $k-\varepsilon$ model is active in free turbulence zones far away from the walls when using the *SST* $k-\omega$ model, whereas the $k-\omega$ model is initiated in near-wall regions when using the *SST* $k-\omega$ model. [113].

III) Large Eddy Simulation (LES)

An intermediate numerical approach between DNS and RANS is the Large Eddy Simulation (LES) approach. In this method, eddies of larger sizes are resolved directly and filtered out. In contrast, smaller eddies, which are universal and nearly isotropic with sizes less than the filter width, are modeled [104]. This makes a critical difference between RANS and LES, such that not all the whole turbulent structures are modeled. Unlike the time-averaging technique followed in the RANS approach, LES applies a spatial filtering procedure to separate the small eddies from the larger ones. Due to that, the information related to the filtered-out turbulence structures or smaller eddies is lost [114]. This and the interaction effect between larger resolved eddies and the unresolved turbulent structures produces stresses known as Subgrid Scale Stresses (SGS), which require modelling by a subgrid-scale model. In the case of reactive flows, the modelling of SGS becomes more complicated as the chemical reaction is characterized by a propagating surface that is much thinner than the width of a typical filter. Therefore, the turbulence-chemistry interactions need considerable attention and should be modeled entirely [115].

The spatial filtering process in LES is applied through a filter function $F(\vec{x} - \overrightarrow{x^*})$ as the following [49]:

$$\bar{q}\,(\vec{x}) = \int_{-\infty}^{\infty} q\left(\overrightarrow{x^*}\right) F(\vec{x} - \overrightarrow{x^*})\,\mathrm{d}\overrightarrow{x^*} \tag{46}$$

In the three-dimensional computations, the spatial filters that are commonly used are [49]:

- Box filter or top-hat

$$F(\vec{x}) = F(x_i) = \begin{cases} \frac{1}{\Delta^3}, & if|x_i| \leq \frac{\Delta}{2}, \quad i = 1,2,3 \\ 0, & otherwise \end{cases} \tag{47}$$

- Gaussian filter

$$F(\vec{x}) = F(x_i) = \left(\frac{6}{\pi\Delta^2}\right)^{3/2} exp\left[-\frac{6}{\Delta^2}\,(x_1^2 + x_2^2 + x_3^2)\right] \tag{48}$$

Where Δ is the filter width, and x_1, x_2, x_3 are the spatial coordinates of a particular location $\vec{x}$. The filter is defined in functions such that their integral through the whole spatial domain is equal to 1[49]:

$$\int_{-\infty}^{\infty}\int_{-\infty}^{\infty}\int_{-\infty}^{\infty} F(x_1, x_2, x_3)dx_1\,dx_2dx_3 = 1 \tag{49}$$

In the case of reactive flows, a Favre density-weighted filtering process can be applied such that [49]:

$$\bar{\rho}\,\breve{q}(\vec{x}) = \int_{-\infty}^{\infty} \rho q\left(\overrightarrow{x^*}\right) F(\vec{x} - \overrightarrow{x^*})\,\mathrm{d}\overrightarrow{x^*} \tag{50}$$

For an anisotropic field, the filter width size is calculated as: $\Delta = (\Delta_{x_1}\Delta_{x_2}\Delta_{x_3})^{1/3}$.

The LES spatial filtering procedures are applied in the LES-filtered equations of mass, momentum, energy, and species. For further discussion about LES governing equations and the modelling of turbulent stresses in the LES approach, the reader is directed to the following Reference [49].

3.3.2 Premixed Combustion Models

A combustion model is used to close the source terms in the governing equations, which relate the enthalpies and species and predict the overall heat release rate. This subsection is dedicated to discussing the different numerical closure models, which have been used previously in various studies through a RANS approach.

I) Arrhenius Rate

This model assumes that chemistry only plays a major role in identifying the combustion reaction rate. Therefore, it is considered to be the simplest model. The reaction rate in this model is represented in terms of mean quantities. The rate constant *k* in the Arrhenius equation depends on the temperature and the activation energy. For a certain reaction [105]:

$$Fuel\ (F) + Oxidiser\ (O) \rightarrow \quad Products\ (P) \tag{51}$$

The reaction rate is given as [49]:

$$\dot{\omega} = -k_r \rho Y_F Y_0 \tag{52}$$

$$k_r = A_f T^b \exp\left(\frac{-E_a}{RT}\right) \tag{53}$$

where,

E_a is the chemical reaction activation energy

K_r is the reaction rate constant

A_f is a pre-exponential factor

Y_F and Y_o are the fuel and the oxidizer mass fractions, respectively.

The effect of turbulence is completely neglected in this approach, and it is assumed that only chemistry plays a major role. Based on that, the heat release rate is formulated as [105]:

$$\widetilde{\dot{\omega}} = -A_f \bar{\rho}\, T^b\, Y_F Y_0 \exp\left(\frac{-E_a}{RT}\right) \tag{54}$$

This model is considered inaccurate; because the rate of reaction non-linearly depends on the temperature and due to large fluctuations in the temperature within the turbulent flame. In addition, this model can be applicable only at low values of Damkohler numbers (*Da*), where the reactants mix rapidly but burn slowly. Arrhenius model has been implemented using a DNS approach [116] and using an LES approach [117] using a new reaction rate source term. It was found that the Arrhenius model's computational results have been enhanced over a wide range of density ratios and activation energies when using this surrogate source. This model has also studied turbulence in air pollution dispersion using an LES approach [118]. Nevertheless, its application is still considered to be inadequate in the field of premixed combustion, and significant errors of high magnitudes may arise [109][110].

II) Eddy Break-up (EBU)

This model has been introduced by Spalding [119], and it is applicable for the cases of fast reactions ($Da >> 1$) and high turbulent Reynolds number (Re_T). Contrary to the Arrhenius model, the eddy brake-up model assumes that the rate of reaction is controlled solely by turbulent mixing. Based on that, the effect of chemical kinetics rates is neglected, and the rate of heat release is given as [105]:

$$\widetilde{\omega} = C_{EBU} \frac{\tilde{\rho}}{\tau_{EBU}} \tilde{c}(1 - \tilde{c}) \quad (55)$$

where,

$\tau_{EBU} = k / \varepsilon$ is the turbulent time scale

C_{EBU} is the model constant

$\tilde{c}$ is the mean reaction progress variable

Due to the simple formulation of the EBU model, its application is found in several commercial codes. However, its expression has some evident shortcomings due to the assumption that the reaction rate explicitly depends on the turbulent mixing and ignores the effect of the chemistry on the reaction. In addition, the reaction rate in this model is over predicted in zones of high strain rates (ε / k is large). Moreover, C_{EBU} is considered one of the model drawbacks because it depends on several parameters and thus needs to be adjusted in each test run [120]. Said and Borghi [121] have proposed slight modifications for C_{EBU} to incorporate the effect of chemistry on the reaction. Fureby [122] coupled the Arrhenius law with the EBU model to limit the mean reaction rate using the effect of chemistry. Yaxin et al. [123] have also simulated the high air temperature in combustion using a modified EBU model, while Dhuchakallaya [124] has studies diesel spray auto-ignition using a PDF-EBU model.

III) Eddy Dissipation Concept (EDC)

This model has been proposed by Magnussen and Hjertager [125], and it is applied to a wide range of non-premixed and premixed combustion problems that are characterized by a faster chemical reaction rate compared to mixing within a finite

structure [126]. Unlike the EBU model, the reaction rate is limited by the amount of energy that can sustain the combustion (presented as the amount of the mixture's products) or the fractions of deficient species, usually the fuel or oxidizer. The formulation of the model is given as:

$$\tilde{\dot{\omega}} = B_1 \tilde{\rho} \frac{\epsilon}{k} min\left(\widetilde{Y_F}, \frac{\widetilde{Y_o}}{\emptyset}, B_2 \frac{\widetilde{Y_p}}{(1+\emptyset)} \right) \quad (56)$$

where,

B_1 and B_2 are the model constants

Φ is the equivalence ratio

This model has been applied in many industrial applications. Its success can be referred to incorporating detailed chemical mechanisms at an affordable computational cost compared to other models. However, there are some limitations found in the EDC model. These limitations can be explained by the absence of detailed chemical kinetics mechanisms, which are necessary to establish a strong coupling between chemistry and turbulence, especially for the cases of weak turbulent reacting flows [127]. In addition, recent modelling research has found the EDC model's limitations when applied to the simulation of Moderate and Intense Low-oxygen Dilution (MILD) systems in non-premixed combustion applications, where the temperature levels have been significantly overestimated [128]. Subsequently, in many studies [128]–[130], the constant coefficients have been modified to enhance the prediction of the dilution effect on the reaction rate and temperature.

IV) G-Equation Modelling

The *G*-equation model uses a scalar field variable *G* that has completely an arbitrary definition. The variable *G* is used to represent an arbitrary flame isosurface that is fixed at a certain value G_0, such that $G(x,t) = G_0$, where G_0 represents the spatial location that corresponds to the flame surface [104]. The application of the *G*-equation model with RANS approach in practical and industrial combustion systems demands the use of Favre decomposition, such that $G = \bar{G} + G''$ .The averaged G-equation is expressed as [105]:

$$\bar{\rho}\,\frac{\partial(\bar{G})}{\partial t} + \bar{\rho}\,\breve{u}_j\frac{\partial \bar{G}}{\partial x_j} = \bar{\rho}\,D_t|\nabla\bar{G}|\nabla\left(\frac{\nabla\bar{G}}{|\nabla\bar{G}|}\right) + \bar{\rho}\,S_t|\nabla\bar{G}| \qquad (57)$$

where,

$\bar{\rho}\,S_t|\nabla\bar{G}|$ represents the mean reaction rate $\tilde{\omega}$

S_t is the turbulent flame speed, which is closed by a correlation proposed by Peters [116]

D_t is the turbulent diffusivity

The *G*-equation modelling has been implemented through a RANS approach [131]. In addition, this model has been intensively implemented through an LES approach [132]–[134].

V) Flame Surface Density (FSD)

FSD expresses algebraically the amount of flame surface area that lies within a unit volume Σ of the turbulent flame brush. In case the assumption of flamelet holds, then the structure of the flame keeps quasi-laminar, and the propagation speed of the flame

is locally similar to the unstretched laminar flame speed S_L^o. Therefore, the reaction rate $\bar{\omega}$ is given as [104] :

$$\bar{\omega} = \overline{\rho_R}\, \Sigma\, S_L^o I_0 \tag{58}$$

where,

$\overline{\rho_R}$ is the reactants mean density

I_0 is a factor that accounts for the curvature effects on local burning velocity [135]

I_0 and S_L^o are quantities that depend on the thermochemistry of the problem, and the main challenge arise from the determination of Σ. This issue could be resolved experimentally using a flame imaging technique that has counted the number of points that an instantaneous flame surface cuts a two-dimensional image contour. This process could be used on a vast number of captured images [136]. It was found that the number of crossings through a unit length ($\overline{v_y}$) can be expressed as:

$$\overline{v_y} = \frac{g\bar{c}(1-\bar{c})}{\widehat{L_y}} \tag{59}$$

where,

g: is a constant

$\widehat{L_y}$: the crossing flame's integral length scale

The mass flow of the crossing flame is geometrically rectified using a crossing angle θ to produce the mean reaction rate per crossing:

$$\overline{\omega_y} = \frac{\overline{\rho_R} S_L^o I_0}{\overline{|cos\,\theta|}} \tag{60}$$

Hence, the mean turbulent reaction rate is obtained from the product of the mean reaction and the mean number of crossings per unit length. Under the assumption of an isotropy field, the mean turbulent reaction rate per unit volume is obtained as:

$$\bar{\omega} = \overline{\rho_R} S_L^o I_0 \frac{g\bar{c}(1-\bar{c})}{\widehat{L_y}\overline{|cos\,\theta|}} \tag{61}$$

The comparison of Equation 58 with Equation 61 indicates that Σ can be expressed as:

$$\Sigma = \frac{g\bar{c}(1-\bar{c})}{\widehat{L_y}\overline{|cos\,\theta|}} \tag{62}$$

The quantities $\overline{|\cos\theta|}$ and g have been determined empirically through the experiment [137], whereas $\widehat{L_y}$ is modeled with respect to the integral length scale [136]. Also, it is worthnote that the *G*-equation model requires the specification of S_t to obtain the mean reaction rate, however, in the FSD model, S_t emerges as one of the computational results [138]. Models based on Equation 61 have been extensively employed in RANS and have proved to be effective in a variety of applications [138], [139]. In addition, FSD modelling has been extensively used in several premixed turbulent combustion studies through an LES approach [49], [139], [140].

VI) Zimont Model

Zimont Turbulent Flame Closure (TFC) model was developed in 1979, and it can be implemented through a RANS or LES approach [27]. It implements a pressure-based solver technique and is largely used to analyze reactive flow behavior and study turbulent combustion of the premixed charge at high Re_T [25], [141]. The combustion process is defined in this model by a single transport equation (*C*-equation) for the

progress variable *C*; turbulent closure for the progress variable's source term is determined by a model parameter utilized for turbulent flame speed computation.

The progress variable (*C*) is revealed to be a statistically significant parameter in premixed turbulent combustion. It is calculated using scaling principles and theoretical considerations, considering local turbulent conditions and the combustible mixture's physicochemical parameters. The turbulent flow field is primarily responsible for wrinkling, thickening, and straining the flame front, resulting in a closed-form expression of the turbulent flame speed that includes a critical gradient of the laminar flame thickness and speed, fluctuation intensity, and the local turbulent length scales. This closure method is elegant and efficient, as it only requires one additional transport equation compared to the non-reacting flow case and avoids any costly chemical source term assessment or integration over probability density functions [27].

Zimont TFC model was tested in a finite-volume-based fluid dynamics code and then validated against data from a large-scale gas turbine burner stand [26]. The computational results compared well to the experimental ones, and it has been noticed that this model is computationally more efficient when compared to other numerical models such as Flame Surface Density (FSD) model or Sub-Grid Scalar Flux (SGSF) model [26]. These features make this model particularly appealing and well-suited to applications involving large three-dimensional, complex geometries. [142]. Besides, the Zimont TFC model has been validated for use in different configurations, e.g., stationary flames [143], highly turbulent confined bluff-body flame [144], Bunsen

flame [145], turbulent V-flames [146], statistically spherical expanding flames in a fan-stirred vessel [147]–[149] and swirling premixed turbulent flames [150], [151]. Some of these cases have been implemented using Large Eddy Simulation (LES) approach [115], [151]–[153], while others have been performed using Reynolds Average Navier-Stokes (RANS) approach [154], [155]. Furthermore, the model has been used with different fuels e.g., propane/butane [156], methane [157], [158], and hydrogen [159], [160].

According to Zimont [26], this model behaves effectively when any of the following physical mechanisms exist, (i) a gradual increase in the average propagating flame thickness, which can be interpreted by the turbulent diffusion's law [161], (ii) flame distortion by large scale vortices and broadening of local reaction zones by the effect of small-scale eddies, (iii) preferential diffusion of oxidizer or fuel into curved local reaction zones. Zimont model and its governing equations will be discussed in more details in Chapter 5.

VII) Other Models

The modelling of premixed turbulent combustion has been dominated by numerical models widely based on the flamelets phenomenology. The applicability of these models can be highly supported through the Borghi diagram, and their effectiveness is abundantly essential. Nonetheless, it is evident that the flamelet structure cannot be used under all conditions. When turbulence intensities near extinction or conditions near the flammability limit are high, the balance between reaction and diffusion is

weakened, making it difficult to determine a representative structure for the flame [104].

Therefore, in these situations, more generalized modelling is recommended. The transported Probability Density Function (PDF) model does not require any assumptions about the flame structure, and it has proved its success in different non-premixed combustion applications [162], [163]. In addition to that, PDF transport modelling was found to give convincing results in applications of premixed flames [164], [165]. The benefit of this model is its generality, which is especially useful in conditions where the direct effect of chemistry is significant. However, it has a high computing cost. The modelling of mixing phases in the presence of significant scalar gradients has certain technical challenges, typically encountered in premixed turbulent combustion applications.

The Conditional Moment Closure is another model that has proven successful in non-premixed combustion (CMC). The variables fluctuate slightly around the mixture fraction conditional mean. CMC modelling can theoretically be expanded to handle premixed flames by using the CMC conditioning variable's reaction progress variable [166]. Additionally, utilizing a marker field variable can be recommended. However, whether this would provide any benefit over the conventional *G*-equation model remains to be investigated. The Conditional Source Term Estimation (CSTE) model [167], which is connected to CMC and can provide more realistic approaches to modelling the effect of chemistry in premixed flames, is one potential theme.

In general, turbulent premixed flames at intensities well below extinction can be approximated without explicitly accounting for the chemical reaction rate. Chemical information is encoded in variables like laminar flame burning velocity and strain rates. Because thorough chemistry simulations are computationally expensive, treating chemical effects separately from turbulent flame calculations is desirable. A number of alternative approaches can be used to store and precompute chemistry in encapsulated form. The simplest option is to create a premixed flamelet library, which can store the laminar burning velocity as a function of reactant temperature, pressure, and mixture's equivalence ratio. Other independent variables can be incorporated, such as mean curvature and strain rate [104].

Using laminar burning velocity correlations generated from either one-dimensional computer runs or experiments [168], it is possible to reduce the high computational cost of finding data in tables. A more advanced strategy would be to apply notions from Intrinsic Low Dimensional Manifolds (ILDM) [169], which can robustly account for the flamelet's molecular transport effects. Flamelet Prolongation of ILDM (FPI) [170] or Flamelet Generate Manifolds (FGM) [171] are examples of methodologies that allow for the influence of chemical detail at an acceptable level with a low computational cost and away from the restrictions of the widely used flamelet concept (al least within the calculations of turbulent flame speeds).

Summary

A summary of different RANS numerical models is provided in Table 4. The features and drawbacks of each model are listed, in addition to the studies that have previously used each model.

Table 4. A Summary of Different RANS Numerical Models Used for Premixed Turbulent Combustion

S.N.	Numerical Model	Features	Drawbacks	Previous Studies
1	Arrhenius Rate	Very simple (the simplest model)	1) The effect of turbulence is completely neglected. 2) Inaccurate 3) Applicable only to flows of low Da	[172]
2	Eddy Break-up (EBU)	1) Simple formulation 2) Applicable for the cases of fast reactions (Da >> 1) and high turbulent Reynolds number (Re_T)	1) Chemical kinetics rates are neglected 2) The reaction rate is over predicted in zones of high strain rates 3) The model constant needs to be adjusted at each test run	[121]

S.N.	Numerical Model	Features	Drawbacks	Previous Studies
3	Eddy Dissipation Concept (EDC)	Applicable for premixed and non-premixed combustion applications	1) Requires detailed chemical kinetics mechanisms to establish a strong coupling between chemistry and turbulence 2) Some limitations when applied to the simulation of Moderate and Intense Low-oxygen Dilution (MILD) systems	[127]
4	G-Equation	Decouples the turbulent flow from the chemistry by transporting a scalar field	Limitations of modelling the non-linear heat release generated by sophisticated flames and flame-pinching	[131]
5	Flame Surface Density (FSD)	1) Accounts for flame curvature and stretch effects 2) Unlike the G-equation model, the flame propagation is represented in terms of physical quantities such as the progress variable	1) In the near-wall region, the flow behavior in terms of molecular diffusion and reaction rate are over-predicted. 2) The modelling of mixing phases in the presence of significant scalar gradients has certain technical challenges	[138], [139]

S.N.	Numerical Model	Features	Drawbacks	Previous Studies
6	Zimont Model	1) The combustion process is described by a single transport equation for a progress variable, *C* 2) Phenomena like wrinkling, thickening, and straining of the flame front by the turbulent flow field are considered 3) Exclude any costly evaluation of the chemical source terms or integration over probability density functions	1) Has to be used with pressure-based solver 2) Limitations for the large scale applications due to the assumption of mean flame brush thickness in this model	[154], [155], [173], [174]
7	Transported PDF	1)Does not require any assumptions about the flame structure 2) Capability for generalization 3) Applicable for premixed and non-premixed flames	1) High computational cost 2) Some technical issues associated with the modelling of mixing phases in the presence of high scalar gradients	[164], [165], [175]

S.N.	Numerical Model	Features	Drawbacks	Previous Studies
8	Conditional Moment Closure (CMC)	1) accounts for the interaction between chemistry and scalar dissipation while decoupling the bulk flow from the mixing 2) CSTE model may provide more realistic approaches to model the effect of chemistry in premixed flames.	Becomes less efficient in applications that involve recirculating flows and variable density	[166]

In order to verify and extend the experimental findings, a suitable numerical model should be selected to well interpret the physical phenomena of the present problem. Therefore, this literature survey has been performed to match this purpose and a summary of the features and limitations of each numerical model are presented in Table 4. Typically, there should be a strong coupling between turbulence and chemistry, and phenomena such as flame wrinkling and thickening by turbulent eddies should be well interpreted by the used model. It was found that some numerical models such as the Arrhenius rate, EBU, and EDC have severe limitations due to the complete ignorance or the weak coupling between chemistry and turbulence. Those are not recommended for use, where significant errors were

produced from their use [125], [131], [176]. Other models such as G-equation, FSD, transported PDF, and CMC have strong coupling between turbulence and chemistry, however, they become inefficient under some physical constraints near the vessel walls, or when then there exists a wake region in the turbulence domain. Moreover, they over-predict the heat release rate when flame grows in an irregular or sophisticated manner [135], [143], [170], [180]. Out of those models, Zimont model was found to be the most widely used for applications such as the one in present study. This model behaves effectively when any of the following physical mechanisms exist [29], (i) a gradual increase in the average propagating flame thickness, which can be interpreted by the turbulent diffusion's law [165], (ii) flame distortion by large scale vortices and broadening of local reaction zones by the effect of small-scale eddies, (iii) preferential diffusion of oxidizer or fuel into curved local reaction zones. Due to that, this model has been selected to bridge the missing research gap in the literature through the following:

(i) Investigating the existence of HIT condition in the combustion bomb by conducting a mean turbulent kinetic energy balance study.

(ii) Studying the premixed turbulent combustion of the three tested fuels at a broad range of turbulence intensities ($u^{`}$), equivalence ratios (Φ), Reynolds numbers (Re_T) and Damkohler numbers (Da), which have not been studied before.

CHAPTER 4. EXPERIMENTAL METHODOLOGY

In this dissertation, the spherical propagation flame's laminar and turbulent flame speeds are measured using the pressure trace in a fan-stirred combustion bomb. Four mixing fans are installed inside the combustion bomb to attain the required level of turbulence in near Homogeneous and Isotropic Turbulence (HIT) conditions. The enhanced flame combustion bomb features and the various systems and measurement devices used in the test rig are detailed in Section 4.1. Section 4.2 presents all the measurement devices' specifications and features and explains the methodology followed to install them on the combustion bomb. This is followed by a discussion of the different experimental tests used to confirm the readiness of the test rig in Section 4.3. Section 4.4 explains the procedures for characterizing the turbulent flow field in the combustion bomb and measuring the various turbulent length and time scales. The chemical and physical parameters of the three studied fuels are provided in Section 4.5, while Section 4.6 discusses the experimental methodology used to conduct the flame speed experiments. Finally, the systematic uncertainties (bias) calculations that result from the measurement of the turbulent flame speeds (S_t) are previewed in Section 4.7.

4.1 Combustion Bomb Experimental Setup

Turbulent flame speeds (S_t) of diesel, GTL, and 50/50 diesel-GTL fuel blend are measured using a constant-volume, high-pressure, cylindrical fan-stirred combustion bomb under near HIT conditions at 463K only under atmospheric pressure due to the strict regulations and the highly challengeable manufacturing of high-pressure combustion bombs. The experiments are conducted at a wide range of equivalence ratios (Φ) from 0.7 to 1.3, and turbulence intensities ($u`$) that vary between 0.5m/s and 3.0m/s at an integral length scale, L_t=20mm. The test rig includes the main key features found in several experimental setups. Figure 16 shows a schematic layout for the test rig, and Figure 17 shows the final test rig setup.

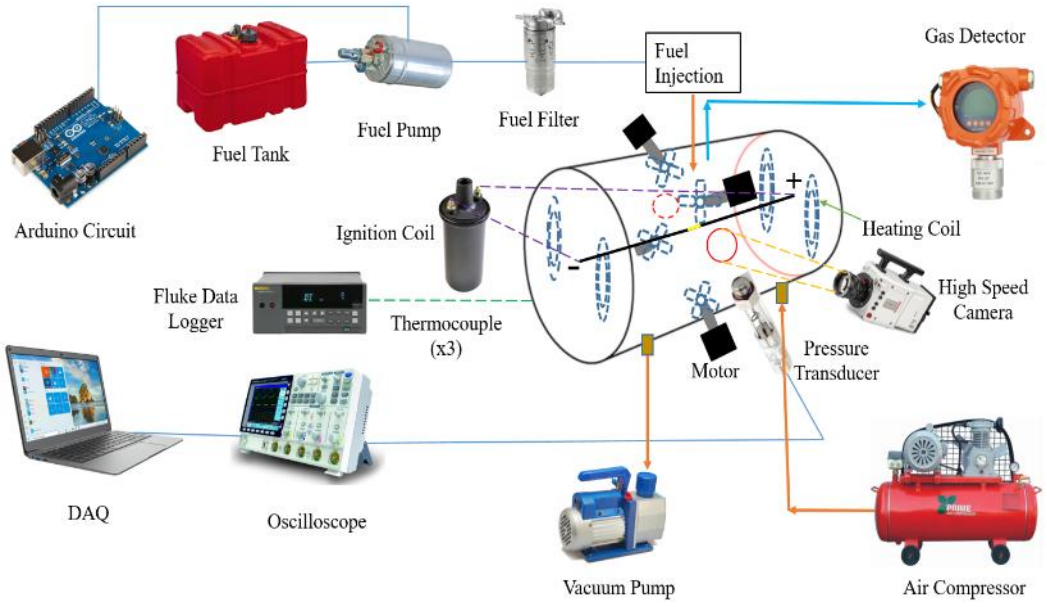

Figure 16. Schematic diagram for the experimental test rig

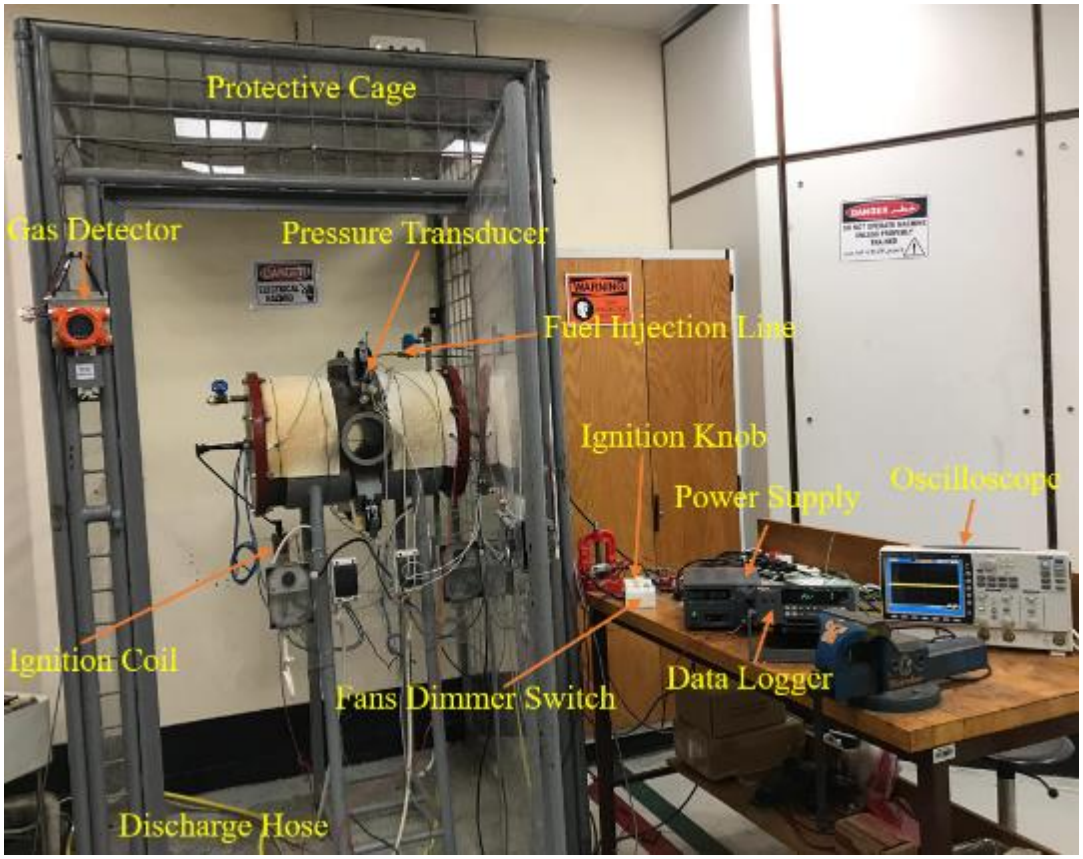

Figure 17. The actual test rig setup

A cylindrical combustion bomb is used in the proposed test rig that is made of steel and has the following dimensions: internal diameter = 400mm, thickness= 5mm, and length= 650 mm. As a safety precaution, a protective cage was placed around the test rig to ensure the operation of the experiments with the minimum hazard possibility, and the dimmer switches and knobs were controlled from a long distance away from the bomb.

The bomb is equipped with four internal electric heating coils, each with a heating capacity of 2.1 KW, and can reach a maximum temperature of 255^{o}C in around 40

minutes. Ceramic sheet layers are wrapped around the combustion bomb body for insulation, significantly accelerating the temperature rise. Three k-type thermocouples wires are used to monitor the temperature variations inside the bomb, which have a measurement accuracy of 1.5^{o}C. In addition, the bomb is equipped with four axis-symmetric stirrer fans, two 150 mm-diameter collinear optical quartz glass windows, three ports, a pressure transducer (model 35XHTC), a gas detector (oxygen sensor), a computer-based Arduino controlled circuit for fuel injection, in addition to two stainless steel electrodes to generate the combustion spark. Besides, the test rig includes a vacuum system, an air supply system, and a Data Acquisition (DAQ) system connected to a digital storage oscilloscope and the pressure transducer. The air compressor is used to charge the combustion bomb with a calculated amount of air, and the vacuum pump is used to discharge the bomb of any residual gases when the experiment is completed. The equivalence ratio of the air-fuel mixture can be confirmed through a wall-mounted OC-F08 fixed gas detector that senses the percentage volume of oxygen in the combustion bomb (0-30.0%O_2vol) before the ignition phase. The fuel is injected with a pre-specified volume flow rate to match the desired equivalence ratio. For this purpose, a computer-based Arduino controlled circuit sends a signal to the fuel pump to starts the fuel injection. The volume of fuel injected versus time can be shown in Figure 34 in subsection 4.3.5, while the Arduino code and circuit diagram designed by Fritzing software can be viewed in Appendix A. A schematic diagram of the entire fuel injection system is shown in Figure 18.

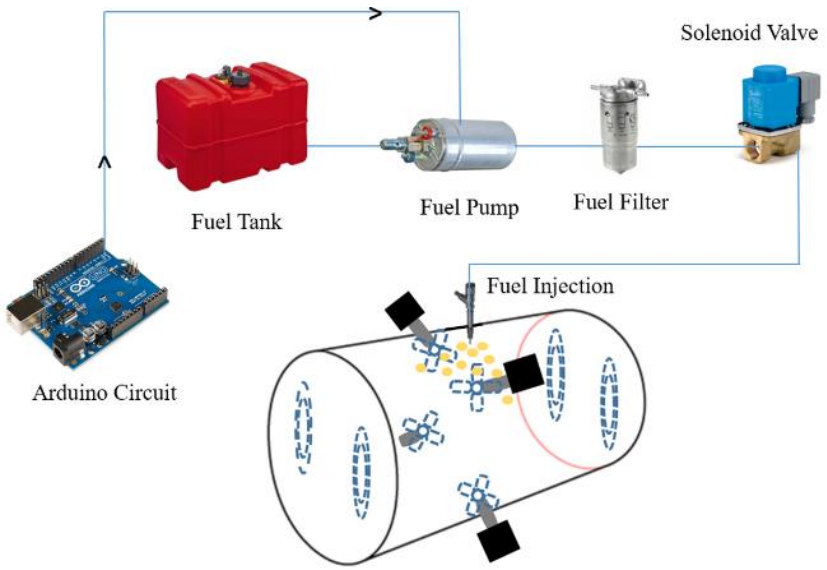

Figure 18. Schematic diagram of the entire fuel injection system

To ensure adequate air-fuel mixing and a homogeneous charge inside the combustion bomb, four electrically operated eight-bladed steel fans are used. The fans are turned off for around 2-5 minutes when measuring laminar flame speeds to obtain the equilibrium state. However, in the turbulent flame speeds measurement, a dimmer switch is used to generate the desired turbulence intensity (u`=0.5m/s -3.0m/s) within the combustion bomb. Each fan has eight blades bent at a 60^{o} angle to generate different turbulence intensities and ensure the proper air-fuel mixing. Figure 19 illustrates the shape and number of blades of the used fan.

Figure 19. Geometry and design of the mixing fan

Once these steps are accomplished, the fuel-air mixture is ignited using central electrodes connected to the spark ignition coil circuit. An automobile ignition coil, a capacitor, and an AC mains-connected dimmer switch constitute the ignition system, as shown in Figure 20.

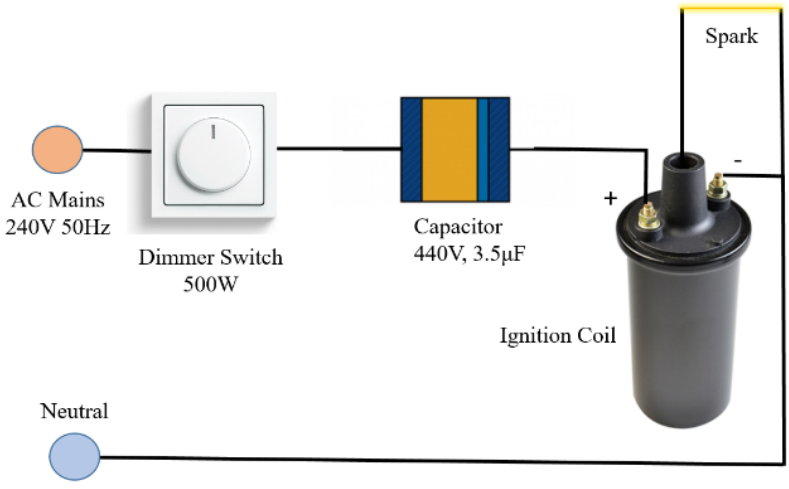

Figure 20. Schematic diagram for the ignition system

The ignition coil's positive terminal is connected to a 440V, 3.5F capacitor on one side, while the negative terminal is connected to neutral in this setup. The capacitor is used to store the electrical energy supplied from the 240V AC mains and feeds the ignition coil, while a 500W dimmer switch is used in this circuit to control the amount of current the passes through the capacitor up to the ignition coil. High tension cables are connected to the two stainless steel electrodes, separated with a distance of 2mm. Figure 21 shows the ignition coil and the capacitor after being installed on the combustion bomb.

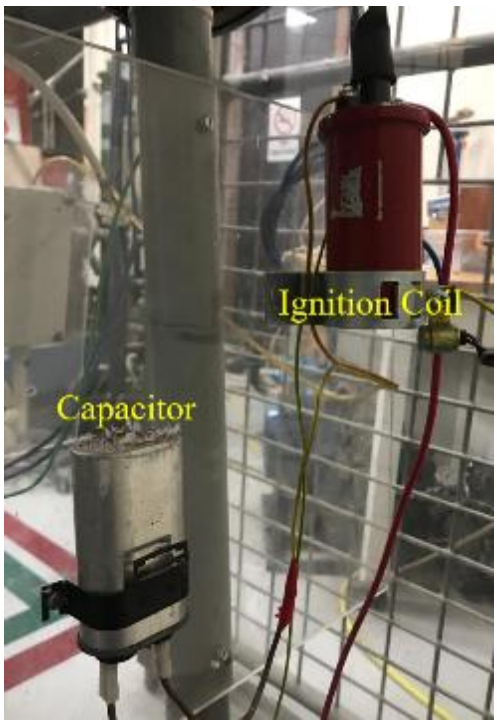

Figure 21. The ignition coil and the capacitor mounted on the test rig

This circuit produces a spark with a voltage of around 20kV and a current of about 200mA, which is sufficient to ignite the air-fuel mixture under any condition. Figure 22 shows the spark produced by this arrangement.

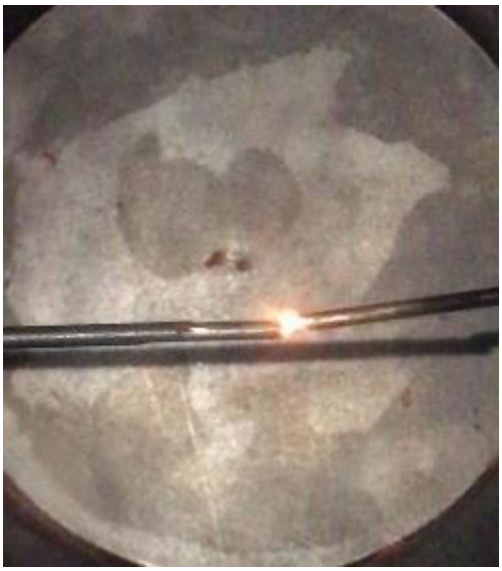

Figure 22. The spark produced between the two electrodes

The pressure transducer is used to detect the pressure rise signal once the mixture is ignited, which can be used to measure the flame speed using a suitable correlation from the literature [15]. It has a measurement range from 0 to 1000 bars and can work at high temperatures experiments up to 300^{o}C, with an accuracy of ±0.05% Full Scale (±0.05% FS). One side of the pressure transducer is bolted on the combustion bomb body, while the other side is connected to a GW-Instek oscilloscope (Model GDS-3152) that has a sampling rate of 150 MHz and a deep memory of 25K points

recording length, in addition to its ability to save screenshots of the pressure waveforms. The reader is directed to Reference [10] for more details about the steps followed for designing the test rig and the associated fabrication processes.

4.2 Measurement Devices

This section presents all the measuring devices' specifications and features and explains the methodology followed for installing them on the combustion bomb.

4.2.1 The Pressure Transducer

Two pressure transducers were used in this dissertation. The first is a pressure sensor from PCB Piezotronics (Model 116B03), which has a pressure measurement range of 0 to 7 bars and an operating temperature range of 0 to 343°C. It has a pressure output response of 10pC/psi converted to a voltage reading using an inline PCB Pierzotronics charge converter (Model 422E35). Therefore, the final conversion factor gained by the transducer is 6.238 mV/psi. This pressure transducer was used only for generating the pressure-voltage calibration chart for the hotwire anemometer and perform the cold and hot leak tests, as discussed in Section 4.3. The calibration certificate of this pressure transducer is attached in Appendix B. The second pressure transducer used in the flame speeds experiments is the 35XHTC piezo resistive high temperature and pressure transmitter, suited for use in environments such as the present work. The pressure that acts on the flush diaphragm transfers through an oil-filled capillary to the silicon measurement cell. A cooling spiral function is embedded on the capillary, allowing the media temperature to reach 300^{o}C. The remote

electronics temperature is designed to work on media of less than 120^{o}C. It uses the digital polynomial compensation mathematical function through PROG30 software to achieve an accuracy of about 0.5%FS [176]. The use of the KELLER software PROG30 and READ30 along with the K-102 cable and GW-Instek digital storage oscilloscope (Model GDS-3152) allows for the pressure to be displayed and the units to be converted. Figure 23(a, b) show the 35XHTC pressure transducer and a schematic diagram for its different dimensions, respectively [176].

(a)

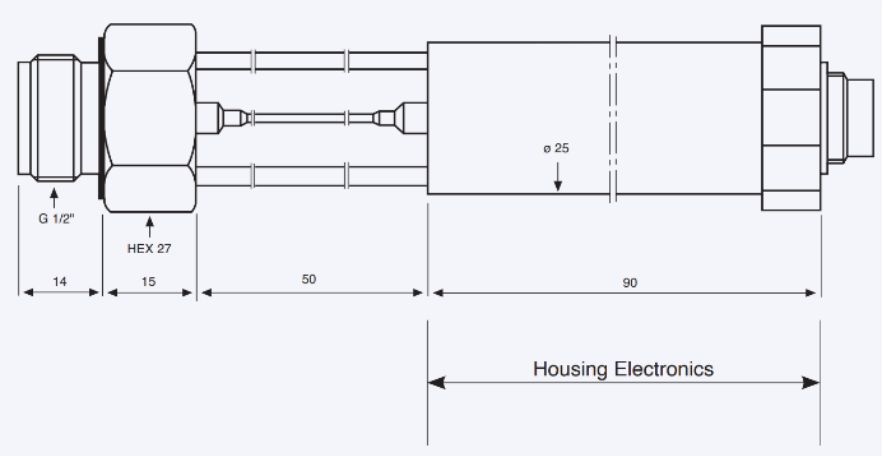

(b)

Figure 23. (a) the pressure transducer (model 35XHTC), (b) schematic diagram for the pressure transducer dimensions

A local company in Qatar has calibrated the pressure transducer to generate the pressure-current calibration charts. These charts can be found on the calibration certificate received from the company, as attached in Appendix B. After calibrating the sensor; a proper mounting position had to be decided on the combustion bomb's body. The bomb's middle circumference was determined to be the best location for installation. The pressure pickups are received in this manner from the closest place to the spark origin. As a result, G1/2 internal threads were marked by drilling a hole through the bomb's body to install a custom adaptor fitting made at Qatar University's mechanical workshop, as shown in Figure 24.

Figure 24. The pressure transducer mounted on the combustion bomb

The adaptor was connected to the pressure transducer from one side, while the other side was bolted to the body of the combustion bomb, in which pipe thread Teflon tape was wrapped around it to ensure its proper sealing. The major specifications of the used pressure transducer are listed in Table 5 [176].

Table 5. The Major Specifications of the Pressure Transducer

Feature	**Range**
Pressure (bar)	0-1000
Accuracy (%FS)	±0.05
Total Error Band (%FS)	±0.5 @ 20…300 °C
Temperature (°C)	0-300
Interfaces	RS485, 4…20 mA, 0…10 V
Resolution (%FS)	0.002 %FS
Output Rate (Hz)	100
Linearity (%FS)	0.05
Electrical Connection	Binder-Plug 723 (5 pole)
Weight (g)	300

GW-Instek Oscilloscope

The GW-Instek oscilloscope (Model GDS-3152) has been selected for use in this dissertation. It has a sampling rate of 150 MHz and can save screenshots for the waveforms and sampling data on an Excel spreadsheet CSV format for further analysis. At each test condition, 25000 sampling points are provided, which is suitable for dealing with different turbulence statistics, and ensuring the existence of a homogeneous and isotropic field through the combustion bomb, along with the use of a hotwire anemometer (discussed in Section 4.4). Figure 25 shows the GW-Instek oscilloscope (Model GDS-3152) used in this dissertation.

Figure 25. GW-Instek oscilloscope (Model GDS-3152)

The main features of this model are as follows [177]:

- 150MHz sampling rate
- Two Channels, with an independent memory for each
- Large 8-inches 800x600 display
- Visual Persistence Oscilloscope (VPO) Technology
- Split-screen function
- 3 Built-in standard impedances (50Ω,75Ω,1MΩ)
- Optional power analysis software
- Deep memory of 25K points recording length
- 64MB internal flash memory
- On-screen help

4.2.2 Thermocouple Temperature Sensor

In this dissertation, three k-type thermocouple wires were used for measuring the temperature variation during the experiment. They were mounted on the combustion bomb's body at the right, left, and central circumference locations (as close to the spark) to ensure uniform temperature distribution throughout the bomb. The proper calibration process of the thermocouple temperature sensor is explained in subsection 4.3.3. The features of the k-type thermocouple were satisfactory for use in this dissertation, and they are as follows [10]:

- Temperature measurement range from -270°C up to 1260°C
- The melting point is 1400°C
- Accuracy of ±1.5°C
- Easy connection to the data acquisition unit

Data Acquisition Unit

The three thermocouple wires were connected to the Fluke 2625A hydra data acquisition unit to monitor the temperature variation throughout the combustion bomb. Figure 26(a, b) shows the Fluke 2625A data logger and illustrates the connection of the thermocouple wires to the device.

(a)

(b)

Figure 26. (a) the Fluke hydra 2625A data logger, (b) the connection of the thermocouple wires to the data logger

This data logger was selected for use in this dissertation due to the following favorable features [10]:

- 21 measurement channels
- Multi-function display
- Channel monitoring and scanning
- Ability to accept different thermocouple types
- Measurement input range and function (voltage, resistance, frequency, current, and temperature)
- RS-232 computer interface setup
- Non-volatile memory
- Storage of 2047 scans obtained from 21 different channels (total number of scans is 42,987)

4.2.3 Hotwire Anemometer

Constant Temperature Anemometry (CTA), also called thermal anemometry, is a widely used tool in industry and education to measure turbulence fluctuations in 1D, 2D, or 3D liquid or gas flows. This can be achieved by using a hot-film probe or a hotwire exposed to the flow. Mainly, CTA is suitable for measuring the flow's rapid fluctuations (high turbulence) and studying the microstructure of the flow. The small flow eddies are resolved down to the order of a tenth of millimeters. In this dissertation, the mini CTA hotwire anemometer (model 54T42) [178] is used to measure the turbulence statistics and intensities and check for the existence of a

homogenous and isotropic field throughout the combustion bomb. Based on that, the different turbulence length and time scales are estimated. In addition, the mini CTA hotwires measurements are essential to obtain the energy spectrum function. This provides a clear indicator of flow energy transfer from larger to smaller eddies. The mini CTA hotwire is exposed to the flow from one side and connected to a digital storage oscilloscope from another side. The measurements are obtained in voltage and converted to velocity readings. Therefore, it is essential to generate a voltage-velocity calibration chart before using this hotwire probe in any turbulence field measurements [178]. The calibration process has been appropriately performed through a sequence of steps, as explained in subsection 4.3.6. Figure 27 shows the mini CTA hotwire anemometer (model 54T42) used in this dissertation.

Figure 27. The mini CTA hotwire anemometer (model 54T42) [178]

As shown in Figure 27, CTA probes typically have tungsten wire sensors of 1mm length and 5μm diameter. The working principle behind these thin probes is based on the flow's cooling effect on a heated body, in which the CTA measures the velocity at a certain point over a continuous time series. Subsequently, these measurements can be converted into amplitudes and time-domain statistics. Examples are turbulence intensity, mean velocity, two-point velocity correlation, high order moments, and energy spectrum. The mini CTA hotwire anemometer used in this dissertation is characterized by the following features [178]:

- Measures air velocity up to 100m/s
- Bandwidth of 10kHz for hotwire probes in air
- Easy to use software, with an extensive database and graphical display in one platform
- Long cable of length up to 20m
- Multi-directional velocity measurements
- Various calibration systems with high accuracy
- Suitable for industrial, educational, and scientific applications

4.2.4 Gas Detector

The gas detector device is commonly used in safety applications to sense the amount or percentage volume of a specific harmful gas within the space. It can produce a sound of alarm in cases of leakage or when the amount of harmful gas exceeds a certain limit. Such applications can be found in petroleum refineries and stations,

boiler rooms, chemical plants, mining, and others. This project uses a wall-mounted OC-F08 fixed gas detector to sense the percentage volume of oxygen in the combustion bomb (0-30.0%O_2vol) before the ignition phase to determine the equivalence ratio at each test condition. The OC-F08 gas detector has been successfully calibrated before starting using it in experiments, and the calibration certificate can be found in Appendix B. Figure 28 shows the wall-mounted OC-F08 gas detector used in this dissertation.

Figure 28. The OC-F08 gas detector

This model of gas detectors has been selected for use in this dissertation due to several demanded features, as follows [179]:

- Stable signal, good repeatability, quick response, and high precision
- LED screen that displays the gas type and concentration, unit and instrument status etc.
- Protection function and alarm to prevent any high gas concentration leakage or attack
- Display gas concentration in %vol, ppm, %LEL, or mg/m^3
- Infrared remote control operation
- Provided with data logger and data restore
- Suitable for work in combustion applications
- Resolution of 0.1% LEL, a precision of ≤±3%F. S, and a repeatability of ≤±1%
- The response time is less than 20s
- Senses oxygen concertation in the desirable range (19.5% to 20.2%)
- It can be used to sense the concentration of many other gases (CH_4, C_3H_8, H_2, NH_3, CO_2, etc.).

4.3 Test Rig Characterization and Calibration Processes

The various experimental tests needed to prove the readiness of the test rig for conducting the laminar and turbulent flame speed experiments and taking the required measurements are discussed in this section. In addition, it discusses the different calibration tests for the measurement devices and the equivalence ratio calculations. The section starts with discussing the cold and hot leak tests in subsections 4.3.1 and 4.3.2, respectively. After that, the calibration process of the thermocouple k-type wire is described in subsection 4.3.3. Based on that, the maximum temperature test is performed, and the results are illustrated in subsection 4.3.4. The steps followed for equivalence ratio calculations are presented in subsection 4.3.5, and finally, the calibration tests of the pressure sensor and the hotwire anemometer are discussed in subsections 4.3.6 and 4.3.7, respectively.

4.3.1 Cold Leak Test

The pressure leak test determines the weak spots within a particular object and improves the design components. In addition, this test can improve the quality of sealing and identify the weak spots of a pressure component. A cold leak test has been conducted by charging the combustion bomb with air up to 1.5 bars to check if a pressure drop is caused by an unintended hole or crack. The time it takes for the pressure to return to its starting point (one bar) has been measured. The drop in the pressure with time could be tracked by transforming the voltage readings obtained from the digital oscilloscope into pressure readings and plotting a trend line for the

pressure drop with time. During the test, it was figured out that there was an air leakage around some spots of the rotating shafts. Thus, Lithium high-resistant temperature grease was used to block the leakage spots. After that, the cold leak test was repeated following the same procedure, and the two trend lines (before and after sealing) were compared, as shown in Figure 29.

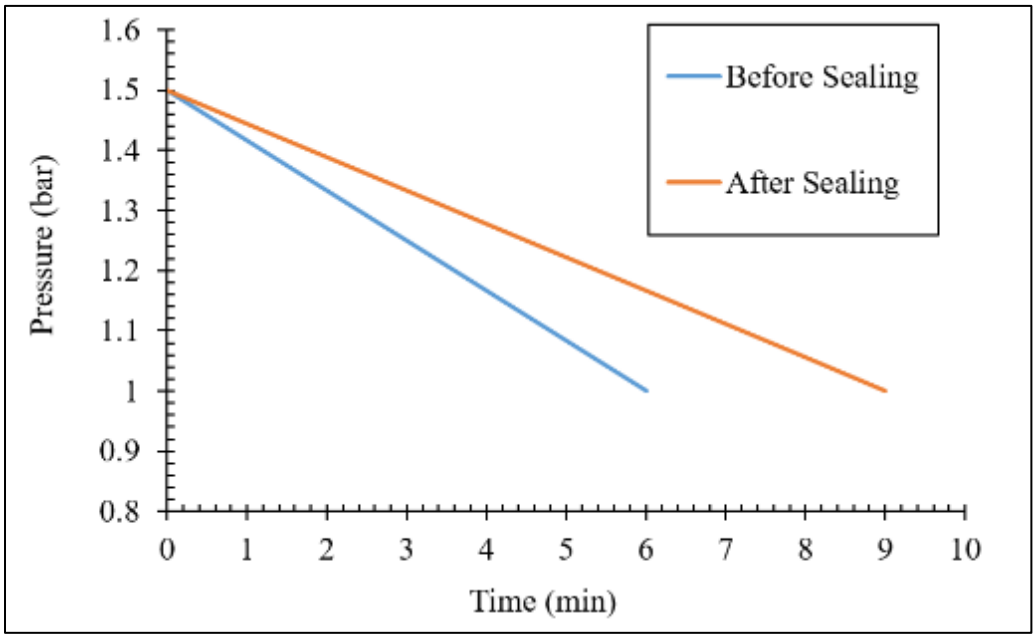

Figure 29. Cold leak test in the combustion bomb before and after shaft's sealing

The required time for the pressure to return to its initial value has increased by 50%, which indicates that the quality of sealing has been remarkably improved.

4.3.2 Hot Leak Test

The second leak test used for investigating any source of leakage when operating the heating coils at elevated temperatures is the hot leak test. Increasing the air temperature will cause the air to expand and build pressure inside the combustion bomb. Since this is a constant volume bomb, the number of air moles inside the bomb should remain constant. Therefore, this test calculates the number of air moles at three different temperatures (298K, 393K, and 453K). The pressure sensor is used to check the pressure at each corresponding temperature, and the number of air moles is calculated using the ideal gas equation of state:

$$PV = RT \tag{63}$$

where R=8.314 m^3. Pa/mol. K is the ideal gas constant, and V=0.082m^3 is the internal volume of the combustion bomb. Table 6 summarizes the results of the hot leak test.

Table 6. Summary of Hot Leak Test

Parameter	**Reading 1**	**Reading 2**	**Reading 3**
Temperature (K)	298	393	453
Pressure (Pa)	77500	102013	117453
Moles of Air (mol)	4.30	4.29	4.28

It can be deduced from these results that the combustion bomb is almost perfectly sealed, especially after performing the shafts sealing using Lithium high-resistant temperature grease and fill the small leaking holes with silicone rubber paste. Therefore, the experimental readings can be obtained with high confidence under these circumstances.

4.3.3 Calibration of Thermocouple

The proper operation of the k-type thermocouple receives high importance because it will be used to conduct the maximum temperature test (explained in subsection 4.3.4) and used during the experiment to monitor the temperature rise at different locations in the bomb. Therefore, it should be appropriately calibrated. For this purpose, a precision heat gun was used to heat the thermocouple wire tip. The temperature readings obtained from the temperature indicator of the heat gun were compared with those of the Fluke 2625A hydra data acquisition unit connected to the thermocouple wire. It was found that both devices' readings match each other up to a temperature equals 550°C.

4.3.4 Maximum Temperature Test

The following important feature that has to be investigated after the proper calibration of thermocouples is the maximum temperature that can be reached within a specific time duration. In addition, this test aims to check for the proper operation of the heating coils. Four circular heating coils, three k-type thermocouple wires, and a display module comprise the test rig's heating system. Before starting the

experiment, three k-type thermocouple wires were connected to the combustion bomb's right, center, and left sides. Figures 30, 31 show the locations of the three thermocouples relative to the combustion vessel.

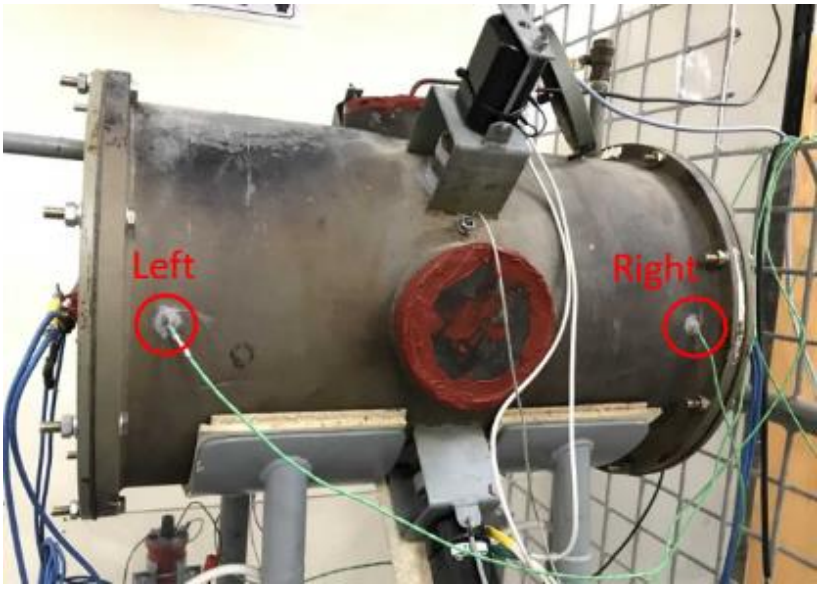

Figure 30. The front side of the combustion bomb showing the location of the right and left thermocouple wires

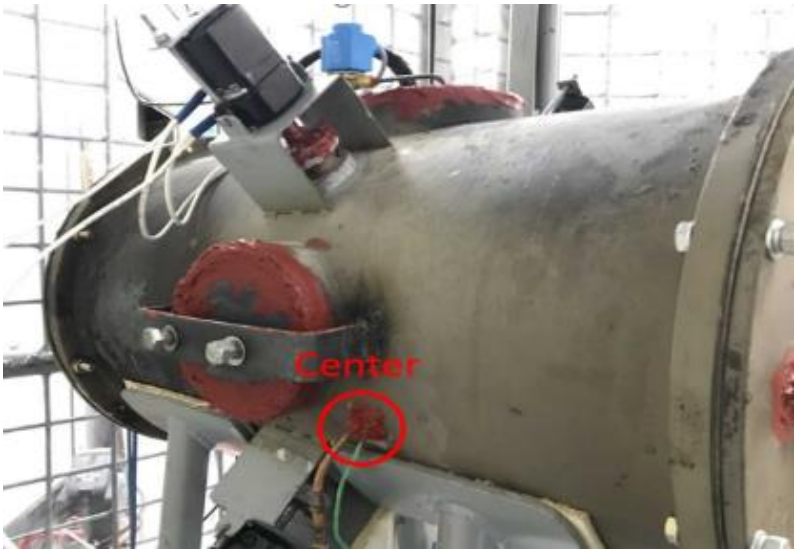

Figure 31. The rear side of the combustion bomb showing the location of the center thermocouple

After that, the four heating coils were switched on, and the readings of the three thermocouples were presented in the display module. Figure 32 shows the temperature increase with time as depicted by the three thermocouples sensors while heating the combustion bomb.

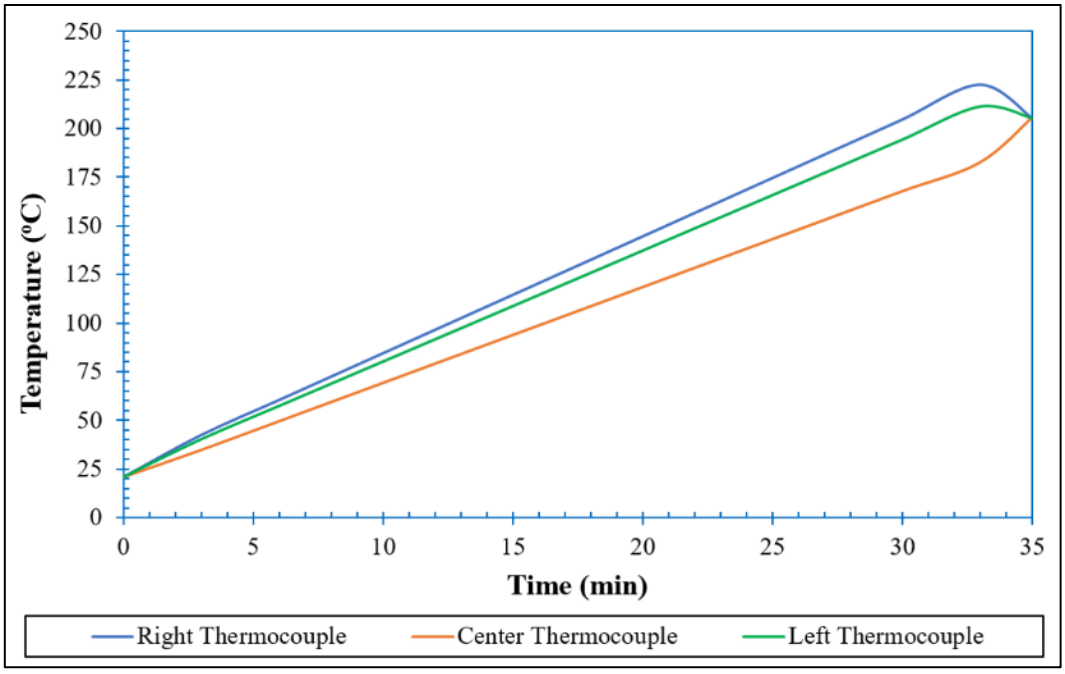

Figure 32. Temperature increase with time when heating the bomb

It can be noticed that there is an apparent variation in the readings of the center thermocouple compared to the right and left ones. This can be referred to the location at which the center thermocouple is placed. It is located in the middle of the bomb, farther from the heating coils than the right and left thermocouples. Therefore, it becomes less affected by radiation generated by the heating coils. To ensure a uniform heat distribution in the combustion bomb, the fans are allowed to operate for around two minutes after reaching the required ignition temperature. Subsequently, the air-fuel mixture becomes homogeneous in all the vessel's domains. After reaching the desired temperature for auto-igniting the diesel (around 205^{o}C), the heaters were switched off, and the bomb was allowed to cool down. The three thermocouple sensors tracked the gradual decrease in temperature with time, as shown in Figure 33.

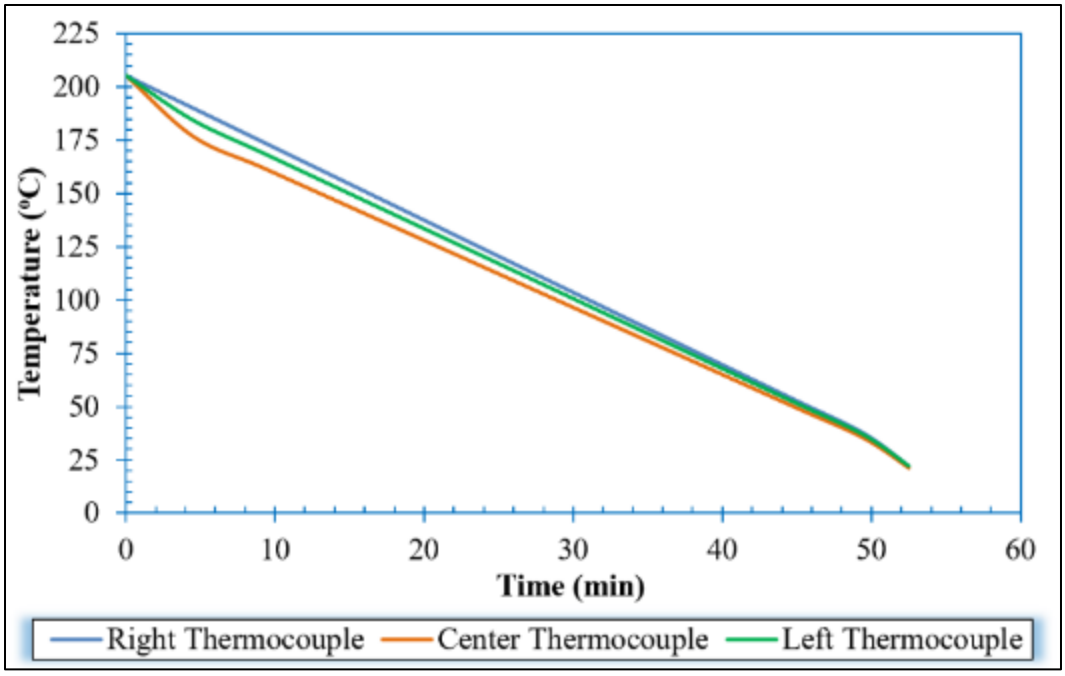

Figure 33. Temperature drop versus time when the bomb cools down

4.3.5 Equivalence Ratio (Φ) Calibration

The equivalence ratio (Φ) is used to describe the state of the air-fuel mixture, indicating whether it is rich (Φ >1), stoichiometric (Φ =1), or lean (Φ <1). In this dissertation, the effect of equivalence ratio variation on turbulent flame speeds must be investigated. As a result, the equivalence ratio at which the experiment is conducted must be determined. The following steps are implemented for calculating the equivalence ratio for all the tested fuels.

Step 1: Calculation of the stoichiometric equivalence ratio, $(A/F)_{stoic}$ from the balanced chemical reaction for one mole of diesel fuel:

$$C_{16}H_{34} + 24.5\ (O_2 + 3.76N_2) \rightarrow 16CO_2 + 17H_2O + 92.12N_2 \qquad (64)$$

Step 2: Calculation of the air mass and the number of moles in the combustion bomb before injecting the fuel:

$$m_{air} = V_{bomb*}\ \rho_{air} \qquad (65)$$

$$n_{air} = \frac{m_{air}}{MM_{air}} \qquad (66)$$

where, m_{air} is the mass of air, V_{bomb} is the bomb's internal volume, ρ_{air} is the air density, n_{air} is the number of air moles, and MM_{air} is the molar mass of air

Step 3: Calculation of the fuel mass injected in the combustion bomb:

$$m_{fuel} = V_{fuel*}\ \rho_{fuel} \qquad (67)$$

where, m_{fuel} represents the mass of fuel injected, V_{fuel} the volume of fuel injected and ρ_{fuel} is the fuel density.

It should be noticed that the fuel is injected into the bomb using a computer-based Arduino circuit and a solenoid valve. The relation between the volume of injected fuel and elapsed time is shown in Figure 34.

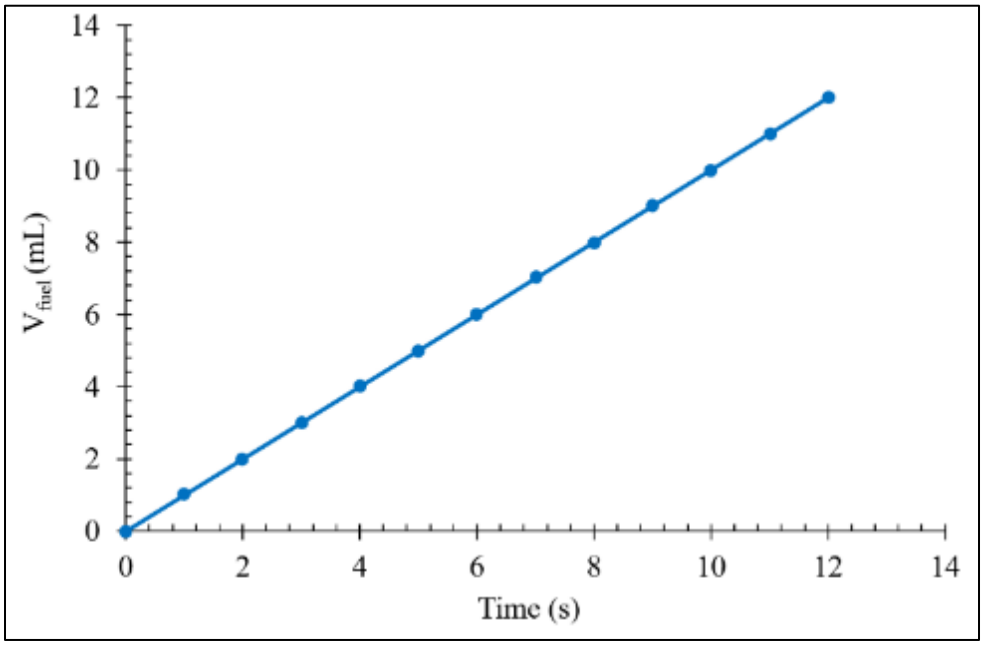

Figure 34. The volume of fuel injected versus time

Step 4: Using the gas analyzer to detect the oxygen percentage in the combustion bomb after injecting the fuel.

Step 5: Calculation of the actual mass and volume of air in the combustion bomb after fuel injection based on the gas analyzer reading:

$$m_{air\ actual} = n_{O2*}\left(MM_{O2} + \left(\frac{79}{21}\right) * \ MM_{N2}\right) \quad (68)$$

$$V_{air\ actual} = m_{air\ actual} / \rho_{air} \tag{69}$$

Step 6: Calculation of the actual volume and mass of fuel in the combustion bomb:

$$V_{fuel\ actual} = V_{bomb} - V_{air\ actual} \tag{70}$$

$$m_{fuel\ actual} = V_{fuel\ actual} * \rho_{fuel} \tag{71}$$

Step 7: Calculation of the actual air to fuel ratio and then the equivalence ratio:

$$\left(\frac{A}{F}\right)_{actual} = \frac{m_{air\ actual}}{m_{fuel\ actual}} \tag{72}$$

$$\Phi = \frac{\left(\frac{A}{F}\right)_{stoic}}{\left(\frac{A}{F}\right)_{actual}} \tag{73}$$

The mixture is in stoichiometric condition if the value of Φ is 1.0. If this value is less (more) than 1.0, the air-fuel mixture is lean (rich).

Following the above steps for the equivalence ratio calculations, an MS Excel calculator has been used to determine the equivalence ratio values at different initial conditions automatically. These calculations are summarized in Table 7.

Table 7. Summary for the Equivalence Ratio Calculations -Diesel

O_2 %	Moles O_2 (mol)	m_{air} (g)	V_{fuel} Injeced (mL)	m_{fuel} Injected (g)	m_{fuel} Evaporaed (g)	$(A/F)_a$	Φ
20.2	0.72	98.2	6.0	5.0	4.6	21.3	0.7
20.1	0.71	97.7	7.0	5.8	5.3	18.6	0.8
19.9	0.70	96.8	8.0	6.6	5.9	16.5	0.9
19.8	0.70	96.3	9.0	7.5	6.5	14.9	1.0
19.7	0.70	95.8	10.0	8.3	7.1	13.5	1.1
19.6	0.69	95.3	11.0	9.1	7.7	12.4	1.2
19.5	0.69	94.8	12.0	10.0	8.4	11.3	1.3

Table 7 shows that a specific fuel volume must be injected to achieve the desired equivalence ratio. It's also worth noting that the amount of fuel evaporated is less than the amount of fuel injected. This can be explained by a few diesel droplets becoming trapped near the bomb's crevices or condensed in the fuel injection line. The same steps have been followed to calculate the equivalence ratio of GTL fuel and the 50/50 diesel-GTL blend, and the results of these calculations can be found in Appendix C.

4.3.6 Hotwire Anemometer Calibration

The hotwire anemometer is used in fluid mechanics and turbulence studies as a research tool to measure the velocity magnitude in different orthogonal directions. It works on the principle of heat loss of the wire that is placed in a fluid stream. Initially, the wire is heated by an electrical current, and it starts losing this heat to the fluid, which causes the temperature of the wire to reduce [178]. In this operation, the

wire resistance is used to indicate the fluid flow rate based on the amount of heat loss. In this work, the hotwire anemometer is used as a tool to study the initial turbulence conditions and conduct the two-point velocity correlation test. Based on these measurements, the mean velocity, the RMS intensities, homogeneity, and isotropy can be analyzed in the combustion bomb. In addition, the different turbulence length and time scales can be determined, and the energy density at different wave numbers can be identified. Before using the hotwire anemometer, a calibration chart must be generated to transform the hotwire readings in voltage to velocity readings in meter per second. To perform this calibration, an air compressor, an air rotameter, and a digital oscilloscope are required to be connected along with the hotwire anemometer. Figure 35 shows a schematic layout for the hotwire calibration process, and Figure 36 shows the actual items used in the calibration process setup.

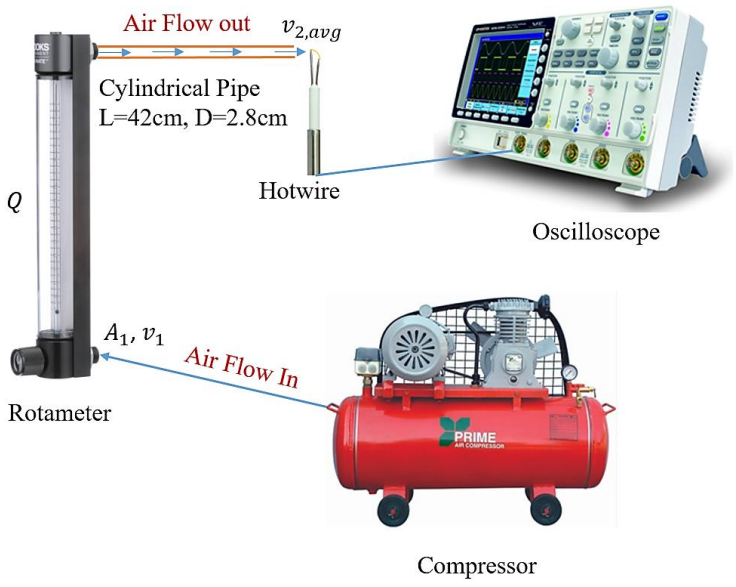

Figure 35. Schematic diagram for hotwire calibration process

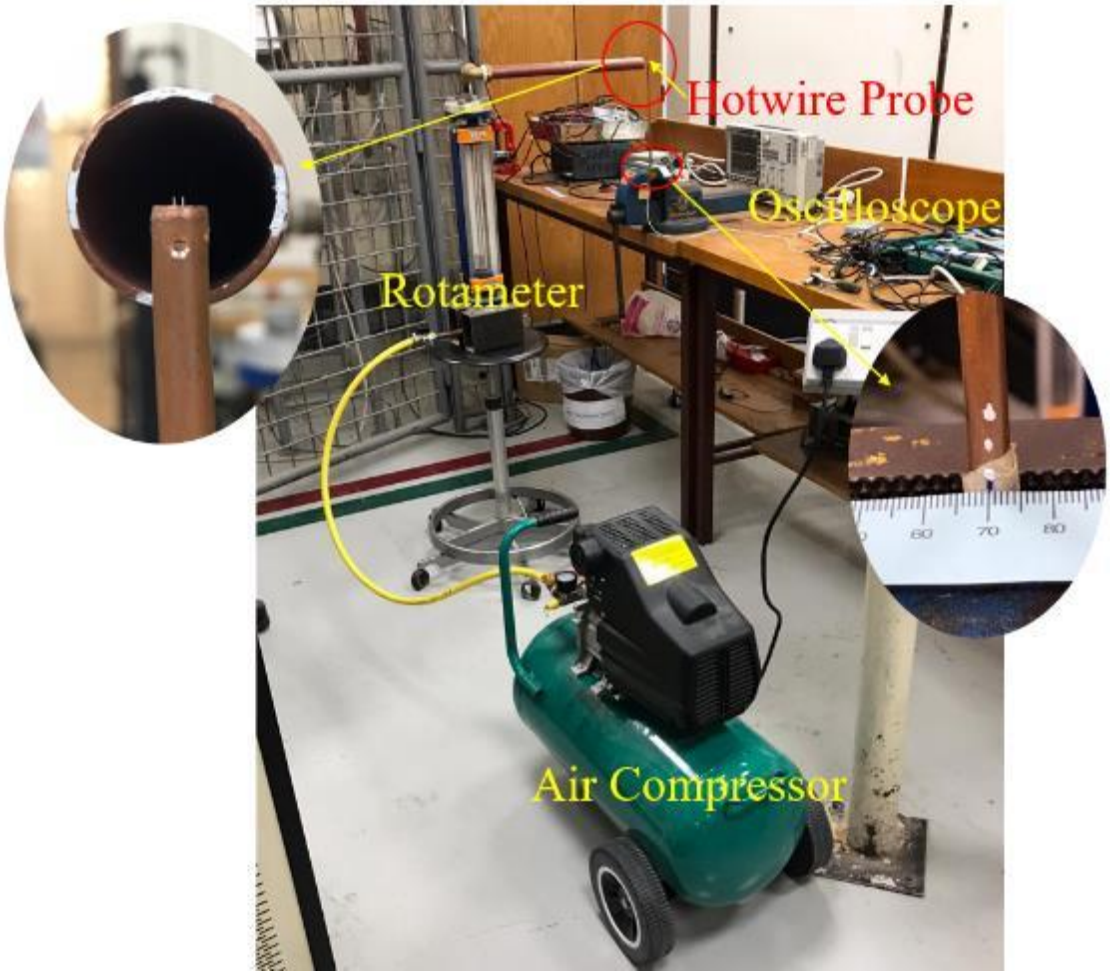

Figure 36. The actual hotwire calibration setup

The following steps are applied:

Step 1: Connecting an air compressor to a rotameter, which can measure the air volume flow rate

Step 2: Connecting the hotwire anemometer to the digital storage oscilloscope

Step 3: Operating the air compressor and using the rotameter's entry valve to control the air volume flow rate

Step 4: At each volume flow rate, the hotwire anemometer is placed at 12 different points. The voltage fluctuations at each point are obtained over 25000 readings and averaged. Figure 37 shows the orthogonal coordinates of the measured points in the velocity profile. The hotwire probe can be located at the desired orthogonal coordinate using the pasted ruler shown in Figure 36 for horizontal dislocation, and the white marked dots for vertical dislocation (e.g., the dots are equally distant with a length of 0.35cm).

Orthogonal Coordinates of the Measured Points in Centimeters:
O: (0,0)
1: (0.35,0)
2: (0.70,0)
3: (1.05,0)
4: (-0.35,0)
5: (-0.70,0)
6: (-1.05,0)
7: (0,0.35)
8: (0,0.70)
9: (0,1.05)
10: (0,-0.35)
11: (0,-0.70)
12: (0,-1.05)

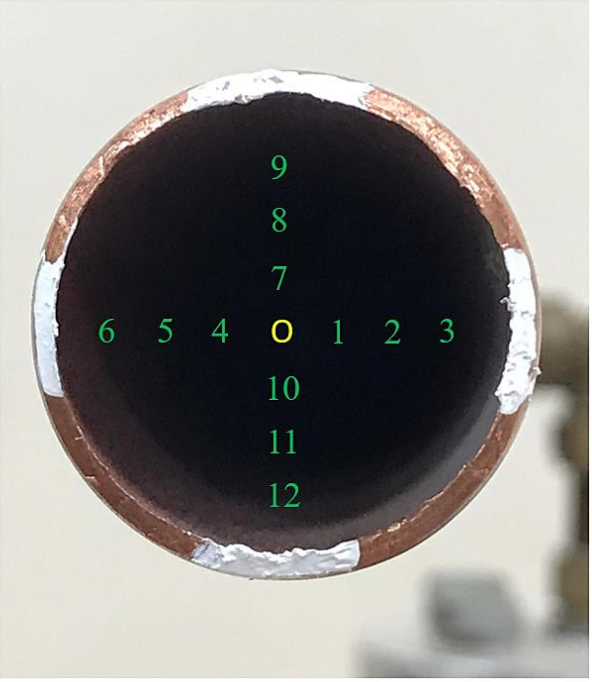

Figure 37. Orthogonal coordinates of the measured points in the fully-developed turbulent velocity profile

Step 5: At each volume flow rate, Reynolds number (*Re*) is calculated to indicate the type of the flow in the circular pipe (e.g., laminar or turbulent):

$$Re = \frac{\rho_{\ v\ D}}{\mu} \tag{74}$$

where, ρ is the density of air at 20 ^{o}C =1.204kg/m^3, v is the flow average velocity, D is the pipe diameter =0.028m, and μ is the air dynamic viscosity at 20 ^{o}C = 0.000018 N.s/m^2.

Step 6: The cases of turbulent flows are considered (Re > 2300), and the following correlations are used to calculate the velocity at the desired locations for the fully developed turbulent flow (L_{pipe} / D_{pipe} =15) [185]:

$$\bar{v}\,(r) = v_{max}\left[1 - \frac{r}{R}\right]^{1/n} \tag{75}$$

$$n = -1.7 + 1.8\log Re_{max} \tag{76}$$

$$Re_{max} = \frac{\rho_{\ v_{max}\ D}}{\mu} \tag{77}$$

$$\bar{v} = \frac{Q}{A_c} \tag{78}$$

$$\frac{\bar{v}}{v_{max}} = \frac{2n^2}{(n+1)(2n+1)} \tag{79}$$

where, r indicates for radius of the pipe, R is the full radius of the pipe= 0.014m, $\bar{v}\,(r)$ is the mean velocity at any radius, v_{max} is the maximum flow velocity, Re_{max} is Reynolds number based on the maximum flow velocity, Q is the volume flow rate,

A_c is the cross-sectional area of the pipe, n is the power-law exponent that depends on Reynolds number value. Table 8 shows a summary of these calculations.

Table 8. Velocity calculations at the desired orthogonal coordinates

Q (m^3/h)	$\bar{v}$ (m/s)	Re	n	v_{max} (m/s)	v at r =0.35cm (m/s)	v at r =0.70cm (m/s)	v at r =1.05cm (m/s)
3.0	1.35	2370	4.92	1.80	1.69	1.56	1.35
4.0	1.81	3159	5.14	2.37	2.24	2.07	1.81
5.0	2.26	3949	5.32	2.93	2.78	2.58	2.26
6.0	2.71	4739	5.46	3.50	3.32	3.08	2.71
7.0	3.20	5529	5.58	4.06	3.86	3.59	3.17
8.0	3.61	6319	5.68	4.62	4.39	4.09	3.62
9.0	4.06	7109	5.78	5.18	4.93	4.59	4.07
10.0	4.51	7899	5.86	5.74	5.46	5.10	4.53

Step 7: At each volume flow rate, the values for the voltage and velocity are averaged over the 12 points to plot velocity-voltage calibration chart shown in Figure 38. The average voltage readings at each point can be shown in Appendix D.

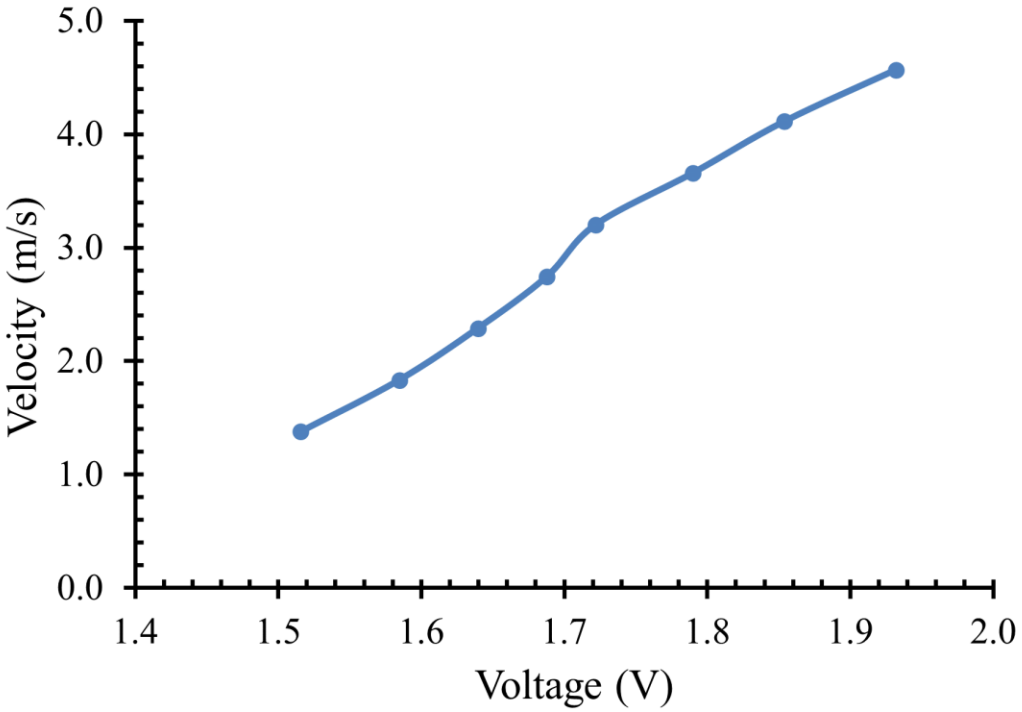

Figure 38. Hotwire anemometer's calibration chart

4.4 Turbulence Statistics

This section explains in detail the steps followed for characterizing the turbulent flow field in the combustion bomb before the experiments, and it is organized as follows. Subsection 4.4.1 presents the turbulence intensities obtained in the middle of the combustion bomb at each fan's rotational speed. The existence of a HIT condition is verified by finding the homogeneity and isotropy ratios, as discussed in subsection 4.4.2. After that, two-point velocity correlation (4.4.3) and the turbulence kinetic energy and dissipation rates (4.4.4) are used to estimate the different turbulence length and time scale in subsection 4.4.5. Finally, the energy transfer between the different size eddies is analyzed in subsection 4.4.6.

4.4.1 Mean Flow and RMS Intensities

The four axis-symmetric fans were operated at different rotational speeds (7000RPM < ω < 21000RPM). To obtain the instantaneous velocity vectors, u_x, and u_y, the hotwire anemometer sensor was placed in the center of the combustion bomb. The instantaneous velocities were then ensemble-averaged over 25000 observations to estimate the mean velocity in *x* and *y* directions, $\overline{U}_x$ and $\overline{U}_y$. The velocity fluctuations, $u`_x$ and $u`_y$ were calculated by subtracting the mean velocities from the instantaneous ones, yielding the values of RMS intensities in the two orthogonal directions (*x* and *y*). In addition, high-order standardized moments such as third-order moment-skewness (*Sk*) and fourth-order moment kurtosis (*K*) were calculated to ensure that the velocity field is following a Gaussian profile in both directions. Table 9 summarizes the mean flow ($\overline{U}$) and RMS velocities ($u`_i$ ) in the two orthogonal directions, along with the skewness *(Sk)* and kurtosis *(K)* at each rotational speed (*ω)* and turbulence intensity *(u`)*.

Table 9. Mean, RMS, and Higher-Order Moments (Skewness and Kurtosis)

ω (RPM)	$u`$(m/s)	i	$\bar{U}$ (m/s)	$u`_i$ (m/s)	Sk	K
7000	0.50	x	0.02	0.36	0.19	3.70
		y	0.01	0.33	0.15	3.50
9800	1.00	x	0.02	0.66	0.17	3.60
		y	0.01	0.63	0.15	3.50
11600	1.50	x	0.02	0.86	0.18	3.70
		y	0.01	0.82	0.17	3.60
14400	2.00	x	0.03	1.06	0.19	3.90
		y	0.02	1.02	0.17	3.70
17200	2.50	x	0.03	1.27	0.20	3.70
		y	0.02	1.21	0.18	3.60
21000	3.00	x	0.04	1.46	0.21	3.50
		y	0.03	1.42	0.19	3.50

As evident, the mean flow velocity is negligible at all conditions (e.g., $\bar{U} < 0.1u`$), which indicates that the flow is uniform in the combustion bomb. Small $\bar{U}$ values can be attributable to a modest variation in motor speeds or a minor misalignment of the fans. Regardless, the mean flow value is considered negligible compared to turbulence intensity. Furthermore, increasing the motors RPM leads to an increase in the intensity level. These findings are congruent with what has been reported in the literature.

The skewness factors are close to zero, indicating that the velocity field is not biased. As evidenced by the kurtosis factors, the velocity PDF profiles were rather peaked up. These peaks are typical in fan-stirred bombs and are caused by a lack of auxiliary devices such as perforated plates that can be placed in front of the impellers. According to the vortex breakdown principle, these plates can help introduce intermediate scales. With an increase in the intensity level, Abdel Gayed et al. [180] demonstrated that the velocity PDFs acquire a near-Gaussian form. The range of velocity scale is broadened at high-intensity levels, and employing the perforated plate causes a relaxation in the peaks.

In addition, the satisfaction of HIT condition in the center of the combustion bomb has been confirmed by studying the velocity fluctuations throughout the vessel domain by placing the hotwire probe at different vessel radiuses (2cm, 6cm, 10cm and 14cm from the center point). A hollow cylindrical socket has been inserted into a custom hole that exists in the outer surface of the bomb (also used for mounting the pressure transducer during the experiments). The hotwire anemometer has been placed inside the cylindrical socket, and the spark electrodes were used to ensure that the hotwire probe exists at the center point of the bomb, which could be further proved visually through the quartz glass windows. The hotwire was then fixed, and the spark electrodes were removed. After that, the electric motors were operated at the maximum rotational speed to ensure the existence of HIT condition at the center of the vessel up to the maximum operating turbulence level. At each vessel radius, 25000 readings were imported from the digital storage oscilloscope to represent the

velocity fluctuations at that point. The hotwire anemometer could be placed at different radiuses by moving it inwardly and outwardly using the marking dimensions drawn on its surface. Figure 39 shows the velocity fluctuations at different vessel radiuses.

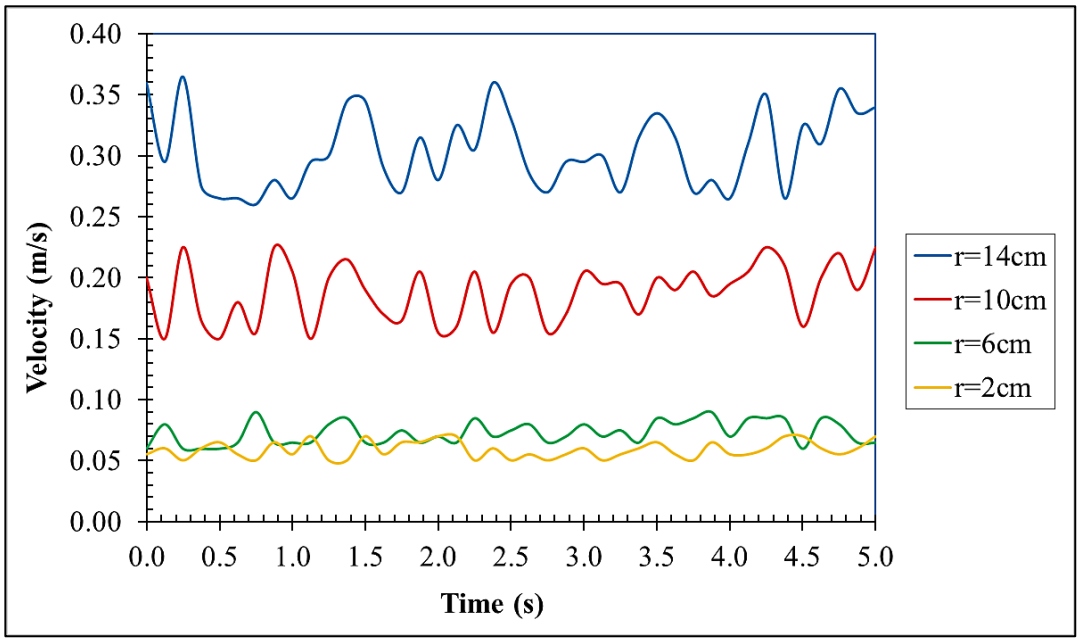

Figure 39: Velocity fluctuations at different vessel radiuses and u`=3.0m/s

It can be observed from the velocity fluctuations in Figure 39 how turbulence is characterized by its chaotic and random nature. In addition, the velocity magnitudes near the center of the combustion bomb ($r \leq 6$cm) have almost remained constant and they are fluctuating within a narrow range when compared with those at r=10cm and r=14cm (i.e., turbulent eddies are anisotropic at these regions), which indicates that

the turbulent flow field is satisfying HIT condition at this zone, and the turbulent kinetic energy has reached its minimum value at this region [55]. The turbulent kinetic energy that is produced from the fan's region starts to be gradually converted into a thermal internal energy by the effect of eddy viscosity until it becomes completely dissipated into heat at the smallest level of turbulent eddies (e.g.: Kolmogorov length scale) which are universal and isotropic [14]. Also, it is worth noting that these observations match the principles of the energy cascade theorem.

4.4.2 Homogeneity and Isotropy Ratios

The homogeneity ratio (*H*) is used to measure the uniformity of the turbulent flow field, and it demonstrates that the flow is unaffected by a dislocation in the coordinate system. This ratio is calculated by multiplying the local RMS velocity by the spatially mean RMS velocity in the same direction, as follows:

$$H = u_{i,rms}(x,y) / \overline{u_{1,rms}(x,y)} \tag{75}$$

The isotropy ratio (*I*) demonstrates that the flow field is statistically invariant to a coordinate system rotation or reflection. This ratio can be calculated by dividing the local RMS values in two directions as the following:

$$I = u_{1,rms}(x,y) / u_{2,rms}(x,y) \tag{76}$$

For perfectly homogenous and isotropic turbulence, these ratios are equal to one. Thus, the HIT field can be characterized by a single root mean square (RMS) intensity value that encompasses all of the velocity components and considers their

spatial variability. In a turbulent flame speed experiment, the concept of RMS intensity is physically transformed to a perturbation in the flame ball surface by the action of external disturbances that acts equally and uniformly in all directions. The PDFs for homogeneity and isotropy ratios were computed to check for the existence of HIT condition in the combustion bomb, as shown in Figures 40 and 41, respectively.

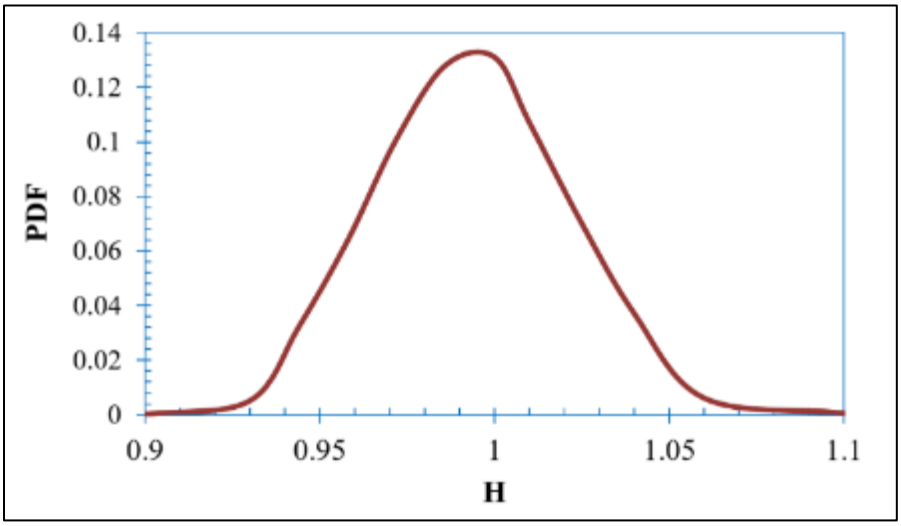

Figure 40. PDF for homogeneity ratio

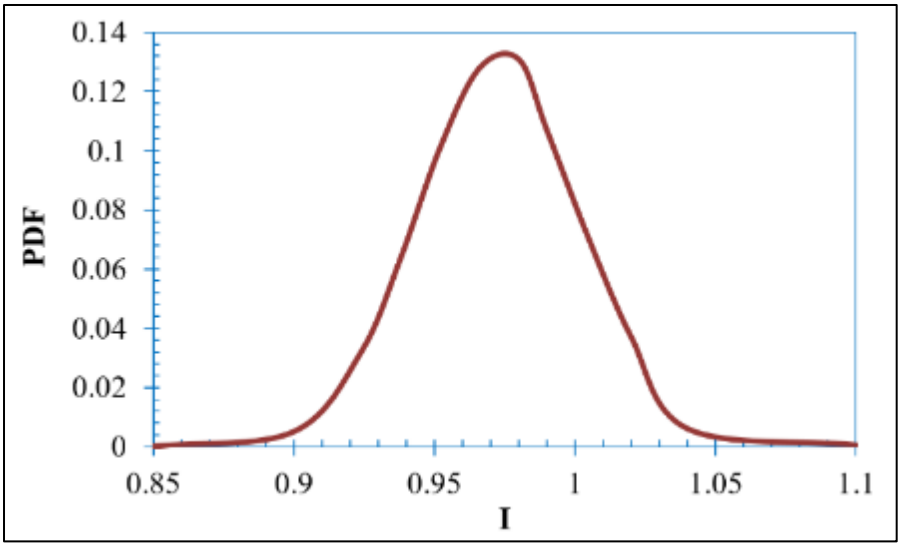

Figure 41. PDF for isotropy ratio

Figures 40 and 41 reveal that the majority of the captured points (> 95%) are close to unity and fall within a particular narrow range (0.9 to 1.1) for both the homogeneity and isotropy ratio. Therefore, this indicates the existence of HIT condition in the combustion bomb.

4.4.3 Two-Point Velocity Correlations

Following Hwang and Eaton's technique [64], two-point velocity correlations are derived using fluctuating fields in two orthogonal directions. For this purpose, the hotwire anemometer is used to conduct high-frequency measurements and is deployed at various separation distances. The longitudinal correlation coefficients are defined as,

$$F_{11}(r) = \langle \overline{u`_1\,(x,y)u`_1\,(x+r,y)} \rangle / \overline{u_{1,RMS}}^2 \quad (77)$$

$$F_{22}(r) = \langle \overline{u`_2\,(x,y)u`_2\,(x,y+r)} \rangle / \overline{u_{2,RMS}}^2 \quad (78)$$

And the lateral correlation coefficients are defined as,

$$G_{11}(r) = \langle \overline{u`_1\,(x,y)u`_1\,(x,y+r)} \rangle / \overline{u_{1,RMS}}^2 \tag{79}$$

$$G_{22}(r) = \langle \overline{u`_2\,(x,y)u`_2\,(x+r,y)} \rangle \overline{u_{2,RMS}}^2 \tag{80}$$

where *r* is the separation distance, and $\langle\ \overline{\rangle}$ indicates a spatial and ensemble average.

The longitudinal and lateral correlation coefficients in isotropic turbulence are related by:

$$G(r) = F(r) + \frac{r}{2}\frac{\partial F(r)}{\partial r} \tag{81}$$

The longitudinal and lateral correlation coefficients are plotted, as shown in Figure 42. The calculated lateral coefficients are also shown in Figure 42, which are used for investigating the existence of isotropic fields.

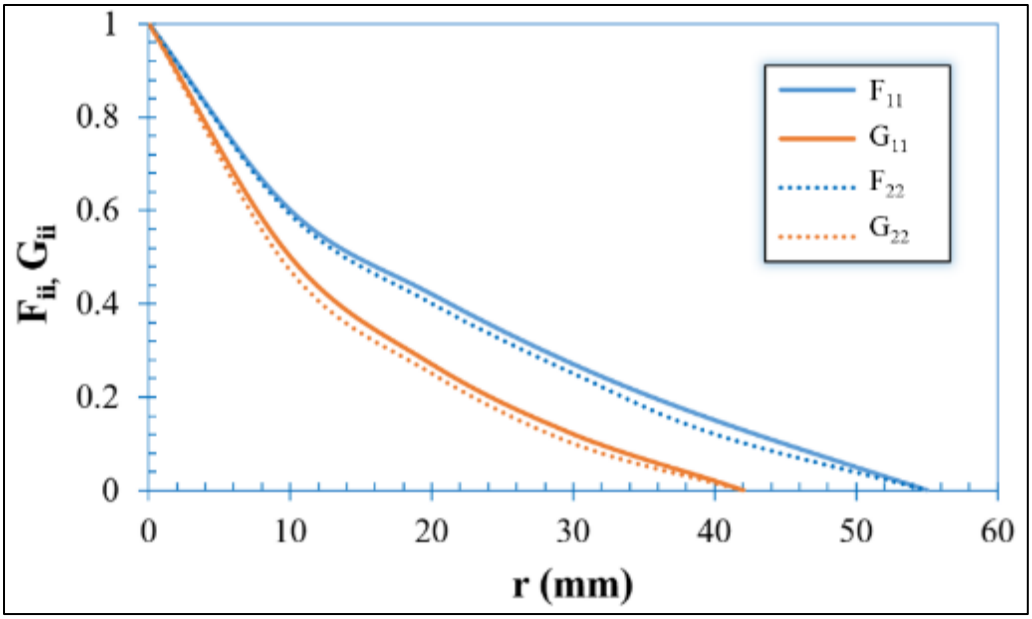

Figure 42. Longitudinal and lateral correlation coefficients

The estimated lateral correlation coefficient closely matches the measured one, as shown in Figure 42. As a result, isotropic turbulence fields are present. In addition, the longitudinal coefficients F_{11} and F_{22} have almost identical values at different separation distances, which implies that the turbulence field is also characterized to be homogeneous. This conclusion can also be further approved by looking at the negligible difference between the lateral correlation coefficients G_{11} and G_{22}. Integrating the longitudinal correlation curve yields the integral length scale. This calculation has returned L_t = 19.8mm, equivalent to the value found in most turbulence studies conducted in fan-stirred combustion bombs [11], [15], [47], [68]. Furthermore, the Taylor microscale (λ) was estimated by calculating the radius at which an osculating parabola intersects the x-axis, which has yielded λ =3.62mm.

4.4.4 Turbulence Kinetic Energy, q^2 and Dissipation Rate, ε

Estimating the turbulent kinetic energy (q^2) and dissipation rate (ε) at the respective operating turbulence intensities is required before determining the various turbulence length and time scales. Turbulent kinetic energy is characterized by measured root mean square (RMS) velocity fluctuations and is correlated with eddies in the flow. Typically, it is used as a measure for the turbulence intensity level and is estimated as:

$$q^2(x,y) = u_{i,RMS}(x,y)u_{i,RMS}(x,y) \cong 3\frac{u_{1,RMS}^2(x,y) + u_{2,RMS}^2(x,y)}{2} \qquad (82)$$

The in-plane turbulence intensity is assumed to be equal to the out-of-plane turbulence intensity in Equation 82. The dissipation rate is calculated using the ensemble-averaged of the square of the strain rate tensor (δ_{ij}):

$$\varepsilon = 2\nu \langle \delta_{ij}\, \delta_{ij} \rangle = \nu \langle \frac{\partial u_i}{\partial x_j}\frac{\partial u_i}{\partial x_j} + \frac{\partial u_i}{\partial x_j}\frac{\partial u_i}{\partial x_j} \rangle \qquad (83)$$

where ν is the kinematic viscosity

Table 10 illustrates the estimated turbulent kinetic energy and the rate of kinetic energy dissipation at each turbulence intensity (u`).

Table 10. Turbulence Operating Conditions

u`(m/s)	q^2 (m^2/s^2)	ε (m^2/s^3)
0.50	0.36	2.28
1.00	1.55	18.70
1.50	3.25	62.10
2.00	6.15	148.70
2.50	9.50	289.80
3.00	13.20	492.40

4.4.5 Turbulence Length and Time Scales

The various turbulence length and time scales can be estimated using the spatial averages for each quantity after computing turbulence kinetic energy and dissipation rates. Equations 84 and 85 are used to calculate the integral length scale (L_t) and Eulerian time macroscale (τ_E), respectively [11]:

$$L_t \cong \left(\frac{\overline{(q^2/3)^{3/2}}}{\varepsilon}\right) \tag{84}$$

$$\tau_E \cong \left(\frac{\overline{q^2/2}}{\varepsilon}\right) \tag{85}$$

Equations 86 and 87 are used to compute the Taylor microscale (λ) and its corresponding Reynolds number (Re_λ), respectively [11]:

$$\lambda \cong \overline{\left(\frac{5\nu q^2}{\varepsilon}\right)^{1/2}} \tag{86}$$

$$Re_\lambda \cong \frac{\overline{\lambda(q^2/3)^{1/2}}}{\nu} \tag{87}$$

where ν=15.51x10^{-6} m^2/s is the air kinematic viscosity at 298K and 1atm.

The Kolmogorov length (η), time (τ_k), and velocity (u_η) scales are estimated using Equations 88, 89, and 90, respectively [11]:

$$\eta \cong \overline{\left(\frac{\nu^3}{\varepsilon}\right)^{\frac{1}{4}}} \tag{88}$$

$$\tau_k \cong \overline{\left(\frac{\nu}{\varepsilon}\right)^{\frac{1}{2}}} \tag{89}$$

$$u_\eta \cong \overline{(\nu\varepsilon)^{\frac{1}{4}}} \tag{90}$$

Table 11 summarizes the spatial averages of the above length and time scales

Table 11. Estimated Turbulence Length and Time Scales

Quantity	**Estimated Value**
Integral Length Scale, L_t	20.00mm
Eulerian time macroscale, τ_E	40.00ms
Taylor microscale, λ	3.64mm
Taylor Reynolds number, Re_λ	220.00
Kolmogorov length, η	0.13mm
Kolmogorov time, τ_k	0.47ms
Kolmogorov velocity, u_η	0.22m/s

The integral length scale (L_t) and the Taylor microscale (λ) were also obtained using a two-point velocity correlation in subsection 4.4.3, and they were found to be 19.8mm and 3.62mm, respectively. This slight discrepancy can be attributed to the assumption that the in-plane and out-of-plane turbulence intensities are the same when computing the turbulent kinetic energy (q^2) using Equation 82. Regardless, the difference between the two values is marginal, and the values listed in Table 11 will be used in the following sections.

4.4.6 Energy Spectrum

Turbulence's kinetic energy (k) is spread among eddies of different sizes. The magnitude of energy contained within a particular wavenumber range (k_A, k_B) is expressed as [11],

$$k_{(k_A,k_B)} = \int_{k_A}^{k_B} E(k)dk \tag{91}$$

where, k_A is the lower bound of the wavenumber range, k_B is the upper bound of the wavenumber range, and $E(k)$ is the energy spectrum function.

The inertial subrange's of the energy spectrum function has a universal form, according to Kolmogorov's second hypothesis, which is written as [11],

$$E(k) = C\varepsilon^{2/3}k^{-5/3} \tag{92}$$

where C is the Kolmogorov universal constant and equals 1.5 according to experimental data [11]. Figure 43 shows a plot of the internal subrange of the energy spectrum function (normalized by the Kolmogorov length scale) versus k_η (e.g., k_η is

a non-dimensional wavenumber calculated as the product of η by 2π/wavelength) at $Re_\lambda = 220$.

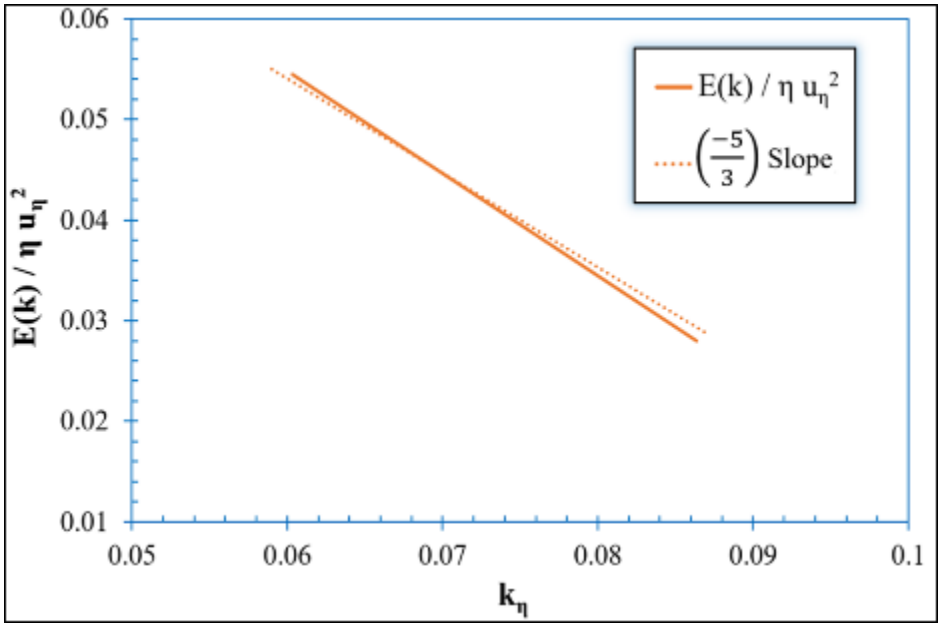

Figure 43. The inertial subrange of the normalized energy spectrum function versus $\boldsymbol{k_\eta}$ at $Re_\lambda = 220$

4.5 Tested Fuel Blends

This study will test the following fuels: conventional diesel, GTL, and a 50/50 diesel-GTL blend. Laminar flame speeds of 50/50 fuel blend have been investigated before by Samim [179], and therefore, this dissertation aims to expand the investigation scope by conducting a fundamental study of turbulent flame speeds of this fuel under different turbulence intensities ($0.5m/s < u` < 3.0m/s$) and equivalence ratios ($0.7 < \Phi < 1.3$) to determine its optimum operating conditions. Table 12 lists the chemical and physical properties of the tested fuels.

Table 12. Properties of Conventional Diesel, GTL and 50-50 Blend [10]

Properties	**Diesel**	**GTL**	**50-50 Blend**
H/C Ratio	2.125	2.1-2.15	2.1-2.125
Approx. Formula	$C_{16}H_{34}$	$C_{16}H_{34}$	$C_{16}H_{34}$
Density at 15^{o}C (kg/m^{3})	830	770	792
Boiling Range (^{o}C)	190-360	160-360	165-360
Flash Point (^{o}C)	55	77	71
Cetane No.	55	75	64
Calorific Value (MJ/kg)	42.9	49.3	46.2

Diesel fuel is mixed with GTL on a 50-50 volumetric basis. The properties of this fuel blend were determined by specialized chemists in the laboratory at Qatar University.

4.6 Experimental Procedure for Flame Speed Measurement

The following experimental procedure gave the successful ignition for the measurement of turbulent flame speed (S_t) at each run:

- A vacuum pump was used for flushing the bomb of exhaust gases while keeping the exhaust port open.
- All the ports were closed, and the heaters were switched on.
- The bomb was allowed to attain a temperature of 220°C and then held there for 15 minutes.
- The interior temperature of the bomb was allowed to cool to the desired initial temperature of 190°C
- Fuel was injected into the bomb at a pre-specified volume to reach the desired equivalence ratio using the Arduino controlled circuit and the fuel injector (Φ= 0.7 to 1.3).
- The electric fans were switched on, and the dimmer switch was used to control the speed of the rotating shafts to generate the desired turbulence intensity (u`=0.5m/s to 3.0m/s). This step is also necessary to ensure the proper mixing of air-fuel mixture throughout the combustion bomb before ignition.
- At this time, the oxygen percentage inside the bomb was noted down using the gas detector. Based on that, the equivalence ratio of the experiment was determined.

- The protective cage was closed before igniting the mixture, and no fuel bottles or flammable materials were kept near the combustion bomb.
- Finally, the mixture was ignited with the assistance of a remote-controlled spark ignition coil circuit.
- The pressure transducer connected to the oscilloscope and DAQ detected the pressure rise signal after igniting the mixture.
- A k-type thermocouple sensor and the Fluke hydra 2625A data logger were used to record the temperature rise.
- The bomb's exhaust port was opened, and the exhaust gases were discharged by flushing the bomb using the vacuum pump
- The test rig is now ready for the next test run after flushing

For the laminar flame speed (S_l) measurement, the electric fans were switched on for only 30seconds after fuel injection, and then they were switched off. In this dissertation, S_l is calculated using the Lewis and Von Elbe correlation in Equations (4-8) [10, 182], from the pressure versus time record, while the turbulent flame speed (S_t) is calculated using the following expressions [15]:

- Radius for Equal Masses, r_m

$$r_m = R\left\{1 - \left(\frac{p_o}{p}\right)^{\left(\frac{1}{y_u}\right)}\left[\frac{p_f - p}{p_f - p_0}\right]\right\}^{\frac{1}{3}} \tag{93}$$

- Turbulent Flame Speed (S_t) at r_m

$$S_t = \frac{R\left(\frac{p_o}{p}\right)^{\left(\frac{1}{\gamma_u}\right)}\frac{dp}{dt}}{3\,(p_f - p_0)\left\{1 - \left(\frac{p_o}{p}\right)^{\left(\frac{1}{\gamma_u}\right)}\left[\frac{p_f - p}{p_f - p_0}\right]\right\}^{\frac{2}{3}}} \quad (94)$$

where,

r_m is the spherical flame radius within which reside all the burned gases inside and outside reside all the unburned gases

p_i, p_f are the initial, and final pressure in explosion, respectively

p is the instantaneous pressure

γ_u is the specific heat ratio of unburned reactants

R is the radius of the cylindrical combustion bomb (R =20cm)

$\frac{dp}{dt}$ is the pressure rise rate

According to References [15], [47], it is essential to determine S_t at a radius where the flame has left the ignition region and it is subjected to a small portion of the turbulence domain. Therefore, in this dissertation S_t is calculated at r_m at the instant that p = 0.5p_f at all conditions. The results of laminar flame speed measurements for validation are presented in subsection 6.1.1, while the results of the turbulent flame speed experiments are presented and discussed in subsection 6.1.5.

4.7 Measurement Uncertainties

This section aims to find the systematic uncertainty (bias) that results from measuring the turbulent flame speeds (S_t). The systematic uncertainty (B_{st}) is defined as the error associated with the use of measuring devices and components (e.g., thermocouple, transducer, hotwire, gas detector, etc.), which cannot be statistically estimated [50]. The systematic uncertainty (B_{st}) can be determined using the following formula [50]:

$$B_{st} = \sqrt{\sum_{i=1}^{n} \left(\frac{\partial y(x_i)}{\partial x_i} B_i \right)^2} \tag{95}$$

where B_i is the element bias uncertainty associated with each component in the experiment (e.g., thermocouple, transducer, etc.), x_i is any variable that y depends on (e.g., temperature, pressure, equivalence ratio, turbulence intensity, etc.), $\frac{\partial y(x_i)}{\partial x_i}$ is the sensitivity of y to the variation of any of these variables (P, T, Φ, $u`$). Table 13 provides the elemental bias uncertainty (B_i) associated with using each measurement device in this experiment and the source of error generation [50].

Table 13. The Elemental Bias Uncertainty (B_i) of Each Measurement Device

Device	**Source of Error**	**Bias (B_i)**
Pressure Transducer	Combined non-linearity, repeatability, and hysteresis [Pa]	±0.5%
Thermocouple k-type	Accuracy [°C]	±1.5°C
Hotwire Anemometer	Combined non-linearity, repeatability and hysteresis [m/s]	±1.0%
Gas Detector	Accuracy [O_2%]	±3%
Fans	Vibrational Loses in Fan Speed [RPM]	±1.0%

B_i of the pressure transducer, thermocouple k-type, the hotwire anemometer, and the gas detector has been obtained from their technical data sheets and calibration certificates. For the fans, a ±1.0% discrepancy has been determined. Afterward, Equations 94 and 95 were used to determine the uncertainty in the measurement of turbulent flame speeds (S_t) at Φ=1.0, respectively, in which MATLAB has been used for differentiation using the function "diff" and then finding the values of B_{st} at each turbulence intensity, u`. Table 14 shows the error calculation of $S_t$ for GTL fuel at $\Phi$=1.0 and $u$`=0.5m/s up to 3.0m/s. In addition, the measurement uncertainties have been also calculated at Φ=0.7 and Φ=1.3 and they can be viewed in Appendix E.

Table 14. The Error Calculations in S_t Measurement for GTL fuel at Φ=1.0, and u`=0.5m/s up to $u$`=3.0m/s

u`(m/s)	**S_t (cm/s)**	**B_{st} (cm/s)**	**Error %**
0.50	93.79	1.15	1.23
1.00	122.68	1.86	1.52
1.50	183.75	3.12	1.70
2.00	255.66	4.96	1.94
2.50	353.67	8.10	2.29
3.00	465.87	11.74	2.52
Mean Error %			**1.87**

CHAPTER 5. NUMERICAL SIMULATION APPROACH

In this chapter, a description of the physical significance of the Zimont TFC model, which will be used to study premixed turbulent combustion of diesel, GTL, and the 50/50 diesel-GTL blend, is discussed in subsection 5.1. The model's governing equations are presented in subsection 5.2. The experimental data used for model validation and obtaining the simulation results are displayed in subsection 5.3. The numerical grid details and the complete description of the meshing process are handled in subsection 5.4. The numerical schemes, boundary conditions, physical constraints, and solution initialization are presented in subsection 5.5. Finally, the results of model validation are discussed in subsection 5.6.

5.1 Model Description

By calculating the Favre averaged equation for the mean reaction progress variable *C*, Zimont [25] introduced a model to solve turbulent premixed flames. The formulation of this model is based on a theoretical analysis that the turbulent flame moves with a constant propagation velocity dependent on the mixture's physicochemical properties and the turbulence effects in the propagation flame front [27]. In this model, combustion occurs in a thin and strongly wrinkled flame sheet that separates the reactants and the products. Thus, this model considers the division of the reacting flow field into regions of unburned and burned species, separated by the thin flame sheet that is propagating with speed called the turbulent flame speed (S_t). Also, in this model, an averaged flame front is tracked out instead of the exact one. Upon

averaging, a region with an instantaneous realization of the flame can be found, and it will be surrounding the mean flame front. The width of this region is known as the turbulent flame brush thickness (δ_t). According to turbulent diffusion law [25], this model assumes an increasing thickness of the flame brush and a constant combustion velocity. Flames following these behaviors are known as Intermediate Steady Propagation (ISP) flames. This further confirms the suitability of the Zimont TFC model to handle the current ISP flames as it is valid for $Re_T >> 1$, $Da >> 1$, and $u` >> S_l$, where S_l is the laminar flame speed.

5.2 Governing Equations

The flame front propagation is modeled by solving the density-weighted mean reaction progress variable's (C) transport equation [25]:

$$\frac{\partial}{\partial t}(\rho C) + \nabla.(\rho \vec{v} C) = \nabla.\left(\frac{\mu_t}{S_{ct}} \nabla C\right) + \rho S_c \tag{96}$$

where ρ is the fuel density, C the mean reaction progress variable, S_{ct} turbulent Schmidt number, μ_t is turbulent viscosity, and S_c is the reaction progress source term.

The reaction progress variable is defined as the normalized sum of the species product's:

$$C = \frac{\sum_{i=1}^{n} Y_i}{\sum_{i=1}^{n} Y_{i,eq}} \tag{97}$$

where n represent the number of product species, Y_i the mass fraction of product species i, and $Y_{i,eq}$ the equilibrium mass fraction of product species i.

As per this definition, *C*=1 when the mixture is burned and *C*=0 when the mixture is unburned. At all flow inlets, the value of *C* is utilized as a boundary condition. *C*=0 (unburned) or *C*=1 (burned) are specified in solution initialization.

The mean reaction rate in Equation (96) is modeled as:

$$\rho S_c = \rho_u S_t |\nabla C| \tag{98}$$

where ρ_u is the unburned mixture density, and S_t is the turbulent flame speed

The laminar flame speed influences the turbulent flame speed normal to the flame surface, and the flame front is wrinkled and stretched by larger eddies. The Zimont turbulent flame speed closure computes S_t according to the following equation:

$$S_t = A(u`)^{0.75} S_l{}^{0.5} \alpha^{-0.25} L_t{}^{0.25} = Au` \left(\frac{\tau_t}{\tau_c}\right)^{0.25} \tag{99}$$

where *A* is a model constant, $u`$ the Root Mean Square (RMS) velocity (m/s), $S_l$ the laminar flame speed (m/s), $\alpha = \frac{K}{\rho c_p}$ is the thermal diffusivity ($m^2/s$), $L_t$ is the turbulence integral length scale (m), $\tau_t = \frac{l_t}{u`}$ is the turbulence time scale (s), and $\tau_c = \frac{\alpha}{S_l{}^2}$ is the chemical time scale (s).

The turbulent kinetic energy, *k*, is computed as:

$$k = \frac{3}{2} u`^2 \tag{100}$$

The turbulence integral length scale, $L_{t,}$ is computed from

$$L_t = C_D \frac{(u`)^3}{\varepsilon} \tag{101}$$

where ε is the turbulence dissipation rate, and C_D is a model constant.

According to this model, the equilibrium small-scale eddies act on the laminar flame, resulting in a turbulent flame speed formula completely defined by large-scale turbulent eddies. The default values of 0.52 for A and 0.37 for C_D are appropriate for most premixed flames [182], [183].

The thin reaction zone combustion regime occurs when the Kolmogorov scales (e.g., the smallest turbulent eddies in the flow) are smaller than the laminar flame thickness and penetrate the flame zone. The Karlovitz number, *Ka*, can be used to quantify this regime and is defined as:

$$ka = \frac{t_l}{t_\eta} = \frac{{\nu_\eta}^2}{{S_l}^2} \tag{102}$$

where t_l is the characteristic flame time scale, t_η is the Kolmogorov (smallest) turbulence time scale, $\nu_\eta = (\nu\varepsilon)^{0.25}$ is the Kolmogorov velocity, and ν is the Kinematic viscosity.

Finally, it should be mentioned that this model is only applicable for the cases where the width of the flame brush expands with time, which is encountered in most industrial systems. Flames that propagate for an extended time reach a constant flame width, which contradicts the physical principles found in this model.

5.3 Experimental Data for Validation

In this dissertation, two cylindrical fan-stirred combustion vessels are modeled. The first one is the Texas A&M vessel, which is used for model validation by comparing the numerically computed methane-air turbulent flame speeds with the experimental ones [11]. The other one is the Qatar University vessel, which is used for studying the premixed turbulent combustion of the three liquid fuel blends (diesel, GTL, 50/50 diesel-GTL blend). This vessel was designed at Qatar University in 2012, and it was used for obtaining the laminar flame speeds for the three liquid fuel blends in 2016 [10]. Therefore, it is modeled in this dissertation to compute the turbulent flame speeds for the three liquid fuels at different turbulent intensities and equivalence ratios. For simplicity, the name "QU vessel" is used to indicate the use of Qatar University combustion vessel. Table 15 summarizes the geometrical specifications and operating conditions for the two vessels.

Table 15. Geometrical Specifications and Operating Conditions for Texas A&M and QU Vessel

Vessel Name	**Texas A&M Vessel [11]**	**QU Vessel [10]**
Geometrical Specifications		
Vessel Shape	Cylindrical	Cylindrical
Internal Diameter (ID in cm)	30.5	40.0
Internal Length (IL in cm)	35.6	65.0
No. of Fans	4	4
No. of Blades of Each Fan	3	8
Fans Outer Diameter (OD in cm)	7.62	8.00
Pitch Angle (Degrees)	20	60
Operating Conditions		
Initial Temperature (T_o in K)	298	463
Initial Pressure (P_o in atm)	1	1
Equivalence Ratio (Φ)	0.7-1.3	0.7-1.3
Turbulence Intensity ($u`$ in m/s)	0.85-1.30	0.50-3.00
Integral Length Scale (L_t in mm)	27	20
Fuel	Methane	Diesel, GTL, 50/50 diesel-GTL blend

5.4 Numerical Grid Details

The geometrical domain of the problem consists of a cylindrical; steel vessel with a diameter of 40cm and a volume of 81.7L. Two optical glass windows are installed on the vessel's outer shell for tracking the flame propagation using Schlieren photography. Four fans are installed on the vessel's inner wall, located at the vessel's central circumference with an equal distance from each other. The fan's axes are oriented collinearly with the central point of the vessel, aiming to generate HIT flow field inside the vessel. The axial distance between one fan and the opposite one is 30cm. Each fan has an outer diameter of 8cm and consists of eight blades of 3.5cm in

length each and a pitch angle of 60^0. The complete description of the test rig can be found in Reference[10].

The computational domain covers the whole vessel's internal volume approximated by a cylinder with four fans mounted on the vessel's wall. The combustion vessel model was designed using SOLIDWORKS 2020 and then exported to ANSYS Fluent 17.0 to generate the mesh. Figure 44(a, b) shows the model's geometry with basic dimensions and describes its main components.

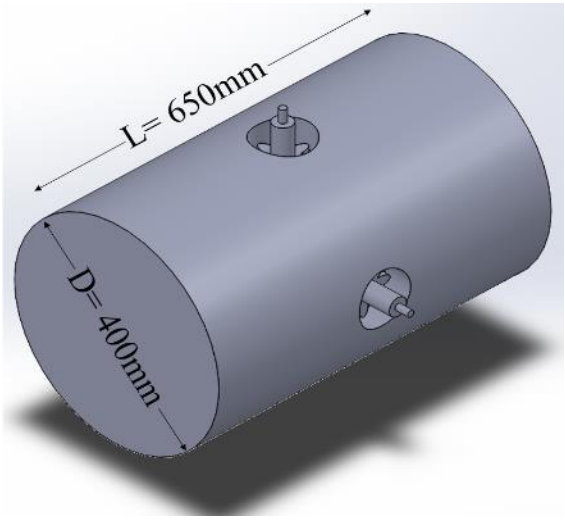

(a)

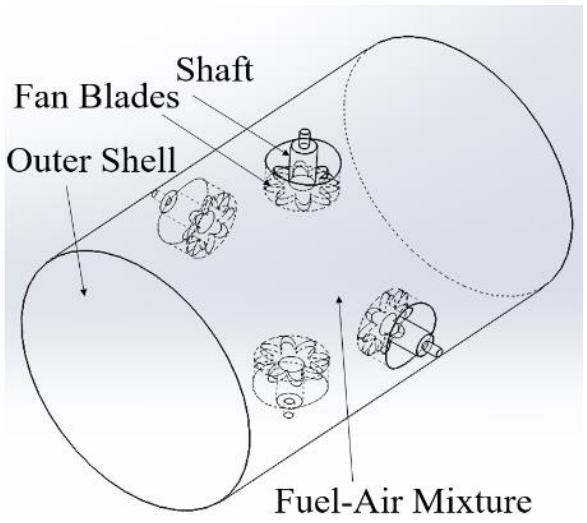

(b)

Figure 44. (a) QU vessel's SOLIDWORK model with basic geometrical dimensions, (b) schematic diagram that shows the component of QU vessel model

Tetrahedral, quasi-equidistant elements are used to build the computational domain, using an adaptive size function, where each element has a size of 2mm. The computational mesh domain was built using 7.8 million cells in total. Figure 45 shows the meshed geometry and a cross-section view for the mesh at the central circumference of the combustion vessel.

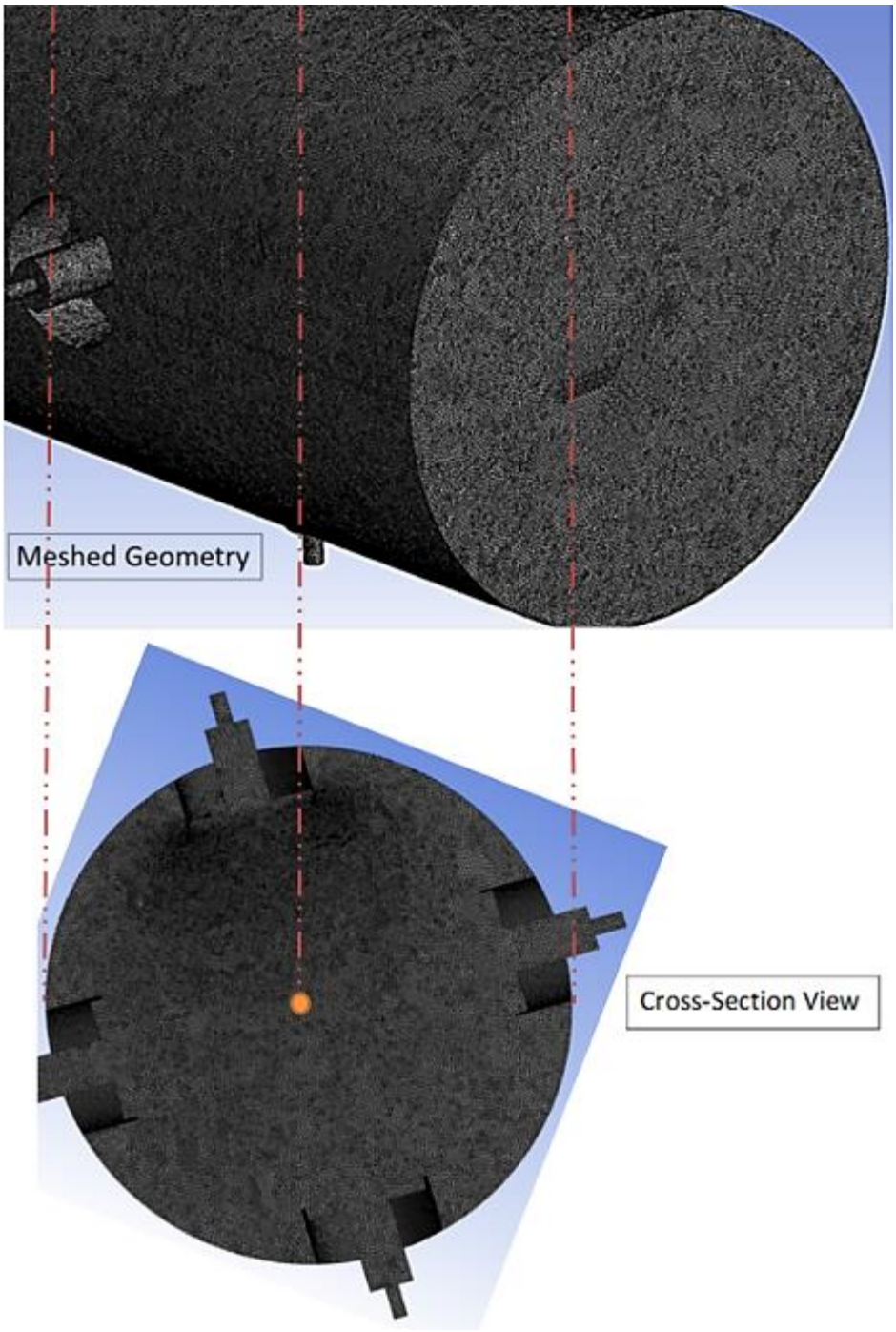

Figure 45. Perspective view of numerical grids on the combustion vessel surface

The grid size is determined based on a grid detailed independence study, discussed in subsection 5.6. Table 16 summarizes the mesh details used throughout this numerical study.

Table 16. Mesh Details and Statistics

Parameter	**Type (or Value)**
Size function	Adaptive
Relevance center	Fine
Smoothing	Medium
Span Angle Center	Fine
Element Size (mm)	2.00
Minimum Edge Length (mm)	0.59
Inflation Option	Smooth Transition
Nodes	1422642
Elements	7844078
Average Element Quality	0.84
Average Skewness	0.22
Orthogonal Quality	0.86

5.5 Numerical Model Settings, Discretization and Initialization

In this dissertation, Zimont TFC model was selected to investigate the flame propagation and obtain turbulent flame speeds for the three liquid fuel blends (diesel, GTL, 50/50 diesel-GTL blend) at different equivalence ratios ($\emptyset$=0.7 to 1.3) and turbulence intensities ($u`$= 0.5m/s to 3.0m/s). The second-order upwind has been selected as the discretization scheme; to ensure the convergence of the solution with a high accuracy and with an insensitivity to grid size variation.

Unlike the segregated pressure base algorithm, the coupled algorithm simultaneously solves a system of continuity and momentum equations; subsequently, this results in a faster solution convergence while consuming a larger memory size. As this study comprises a large number of results, this algorithm has been selected for use. According to the literature review, many studies have considered running the turbulent flame speed experiment using an integral length scale, L_t = 20mm [11], [15], [47], [68], [184]. Therefore, this value is used in the solution initialization to obtain the turbulence dissipation rate in Equation (101).

$k-\varepsilon$ has been selected as the viscous model to estimate the Reynolds stresses and the conversion of turbulent kinetic energy into thermal internal energy by the effect of eddy viscosity. This model has shown satisfactory performance in many industrial relevant applications, particularly for thin shear layer flows accompanied by small pressure gradients [55]. In addition, it has demonstrated its success in problems where there is a dominance of Reynolds shear stresses, such as in confined flows [114]. Moreover, the model has shown moderate agreement in flows of free turbulence such

as in free jet flows, wake, or mixing layers [115]. Therefore, it has been selected for use rather than the $k-\omega$ model, which does not perform well in regions of free-stream turbulence (e.g.: at the center of combustion bomb) and does not show a satisfactory performance in applications of high Re_T [117]. In addition, $k-\varepsilon$ model has been used for conducting a mean turbulent kinetic energy balance study in subsection 6.2.1, and it has well demonstrated the gradual dissipation of turbulent kinetic energy from the fan's region up to the center of the bomb, and therefore, matching the principles of the energy cascade theorem.

Moreover, it should be noticed that a value of C=0 must be used in the solution initialization to indicate the unburned mixture before the ignition. A spark plug with a 40mJ energy is placed in the center of the combustion vessel, where the flame kernel initiates and starts to propagate spherically in all directions. Table 17 lists the details of the used numerical models and spark plug, and Table 18 lists all the information used in the settings of the solution initialization.

Table 17. Numerical Model Settings of the Spark Plug

Parameter	**Type (or Value)**
Processor Option	Serial
Solver Type	Pressure-Based
Velocity Formulation	Absolute
Time	Transient
Discretization	2nd Order Upwind
Species Model	Premixed Combustion Model
Flame Speed Model	Zimont Model
Viscous Model	K-epsilon, Realizable with Enhanced Wall Treatment
Premixed Charge	Diesel, GTL, 50/50 Diesel-GTL Blend (Methane Used for Validation Case)
Equivalence Ratio (Ø)	0.7 to 1.3
Spark Location	At the Center of the Vessel
Spark Energy (mJ)	40
Spark Duration (s)	0.0001
Spark's Transition Radius (mm)	0.5

Table 18. Solution Initialization

Parameter	**Type (or Value)**
Solution Scheme	Coupled
Solution Initialization	Standard
Initial Pressure (atm)	1
Initial Temperature (K)	463
Integral Length Scale, L_t (mm)	20
Reaction Progress Variable, C at t=0s	Zero (at All Zones)
Time Step Size (s)	0.00025
Number of Time Steps	120
Maximum Iterations/Time Step	25

5.6 Model Validation

The case of cylindrical combustion vessels is considered to demonstrate the validity of using the Zimont TFC model to predict turbulent flame propagation. In this validation, turbulent flame speeds are computed for a fully premixed methane-air mixture and compared to the experimental ones found in the work of Ravi [11]. The numerical scheme followed to perform the Computational Fluid Dynamics (CFD) calculations is described in subsection 5.6.1. After that, the validation results are presented in subsection 5.6.2 by conducting a grid independence study.

5.6.1 CFD Solution Method

Turbulent flame speeds experiments performed for methane-air mixture using Texas A&M vessel [11] are used to compare with CFD results. The experiment's geometrical specifications and operating conditions are listed in Table 15, and the solver details were listed in Table 17 in Section 5.5. Tetrahedral, quasi-equidistant elements have been used to mesh the computational domain, using an adaptive size function, where each element has a size of 2mm. A total number of 2.8 million cells were used to build up the computational mesh domain. Burned and unburned density, thermal conductivity, specific heat, molecular weight, viscosity, and laminar flame speeds have been formulated as constants in ANSYS Fluent. The Laminar flame speed readings at the corresponding equivalence ratios have been extracted from the same experimental work [11]. A spark plug with a 40mJ energy is placed in the center of the combustion vessel to ensure the ignition of the flammable mixture, where the

flame kernel initiates and starts to propagate spherically in all directions [185]. The experiment was conducted under atmospheric pressure at an initial temperature of 298K. Turbulent kinetic energies and turbulent dissipation rates at the corresponding turbulence intensities were obtained using Equations (100) and (101), respectively. Table 19 summarizes all the test points used in this validation case.

Table 19. Turbulence Initial Conditions for the Validation Case

Turbulence Intensity, u` (m/s)	**Turbulent Kinetic Energy, k (m^2/s^2)**	**Turbulence Dissipation Rate, ε (m^2/s^3)**
0.85	1.08	8.42
0.90	1.22	9.99
1.00	1.50	13.70
1.10	1.82	18.24
1.20	2.16	23.68
1.30	2.54	30.11

5.6.2 Validation Results

The methodology followed to validate the model and present the results comprises a grid independence study, a time-step independence study and finally, the correct grid and time step sizes were used to conduct the full-validation study. For this case, three structured grids of different mesh sizes, each with tetrahedral cells, were used to perform the mesh sensitivity study in the proposed geometry. Table 20 summarizes all the details of Grid I, II, and III.

Table 20. Grids Used to Perform the Mesh Sensitivity Study for the Validation Case.

Grid No.	**Element Size (mm)**	**No# Elements**	**No# Nodes**	***u`*(m/s)**					
				0.85	**0.90**	**1.00**	**1.10**	**1.20**	**1.30**
				***S_t* (cm/s)**					
I	3.00	1136343	213452	43.6	52.8	58.9	66.0	79.0	108.0
% ε				3.9	10.1	6.5	4.5	1.8	0.4
II	2.00	2793222	518912	42.2	51.2	58.0	65.6	78.9	107.9
% ε				0.4	6.7	4.9	3.7	2.0	0.3
III	1.00	17702581	3164221	42.1	51.1	57.8	65.5	78.8	107.8
% ε				0.2	6.6	4.5	3.6	2.0	0.3
Experimental [14]				42.0	48.0	55.3	63.2	80.5	107.6

Turbulent flame speed results at different turbulence intensities are shown in Figures 46(a-c). The results indicate that Grid I gives mesh independence only at high turbulence intensities (u` > 1.0 m/s). However, at lower turbulence intensities, Grid I fails to capture the precise value of the turbulence flame speed. On the other hand, Grid II is sufficient to give a grid-independent solution at all turbulence intensities with an average relative error percentage of 3%. According to Zimont's turbulent diffusion theory [161], the flame brush thickness becomes thinner at low u` levels. Consequently, more flame grid points are required to resolve the flame. As u` increases, the thickness of the flame brush becomes thicker; thus, the flame can be resolved using the same grid size. As Grid II provides a grid-independent solution, it can be further used to conduct a time-step independence analysis.

Three different time step sizes have been used to demonstrate a time-step independent solution (Δt=2.5*10-4 s, 1.5*10-4 s, and 5.0*10-5 s). As seen from the plot in Figure 46(b), the results are independent of all the used time step sizes, which indicates that the use of a time-step Δt=2.5*10-4 s is fine enough for achieving a converged and stable solution. Based on this conclusion, a grid size of 2mm and a time step of Δt=2.5*10-4 s will be used in the coming full validation.

The study of the flame ignition region located at the vessel's center, which is identified by the small transition radius (r_{max}), is an important parameter when performing premixed turbulent combustion calculations. This can be interpreted by the large augmentation of the flame speed at high values of $r_{max.}$ Subsequently, calculations with various sizes of r_{max} were carried out to confirm if the computed

results were responsive to fluctuations in the transition radius size. Turbulent flame speeds at three different values of r_{max} were computed, as shown in Figure 46(c). It can be clearly noticed that the results are independent of all the used transition radius sizes, which indicates that the use of r_{max}=0.5mm is fine enough to reach a converged solution.

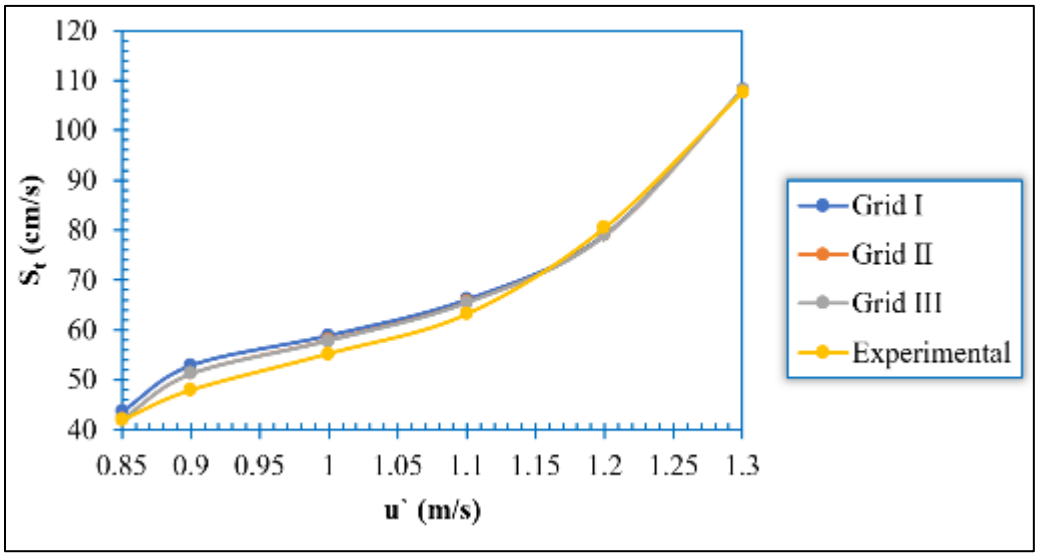

(a)

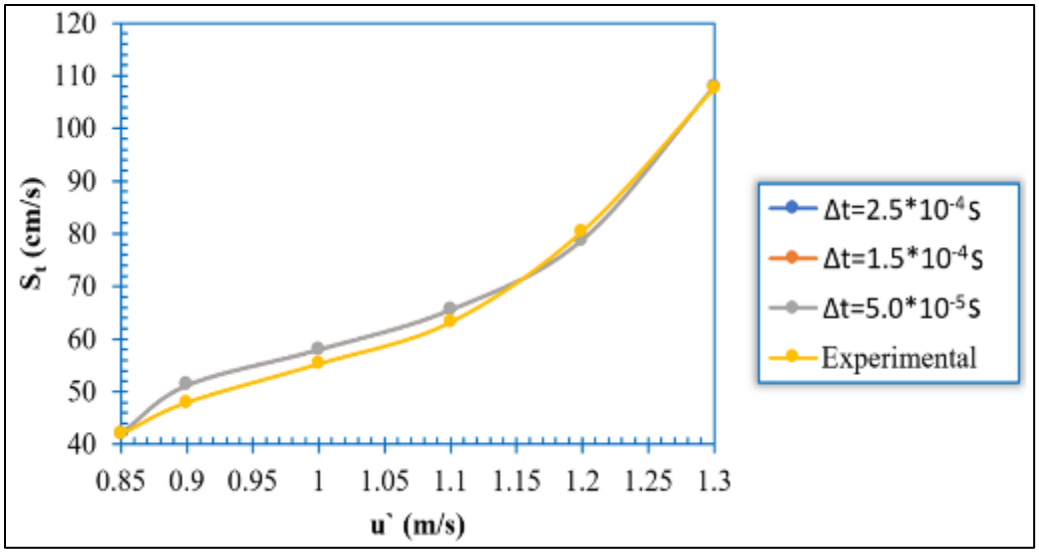

(b)

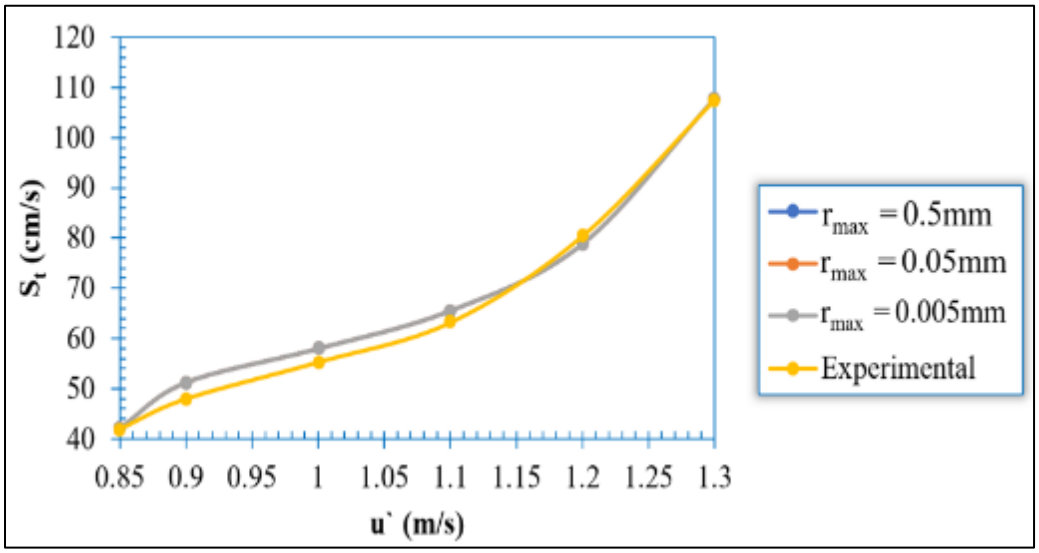

(c)

Figure 46. (a) grid independence results for the validation case, (b) time-step independence results for the validation case, (c) final geometry validation results using different ignition region sizes

CHAPTER 6. RESULTS AND DISCUSSIONS

This chapter presents the experimental (Section 6.1) and CFD (Section 6.2) results of turbulent flame studies conducted on the three investigated liquid fuel blends (diesel, pure GTL, 50/50 diesel-GTL blend), and compare between them in Section 6.3.

6.1 Experimental Results

The experimental results are presented in four categories after discussing laminar flames speed (S_l) results used for validation in subsection 6.1.1. These four categories are presented in the corresponding subsection as follows: (6.1.2) flame propagation visualization, (6.1.3) pressure-time diagram, (6.1.4) maximum pressure rise rate (*dp/dt*), and (6.1.5) turbulent flame speeds (S_t) results.

6.1.1 Laminar Flames Speed (S_l) Results and Validation

Laminar flame speeds (S_l) experiments were conducted following the experimental procedures explained in Section 4.6. S_l was calculated from the pressure versus time records using the correlation of Lewis and Von Elbe in Equations (4-8) [180]. After that, the results were compared with those of Samim [5] at the same operating conditions. At each condition, the measurement has been repeated three times to ensure the repeatability of the results. In addition, the mean value (*M*), the standard deviation (σ), and the Standard Error of Mean (*SEM*) were calculated and tabulated in Appendix F to study the dispersion of points around the mean. Figure 47 shows the

present work S_l measurements, compared with those of Samim [5] using the same combustion bomb.

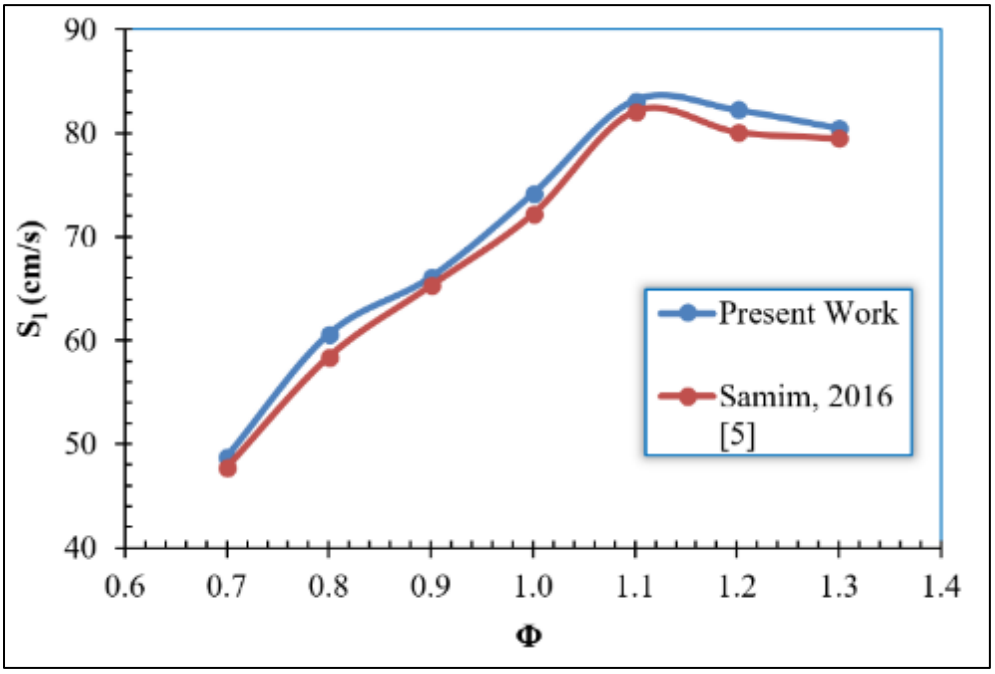

Figure 47. Laminar flame speed results used for validation

It can be observed that the values of laminar flame speeds for the present work are almost matching those obtained by Samim [5]. The relative error percentage for all the values is less than 3.0%, which indicates that the results obtained from this test rig are highly reliable and precise. This point could be emphasized by further looking at the statistics obtained by the repeatability test in Appendix F, in which the maximum percentage of *SEM* was 0.53% (at Φ=0.8). The slight variations between the readings of the two works can be attributed to a set of different factors. The number of crevices

and the amount of air leakage between the two experiments employ as major factors in this interpretation. In addition, some measuring devices such as the oxygen sensor and the pressure transducer have been renewed, and those have different measurement uncertainties compared to those used by Samim [5]. Moreover, each experiment has used a unique fuel injection method, affecting the precision of the desired equivalence ratio.

6.1.2 Flame Propagation Visualization

Although the present study relies on pressure signals to measure the turbulent flame speeds of the three tested fuels (diesel, GTL, 50/50 diesel-GTL blend), it is also feasible to use high-speed imaging to visually track the flame propagation through different growth stages. Therefore, the steel cover has been replaced by an optical quartz glass window for flame visualization. The present work used a video camera that captures 1000 frames per second to track the premixed GTL-air flame development between zero to 50ms at T_i = 190°C, Φ=1.0, and u`=3.0m/s, as shown in Figure 48.

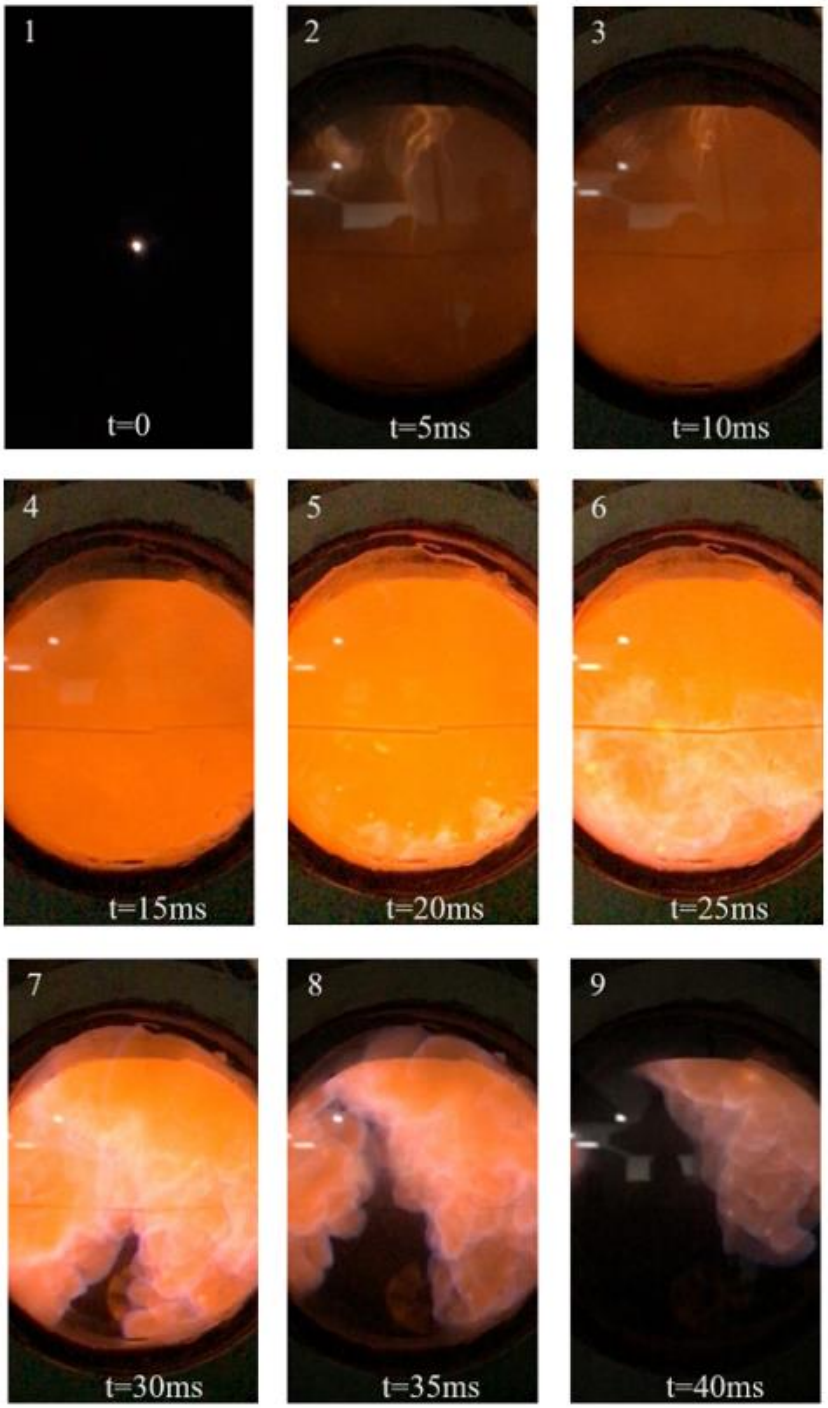
1
t=0
2
t=5ms
3
t=10ms
4
t=15ms
5
t=20ms
6
t=25ms
7
t=30ms
8
t=35ms
9
t=40ms

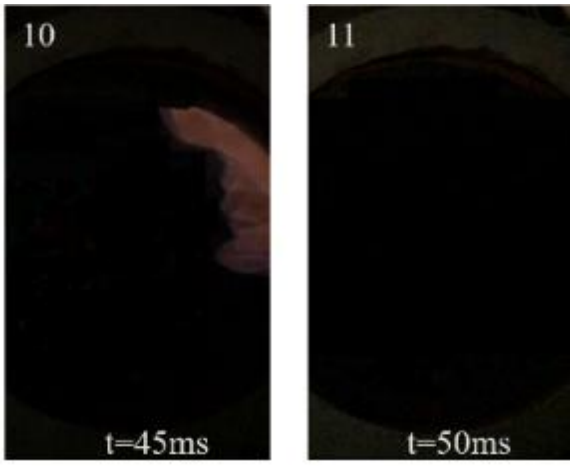

Figure 48. Representative images for GTL-air premixed flame propagation from t=0 to t=50ms at T_i =190°C, Φ=1.0 and u`=3.0m/s

Figure 48 shows a sequence of eleven images, each captured at a specific instant with a time step of 5ms separating each two consecutive images. Those images could represent the entire combustion process starting from flame kernel initiation at t=0, then passing through the full development of the flame brush at t=25ms, and finally producing the combustion exhaust gases (t=30ms to t=45ms) and ending with the complete decay at t=50ms. After the spark generation at t=0, the GTL-air premixed flame was characterized by a dark brown color at image sequence number 2, which has evenly spread towards the combustion bomb surface. The dark brown premixed flame starts to become brighter (image sequence number 3) gradually and is distinguished with an orange color (image sequence number 4) as the concentration of oxygen increases in the visualized field by the effect of turbulence generated by the four mixing fans [90]. At t=20ms (image sequence number 5), the brightness of the flame's natural luminosity increases, and the flame is characterized by a light orange

color with multiple distributed yellow spots. The brightness of the flame is identified by the flame temperature and soot incandescence [86]. Therefore, at *t*=25ms (image sequence number 6), the majority of the bright regions have been occupied by the high-temperature diffusion flame, with the appearance of soot clouds in multiple spots, characterized by stronger radiation compared to those in image sequence number 5. The emergence of more soot clouds in image sequence number 6 causes the premixed flame to appear in a brighter color, and it is also used to indicate the completeness of combustion. At this instant (*t*=25ms), the combustion peak pressure and temperature are reached, which causes the heat release rate to be the highest [86]. This observation can be emphasized by looking at the pressure-time combustion wave in Figure 49 in subsection 6.1.3. After the end of combustion (image sequence numbers 7 to 10), the oxygen and fuel volume fractions are completely consumed, and the exhaust gases such as CO_2, $NO_{x,}$ and others are produced, which are evacuated from the bomb using a vacuum pump before starting the following experiment. After each set of experiments, the internal surface of the bomb, the fans, the fuel injector, and the heaters are all flushed with compressed air, cleaned with pure water, and then polished with a degreaser to remove any dispersed fuel contaminants at these surfaces. In addition, the optical window is cleaned with suitable detergent to maintain it transparent for high-quality flame imaging and visualization. Subsequently, this ensures the successful ignition and operation at the desired equivalence ratio.

6.1.3 Pressure-Time Diagram

Figure 49 shows the pressure-time combustion wave for stoichiometric diesel, GTL, and 50/50 diesel-GTL blend at $u`$=3.0m/s.

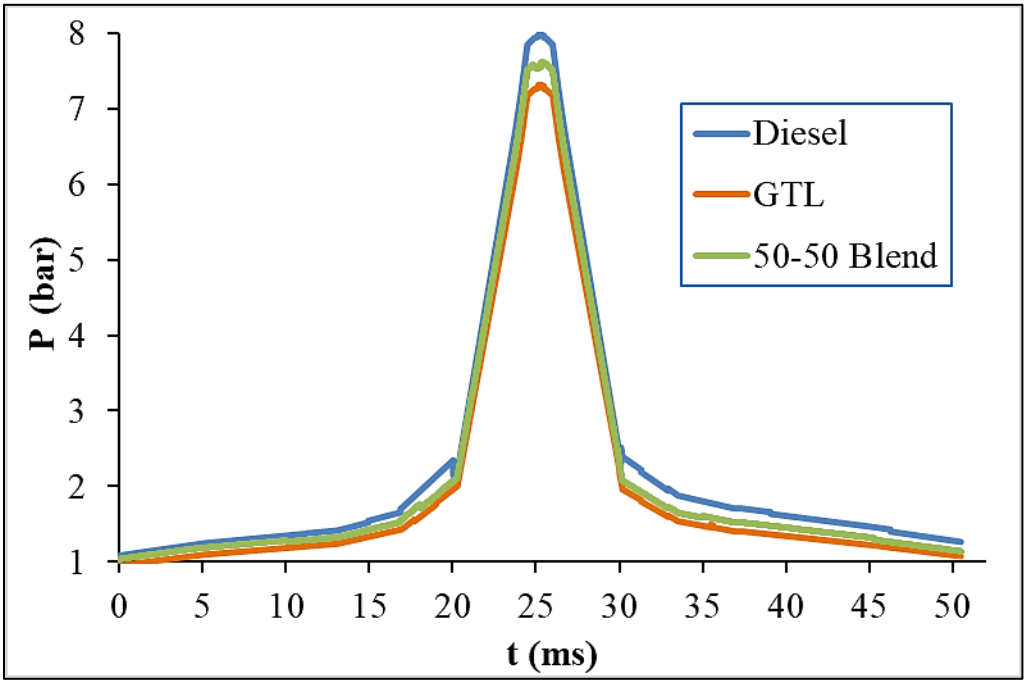

Figure 49. Comparison of the pressure-time combustion waves for stoichiometric diesel, GTL, and 50/50 diesel-GTL blend at $u`$=3.0m/s

The investigation of the combustion characteristics of the tested fuel relies to a large extent on the analysis of this chart type, which also represents the actual scenario of the diesel auto-ignition phenomenon that takes place in real automotive diesel engines. Generally, a lower peak pressure indicates better air-fuel mixing due to less burned fuel in the premixed phase combustion process [9]. As observed, the pressure

at the ignition instant is almost around eight times the initial pressure, and higher values of around ten to twelve times were noticed in cases of lower turbulence intensities ($u` < 3.0$m/s). This observation emphasizes the role that the turbulence level plays in accelerating the process of air-fuel mixing, which results in lower peak pressure, and thus a higher turbulent flame speed. The same conclusion has been derived in the work of References [9], [15]. Another observation from Figure 49 is the very short ignition duration down to the order of a tenth of milliseconds, where a short delay in the fuel-air mixing causes the ignition to be delayed (ignition delay), causing more heat to be released and more particulate matters, Nitrogen oxides (NO_x), and soot to be formulated in the exhaust products. In this context, the combustion properties of the fuel used can contribute to a significant increase in lowering the combustion peak pressure, which can thus enhance the engine performance and lower the exhaust emissions. Fuel properties such as density, kinematic viscosity, hydrocarbons and oxygen content, cetane number and energy content are all factors that influence the combustion peak pressure, and the maximum pressure rise rate. Although the three tested fuels have the same hydrocarbons content (H/C ratio), however GTL fuel is characterized by a lower kinematic viscosity and density compared to diesel and 50/50 diesel-GTL blend, therefore enhancing the fuel atomization process, and accelerating the flame propagation throughout the unburned mixture (e.g.: higher turbulent flame speed) [186]. The use of GTL fuel and the 50/50 blend has decreased the combustion peak pressure by 8.9% and 4.9%, respectively compared to diesel at stoichiometry. Other factors that can also affect the magnitude

of peak pressure are the fuel cetane number, the spark energy, the equivalence ratio, and the turbulence intensity level.

6.1.4 Maximum Pressure Rise Rate (*dp/dt*)

The relation between the maximum pressure rise rate and turbulence intensity for the three tested fuels at varying equivalence ratios is shown in Figure 50(a-c).

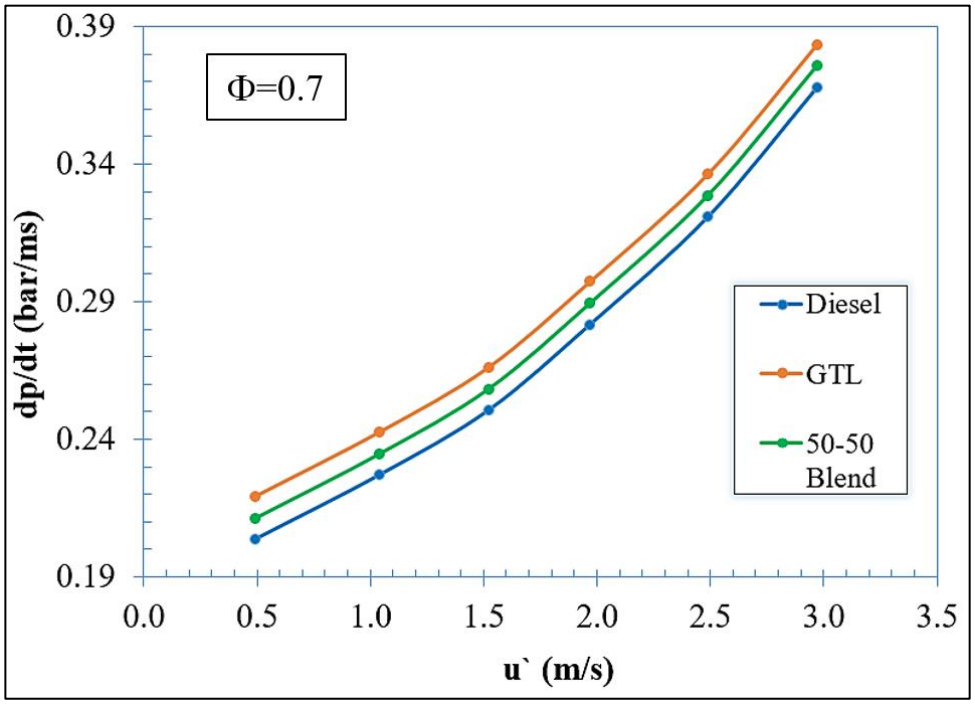

(a)

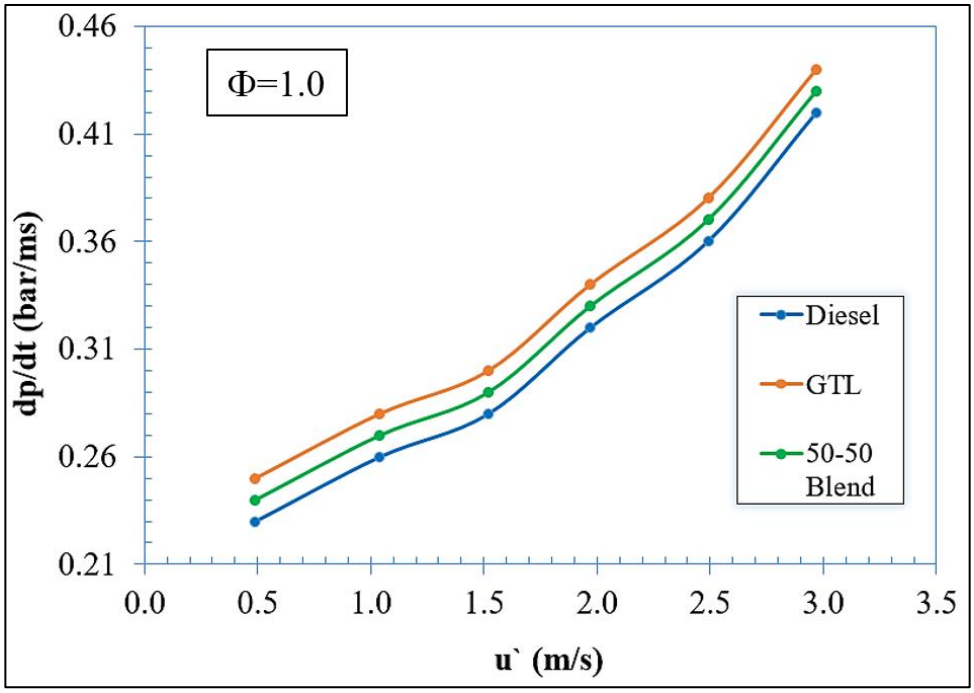

(b)

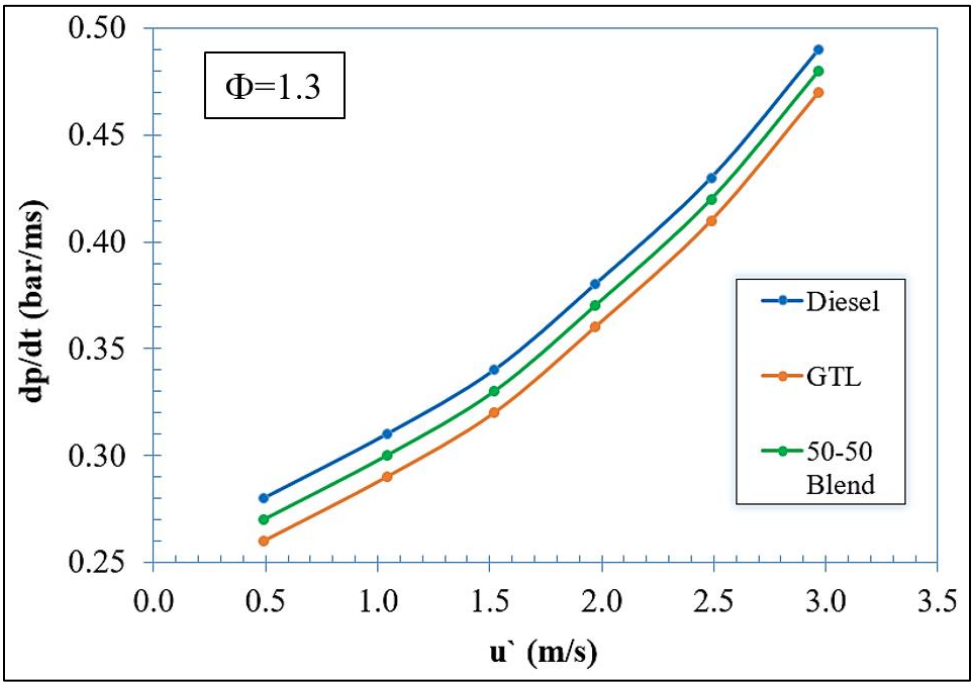

(c)

Figure 50. The maximum pressure rise rate (*dp/dt*) versus turbulence intensity (*u`*) for the three fuels at: (a) *Φ*=0.7, (b) *Φ* =1.0, (c) *Φ*=1.3

Values for *dp/dt* were obtained from the pressure transducer measurements by central differencing seven closely spaced time intervals. Typically, a higher *dp/dt* indicates that the flame propagates faster through the unburned mixture, and the combustion is more efficient. In addition, it is a direct indication of the ignition delay for the injected fuel, such that the ignition becomes faster when *dp/dt* becomes higher. It can be observed from Figures 50(a-c) that the values of *dp/dt* increase with *u`*at all equivalence ratios, which emphasizes the role that the turbulence plays in enhancing the air-fuel mixing process during the premixed phase through better evaporation, penetration, and atomization of the mixture. This conclusion can be further proved by referring to the work of Reference [9]. In Figures 50(a, b), *dp/dt* values were higher for GTL fuel than other fuels. This can be interpreted by referring to the properties of the selected fuels. Since GTL fuel is characterized by the lowest kinematic viscosity and the highest cetane number, this has caused *dp/dt* to be higher and the flame propagation to be faster. At these two conditions, the use of GTL fuel and the 50/50 blend has increased *dp/dt* by around 6.3% and 3.0%, respectively, compared to diesel fuel. In contrast, at Φ=1.3 in Figure 50(c), diesel fuel was characterized by the highest values of *dp/dt* compared to other fuels. The effect of Lewis number (*Le*) on flame leading edge propagation can interpret this trend [11]. At rich operating conditions, $Le < 1.0$ for diesel fuel, and $Le > 1.0$ for GTL and the 50/50 diesel-GTL blend. As a result, the flame's mean strain rate and mean curvature at the flame front are positive, increasing flamelet surface area and accelerating flame propagation through the unburned air-fuel mixture. Therefore, the diesel-air mixture is burned faster than other selected mixtures, which causes *dp/dt* to be higher and the

ignition delay to be shorter. In addition, it can be noticed from Figures 50(a-c) that the 50/50 diesel-GTL blend exhibits an intermediate behavior between GTL and diesel fuels at all the equivalence ratios.

6.1.5 Turbulent Flame Speeds (S_t)-Experimental

Turbulent flame speeds of the three liquid fuel blends were experimentally investigated at different equivalence ratios (Ø=0.7 to 1.3) and turbulence intensities (u`=0.5m/s to 3.0 m/s), and the results are presented in tables in Appendix G and plotted in Figure 51(a-c).

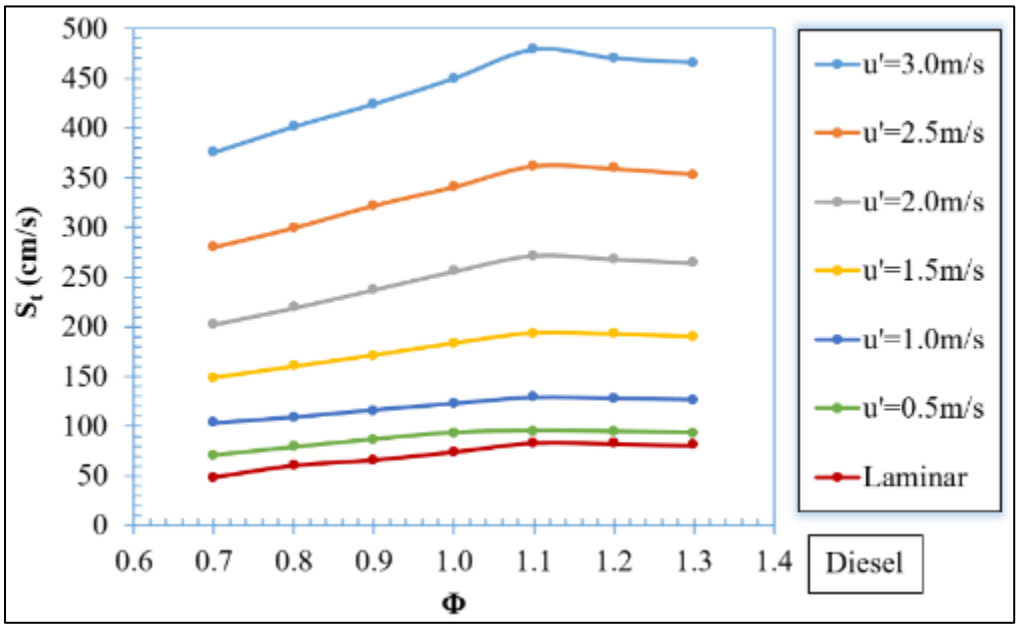

(a)

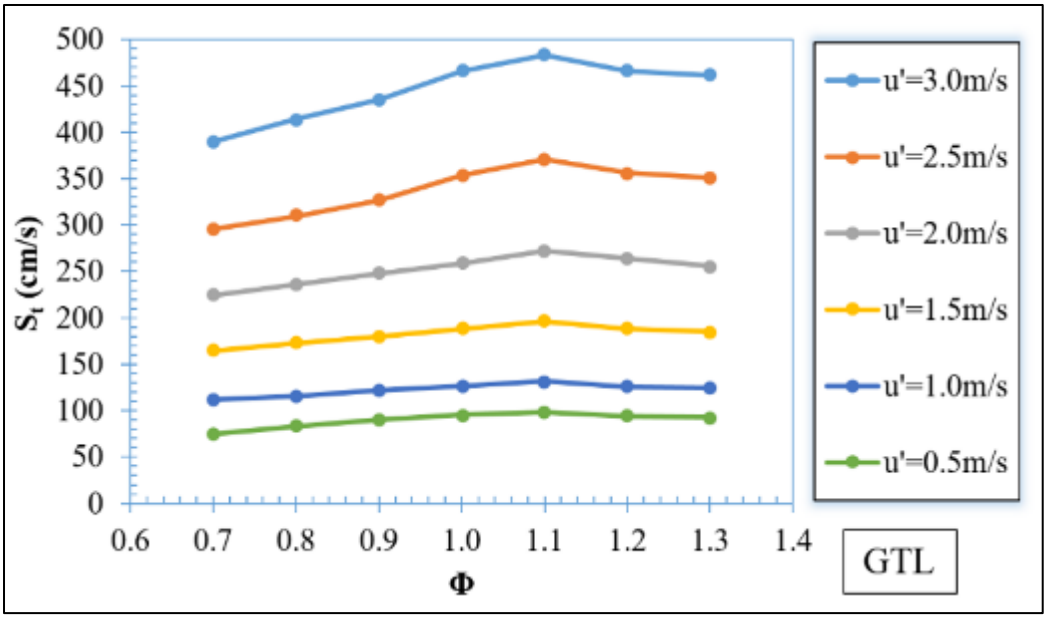

(b)

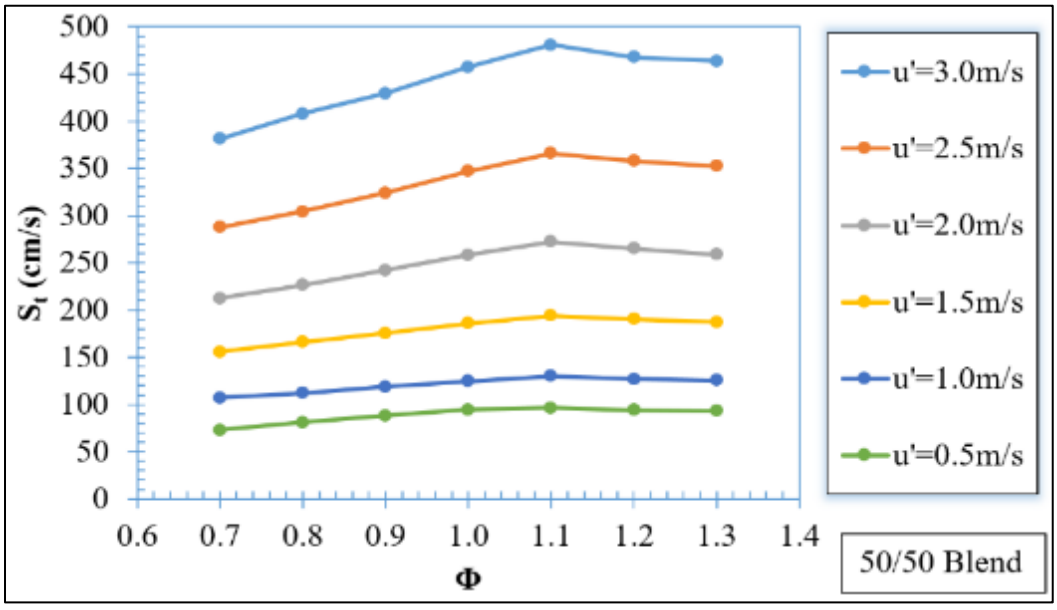

(c)

Figure 51. Turbulent flame speeds versus equivalence ratios at different turbulence intensities and T_i = 463K for: (a) diesel, (b) GTL, (c) 50/50 diesel-GTL blend

It can be clearly noticed that all the curves are “bell-shaped” where the laminar or turbulent flame speed peaks at near-stoichiometric condition (Ø=1.1) and falls when the mixture becomes leaner or richer. Furthermore, at all equivalence ratios, the steep increment in turbulence intensity augments turbulent flame speeds to higher values. Figure 52(a-c) shows the effect of varying the equivalence ratio on the turbulent flame speeds of the three hydrocarbon fuels at three different turbulence intensity levels ($u`$=0.5m/s, $u`$=1.5m/s, and $u`$=3.0m/s).

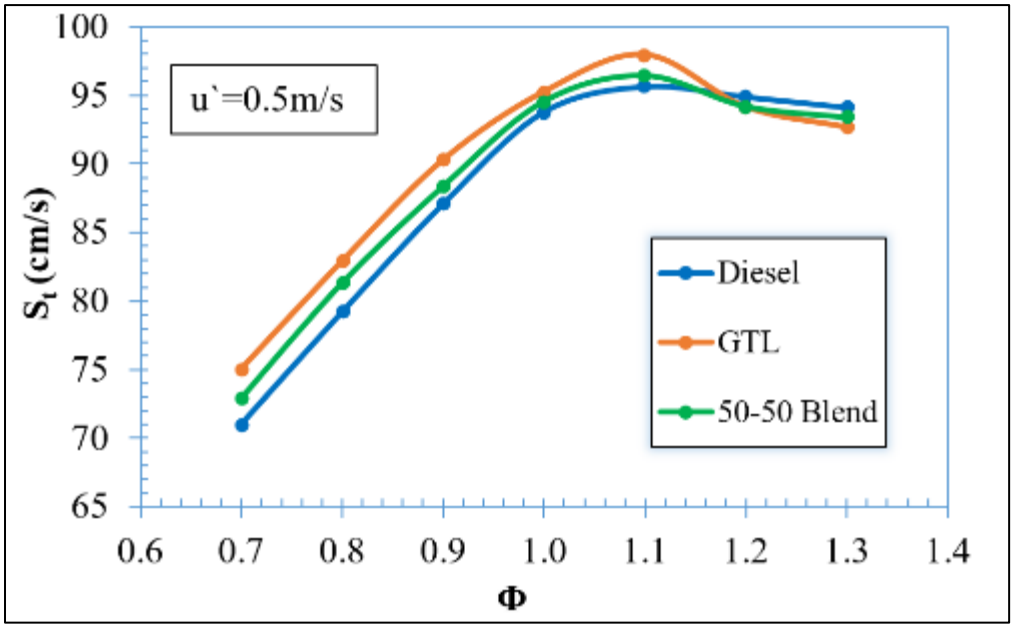

(a)

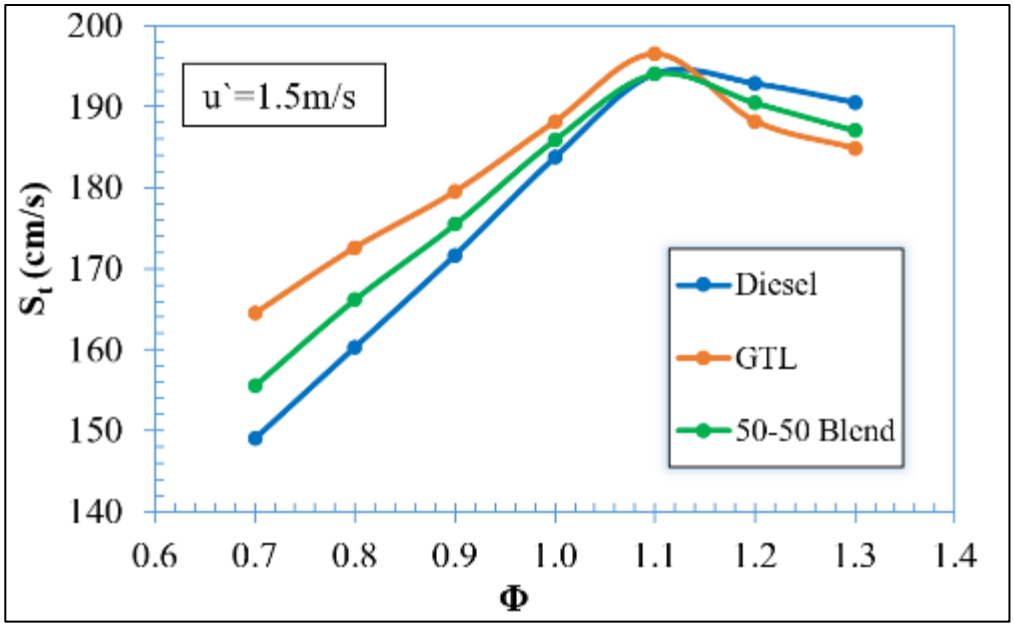

(b)

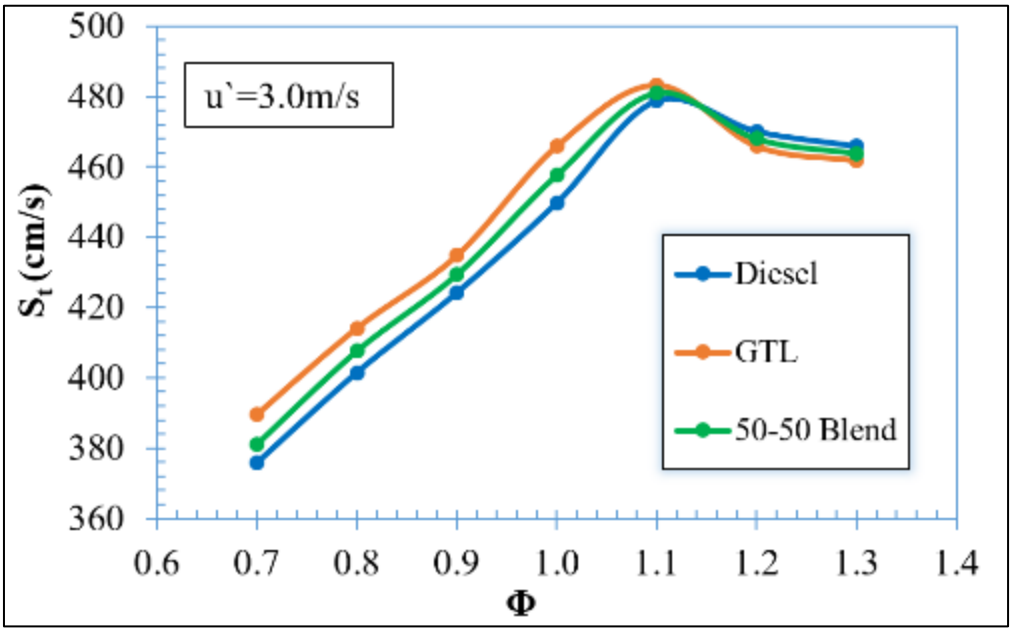

(c)

Figure 52. Turbulent flame speeds versus equivalence ratios for the three fuels at T_i = 463K and: (a) u`=0.5m/s, (b) $u$`=1.5m/s, (c) u`=3.0m/s

As observed, increasing the turbulence intensity level causes a remarkable increase in the turbulent flame speeds for all the fuels. S_t increases roughly linearly with $u`/S_l$ (low turbulence region), then levels off (bending region), and finally decreases again as it approaches the quenching limit [187]. Also, it can be observed from Figures 49(a-c) that the turbulent flame speeds of lean GTL fuel are higher than lean diesel and lean 50/50 diesel-GTL blend, while diesel being the lowest. In contrast, rich diesel is characterized by a higher turbulent flame speed when compared to rich GTL and rich 50/50 diesel-GTL blends. The effect of *Le* on turbulent flame speeds is used to interpret these trends. *Le* defines the ratio between the combustible mixture's thermal and mass diffusivity [11]. Non-unity Lewis number can have a negative or positive impact on the rate of local burning. The local burning velocity reduces (enhances) when $Le > 1$ ($Le < 1$) due to an increase (reduction) heat release in the positively curved flamelets [188]. When $Le < 1$, the mean curvature and mean strain rate become positive at the flame front. Subsequently, the propensity of finding positively stretched, curved flamelets (convex to the direction of unburned gas) becomes higher for premixed turbulent reacting flow. Turbulent eddies stretch the laminar flametlets, causing a significant variation in the local burning rate. As a result, for mixtures characterized by $Le < 1$, an increase in the flamelet surface area and the local burning rate cause turbulent flame speeds to increase [11].

These impacts interpret the higher S_t values for lean GTL (or rich diesel), which are characterized by $Le < 1$. Similar trends have also been documented by [62], [189]. The use of GTL fuel and the 50/50 blend at $u`$=0.5m/s ($u`$=1.5m/s and $u`$=3.0m/s) has

increased turbulent flame speeds by around 3.6% (5.3% and 2.8%) and 1.9% (2.8% and 1.4%), respectively compared to diesel fuel at equivalence ratios that are less than 1.1 ($\Phi < 1.1$).

6.2 CFD Results

In this section, CFD results of turbulent flame studies conducted on the three investigated liquid fuel blends (diesel, pure GTL, 50/50 diesel-GTL blend) using Zimont model and implemented in RANS approach are presented in four categories; (6.2.1) mean turbulent kinetic energy balance, (6.2.2) flame radius evolution, (6.2.3) turbulent flame speeds (S_t) and (6.2.4) dimensionless numbers for turbulent combustion. The mixture properties and the laminar flame parameters were estimated using GASEQ [190] and PREMIX calculations from CHEMKIN-PRO [191]. Mixture properties such as burned and unburned density, thermal conductivity, specific heat, molecular weight, viscosity, and laminar flame speeds have been formulated as constants in ANSYS Fluent. Table 21 lists the major flame parameters related to this study. In addition, it should be mentioned that the results of this study have been smoothed and filtered out, allowing the important patterns to stand out.

Table 21. Properties of the Flames Studied in the Present Work

Fuel	**Diesel**	**GTL**	**50/50 Blend**
Property	**Φ=0.7**		
Laminar Flame Speed, S_l (cm/s)	42.88	55.88	50.43
Laminar Flame Thickness, δ_l (cm)	0.047	0.042	0.043
Density Ratio, σ	0.232	0.226	0.229
Reynolds Number, *Re*	480.2	519.0	513.2
Lewis number, *Le*	1.204	0.988	1.096
	Φ=1.0		
Laminar Flame Speed, S_l (cm/s)	80.24	85.49	81.55
Laminar Flame Thickness, δ_l (cm)	0.034	0.033	0.033
Density Ratio, σ	0.194	0.186	0.190
Reynolds Number, *Re*	571.4	528.0	534.5
Lewis number, *Le*	1.039	0.985	1.012
	Φ=1.3		
Laminar Flame Speed, S_l (cm/s)	78.78	82.17	79.04
Laminar Flame Thickness, δ_l (cm)	0.027	0.030	0.029
Density Ratio, σ	0.201	0.210	0.206
Reynolds Number, *Re*	406.9	392.5	398.4
Lewis number, *Le*	0.947	1.138	1.042

The simulation has been conducted under atmospheric pressure at an initial temperature of 463K. Turbulence intensities were varied by changing the fan's speeds. Turbulent kinetic energies and turbulent dissipation rates at the corresponding turbulence intensities were obtained using Equations (100) and (101), respectively. Table 22 lists all the turbulence initial conditions used in the present numerical study.

Table 22. Turbulence Initial Conditions used in CFD Simulation

Turbulence Intensity, u`(m/s)	**Turbulent Kinetic Energy, k (m^2/s^2)**	**Turbulence Dissipation Rate, ε (m^2/s^3)**
0.50	0.38	2.31
1.00	1.50	18.50
1.50	3.38	62.40
2.00	6.00	148.00
2.50	9.38	289.10
3.00	13.50	499.50

6.2.1 Mean Turbulent Kinetic Energy Balance

The objective of studying the mean turbulent kinetic energy balance; is to show how the turbulence generated in the fan's region is transferred to the vessel's center. Turbulence is characterized by its dissipative nature, in which the flow's turbulent kinetic energy is converted into internal energy due to eddy viscosity, which is also explained by the energy cascade theorem [192]. The mean turbulent kinetic energy is a relevant quantity used to characterize the turbulence inside the vessel in terms of dissipation, production, and transport. In addition, studying this quantity ensures the existence of HIT condition in the center of the vessel. Besides, analyzing the attitude of this quantity before ignition assists in selecting a suitable flame radius at which the computational results will be obtained [193]. The mean turbulent kinetic energy and turbulent eddy viscosity are plotted against the vessel's radius (r) at u`=3.0m/s and Φ=1.0, as shown in Figure 53. The mean turbulent kinetic energy balance has been

conducted at $u`$=3.0m/s rather than other turbulence intensities to ensure the existence of HIT condition at the center of the vessel up to the maximum operating turbulence level.

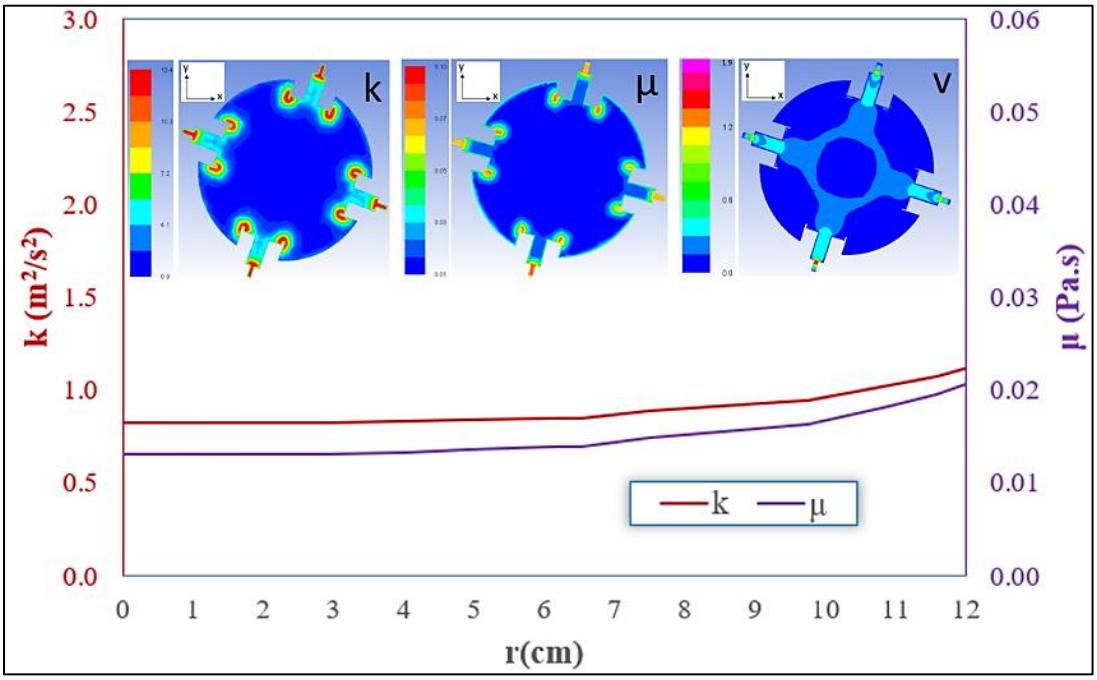

Figure 53. Mean turbulent kinetic energy and turbulent eddy viscosity throughout the combustion vessel up to r =12cm, at $u`$=3.0m/s and Φ=1.0

It can be clearly noticed that both quantities reach their maximum value near the mixing fans (e.g., at higher turbulence intensities) and start to gradually decrease until reaching their minimum value at the center point of the vessel. Also, it can be observed that the value of these quantities remains almost constant up to a vessel radius of around 5cm, which indicates that the turbulent flow field is homogeneous

(e.g., the flow is unaffected by a dislocation in the coordinate system). In addition, the CFD turbulent kinetic energy contour indicates that the flow field is isotropic (invariant to coordinate system reflections or rotation). The *x* and *y* velocity magnitudes were found to be similar in the central region of the vessel, as shown in the CFD velocity contour, which further confirms the isotropy of the turbulent flow field. Furthermore, it can be observed from the plot in Figure 53 that the turbulent eddy viscosity is close to zero at the vessel's central region, which indicates that the turbulence is uniform at the area of kernel development. Therefore, satisfying the HIT condition in the center of the vessel with a mean velocity ($\overline{U}$= zero < 0.1$u`$=1.35m/s), which confirms that turbulence is not convicted. However, it diffuses towards the vessel center from the fan's region [194]. According to Reference [50], it is important to determine the turbulent flame speeds at a flame radius (reference point) where the flame has left the ignition region and is only affected by a small portion of the turbulent velocity field. Consequently, the turbulent flame speeds are computed in this dissertation at a flame radius equal to 6cm. In addition, it should be noticed that a full CFD domain is used for showing the simulation contours rather than a slice of it, to ensure that the outwardly propagating flame has grown evenly and uniformly in all the directions.

6.2.2 Flame Radius Evolution

A sequence of frames for the flame radius evolution of stoichiometric GTL-air mixture at 1atm and $u`$=3.0m/s is presented in Figure 54.

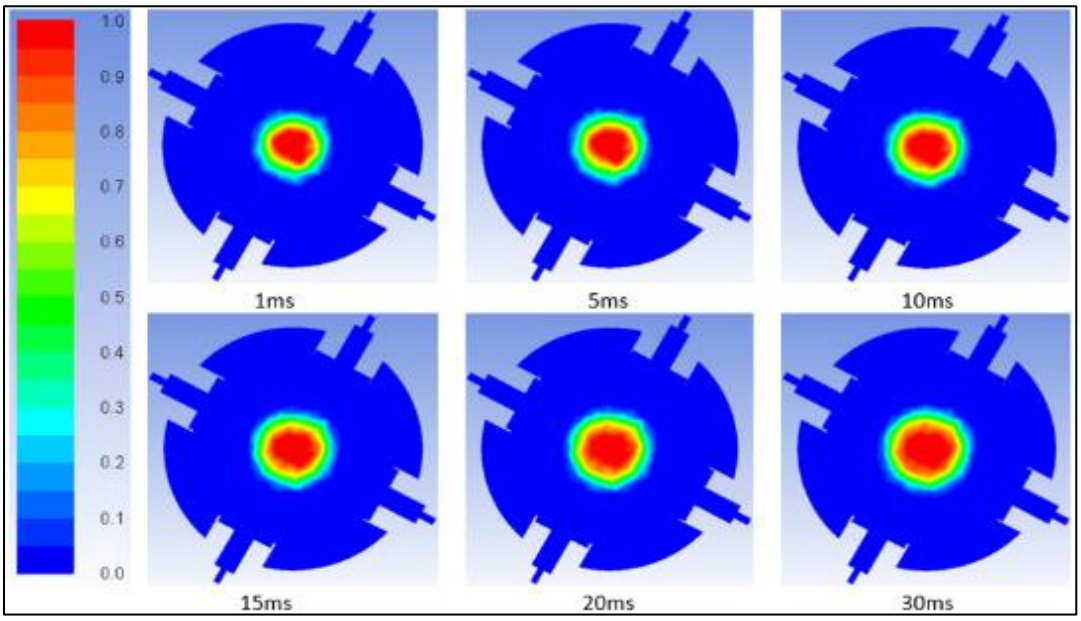

Figure 54. Flame radius evolution for stoichiometric GTL-air mixture at 1atm, T_i = 463K and u`=3.0m/s

The developing kernel is exposed to an increasing spectrum of turbulence velocity scales as the flame grows and approaches the fans region, thus the propagation rate increases. Before ignition, the turbulence was homogeneous and isotropic with an intensity level of u`=3.0m/s and a reaction progress C=0 in all the vessel's domains. Just after ignition, the surface of the flame is relatively smooth (except of some distortions caused by the sparks), and it is "laminar-like" [19]. As the flame develops, the surface of the flame becomes progressively wrinkled, on which the flame surface area, the flame thickness, and the burning rate all increase. For the laminar cases (t < 25ms), the flame radius develops linearly with time (e.g., flame acceleration is zero).

However, for turbulent cases (t > 25ms), the radius grows rapidly and non-linearly with time. In addition, the flame brush is thickening as the flame develops, while having islands of burned gases inside it (C=1 in CFD color bar) and islands of unburned gases outside it (C=0 in CFD color bar) [105]. As a result, spherically expanding flame vessels are utilized to measure turbulent flame speeds throughout a broad range of turbulence intensity levels by referring to the flame radius evolution history. According to the Zimont TFC model [25], the mean flame front is assumed as a circle whose center is at the centroid of the flame. Similar trends for the flames radius evolutions were obtained at other equivalence ratios. However, the propagation speeds were slightly different. Figure 55(a-c) compare the flame radius evolution for diesel, GTL, 50/50 diesel-GTL blend at Φ=0.7, 1.0 and 1.3, respectively.

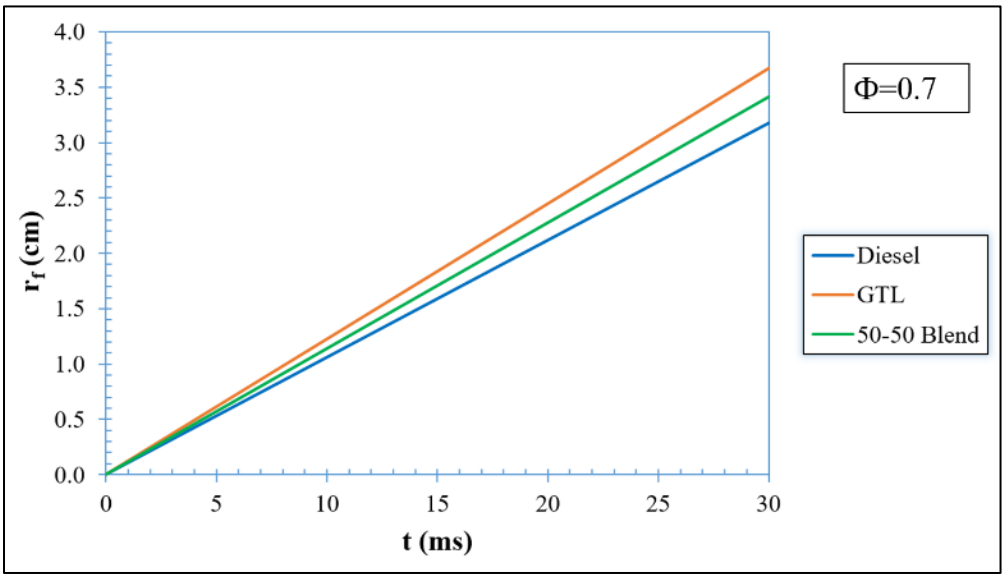

(a)

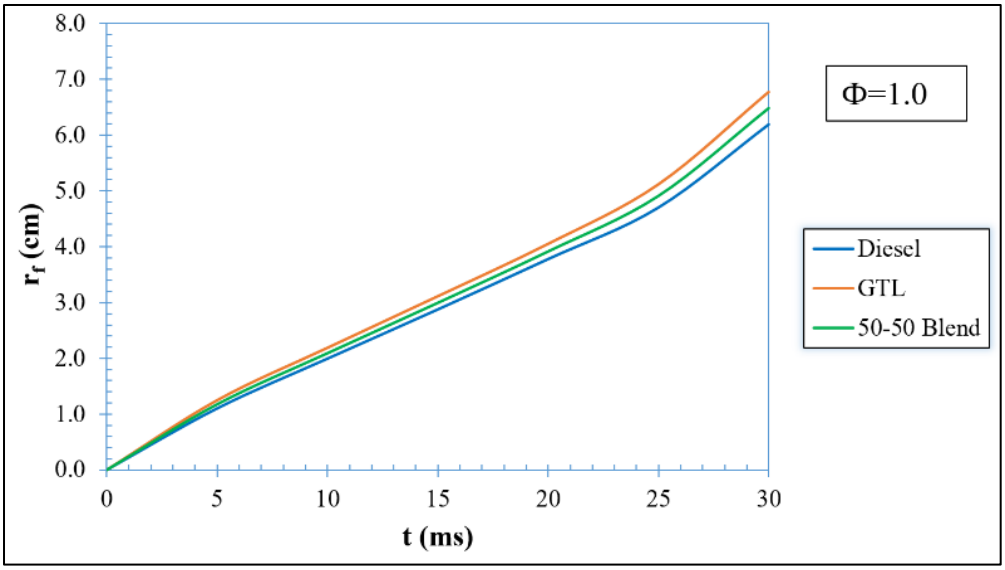

(b)

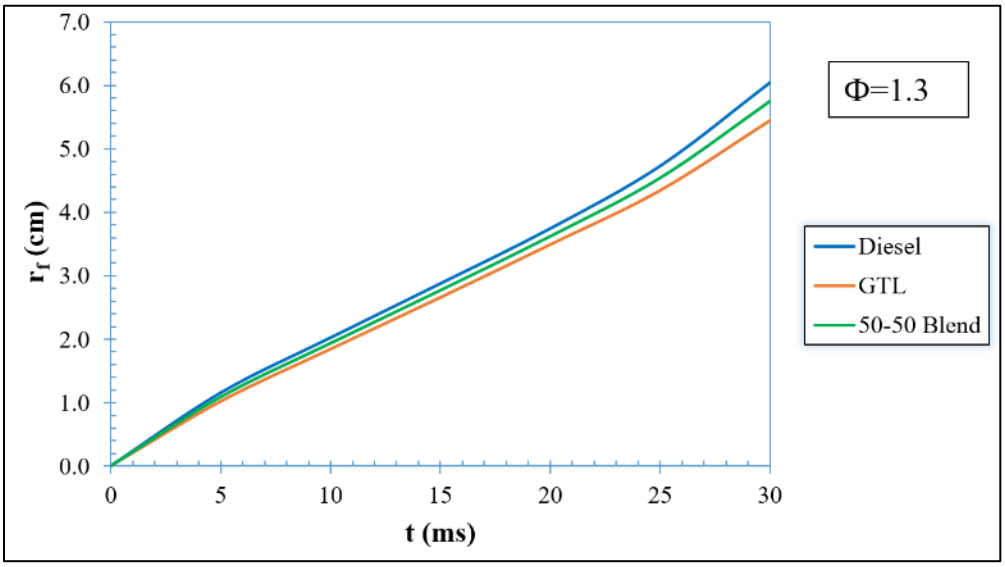

(c)

Figure 55. Flame radius evolution for diesel, GTL, 50/50 diesel-GTL blend at: (a) Φ=0.7, (b) Φ=1.0, (c) Φ=1.3

It can be clearly noticed from Figure 55(a-c) that the flame radius evolution for the lean mixtures (Φ=0.7) is the slowest. In contrast, the fastest radius evolution is depicted at the stoichiometric condition for all the fuels. According to Reference [11], the unburned to burned density ratio ($\sigma = \frac{\rho_u}{\rho_b}$) has a monotonic behavior with the equivalence ratio, where the minimum value occurs at stoichiometric (Φ=1.0) condition for all tested fuels. Furthermore, when compared to fuel-rich conditions, the density ratio for lean mixtures is higher. The local burning rate for stretched flamelets (the portion of stretched laminar flame through the turbulent flow field) is substantially increased as σ decreases, resulting in a faster flame radius evolution (and hence a higher burning velocity). As observed in Figure 55(a), lean GTL fuel is characterized by the fastest flame radius development due to its lowest density ratio ($\sigma = 0.226$ for GTL, 0.229 for 50/50 diesel-GTL blend, 0.232 for diesel). However, for the fuel-rich case (Φ=1.3) in Figure 55(c), diesel is characterized by the fastest flame development due to its lowest density ratio ($\sigma = 0.201$ for diesel, 0.206 for 50/50 diesel-GTL blend, and 0.210 for GTL). In all three cases, it can be noticed that the 50/50 diesel-GTL blend exhibits an intermediate behavior between diesel and GTL fuels. In addition, it should be noticed how the behavior of the flame starts to change from linear (laminar) to non-linear (turbulent) as the flame radius exceeds 5cm.

6.2.3 Turbulent Flame Speeds (S_t)-CFD

Turbulent flame speeds of the three liquid fuel blends were computed at different equivalence ratios ($\emptyset$=0.7 to 1.3) and turbulence intensities (u`=0.5m/s to 3.0 m/s) as

shown in Figure 56(a-c). In addition, the laminar flame speeds were computed using the CFD solver using a laminar flame mode, and the numerical results were plotted versus the experimental ones [10]. The raw, filtered, and preprocessed data associated with the premixed turbulent combustion of the three fuels were imported from ANSYS Fluent and then listed on filtered tables for ease of accessibility. A full description of these datasets can be found in Reference [195], and MS Excel datasets can be accessed through the following Mendeley data link repository:

http://dx.doi.org/10.17632/ts2jd8zc9r.3

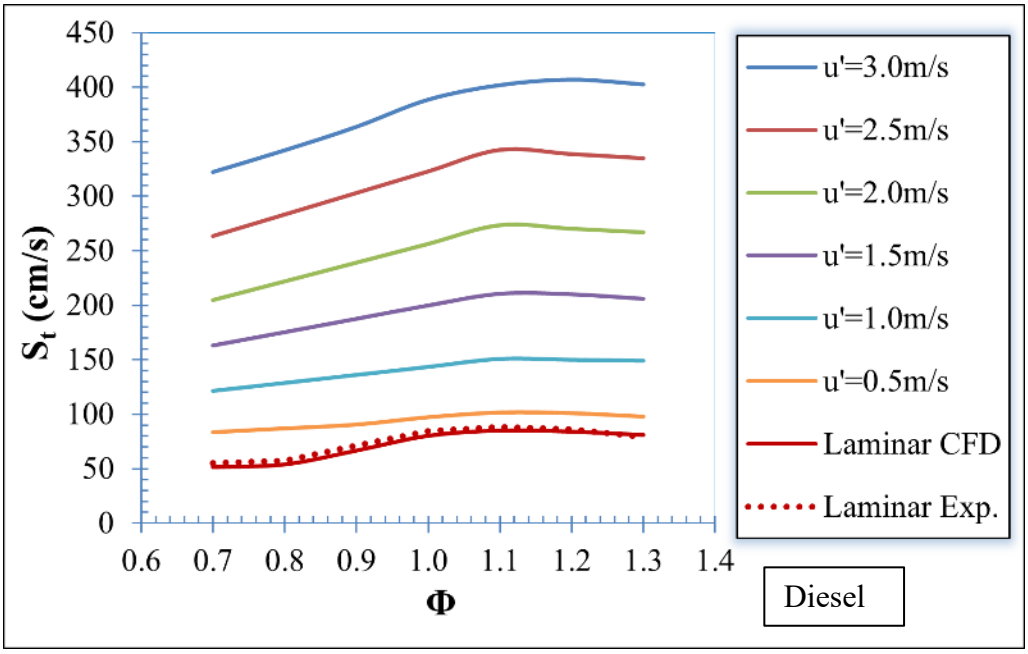

(a)

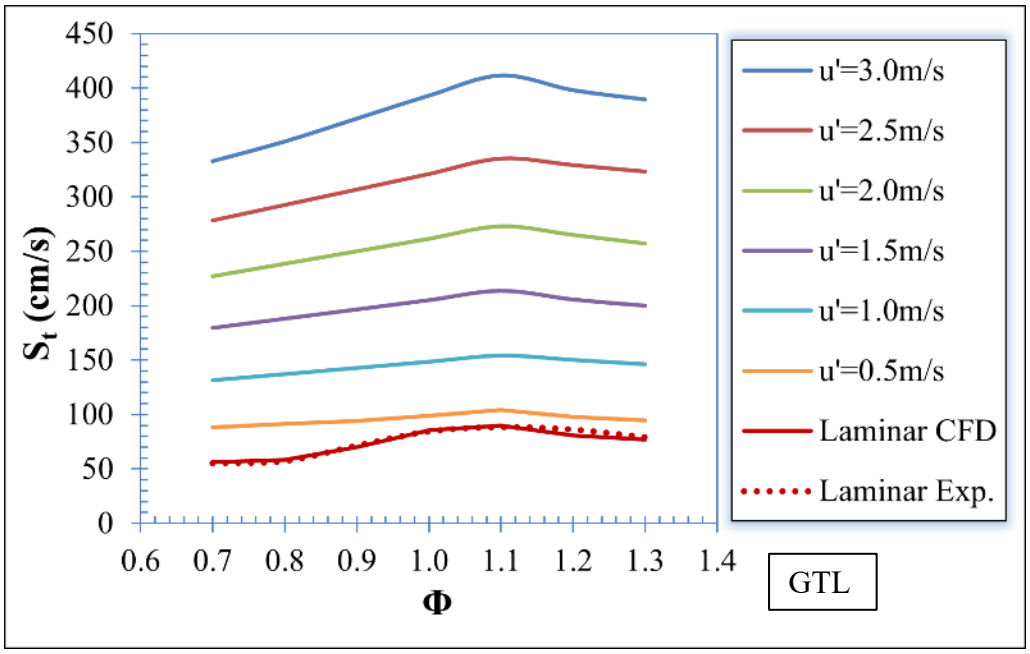

(b)

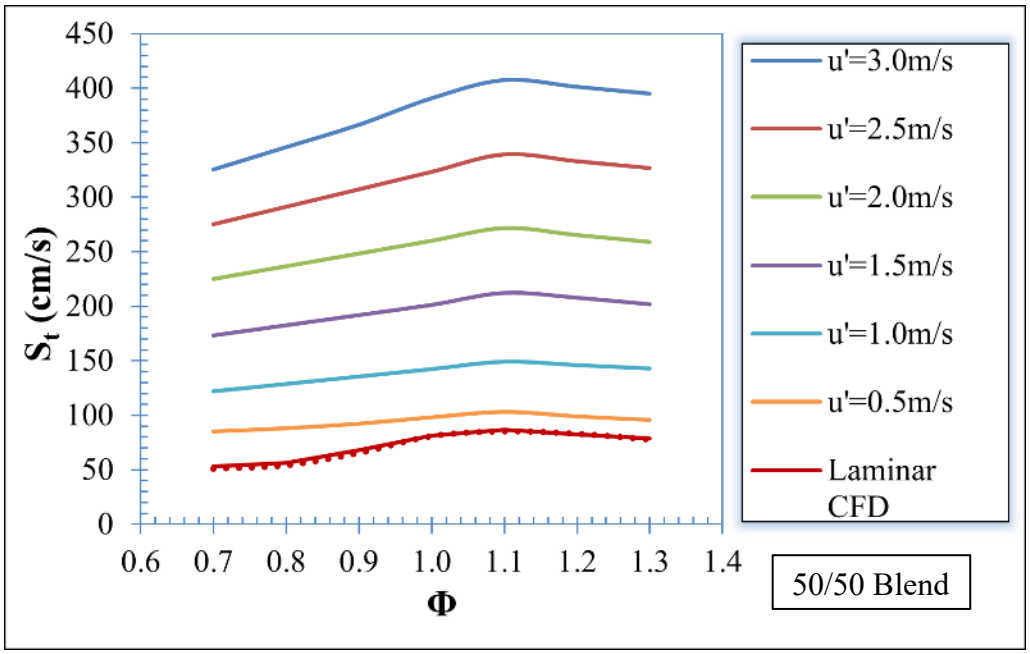

(c)

Figure 56. Turbulent flame speeds versus equivalence ratios at different turbulence intensities and T_i = 463K for: (a) diesel, (b) GTL, (c) 50/50 diesel-GTL blend

It can be clearly noticed that the laminar flame speeds readings computed by CFD solver are remarkably close to the experimental ones, where the relative error percentage was found to be less than 4% at all the equivalence ratios. Third order least square fits were used to plot the turbulent flame speeds curves through each set of numerical data with a maximum standard deviation of ±1.1 cm/s. As noticed, the laminar or turbulent flame speed peaks at near-stoichiometric conditions (Φ=1.1) and diminishes as the mixture becomes leaner or richer. Furthermore, at all equivalence ratios, the steady increase in turbulence intensity results in an increase in turbulent flame speeds. Figure 57(a-c) show the effect of changing the equivalence ratio on the turbulent flame speeds of the three hydrocarbon fuels at three different turbulence intensity levels ($u`$=0.5m/s, $u`$=1.5m/s, and $u`$=3.0m/s).

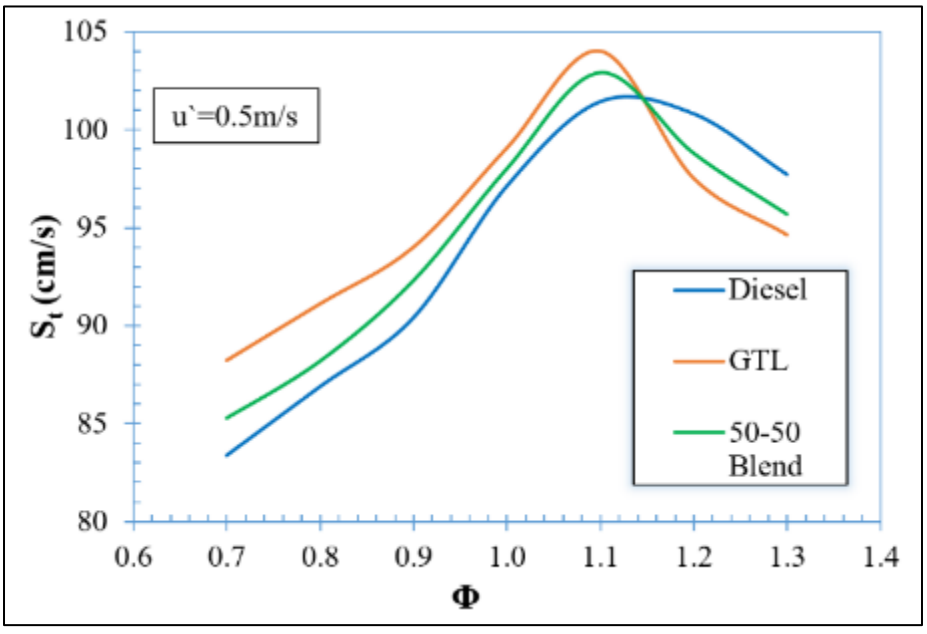

(a)

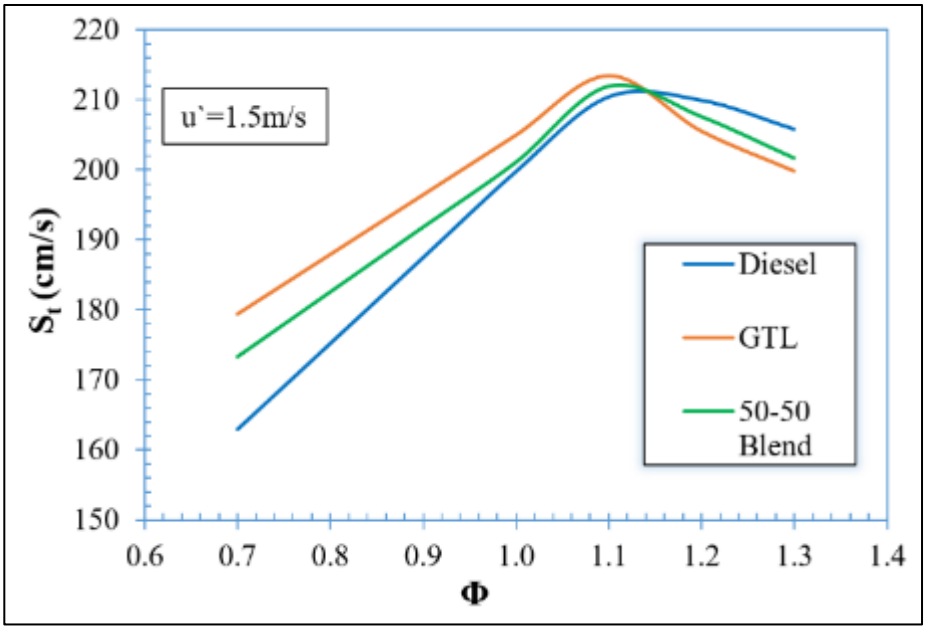

(b)

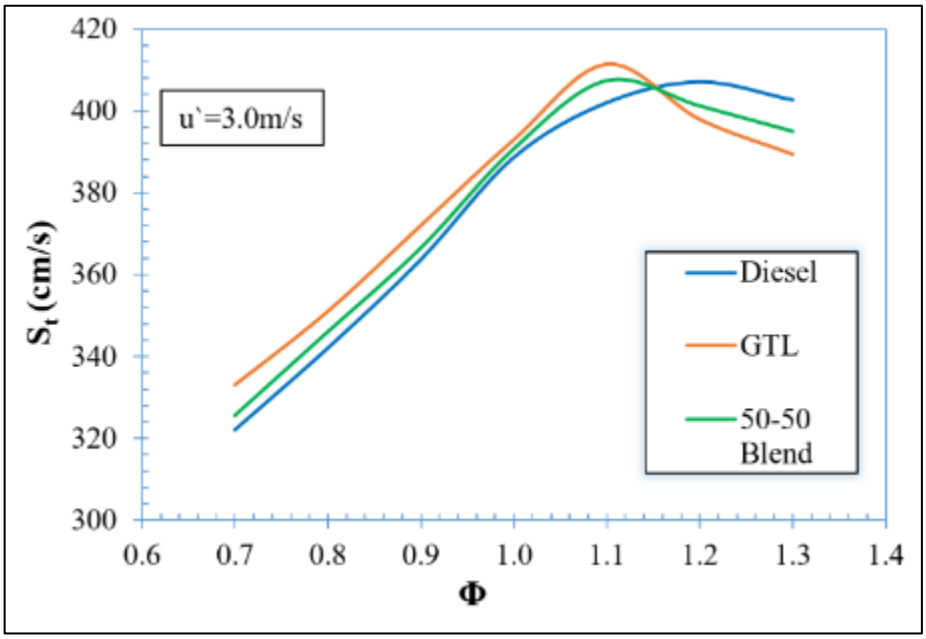

(c)

Figure 57. Turbulent flame speeds versus equivalence ratio for the three fuels at: (a) *u*`=0.5m/s, (b) *u*`=1.5m/s, (c) *u*`=3.0m/s

It is prevalent that higher levels of turbulence intensities result in a remarkable increase in turbulent flame speeds for all the tested fuels. In general, S_t increases proportionally with $u`/S_l$ in the low turbulence zone, then plateaus (bending region), and eventually falls as it approaches the quenching limit [187]. Figures 57(a-c) also show that lean GTL fuel has higher turbulent flame speeds than lean diesel and lean 50/50 diesel-GTL blend, with diesel having the lowest. Rich diesel, on the other hand, has a faster turbulent flame speed than rich GTL and rich 50/50 diesel-GTL blends. The effect of Lewis number (*Le*) on turbulent flame propagation can be used to interpret these trends. The ratio of a mixture's thermal diffusivity to its mass diffusivity is defined by the Lewis number [20]. Non-unity Lewis number can have a negative or positive impact on the rate of local burning. Because of the reduced (increased) heat loss in the positively curved segments when Le <1 (Le >1), the local burning rate is enhanced (reduced) [188]. At the flame front leading edge, with Le <1, the mean curvature and mean strain rate both become positive. As a result, for premixed turbulent reacting flow, the probability of identifying positively curved, stretched flamelets (convex towards the direction of unburnt gas) increases. When turbulent eddies stretch laminar flametlets, the local burning rate differs significantly from the unstretched laminar flame speed. As a result, for mixtures with Le <1, an increase in the flamelet surface area, as well as an increase in the local burning rate, augments turbulent flame speeds [19]. These effects account for the increased turbulent flame speeds observed in lean GTL (or rich diesel) characterized by Le <1 (values for Le are listed in Table 21. Similar patterns have been observed by References [70], [71]. The use of GTL fuel and the 50/50 blend at $u`$=0.5m/s

(u`=1.5m/s and $u$`=3.0m/s) has increased turbulent flame speeds by around 3.8% (5.3% and 2.4%) and 2.1% (2.2% and 1.3%), respectively compared to diesel fuel at equivalence ratios less than 1.1 ($\Phi < 1.1$).

6.2.4 Dimensionless Numbers for Turbulent Combustion

Reynolds number (Re_T) is an important dimensionless quantity used in fluid mechanics to define the ratio between inertial and viscous forces. Thus, a higher value of Re_T indicates a higher level of turbulence [196]. On the other hand, Damkohler number (Da) is used in premixed turbulent combustion to define the ratio between the characteristic eddy time scale and chemical time scale [197]. Typically, S_t is proportional to $Re_{T,}$ and it is inversely proportional to Da. Figure 58 shows the relation between the normalized turbulent flame speeds, turbulent Reynolds numbers, and Damkohler numbers throughout the vessel radius ($0 < r < 12$cm) for stoichiometric GTL fuel at u`=3.0m/s, and t=30ms.

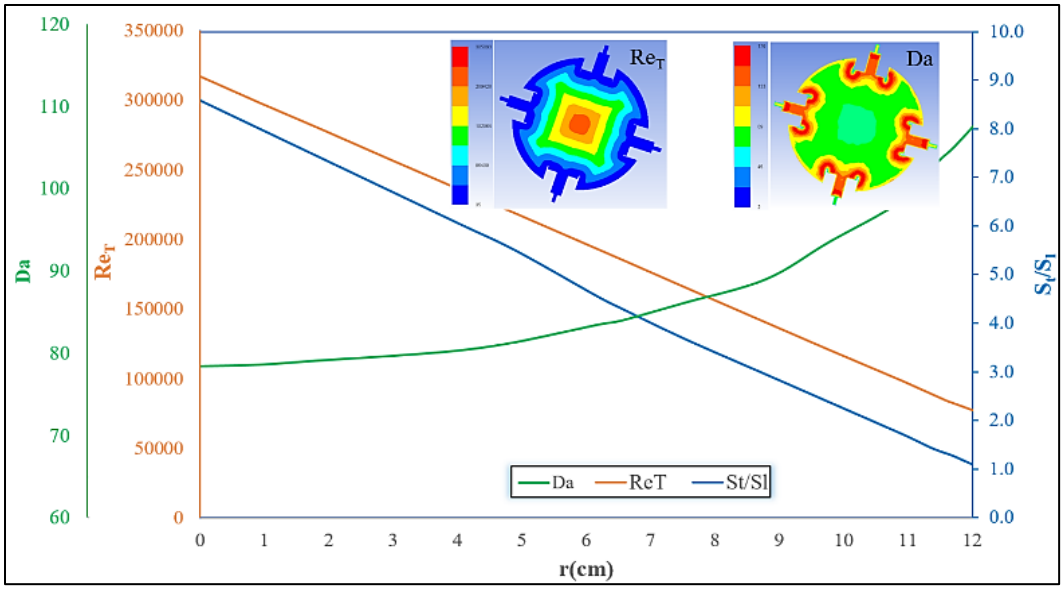

Figure 58. The relation between the normalized turbulent flame speeds, turbulent Reynolds number, and Damkohler number throughout the vessel radius ($0 < r < 12$cm) for stoichiometric GTL at $u`$=3.0m/s and t=30ms

It can be observed from Figure 58 that Re_T peaks at the center of the vessel. This region is characterized by the lowest turbulent eddy viscosity and turbulent kinetic energy (as was indicated in Figure 53), which increases gradually until reaching its maximum value near the mixing fans. Subsequently, the peak value of Re_T is found at the center of the vessel. S_t/S_l is proportional to Re_T, and this correlation is supported by the definition of this non-dimensional number, which states that Re_T is proportional to $u`/S_l$. Furthermore, the results are consistent with the kinematic restriction that turbulent flame speeds should equal laminar flame speeds (i.e., $S_t/S_l \rightarrow 1$), as $u' \rightarrow 0$ (which implies, $Re_T \rightarrow 0$) [72]. Da >1 throughout the flame radius indicates that the chemistry has dominated the turbulence at all regions with different

reaction rates, and the flame is propagating towards the vessel's wall. S_t/S_l is inversely proportional to *Da*, which is consistent with this dimensionless definition, which states that *Da* is inversely proportional to $u`/S_l$. Furthermore, the data support the kinematic constraint that turbulent flame speeds should equal laminar flame speeds (i.e., $S_t/S_l \rightarrow 1$), as $u' \rightarrow 0$ (which implies, $Da \rightarrow \infty$) [72]. S_t/S_l has been plotted as a function of Re_T and *Da* for the three fuels at t=30ms, as illustrated in Figure 59(a, b).

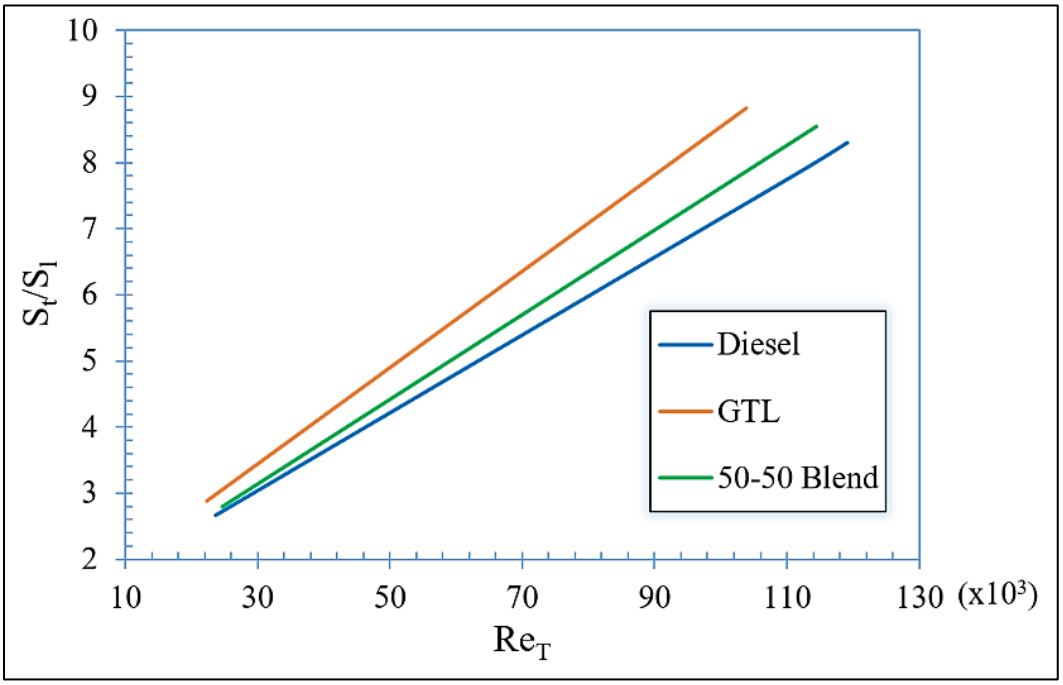

(a)

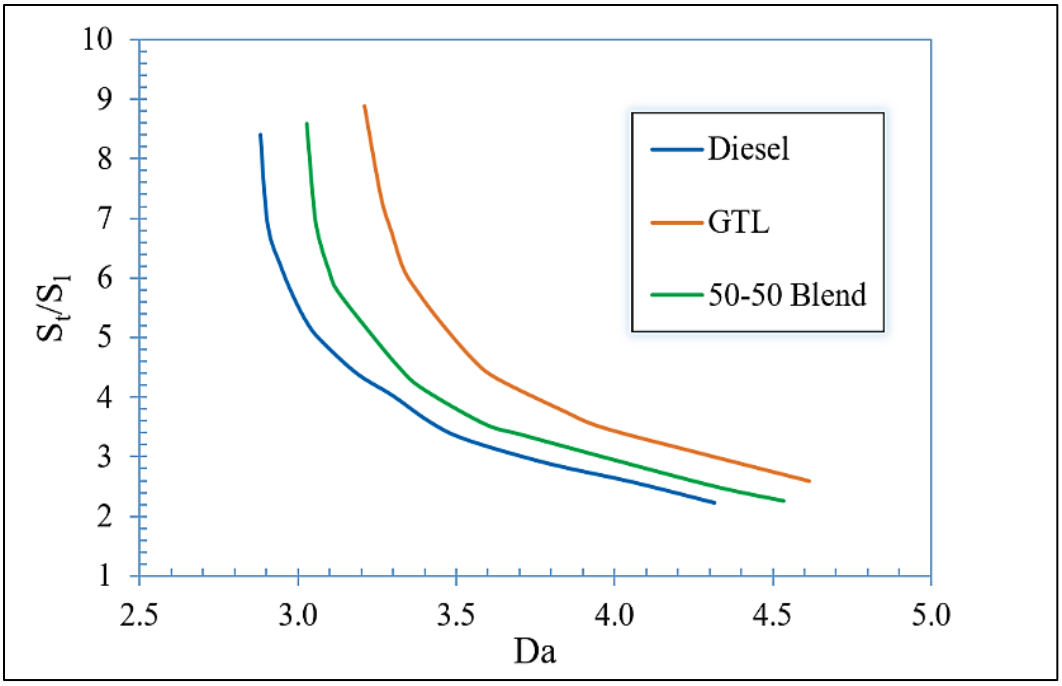

(b)

Figure 59. a) S_t/S_l versus Re_T, b) S_t/S_l versus Da for the three fuels at u`=3.0m/s, $\emptyset$=1.0 and t=30ms

At the same elapsed time (t=30ms), Re_T and Da are greater for GTL fuel than diesel and 50/50 diesel-GTL blend. This indicates that the flame is propagating towards the vessel's wall faster in the case of using GTL fuel instead of other fuels. In addition, the flame radius evolution is quicker, and the chemistry has dominated turbulence in a shorter time for GTL fuel than other fuels. These observations emphasize the conclusions reached in Figure 55 and Figure 57, which have revealed that stoichiometric GTL fuel is characterized by a faster flame radius development and a higher turbulent flame speed, respectively.

6.3 Comparison between Experimental and CFD Results

This section compares between the experimental and CFD results in two categories: (6.3.1) turbulent flame speeds (S_t) results, (6.3.2) flame morphology in Borghi diagram.

6.3.1 Turbulent Flame Speeds (S_t)-Comparison

Figure 60 compares the experimental turbulent flame speeds measurements and those numerically computed by Zimont TFC model for GTL fuel at three different turbulence intensities.

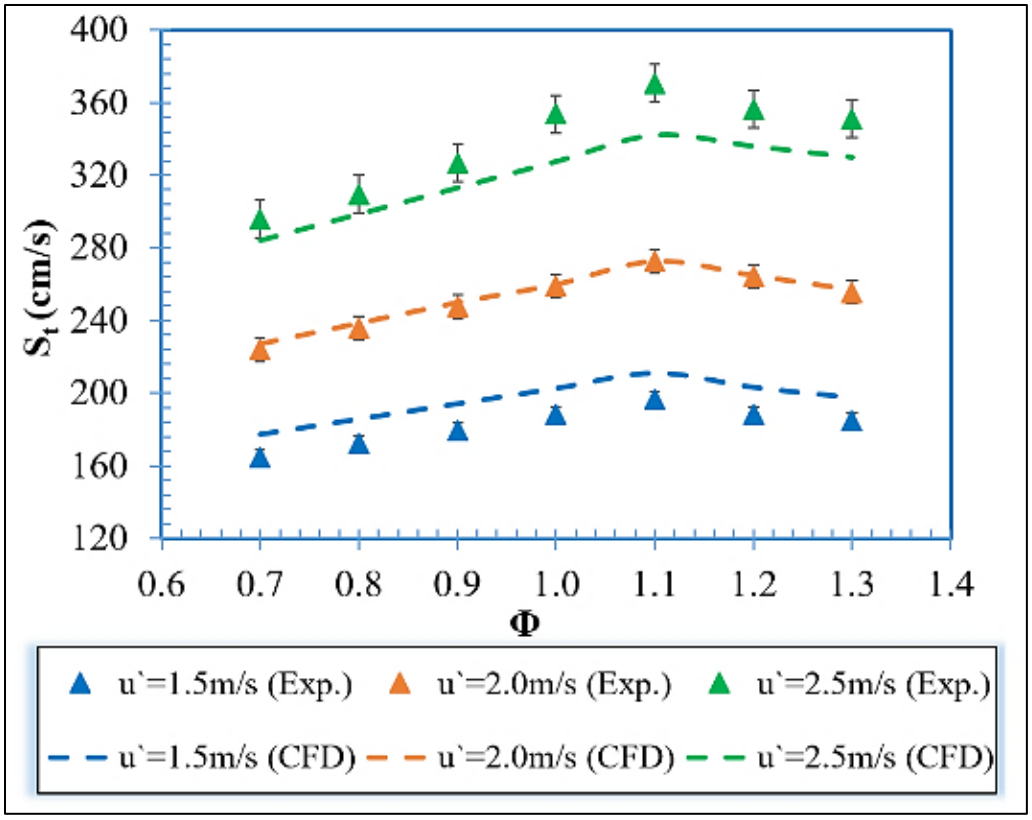

Figure 60. Comparison of experimental and numerical GTL turbulent flame speeds results at three consecutive turbulent intensities (u`=1.5m/s, $u$`=2.0m/s and u`=2.5m/s)

It can be noticed that CFD results have almost perfectly predicted turbulent flame speeds (S_t) at u`=2.0m/s, where the absolute error ($\varepsilon_a$) percentage was found to be around 0.65%. However, the CFD model has slightly over-predicted $S_t$ at $u$`=1.5m/s (ε_a= 4.1%), and under-predicted S_t at u`=2.5m/s (ε_a= 5.6%). The turbulent flame brush that expands by the increasing flame wrinkling and local strain rates contains different isosurfaces. Each is characterized by a reaction progress value (C) that varies spatially and temporally as the spherical flame propagates outwardly. For S_t to

be properly compared between different methods, all the measurements (and computations) have to be obtained at the same isosurface [15]. In this work, S_t results were numerically computed at a flame radius that equals 6cm (r_f=6cm). At this location, S_t values were found to become more stable as the flame has left the ignition region and is slightly affected by the turbulence domain [50]. In addition, it was found that after 30ms of flame propagation at r_f =6.0cm, the value of C ranges between 0.46 at $u`$=1.5m/s and 0.55 at $u`$=2.5m/s. However, the correlation used for obtaining S_t experimentally (Equation 94) has constrained that C=0.50 at the measurement location (radius of equal masses, r_m), which was calculated at the instant that $p = 0.5p_f$. The values of S_t at $u`$=2.0m/s were closely matching in Figure 60, where $r_f \approx$6.0cm, and $C \approx$0.50. However, in the other two cases ($u`$=1.5m/s and $u`$=2.5m/s), the flame radius (r_f) and the reaction progress variable (C) were not coincident. Hence S_t values were not well-predicted by the Zimont TFC model. In addition, it can be observed from the error bars in Figure 60 that the standard error becomes higher as the turbulence intensity level increases. This can be referred to the higher measurement uncertainty depicted at increased $u`$ levels due to vibrational losses in fan's speeds, as was indicated to in Table 14. These findings suggest that CFD modelling of S_t can be used to predict well the experimental measurements only within the domains where the experimental correlation and the used numerical model are not bounded by their constraints.

6.3.2 Borghi Diagram

Borghi diagram is used in premixed turbulent combustion to indicate the typical structure of the flame surface [54]. The flame morphologies for stoichiometric GTL fuel are determined experimentally and by CFD at three different turbulence intensities, u`=0.5m/s, $u$`=1.5m/s, and u`=3.0m/s, as shown in Figure 61.

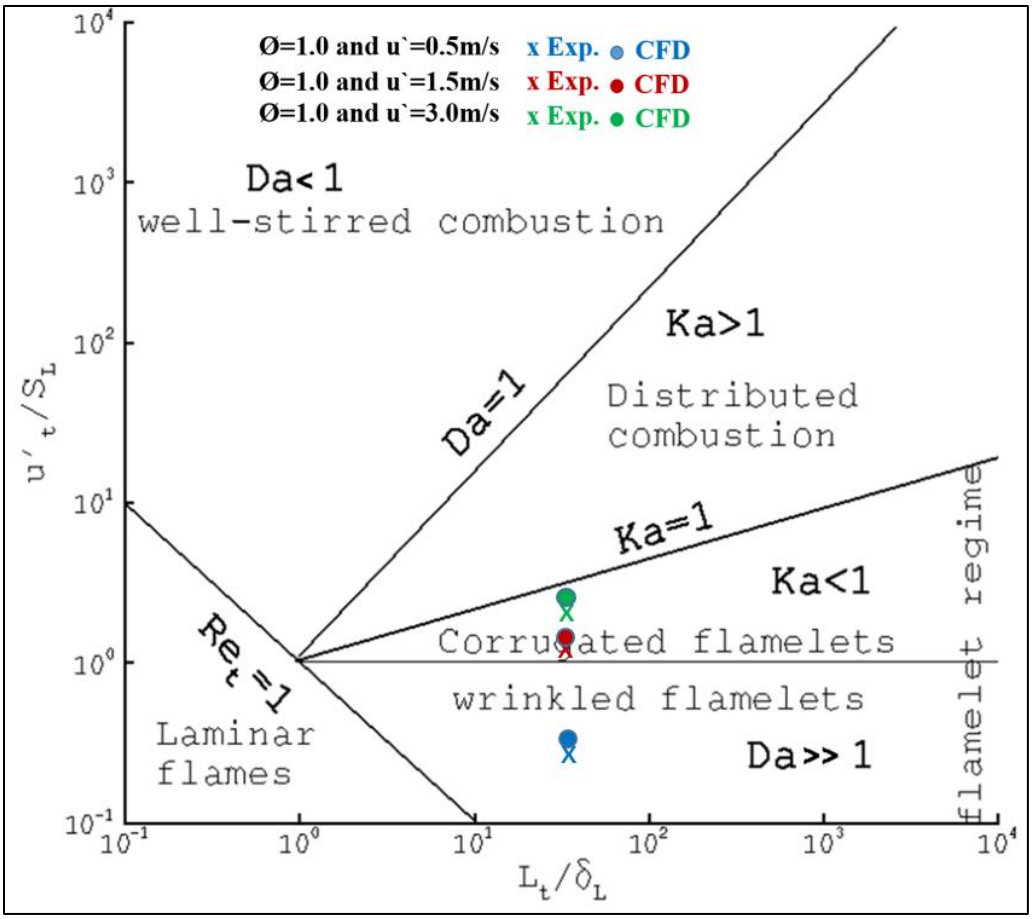

Figure 61. Determination of stoichiometric GTL fuel combustion regime on Borghi diagram at three different turbulence intensities, u`=0.5m/s, $u$`=1.5m/s, and u`=3.0m/s, as obtained from experiment "x" and CFD solver "o"

At $\emptyset$=1.0 and $u`$=0.5m/s, the turbulence intensity is low, i.e., $u`/S_l < 1$, which leads to a wrinkled flamelet regime. Therefore, the reaction is confined by a highly wrinkled, thin interface separating burned products from unburned reactants. Commonly, this structure is referred to as flamelets, which is assumed to have a local structure similar to that of a stretched laminar flame.

The turbulence intensity is larger than the laminar flame speed in the other two cases ($u`$=1.5m/s and $u`$=3.0m/s), i.e., $u`/S_l > 1$, and the flame structure is described by the corrugated flamelets regime. The significance of laminar flamelet instabilities is reduced, and turbulence influences combustion, primarily by increasing the flamelet surface area [105], [198]. In addition, it can be noticed that the flame morphology determined on the Borghi diagram using CFD results closely matches with the experimental measurements with an absolute error percentage (ε_a) of around 4.9%.

CHAPTER 7. CONCLUSIONS, RECOMMENDATIONS, AND FUTURE WORK

Turbulent flame speeds of GTL fuel (and its 50/50 blend with diesel) were investigated and compared with diesel fuel under a wide range of turbulence intensities (0.5m/s < $u`$< 3.0m/s), and equivalence ratios (0.7<$\Phi$<1.3) under atmospheric pressure at an initial temperature of 463K. The experiments were conducted in an 81.7L fan-stirred cylindrical combustion bomb that operates under near HIT conditions, with a negligible mean flow (<10% $u`$) and an integral length scale, L_t=20mm. The homogeneity and isotropy of the turbulence flow field were verified experimentally using the hotwire anemometer, and the turbulent kinetic energy balance was numerically studied using the Zimont TFC model. Four axis-symmetric fans were used to vary the turbulence intensity ($u`$). A computer-based Arduino-controlled circuit was used to control the fuel injection amount (e.g., the equivalence ratio). The turbulent flame speeds of the outwardly propagating GTL flame were measured using a 35XHTC piezo resistive pressure transducer, and the flame propagation was visually tracked using high-speed imaging. The experimental findings were verified and broadened using the Zimont TFC numerical model, which was adapted and implemented into ANSYS Fluent through a Reynolds Averaged Navier-Stokes (RANS) approach to study the influence of turbulence on GTL premixed combustion. The main findings and observations of the present study were as follows:

(i) The turbulent kinetic energy and eddy viscosity reach their maximum value near the mixing fans (e.g., at higher turbulence intensities) and start to gradually decrease until reaching their minimum value at the center point of the vessel, where it was found that *x* and *y* velocities remain almost constant and identical up to a vessel radius equals to 5cm. Subsequently, this observation indicates the existence of HIT at the center of the bomb.

(ii) The use of stoichiometric GTL fuel and 50/50 diesel-GTL blend has decreased the combustion peak pressure by 8.9% and 4.9%, respectively, compared to diesel fuel. This can be attributed to the lower density and kinematic viscosity of GTL fuel (and the 50/50 blend) compared to pure diesel, which enhances the air-fuel mixture atomization, and thus the combustion efficiency.

(iii) Rich diesel and lean GTL fuels were characterized by a faster flame radius evolution, a higher pressure rise rate (*dp/dt*), and, thus, higher turbulent flame speeds. In addition, Lewis number (*Le*) of those fuels is less than unity, which enhances the flame-turbulence interaction.

(iv) The use of GTL fuel and the 50/50 blend at $u`$=0.5m/s ($u`$=1.5m/s and $u`$=3.0m/s) has increased turbulent flame speeds by around 3.6% (5.3% and 2.8%) and 1.9% (2.8% and 1.4%), respectively compared to diesel fuel at equivalence ratios less than 1.1 ($\Phi < 1.1$).

(v) At the same elapsed time, turbulent Reynolds numbers (Re_T) and Damkohler numbers (Da) were found to be greater for stoichiometric GTL fuel compared to diesel fuel and 50/50 diesel-GTL blend, which indicates that the flame propagates towards the vessel's wall at a faster rate, and the chemistry has dominated turbulence in a shorter time.

(vi) At a low turbulence intensity level ($u`$=0.5m/s), the flame morphology is defined by a wrinkled flamelet regime in the Borghi diagram. However, at moderate and higher turbulence levels ($u`$=1.5m/s and $u`$=3.0m/s, respectively), the corrugated flamelets regime defines the flame structure.

(vii) The CFD results were found to be in excellent agreement with the experimental measurements at $u`$=2.0m/s, where the absolute error percentage ($\varepsilon_a$) was found to be around 0.65%. However, the CFD model has slightly over-predicted $S_t$ at $u`$=1.5m/s (ε_a= 4.1%), and under-predicted S_t at $u`$=2.5m/s (ε_a= 5.6%). Therefore, it was concluded that CFD modelling of S_t can be used to predict well the experimental measurements only within the domains where the experimental correlation and the used numerical model are not bounded by their constraints

Further improvements in this work's experimental apparatus and methodologies are encouraging and are highly recommended for a more comprehensive database. Although the application of some of these recommendations is a little bit costly, the study of turbulent flame speed and combustion characteristics of GTL fuel is highly

demanded in different fields, in addition to validating various numerical codes. Some of the suggested recommendations for future work are summarized as follows:

(i) Although the pressure leakage from the cylindrical bomb was relatively meager, reducing this leakage through the improvement of sealing can lead to less uncertainty in the amount of fuel injected into the bomb and improve the accuracy of the desired equivalence ratio.

(ii) Despite the existence of a near homogeneous and isotropic turbulence in the center of the cylindrical bomb, the alignment of the symmetrically opposed fans needs some improvement to encounter vibrational stresses at high fan's rotational speeds.

(iii) The temperature rise rate inside the bomb was slightly slow. Therefore, it is suggested to use heating coils of higher heating capacities to accelerate the temperature rise in the future.

(iv) Although the temperature variations inside the bomb were monitored using thermocouple wires fixed at three different locations, the infrared thermal imaging camera serves as a more advanced technique for achieving a more uniform air-fuel mixture inside the bomb before ignition.

(v) In this dissertation, a homogeneous and isotropic field in the center of the bomb was verified experimentally using the hotwire anemometer. However, the Particle Image Velocimetry (PIV) technique is more practical for displaying the uniform spatial map of the velocity field inside the bomb.

(vi) It is highly recommended to investigate that the turbulent flame speeds of the tested fuels at varying initial temperatures and pressures. However, this should only be conducted after properly inspecting the test rig for safe operation.

(vii) The results and outcomes of this work can be further verified and improved using other flame speed measurement techniques such as Schlieren Imaging and other optical measurement techniques. In addition, it is intended to extend the scope of this study in the future by using OH-Chemiluminescence and OSCE as an advanced flame visualization tools. Apart from the experimental work, the implementation of the Zimont TFC model using an LES approach can serve as a good basis for validating different numerical codes against experimental results.

(viii) In the future, diesel and GTL fuels can be blended at different volumetric compositions rather than the tested 50/50 diesel-GTL blend. Subsequently, this will enhance the understanding of the effect of blending these two fuels at different compositions. In addition, other biofuels such as corn oil and jojoba oil can be blended to varying compositions with diesel and GTL fuels, and the combustion characteristics of these new fuel blends can be compared with pure diesel.

REFERENCES

[1] A. Demirbas, “Progress and recent trends in biofuels,” *Prog. Energy Combust. Sci.*, vol. 33, no. 1, pp. 1–18, 2007, doi: 10.1016/j.pecs.2006.06.001.

[2] U. S. E. Information, “Annual Energy Outlook 2015 with projections to 2040,” Off. Integr. Int. Energy Anal., vol. 1, pp. 1–244, 2015, doi: DOE/EIA-0383(2013).

[3] N. L. Panwar, S. C. Kaushik, and S. Kothari, “Role of renewable energy sources in environmental protection: A review,” *Renew. Sustain. Energy Rev.*, vol. 15, no. 3, pp. 1513–1524, 2011, doi: 10.1016/j.rser.2010.11.037.

[4] A. Evans, V. Strezov, and T. J. Evans, “Assessment of sustainability indicators for renewable energy technologies,” *Renew. Sustain. Energy Rev.*, vol. 13, no. 5, pp. 1082–1088, 2009, doi: 10.1016/j.rser.2008.03.008.

[5] S. Samim, A. M. Sadeq, and S. F. Ahmed, “Measurements of Laminar Flame Speeds of Gas-to-Liquid-Diesel Fuel Blends,” *J. Energy Resour. Technol. Trans. ASME*, vol. 138, no. 5, pp. 1–8, 2016, doi: 10.1115/1.4033627.

[6] J. Delbeke, A. Runge-Metzger, Y. Slingenberg, and J. Werksman, *The paris agreement*. 2019, pp. 24–45.

[7] K. Choi, S. Park, H. G. Roh, and C. S. Lee, “Combustion and emission reduction characteristics of GTL-biodiesel fuel in a single-cylinder diesel engine,” *Energies*, vol. 12, no. 11, 2019, doi: 10.3390/en12112201.

[8] Shell Qatar, “Shell Qatar, 2010, ‘Pearl GTL, Overview’.,” Faculty of Engineering, Alexandria University, 2010. doi: 10.1016/j.aej.2016.06.026.

[9] A. M. Sadeq, M. A. Bassiony, A. M. Elbashir, S. F. Ahmed, and M. Khraisheh, “Combustion and emissions of a diesel engine utilizing novel intake manifold designs and running on alternative fuels,” *Fuel*, vol. 255, no. July, p. 115769, 2019, doi: 10.1016/j.fuel.2019.115769.

[10] S. Samim, “Investigation of Laminar Flame Speed of Alternative Liquid Fuel Blends,” Qatar University, 2016.

[11] S. Ravi, “Measurement of Turbulent Flame Speeds of Hydrogen and Natural Gas Blends (C1-C5 Alkanes) Using a Newly Developed Fan-Stirred Vessel,” Texas A&M, 2014.

[12] A. D’adamo, C. Iacovano, and S. Fontanesi, “A data-driven methodology for the simulation of turbulent flame speed across engine-relevant combustion regimes,” *Energies*, vol. 14, no. 14, 2021, doi: 10.3390/en14144210.

[13] A. Kianifar, N. Ghafoorianfar, M. R. Kianifar, and F. Alam, “Numerical combustion modelling of a gas-burner,” *Int. J. Mech. Mater. Eng.*, vol. 4, no. 3, pp. 211–219, 2009.

[14] A. M. Sadiq, A. K. Sleiti, and S. F. Ahmed, “Turbulent Flames in Enclosed Combustion Chambers: Characteristics and Visualization—A Review,” *J. Energy Resour. Technol.*, vol. 142, no. 8, 2020, doi: 10.1115/1.4046460.

[15] D. Bradley, M. Lawes, and M. S. Mansour, “Correlation of turbulent burning velocities of ethanol-air, measured in a fan-stirred bomb up to 1.2MPa,” *Combust. Flame*, vol. 158, no. 1, pp. 123–138, 2011, doi: 10.1016/j.combustflame.2010.08.001.

[16] B. Galmiche, N. Mazellier, F. Halter, and F. Foucher, “Turbulence characterization of a high-pressure high-temperature fan-stirred combustion vessel using LDV, PIV and TR-PIV measurements,” *Exp. Fluids*, vol. 55, no. 1, 2014, doi: 10.1007/s00348-013-1636-x.

[17] D. Bradley, M. Lawes, and M. E. Morsy, “Measurement of turbulence characteristics in a large scale fan-stirred spherical vessel,” *J. Turbul.*, vol. 20, no. 3, pp. 195–213, 2019, doi: 10.1080/14685248.2019.1610566.

[18] P. Griebel, P. Siewert, and P. Jansohn, “Flame characteristics of turbulent lean premixed methane/air flames at high pressure: Turbulent flame speed and flame brush thickness,” *Proc. Combust. Inst.*, vol. 31 II, no. 2, pp. 3083–3090, 2007, doi: 10.1016/j.proci.2006.07.042.

[19] A. Morones *et al.*, “Laminar and turbulent flame speeds for natural gas/hydrogen blends,” *Proc. ASME Turbo Expo*, vol. 4B, no. January 2015, 2014, doi: 10.1115/GT2014-26742.

[20] M. T. Nguyen, D. Yu, C. Chen, and S. S. Shy, “General Correlations of Iso-octane Turbulent Burning Velocities Relevant to Spark Ignition Engines,” *energies*, vol. 12, p. 1848, 2019, doi: 10.3390/en12101848.

[21] O. Mannaa *et al.*, “Turbulent burning characteristics of FACE-C gasoline and TPRF blend associated with the same RON at elevated pressures,” *Exp. Therm. Fluid Sci.*, vol. 95, pp. 104–114, 2019, doi: 10.1016/j.expthermflusci.2018.02.019.

[22] L. Gillespie, M. Lawes, C. G. W. Sheppard, and R. Woolley, “Aspects of laminar and turbulent burning velocity relevant to SI engines,” *SAE Tech. Pap.*, no. February 2015, 2000, doi: 10.4271/2000-01-0192.

[23] W. Leuckel, W. Nastoll, and N. Zarzalis, “Experimental Investigation of the Influence of turbulence on the Transient Premixed Flame Propagation Inside Closed Vessels,” in *The Combustion Institute*, 1990, pp. 729–734.

[24] P. O. Ayegba, “Turbulence statistics and flow structure in fluid flow using particle image velocimetry technique : A review,” *Wiley Online Libr.*, vol. 10, no. August 2019, pp. 1–49, 2020, doi: 10.1002/eng2.12138.

[25] V. L. Zimont, “Theory of turbulent combustion of a homogeneous fuel mixture at high reynolds numbers,” *Combust. Explos. Shock Waves*, vol. 15, no. 3, pp. 305–311, 1979, doi: 10.1007/BF00785062.

[26] V. Zimont, W. Polifke, M. Bettelini, and W. Weisenstein, “An efficient computational model for premixed turbulent combustion at high reynolds numbers based on a turbulent flame speed closure,” *J. Eng. Gas Turbines Power*, vol. 120, no. 3, pp. 526–532, 1998, doi: 10.1115/1.2818178.

[27] V. L. Zimont, “Gas premixed combustion at high turbulence. Turbulent flame

closure combustion model," *Exp. Therm. Fluid Sci.*, vol. 21, no. 1–3, pp. 179–186, 2000, doi: 10.1016/S0894-1777(99)00069-2.

[28] J. Gu, "Chemical kinetics modelling study of naturally aspirated and boosted SI engine flame propagation and knock," Loughborough University, 2015.

[29] J. De Vries, "A Study on Spherical Expanding Flame Speeds of Methane, Ethane, and Methane/Ethane Mixtures at Elevated Pressures," Texas A&M University, 2009.

[30] P. Soltic, T. Hilfiker, S. Hänggi, R. Hutter, M. Weissner, and D.- Wolfsburg, "Ignition- and combustion concepts for lean operated passenger car natural gas engines," in *12. Conference on Gaseous-Fuel Powered Vehicles, October 24-25 2017, Stuttgart*, 2017, no. October 2017.

[31] F. Rahim, K. E. Far, F. Parsinejad, R. J. Andrews, and H. Metghalchi, "A thermodynamic model to calculate burning speed of methane-air- diluent mixtures," *Int. J. Thermodyn.*, vol. 11, no. 4, pp. 151–160, 2008, doi: 10.5541/ijot.1034000223.

[32] B. Savard, "Characterization and Modeling of Premixed Turbulent n-Heptane Flames in the Thin Reaction Zone Regime," California Institute of Technology, 2015.

[33] E. V. Vega and K. Y. Lee, "An experimental study on laminar CH4/O2/N2 premixed flames under an electric field," *J. Mech. Sci. Technol.*, vol. 22, no. 2, pp. 312–319, 2008, doi: 10.1007/s12206-007-1043-4.

[34] S. Jerzembeck, C. Glawe, J. Keppner, and N. Peters, “Laminar Burning Velocities from Schlieren-and Pressure History Measurements,” in *5th WSEAS International*, 2008, no. January, pp. 106–113, [Online]. Available: http://www.wseas.us/e-library/conferences/2008/mexico/fluids/13-573-086.pdf.

[35] A. Farhat, R. E. V. Kumar, and O. Samimi-Abianeh, “Laminar Burning Velocity Measurement Using the Filtered Broadband Natural Emissions of Species,” *Energy & Fuels*, vol. 34, no. 3, pp. 3772–3779, 2020, doi: 10.1021/acs.energyfuels.9b04291.

[36] C. A. G. Casanova and M. Birouk, “Measurement of laminar flame speed of a novel liquid biofuel,” University of Manitoba, 2015.

[37] S. Muppala and V. C. Madhav Rao, “Numerical Implementation and validation of turbulent premixed combustion model for lean mixtures,” in *MATEC Web of Conferences*, 2018, vol. 209, pp. 1–5, doi: 10.1051/matecconf/201820900004.

[38] I. Ahmed and N. Swaminathan, “Simulation of spherically expanding turbulent premixed flames,” *Combust. Sci. Technol.*, vol. 185, no. 10, pp. 1509–1540, 2013, doi: 10.1080/00102202.2013.808629.

[39] J. J. H. Brouwers, “Statistical model of turbulent dispersion recapitulated,” *Fluids*, vol. 6, no. 5, 2021, doi: 10.3390/fluids6050190.

[40] T. D. Dunstan, N. Swaminathan, K. N. C. Bray, and N. G. Kingsbury, “The effects of non-unity lewis numbers on turbulent premixed flame interactions in a twin V-flame configuration,” *Combust. Sci. Technol.*, vol. 185, no. 6, pp. 874–

897, 2013, doi: 10.1080/00102202.2013.763801.

[41] Z. X. Chen, N. A. K. Doan, S. Ruan, I. Langella, and N. Swaminathan, "A priori investigation of subgrid correlation of mixture fraction and progress variable in partially premixed flames," *Combust. Theory Model.*, vol. 22, no. 5, pp. 862–882, 2018, doi: 10.1080/13647830.2018.1459862.

[42] F. B. Keil, N. Chakraborty, and M. Klein, "Analysis of the Closures of Sub-grid Scale Variance of Reaction Progress Variable for Turbulent Bunsen Burner Flames at Different Pressure Levels," *Flow, Turbul. Combust.*, vol. 105, no. 3, pp. 869–888, 2020, doi: 10.1007/s10494-020-00161-x.

[43] H. Gupta, O. J. Teerling, and J. A. van Oijen, "Effect of progress variable definition on the mass burning rate of premixed laminar flames predicted by the Flamelet Generated Manifold method," *Combust. Theory Model.*, vol. 25, no. 4, pp. 631–645, 2021, doi: 10.1080/13647830.2021.1926544.

[44] A. N. Lipatnikov, "Testing Premixed Turbulent Combustion Models by Studying Flame Dynamics," *Int. J. Spray Combust. Dyn.*, vol. 1, no. 1, pp. 39–66, 2009, doi: 10.1260/175682709788083362.

[45] R. Prud'Homme, "Laminar and Turbulent Flames," in *Flows and Chemical Reactions in Homogeneous Mixtures*, no. February, Paris, 2013, pp. 79–124.

[46] P. S. Bernard, "Turbulent flow properties of large-scale vortex systems," in *Proceedings of the National Academy of Sciences of the United States of America*, 2006, vol. 103, no. 27, pp. 10174–10179, doi: 10.1073/pnas.0604159103.

[47] A. Ayache, “Experimental Measurement of Turbulent Burning Velocity of Premixed Biogas Flame,” University of Manitoba, 2017.

[48] J. Martin, *Hydrodynamics and Transport for Water Quality Modeling*. 1999.

[49] M. E. U. Allauddin, “Modelling of Turbulent Premixed Combustion using LES and RANS methods Acknowledgments,” Bundeswehr University of Munich, 2017.

[50] A. Ayache, “Experimental Measurement of Turbulent Burning Velocity of Premixed Biogas Flame,” The University of Manitoba, 2017.

[51] J. Mathieu, *An Introduction to Turbulent Flows*. 2016.

[52] F. G. Schmitt, “About Boussinesq’s turbulent viscosity hypothesis: historical remarks and a direct evaluation of its validity,” *Comptes Rendus - Mec.*, vol. 335, no. 9–10, pp. 617–627, 2007, doi: 10.1016/j.crme.2007.08.004.

[53] N. Peters, “The turbulent burning velocity for large-scale and small-scale turbulence,” *J. Fluid Mech.*, vol. 384, pp. 107–132, 1999.

[54] T. Poinsot, D. Veynante, and S. Candel, “Diagrams of premixed turbulent combustion based on direct simulation,” *Symp. Combust.*, vol. 23, no. 1, pp. 613–619, 1991, doi: 10.1016/S0082-0784(06)80308-5.

[55] E. S. Semenov, “Measurement of turbulence characteristics in a closed volume with artificial turbulence,” *Combust. Explos. Shock Waves*, vol. 1, no. 2, pp. 57–62, 1966, doi: 10.1007/BF00757231.

[56] A. Ehn, J. Zhu, X. Li, and J. Kiefer, “Advanced laser-based techniques for gas-phase diagnostics in combustion and aerospace engineering,” *Appl. Spectrosc.*, vol. 71, no. 3, pp. 341–366, 2017, doi: 10.1177/0003702817690161.

[57] Y. Huang, “Combustion dynamics of swirl-stabilized lean premixed flames in an acoustically-driven environment,” University of Iowa, 2008.

[58] D. Bradley, M. Lawes, and M. S. Mansour, “The problems of the turbulent burning velocity,” *Flow, Turbul. Combust.*, vol. 87, no. 2–3, pp. 191–204, 2011, doi: 10.1007/s10494-011-9339-y.

[59] T. Brutscher, N. Zarzalis, and H. Bockhorn, “An experimentally based approach for the space-averaged laminar burning velocity used for modeling premixed turbulent combustion,” *Proc. Combust. Inst.*, vol. 29, no. 2, pp. 1825–1832, 2002, doi: 10.1016/S1540-7489(02)80221-8.

[60] G. Zhen and W. Leuckel, “Effects of ignitors and turbulence on dust explosions,” *J. Loss Prev. Process Ind.*, vol. 10, no. 5–6, pp. 317–324, 1997, doi: 10.1016/S0950-4230(97)00021-1.

[61] W. Leisenheimer, B., and Leukel, “Self-Generated Acceleration of Confined Deflagration Flame Fronts,” *Combust. Sci. Technol.*, vol. 118, no. 1–3, pp. 75–117, 1996.

[62] M. Weiß, N. Zarzalis, and R. Suntz, “Experimental study of Markstein number effects on laminar flamelet velocity in turbulent premixed flames,” *Combust. Flame*, vol. 154, no. 4, pp. 671–691, 2008, doi:

10.1016/j.combustflame.2008.06.011.

[63] M. Birouk, B. Sarh, and I. Gökalp, “An Attempt to Realize Experimental Isotropic Turbulence at Low Reynolds Number,” *Flow, Turbul. Combust.*, vol. 70, no. 1–4, pp. 325–348, 2003, doi: 10.1023/B:APPL.0000004974.74706.6d.

[64] W. Hwang and J. K. Eaton, “Creating homogeneous and isotropic turbulence without a mean flow,” *Exp. Fluids*, vol. 36, no. 3, pp. 444–454, 2004, doi: 10.1007/s00348-003-0742-6.

[65] M. R. H. Sheikhi, M. Safari, and H. Metghalchi, “Large Eddy Simulation for Local Entropy Generation Analysis of Turbulent Flows,” *J. Energy Resour. Technol.*, vol. 134, no. 4, 2012, doi: 10.1115/1.4007482.

[66] S. Kwon, M. S. Wu, J. F. Driscoll, and G. M. Faeth, “Flame surface properties of premixed flames in isotropic turbulence: Measurements and numerical simulations,” *Combust. Flame*, vol. 88, no. 2, pp. 221–238, 1992, doi: 10.1016/0010-2180(92)90053-R.

[67] T. D. Fansler and E. G. Groff, “Turbulence characteristics of a fan-stirred combustion vessel,” *Combust. Flame*, vol. 80, no. 3–4, pp. 350–354, 1990, doi: 10.1016/0010-2180(90)90110-D.

[68] S. S. Shy, W. K. I, and M. L. Lin, “A new cruciform burner and its turbulence measurements for premixed turbulent combustion study,” *Exp. Therm. Fluid Sci.*, vol. 20, no. 3–4, pp. 105–114, 2000, doi: 10.1016/S0894-1777(99)00035-7.

[69] C. Liu, “Self-Contradictions in Current Turbulence Theory,” in *Intech open*, 2015, pp. 1–23.

[70] J. Vancoillie, G. Sharpe, M. Lawes, and S. Verhelst, “The turbulent burning velocity of methanol-air mixtures,” *Fuel*, vol. 130, pp. 76–91, 2014, doi: 10.1016/j.fuel.2014.04.003.

[71] S. A. B. Al Omari, M. O. Hamdan, M. Y. Selim, and E. Elnajjar, “Combustion of jojoba-oil/diesel blends in a small scale furnace,” *Renew. Energy*, vol. 131, no. July, pp. 678–688, 2019, doi: 10.1016/j.renene.2018.07.009.

[72] A. M. Ruelas, E. L. Petersen, N. Donohoe, and A. Heufer, “Laminar and Turbulent Flame Speeds for Natural Gas / Hydrogen Blends,” in *ASME Turbo Expo 2014*, 2014, no. June, pp. 1–9, doi: 10.1115/GT2014-26742.

[73] M. El-Adawy, M. R. Heikal, and A. R. A. Aziz, “Stereoscopic particle image velocimetry measurements and proper orthogonal decomposition analysis of the in-cylinder flow of gasoline direct injection engine,” *J. Energy Resour. Technol. Trans. ASME*, vol. 141, no. 4, 2019, doi: 10.1115/1.4042068.

[74] M. J. Hargather and G. S. Settles, “Recent developments in schlieren and shadowgraphy,” in *27th AIAA Aerodynamic Measurement Technology and Ground Testing Conference 2010*, 2010, vol. 1, no. August, doi: 10.2514/6.2010-4206.

[75] P. Brequigny, C. Endouard, C. Mounaïm-Rousselle, and F. Foucher, “An experimental study on turbulent premixed expanding flames using simultaneously

Schlieren and tomography techniques," *Exp. Therm. Fluid Sci.*, vol. 95, no. December 2017, pp. 11–17, 2018, doi: 10.1016/j.expthermflusci.2017.12.018.

[76] B. Galmiche, N. Mazellier, F. Halter, and F. Foucher, "Turbulence characterization of a high-pressure high-temperature fan-stirred combustion vessel using LDV, PIV and TR-PIV measurements," *Exp. Fluids*, vol. 55, no. 1, pp. 0–20, 2014, doi: 10.1007/s00348-013-1636-x.

[77] A. J. B. Siqueira *et al.*, "Turbulence Mmeasurements in a Fan-Stirred Flame Bomb Using Laser Doppler Velocimetry," *J. Chem. Inf. Model.*, vol. 53, no. 9, pp. 1689–1699, 2019, doi: 10.1017/CBO9781107415324.004.

[78] Y. Wu, "Experimental investigation of laminar flame speeds of kerosene fuel and second generation biofuels in elevated conditions of pressure and preheat temperature," Normandie University, 2017.

[79] H. Kido, M. Nakahara, K. Nakashima, and J. Hashimoto, "Influence of local flame displacement velocity on turbulent burning velocity," *Proc. Combust. Inst.*, vol. 29, no. 2, pp. 1855–1861, 2002, doi: 10.1016/S1540-7489(02)80225-5.

[80] C. A. G. Casanova, "Measurement of laminar flame speed of a novel liquid biofuel," University of Manitoba, 2015.

[81] J. Natarajan, T. Lieuwen, and J. Seitzman, "Laminar flame speeds of H2/CO mixtures: Effect of CO2 dilution, preheat temperature, and pressure," *Combust. Flame*, vol. 151, no. 1–2, pp. 104–119, 2007, doi: 10.1016/j.combustflame.2007.05.003.

[82] J. Kashdan and B. Thirouard, “Optical Engines as Representative Tools in the Development of New Combustion Engine Concepts,” *Oil Gas Sci. Technol.*, vol. 66, no. 5, pp. 759–777, 2011, doi: 10.2516/ogst/2011134.

[83] W. Hopfner and E. Winklhofer, “Optical Single Cylinder Engines in Engine Research and Development,” *Combust. Engines*, vol. 152, no. 1, pp. 71–78, 2013, [Online]. Available: PTNSS-2013-107.

[84] G. Koszalka and A. Suchecki, “Analysis of design parameters of pistons and piston rings of a combustion engine,” in *MATEC Web of Conferences*, 2017, vol. 118, doi: 10.1051/matecconf/201711800013.

[85] X. Zhang, “Power Control of Diesel Engine-Generator Set Subject to Emission Constraints,” University of Windsor, 2012.

[86] Z. Ahmad, O. Kaario, C. Qiang, V. Vuorinen, and M. Larmi, “A parametric investigation of diesel/methane dual-fuel combustion progression/stages in a heavy-duty optical engine,” *Appl. Energy*, vol. 251, no. January, p. 113191, 2019, doi: 10.1016/j.apenergy.2019.04.187.

[87] S. H. Park, S. H. Yoon, and C. S. Lee, “Bioethanol and gasoline premixing effect on combustion and emission characteristics in biodiesel dual-fuel combustion engine,” *Appl. Energy*, vol. 135, no. x, pp. 286–298, 2014, doi: 10.1016/j.apenergy.2014.08.056.

[88] E. Shim, H. Park, and C. Bae, “Intake air strategy for low HC and CO emissions in dual-fuel (CNG-diesel) premixed charge compression ignition

engine," *Appl. Energy*, vol. 225, no. May, pp. 1068–1077, 2018, doi: 10.1016/j.apenergy.2018.05.060.

[89] Q. Cheng, Z. Ahmad, O. Kaario, and L. Martti, "Cycle-to-cycle variations of dual-fuel combustion in an optically accessible engine," *Appl. Energy*, vol. 254, no. February, p. 113611, 2019, doi: 10.1016/j.apenergy.2019.113611.

[90] S. Lee, S. Yoon, H. Kwon, J. Lee, and S. Park, "Effects of engine operating conditions on flame propagation processes in a compression ignition optical engine," *Appl. Energy*, vol. 254, no. March, p. 113642, 2019, doi: 10.1016/j.apenergy.2019.113642.

[91] W. Li, Z. Liu, and Z. Wang, "Experimental and theoretical analysis of the combustion process at low loads of a diesel natural gas dual-fuel engine," *Energy*, vol. 94, pp. 728–741, 2016, doi: 10.1016/j.energy.2015.11.052.

[92] N. N. Mustafi, R. R. Raine, and S. Verhelst, "Combustion and emissions characteristics of a dual fuel engine operated on alternative gaseous fuels," *Fuel*, vol. 109, pp. 669–678, 2013, doi: 10.1016/j.fuel.2013.03.007.

[93] Z. Liu and G. A. Karim, "An examination of the ignition delay period in gas-fueled diesel engines," *J. Eng. Gas Turbines Power*, vol. 120, no. 1, pp. 225–231, 1998, doi: 10.1115/1.2818080.

[94] Q. Wang, C. Yao, Z. Dou, B. Wang, and T. Wu, "Effect of intake pre-heating and injection timing on combustion and emission characteristics of a methanol fumigated diesel engine at part load," *Fuel*, vol. 159, pp. 796–802, 2015, doi:

10.1016/j.fuel.2015.07.032.

[95] F. Y. Hagos, A. R. A. Aziz, and S. A. Sulaiman, “Effect of air-fuel ratio on the combustion characteristics of syngas (H2:CO) in direct-injection spark-ignition engine,” *Energy Procedia*, vol. 61, no. Di, pp. 2567–2571, 2014, doi: 10.1016/j.egypro.2014.12.047.

[96] G. Donadio, C. Poggiani, L. Rondoni, C. N. Grimaldi, M. De Cesare, and N. Bellato, “Combustion analysis in an optical access engine,” in *Energy Procedia*, 2014, vol. 45, pp. 959–966, doi: 10.1016/j.egypro.2014.01.101.

[97] S. Martinez, A. Irimescu, S. S. Merola, P. Lacava, and P. Curto-Riso, “Flame front propagation in an optical GDI engine under stoichiometric and lean burn conditions,” *Energies*, vol. 10, no. 9, 2017, doi: 10.3390/en10091337.

[98] J. Yang, X. Dong, Q. Wu, and M. Xu, “Effects of enhanced tumble ratios on the in-cylinder performance of a gasoline direct injection optical engine,” *Appl. Energy*, vol. 236, no. November 2018, pp. 137–146, 2019, doi: 10.1016/j.apenergy.2018.11.059.

[99] A. Peñaranda, S. D. Martinez Boggio, P. T. Lacava, S. Merola, and A. Irimescu, “Characterization of flame front propagation during early and late combustion for methane-hydrogen fueling of an optically accessible SI engine,” *Int. J. Hydrogen Energy*, vol. 43, no. 52, pp. 23538–23557, 2018, doi: 10.1016/j.ijhydene.2018.10.167.

[100] L. Chen, H. Wei, R. Zhang, J. Pan, L. Zhou, and D. Feng, “Effects of spark

plug type and ignition energy on combustion performance in an optical SI engine fueled with methane," *Appl. Therm. Eng.*, vol. 148, no. September 2018, pp. 188–195, 2019, doi: 10.1016/j.applthermaleng.2018.11.052.

[101] H. Liu *et al.*, "Investigation on blending effects of gasoline fuel with n-butanol, DMF, and ethanol on the fuel consumption and harmful emissions in a GDI vehicle," *Energies*, vol. 12, no. 10, 2019, doi: 10.3390/en12101845.

[102] M. Soder, "Numerical Investigation of Internal Combustion Engine Related Flows," 2013.

[103] S. S. Merola, C. Tornatore, A. Irimescu, L. Marchitto, and G. Valentino, "Optical diagnostics of early flame development in a DISI (direct injection spark ignition) engine fueled with n-butanol and gasoline," *Energy*, vol. 108, pp. 50–62, 2016, doi: 10.1016/j.energy.2015.10.140.

[104] C. E. Frouzakis, *Lattice Boltzmann methods for reactive and other flows*, vol. 95. 2011.

[105] A. Thattai, "A Validation Study For Turbulent Premixed Flame Propagation In Closed Vessels Submitted in Partial Fulfillment," Delft University of Technology, 2010.

[106] B. P. Brener, M. A. Cruz, R. L. Thompson, and R. P. Anjos, "Conditioning and accurate solutions of Reynolds average Navier-Stokes equations with data-driven turbulence closures," *J. Fluid Mech.*, vol. 915, no. July, 2021, doi: 10.1017/jfm.2021.148.

[107] W. R. J. Frohlich, “Introduction to Large Eddy Simulation of Turbulent Flows,” in *Endocrine Reviews*, vol. 35, 2014, pp. 267–298.

[108] R. Sankaran, E. R. Hawkes, J. H. Chen, T. Lu, and C. K. Law, “Direct numerical simulations of turbulent lean premixed combustion,” *J. Phys. Conf. Ser.*, vol. 46, no. 1, pp. 38–42, 2006, doi: 10.1088/1742-6596/46/1/004.

[109] I. B. Celik, “Introductory turbulence modeling,” 1999. [Online]. Available: http://www.fem.unicamp.br/~im450/palestras&artigos/ASME_Tubulence/cds13workbook.pdf.

[110] P. Y. Chou, “On velocity correlations and the solutions of the equations of turbulent fluctuation,” *Q. Appl. Math.*, vol. 3, no. 1, pp. 38–54, 1945, doi: 10.1090/qam/11999.

[111] B. E. Launder and B. I. Sharma, “Application of the energy-dissipation model of turbulence to the calculation of flow near a spinning disc,” *Lett. Heat Mass Transf.*, vol. 1, no. 2, pp. 131–137, 1974, doi: 10.1016/0094-4548(74)90150-7.

[112] M. A. Abd Halim, N. A. R. N. Mohd, M. N. Mohd Nasir, and M. N. Dahalan, “The evaluation of k-ε and k-ω turbulence models in modelling flows and performance of S-shaped diffuser,” *Int. J. Automot. Mech. Eng.*, vol. 15, no. 2, pp. 5161–5178, 2018, doi: 10.15282/ijame.15.2.2018.2.0399.

[113] M. M. Rahman, V. Vuorinen, J. Taghinia, and M. Larmi, “Wall-distance-free formulation for SST k-ω model,” *Eur. J. Mech. B/Fluids*, vol. 75, no. May, pp. 71–82, 2019, doi: 10.1016/j.euromechflu.2018.11.010.

[114] W. Deconinck, “Design and Application of Discrete Explicit Filters for Large Eddy Simulation of Compressible Turbulent Flows,” University of Toronto, 2008.

[115] Ahmed F. Ghoniem, “Large Eddy Simulations of Premixed Turbulent Flame Dynamics: Combustion Modeling, Validation & Analysis,” Massachusetts Institute of Technology, 2014.

[116] M. Pfitzner and M. Klein, “A near-exact analytic solution of progress variable and pdf for single-step Arrhenius chemistry,” *Combust. Flame,* vol. 226, pp. 380–395, 2021, doi: 10.1016/j.combustflame.2020.12.007.

[117] M. Pfitzner, “A New Analytic pdf for Simulations of Premixed Turbulent Combustion,” *Flow, Turbul. Combust.*, vol. 106, no. 4, pp. 1213–1239, 2021, doi: 10.1007/s10494-020-00137-x.

[118] R. Friedrich, “Numerical investigation of premixed methane-air flame in two-dimensional half open tube in the early stages,” *Eur. J. Mech. - B/Fluids,* vol. 17, no. 6, pp. 901–903, 1998, doi: 10.1016/s0997-7546(99)80019-3.

[119] D. B. Spalding, “Mixing and chemical reaction in steady confined turbulent flames,” *Symp. Combust.*, vol. 13, no. 1, pp. 649–657, 1971, doi: 10.1016/S0082-0784(71)80067-X.

[120] A. Brink, C. Mueller, P. Kilpinen, and M. Hupa, “Possibilities and limitations of the Eddy Break-Up Model,” *Combust. Flame,* vol. 123, no. 1–2, pp. 275–279, 2000, doi: 10.1016/S0010-2180(00)00146-2.

[121] R. Saïd and R. Borghi, “A simulation with a ‘cellular automaton’ for turbulent combustion modelling,” *Symp. Combust.*, vol. 22, no. 1, pp. 569–577, 1989, doi: 10.1016/S0082-0784(89)80064-5.

[122] C. Fureby and C. Löfström, “Large-eddy simulations of bluff body stabilized flames,” *Symp. Combust.*, vol. 25, no. 1, pp. 1257–1264, 1994, doi: 10.1016/S0082-0784(06)80766-6.

[123] J. R. Wang, H. T. Lin, H. C. Chen, and C. Shih, “The turbine trip without bypass analysis for Lungmen ABWR using TRACE/PARCS,” in *Energy Procedia*, 2012, vol. 14, pp. 2113–2117, doi: 10.1016/j.egypro.2011.12.906.

[124] I. Dhuchakallaya and A. P. Watkins, “Auto-ignition of diesel spray using the PDF-Eddy Break-Up model,” *Appl. Math. Model.*, vol. 34, no. 7, pp. 1732–1745, 2010, doi: 10.1016/j.apm.2009.09.019.

[125] B. F. Magnussen and B. H. Hjertager, “On mathematical modeling of turbulent combustion with special emphasis on soot formation and combustion,” *Symp. Combust.*, vol. 16, no. 1, pp. 719–729, 1977, doi: 10.1016/S0082-0784(77)80366-4.

[126] M. Mansourian and R. Kamali, “Modifying the constant coefficients of Eddy-dissipation concept model in moderate or intense low-oxygen dilution combustion using inverse problem methodology,” *Acta Astronaut.*, vol. 162, no. July, pp. 546–554, 2019, doi: 10.1016/j.actaastro.2019.07.002.

[127] M. Farokhi and M. Birouk, “Modeling of the gas-phase combustion of a

grate-firing biomass furnace using an extended approach of Eddy Dissipation Concept," *Fuel*, vol. 227, no. May, pp. 412–423, 2018, doi: 10.1016/j.fuel.2018.04.102.

[128] A. Parente, M. R. Malik, F. Contino, A. Cuoci, and B. B. Dally, "Extension of the Eddy Dissipation Concept for turbulence/chemistry interactions to MILD combustion," *Fuel*, vol. 163, pp. 98–111, 2016, doi: 10.1016/j.fuel.2015.09.020.

[129] Y. Kuang, B. He, C. Wang, W. Tong, and D. He, "Numerical analyses of MILD and conventional combustions with the Eddy Dissipation Concept (EDC)," *Energy*, vol. 237, p. 121622, 2021, doi: 10.1016/j.energy.2021.121622.

[130] A. Nassiri Toosi, M. Farokhi, and B. Mashadi, "Application of modified eddy dissipation concept with large eddy simulation for numerical investigation of internal combustion engines," *Comput. Fluids*, vol. 109, pp. 85–99, 2015, doi: 10.1016/j.compfluid.2014.11.029.

[131] A. Kurenkov and M. Oberlack, "Modelling turbulent premixed combustion using the level set approach for Reynolds averaged models," *Flow, Turbul. Combust.*, vol. 74, no. 4, pp. 387–407, 2005, doi: 10.1007/s10494-005-9000-8.

[132] O. Kurenkov and M. Oberlack, "LES of premixed turbulent combustion using the level set approach," *Appl. Math. Model.*, vol. 6, no. 1, pp. 533–534, 2006, doi: 10.1002/pamm.200610247.

[133] H. Pitsch and L. Duchamp de Lageneste, "Large-eddy simulation of premixed turbulent combustion," *Comput. Fluid Solid Mech. 2003*, vol. 29, pp. 1096–1099,

2003, doi: 10.1016/B978-008044046-0.50267-0.

[134] V. Moureau, B. Fiorina, and H. Pitsch, “A level set formulation for premixed combustion LES considering the turbulent flame structure,” *Combust. Flame*, vol. 156, no. 4, pp. 801–812, 2009, doi: 10.1016/j.combustflame.2009.01.019.

[135] N. L. Zhang and X. M. Guo, “Review on multiscale modeling and computation,” *Jisuan Lixue Xuebao/Chinese J. Comput. Mech.*, vol. 28, no. SUPPL. 1, pp. 1–5, 2011.

[136] C. Helzel, R. J. Leveque, and G. Warnecke, “A modified fractional step method for the accurate approximation of detonation waves,” *SIAM J. Sci. Comput.*, vol. 22, no. 4, pp. 1489–1510, 2001, doi: 10.1137/S1064827599357814.

[137] T. C. Chew, R. E. Britter, and K. N. C. Bray, “Laser tomography of turbulent premixed bunsen flames,” *Combust. Flame*, vol. 75, no. 2, pp. 165–174, 1989, doi: 10.1016/0010-2180(89)90094-1.

[138] S. J. Brookes, R. S. Cant, I. D. J. Dupere, and A. P. Dowling, “Computational Modelling of Self-Excited Combustion Instabilities,” *J. Eng. Gas Turbines Power*, vol. 123, no. 2, pp. 322–326, May 2001, doi: 10.1115/2000-GT-0104.

[139] R. Knikker, D. Veynante, and C. Meneveau, “A priori testing of a similarity model for large eddy simulations of turbulent premixed combustion,” *Proc. Combust. Inst.*, vol. 29, no. 2, pp. 2105–2111, 2002, doi: 10.1016/S1540-7489(02)80256-5.

[140] R. Rasool, N. Chakraborty, and M. Klein, “Algebraic Flame Surface Density Modelling of High Pressure Turbulent Premixed Bunsen Flames,” *Flow, Turbul. Combust.*, vol. 106, no. 4, pp. 1313–1327, 2021, doi: 10.1007/s10494-020-00128-y.

[141] V. L. Zimont, W. Polifke, and M. Bettelini, “An Efficient Computational Model for Premixed Turbulent Combustion at High Reynolds Numbers Based on a Turbulent Flame Speed Closure,” no. July, 1998, doi: 10.1115/1.2818178.

[142] M. Bi, C. Dong, and Y. Zhou, “Numerical simulation of premixed methane-air deflagration in large L/D closed pipes,” *Appl. Therm. Eng.*, vol. 40, pp. 337–342, 2012, doi: 10.1016/j.applthermaleng.2012.01.065.

[143] F. Biagioli and V. L. Zimont, “Gas dynamics Modelling of Counter gradient Transport in Open and Impinging Turbulent Premixed Flames,” in *Proceedings of the Combustion Institute*, 2002, vol. 29, pp. 2087–2095.

[144] H. Birkestad, “Separation and Compression of CO2 in an O2/CO2-fired Power Plant,” Chalmers University, 2002.

[145] E. Salaün *et al.*, “Experimental investigation of a spray swirled flame in gas turbine model combustor,” in *18th International Symposium on the Application of Laser and Imaging Techniques to Fluid Mechanics*, 2016, pp. 1–23.

[146] A. Basidh, S. Gunasekar, and D. Devarasu, “Experimentation of Flame Stabilization Using Half V-Gutter Experimentation of Flame Stabilization Using Half V-Gutter,” in *Conference: 29th National Convention of Aerospace*

Engineers. National Seminar on Aerospace Engineering, 2015, no. November, pp. 1–9.

[147] A. Lipatnikov and J. Chomiak, "Turbulent Burning Velocity and Speed of Developing ,Turbulent Burning Velocity and Speed of Developing, Curved, and Strained Flames," 2002, vol. 29, pp. 2113–2121.

[148] J. Goulier, N. Chaumeix, F. Halter, N. Meynet, and A. Bentaïb, "Experimental study of laminar and turbulent flame speed of a spherical flame in a fan-stirred closed vessel for hydrogen safety application," *Nucl. Eng. Des.*, vol. 312, pp. 214–227, 2017, doi: 10.1016/j.nucengdes.2016.07.007.

[149] Y. Wang, X. Zhang, Y. Li, and S. Qin, "Experimental study on premixed turbulent flame of methane/air in a spherical closed chamber," *Energy Convers. Manag.*, vol. 222, no. August, p. 113219, 2020, doi: 10.1016/j.enconman.2020.113219.

[150] F. Z. P. Habisreuther and M. H. H. Bockhorn, "Modelling of a Premixed Swirl-stabilized Flame Using a Turbulent Flame Speed Closure Model in LES," *Flow Turbul. Combust*, vol. 82, pp. 537–551, 2009, doi: 10.1007/s10494-008-9175-x.

[151] L. Palanti, D. Pampaloni, A. Andreini, and B. Facchini, "Numerical simulation of a swirl stabilized methane-air flame with an automatic meshing CFD solver," *Energy Procedia*, vol. 148, pp. 376–383, 2018, doi: 10.1016/j.egypro.2018.08.098.

[152] S. Yu, X. Liu, X. S. Bai, A. M. Elbaz, and W. L. Roberts, “LES / PDF modeling of swirl-stabilized non-premixed methane / air flames with local extinction and re-ignition,” vol. 219, pp. 102–119, 2020, doi: 10.1016/j.combustflame.2020.05.018.

[153] W. P. Jones, A. J. Marquis, and F. Wang, “Large eddy simulation of a premixed propane turbulent bluff body flame using the Eulerian stochastic field method,” *Fuel*, vol. 140, pp. 514–525, 2015, doi: 10.1016/j.fuel.2014.06.050.

[154] U. Ahmed and R. Prosser, “Modelling flame turbulence interaction in RANS simulation of premixed turbulent combustion,” *Combust. Theory Model.*, vol. 20, no. 1, pp. 34–57, 2016, doi: 10.1080/13647830.2015.1115130.

[155] S. Gövert, D. Mira, J. B. W. Kok, M. Vazquez, and G. Houzeaux, “Turbulent Combustion Modelling of a Confined Premixed Methane/Air Jet Flame Using Tabulated Chemistry,” in *Energy Procedia*, 2015, vol. 66, pp. 313–316, doi: 10.1016/j.egypro.2015.02.070.

[156] V. L. Zimont and V. Battaglia, “Joint RANS/LES approach to premixed flame modelling in the context of the TFC combustion model,” *Flow, Turbul. Combust.*, vol. 77, no. 1–4, pp. 305–331, 2006, doi: 10.1007/s10494-006-9048-0.

[157] Q. Wang, H. Ma, Z. Shen, and Z. Guo, “Numerical simulation of premixed methane-air flame propagating parameters in square tube with different solid obstacles,” *Procedia Eng.*, vol. 62, pp. 397–403, 2013, doi: 10.1016/j.proeng.2013.08.081.

[158] H. Deng, M. Huang, X. Wen, G. Chen, F. Wang, and Z. Yao, “Numerical investigation of premixed methane-air fl ame in two-dimensional half open tube in the early stages,” *Fuel*, vol. 272, no. March, p. 117709, 2020, doi: 10.1016/j.fuel.2020.117709.

[159] S. P. R. Muppala and F. Dinkelacker, “A Comparative Study of Different Reaction Models for Turbulent Methane/Hydrogen/Air Combustion,” *J. Therm. Eng.*, vol. 1, no. 1, pp. 367–380, 2015.

[160] B. Bazooyar and H. G. Darabkhani, “Analysis of flame stabilization to a thermo-photovoltaic micro-combustor step in turbulent premixed hydrogen flame,” *Fuel*, vol. 257, no. July, p. 115989, 2019, doi: 10.1016/j.fuel.2019.115989.

[161] V. L. Zimont, “A numerical model of premixed turbulent combustion of gases,” *Chem. Phys. Reports*, vol. 14, no. 7, pp. 993–1025, 2017.

[162] A. N. Gorban, *Invariant Manifolds for Physical and Chemical Kinetics*, no. December 2018. 2005.

[163] P. Lallemand and L. S. Luo, “Theory of the lattice Boltzmann method: Acoustic and thermal properties in two and three dimensions,” *Phys. Rev. E - Stat. Physics, Plasmas, Fluids, Relat. Interdiscip. Top.*, vol. 68, no. 3, p. 25, 2003, doi: 10.1103/PhysRevE.68.036706.

[164] X. He, S. Chen, and G. D. Doolen, “A Novel Thermal Model for the Lattice Boltzmann Method in Incompressible Limit,” *J. Comput. Phys.*, vol. 146, no. 1,

pp. 282–300, 1998, doi: 10.1006/jcph.1998.6057.

[165] D. O. Martínez, W. H. Matthaeus, S. Chen, and D. C. Montgomery, "Comparison of spectral method and lattice Boltzmann simulations of two-dimensional hydrodynamics," *Phys. Fluids*, vol. 6, no. 3, pp. 1285–1298, 1994, doi: 10.1063/1.868296.

[166] P. Koumoutsakos, "Vortex Methods: Theory and Practice," *Meas. Sci. Technol.*, vol. 12, no. 3, pp. 354–354, 2001, doi: 10.1088/0957-0233/12/3/704.

[167] N. Özyılmaz, "Lattice Boltzmann Computations of Grid-generated Turbulence: Lattice-Boltzmann-Berechnungen Von Gittergenerierter Turbulenz," The Friedrich Alexander University of Erlangen, 2010.

[168] T. Abe, "Derivation of the Lattice Boltzmann Method by Means of the Discrete Ordinate Method for the Boltzmann Equation," *J. Comput. Phys.*, vol. 131, no. 1, pp. 241–246, 1997, doi: 10.1006/jcph.1996.5595.

[169] X. He and L. S. Luo, "A priori derivation of the lattice boltzmann equation," *Phys. Rev. E - Stat. Physics, Plasmas, Fluids, Relat. Interdiscip. Top.*, vol. 55, no. 6, 1997, doi: 10.1103/PhysRevE.55.R6333.

[170] S. S. Chikatamarla, C. E. Frouzakis, I. V. Karlin, A. G. Tomboulides, and K. B. Boulouchos, "Lattice Boltzmann method for direct numerical simulation of turbulent flows," *J. Fluid Mech.*, vol. 656, no. February 2020, pp. 298–308, 2010, doi: 10.1017/S0022112010002740.

[171] N. I. Prasianakis, I. V. Karlin, J. Mantzaras, and K. B. Boulouchos, “Lattice Boltzmann method with restored Galilean invariance,” *Phys. Rev. E - Stat. Nonlinear, Soft Matter Phys.*, vol. 79, no. 6, 2009, doi: 10.1103/PhysRevE.79.066702.

[172] A. N. Gortari, “DNS for RANS combustion modelling in multiple injection configurations,” The University of Paris-Saclay, 2020.

[173] U. Ahmed and R. Prosser, “Modelling Flame turbulence interaction in RANS simulation of premixed turbulent combustion Modelling flame turbulence interaction in RANS simulation of premixed turbulent combustion,” *Combust. Theory Model.*, vol. 00, no. 00, pp. 1–16, 2016.

[174] A. M. Sadeq, S. F. Ahmed, and A. K. Sleiti, “Transient 3D simulations of turbulent premixed flames of gas-to-liquid (GTL) fuel in a fan-stirred combustion vessel Transient 3D simulations of turbulent premixed flames of gas-to-liquid (GTL) fuel in a fan-stirred combustion vessel,” *Fuel*, vol. 291, no. February, p. 120184, 2021, doi: 10.1016/j.fuel.2021.120184.

[175] M. M. Salehi and W. K. Bushe, “Presumed PDF modeling for RANS simulation of turbulent premixed flames,” *Combust. Theory Model.*, vol. 14, no. 3, pp. 381–403, 2010, doi: 10.1080/13647830.2010.489957.

[176] Keller, “Series 35XHTC,” 2020.

[177] Gw Instek, “GDS-3152,” 2018.

[178] Dantec, “How to measure turbulence with hot-wire anemometers - a practical guide,” 2002.

[179] Henan Oceanus, “Fixed gas detector Operating Manual,” 2018.

[180] R. G. Abdel-Gayed et al., “Turbulent burning velocities and flame straining in explosions,” *Proc. R. Soc. L.*, vol. 391, no. 1801, pp. 393–414, 1984, doi: 10.1007/978-981-4560-38-2.

[181] M. S. Radwan, M. A. Ismail, and S. M. S. Elfeky, “Jojoba methyl ester as a diesel fuel substitute : Preparation and characterization,” vol. 27, pp. 314–322, 2007, doi: 10.1016/j.applthermaleng.2006.08.004.

[182] T. D. Canonsburg, *ANSYS Fluent Tutorial Guide*, vol. 15317, no. November. 2013.

[183] ANSYS Fluent Tutorial Guide 18, “ANSYS Fluent Tutorial Guide 18,” *ANSYS Fluent Tutor. Guid. 18*, vol. 15317, no. April, pp. 724–746, 2018.

[184] D. Bradley *et al.*, “Turbulent burning velocity, burned gas distribution, and associated flame surface definition,” *Combust. Flame*, vol. 133, no. 4, pp. 415–430, 2003, doi: 10.1016/S0010-2180(03)00039-7.

[185] B. Almansour, “Experimental Investigation of Advanced Ignition Systems for High Efficiency Combustion,” University of Central Florida, 2019.

[186] R. K. Pandey, A. Rehman, and R. M. Sarviya, “Impact of alternative fuel properties on fuel spray behavior and atomization,” *Renew. Sustain. Energy Rev.*,

vol. 16, no. 3, pp. 1762–1778, 2012, doi: 10.1016/j.rser.2011.11.010.

[187] G. Fru, D. Thévenin, and G. Janiga, “Impact of turbulence intensity and equivalence ratio on the burning rate of premixed methane-air flames,” *Energies*, vol. 4, no. 6, pp. 878–893, 2011, doi: 10.3390/en4060878.

[188] Z. Chen, X. Gou, and Y. Ju, “Studies on the outwardly and inwardly propagating spherical flames with radiative loss,” *Combust. Sci. Technol.*, vol. 182, no. 2, pp. 124–142, 2010, doi: 10.1080/00102200903299850.

[189] N. Bouvet, C. Chauveau, I. Gökalp, and F. Halter, “Experimental studies of the fundamental flame speeds of syngas (H 2/CO)/air mixtures,” *Proc. Combust. Inst.*, vol. 33, no. 1, pp. 913–920, 2011, doi: 10.1016/j.proci.2010.05.088.

[190] “A Chemical Equilibrium Program for Windows.” http://www.gaseq.co.uk/.

[191] “CHEMKIN-PRO (x64) 4.5,” 2011. https://chemkin-pro-x64.software.informer.com/4.5/.

[192] E. W. Saw *et al.*, “Experimental characterization of extreme events of inertial dissipation in a turbulent swirling flow,” *Nat. Commun.*, vol. 7, pp. 1–8, 2016, doi: 10.1038/ncomms12466.

[193] A. Bonhomme, F. Duchaine, G. Wang, L. Selle, and T. Poinsot, “A parallel multidomain strategy to compute turbulent flows in fan-stirred closed vessels,” *Comput. Fluids*, vol. 101, pp. 183–193, 2014, doi: 10.1016/j.compfluid.2014.06.010.

[194] S. K. Choi and S. O. Kim, “Turbulence modeling of natural convection in enclosures: A review,” *J. Mech. Sci. Technol.*, vol. 26, no. 1, pp. 283–297, 2012, doi: 10.1007/s12206-011-1037-0.

[195] A. M. Sadeq, S. F. Ahmed, and A. K. Sleiti, “Dataset for transient 3D simulations of turbulent premixed flames of Gas-to-Liquid (GTL) fuel,” *Data Br.*, vol. 36, no. April, 2021, doi: 10.1016/j.dib.2021.106956.

[196] I. L. A. Sequeira, “The Reynolds Number - Units in a Dimensionless Number The Reynolds Number - Units in a Dimensionless Number,” in *PDH online Course M476*, vol. 476, 2013, pp. 1–27.

[197] H. S. Bak, S. R. Lee, J. H. Chen, and C. S. Yoo, “A numerical study of the diffusive-thermal instability of opposed nonpremixed tubular flames,” *Combust. Flame*, vol. 162, no. 12, pp. 4612–4621, 2015, doi: 10.1016/j.combustflame.2015.09.019.

[198] S. Lapointe, “Simulation of Premixed Hydrocarbon Flames at High Turbulence Intensities,” California Institute of Technology, 2016.

APPENDIX A: ARDUINO CODE AND FRITZING CIRCUIT DIAGRAM

Arduino Code

```
1
2
3   int pumpPin = 10;                  // pump connected to digital pin 10
4
5   void setup()
6   {
7     pinMode(pumpPin, OUTPUT);       // sets the digital pin as output
8   }
9
10  void loop()
11  {
12    digitalWrite(pumpPin,HIGH);    // sets the Pump pin on
13    delay(1000);                   // waits for a second
14    digitalWrite(pumpPin,LOW);     // sets the pump pin off
15    delay(1000);                   // waits for a second
16  }
```

Fritzing Circuit Diagram

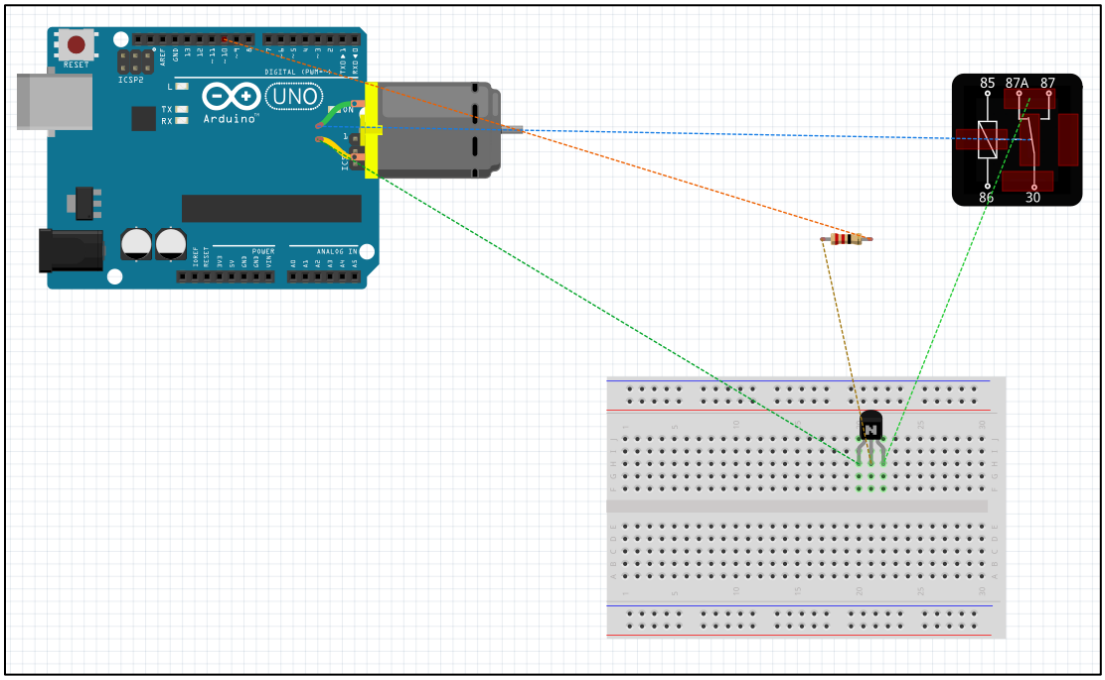

APPENDIX B: CALIBRATION CERTIFICATES

PCB Piezotronics Pressure Transucer

CALIBRATION CERTIFICATE

Model: 116B03
Serial #: 6097
Description: Pressure Sensor
Type: Charge

Capacitance: 25.9 pF
Temp Coeff: +0.016% / deg F at +750 F
+0.029% / deg C at +399 C

Sensitivity*: 6.302 pC/PSI
0.9140 pC/kPa

Linearity*: 0.2% FS
Uncertainty**: +/- 1 %

Date: 7/30/2015
By: Eric Kachermeyer, Cal. Tech.
Station: 903 Pulse #3 (Test procedure AT601-6)

Temp: 74 deg F [23deg C]
Humidity: 44 %

Cert #: 575417

* Zero based, least-squares straight line.
** Measurement uncertainty represented using a coverage factor of k=2 which provides a level of confidence of approximately 95 %.

Condition of Unit:
As Found: Not applicable
As Left: In tolerance, new unit

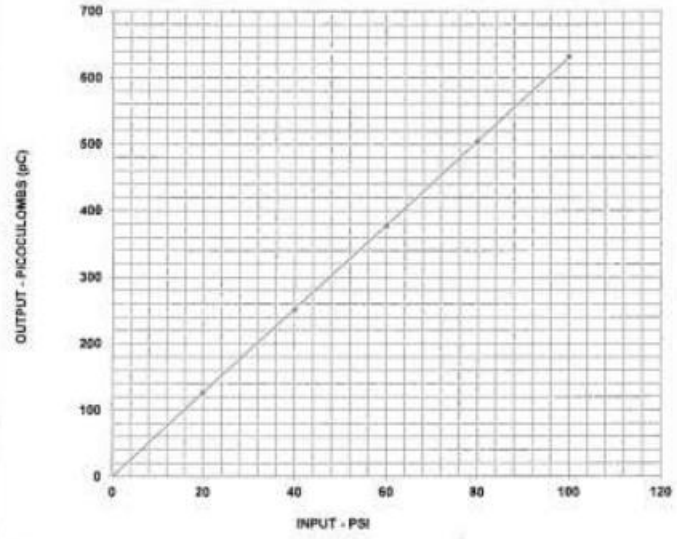

TEST DATA

INPUT (PSI)	OUTPUT (pC)
20.0	126
40.0	251
60.0	377
80.0	504
100	632

Notes:
1 STATION #17
2 Calibration is traceable to NIST and is accredited to ISO 17025 and ANSI/NCSL Z540.3.
3 NIST traceability through PCB control # CA 1296.
4 This certificate may not be reproduced, except in full, without written approval from PCB Piezotronics, Inc.

CALIBRATION CERT #1862-01

PCB PIEZOTRONICS

Tel: 716-684-0001 Fax: 716-684-0987 Email: sales@pcb.com
3425 Walden Avenue, Depew NY 14043

ISO 9001 CERTIFIED

Page 1 of 1

~ Calibration Certificate ~

Model Number: 422E35 Customer:

Serial Number: 43787

Description: Charge Converter P.O.:

Manufacturer: PCB Method : Comparison Method (AT-119-2)

Calibration Data

Temperature: 72 °F (22 °C) Humidity: 57%

Input Parameters :

Frequency 100 Hz Source Capacitance 993.79 pF

Test Results:

Gain: 0.990 mV/pC Bias Voltage: 13.99 VDC

Condition of Unit

As Found: n/a

As Left: New unit, in tolerance

Notes

1. This inverting charge amplifier has a fixed gain, range and feedback resistance.
2. Calibration is N.I.S.T. traceable through PCB control number QC-214.
3. This certificate shall not be reproduced, except in full, without written approval from PCB Piezotronics, Inc.
4. Calibration is performed in compliance with ISO 9001, ISO 10012-1, ANSI/NCSL Z540.3 and ISO 17025.
5. Measurement uncertainty (95% confidence level with a coverage factor of 2) for the sensitivity reading is +/- 0.2 %
6. See Manufacturer's Specification Sheet for a detailed listing of performance specifications.

Technician: Mark Moorhouse MM 3415 Date: 6/9/2015

Due Date:

CALIBRATION CERT #1862.01

PCB PIEZOTRONICS
3425 Walden Avenue
Depew, New York 14043
TEL: 888-684-0013 FAX: 716-685-3886 www.pcb.com

ILE22-3516720911

35XHTC Pressure Transducer

TEYSEER INDUSTRIAL SUPPLIES AND SERVICES CO. W.L.L.
P.O. Box: 40523 St. No. 11 Gate No. 74 Bldg. No. 163
Industrial Area, Doha State of Qatar
Tel: (974) 44585400 Fax: (974) 44607637

ANSI/NCSL Z540-I
ANSI/NCSL Z540.3
AC-1969.28

Certificate of Calibration

Print Date: 13-Jan-2021 **Cert No.** 551220084026883

Customer:
QATAR UNIVERSITY/DR.SAMER AHMED
DOHA-QATAR

Work Order No.	: QA-10042365	Purchase Order No.	: CASH
Cal ID No.	: 233531.0143	Serial No.	: 233531.0143
Equipment ID	: N/A	Department	: N/A
Equipment Type	: PRESSURE TRANSDUCER	Performed By	: JOE MANNIX RETUERNE
Manufacturer	: KELLER	Received Condition	: IN TOLERANCE
Model No.	: PA-35XHTC	Returned Condition	: IN TOLERANCE
Range / Size	: 0 to 1000 bar	Calibration Date	: 12-Jan-2021
Temp/RH	: 20.8°C / 51 %	Calibration Interval	: 12 MONTHS
		Calibration Due Date	: 12-Jan-2022

Calibration Notes:
Site Location: MPC Lab
See attached 1 page calibration data

Reference Instruments Used in Calibration

I.D.	Description.	Model No.	Serial No.	Manufacturer	Cal. Due Date	Traceability No.
3150900	ADVANCE MODULAR CALIBRATOR	DPI620	3150900	DRUCK INC	Dec 16, 2021	551220083995705
DC6341	PORTABLE PRESSURE CALIBRATOR	3130-G2M	3267016	FLUKE	Sep 28, 2021	551220083240137

Procedures Used in Calibration

Procedure Name	Description
MPC-PTD-001	Pressure Transmitters and Switches, General, rev01, Jan-28-2020

Calibration Performed By:
JOE MANNIX RETUERNE
Calibration Technician

QC Approval:
RICHARD POSANSO
QA/QC Inspector

STATEMENTS OF PASS OR FAIL CONFORMANCE: The uncertainty of measurement has been taken into account when determining compliance with specification. All measurements and test results guard banded to ensure the probability of false-accept does not exceed 2% in compliance with ANSI/NCSL Z540.3-2006 and in cases without guard banded the probability of false-accept depending on test uncertainty ratio.

THE CALIBRATION REPORT STATUS:
PASS- Term used when compliance statement is given, and the measurement result is PASS.
PASS*- Term used when compliance statement is given, and the measurement result is conditional passed or PASS*.
FAIL- Term used when compliance statement is given, and the measurement result is FAIL.
FAIL*- Term used when compliance statement is given, and the measurement result is conditional failed or FAIL*.
REPORT OF VALUE - Term used when reported measurement is not requiring compliance statement in report.
ADJUSTED- When adjustments are made to an instrument which changes the value of measurement from what was measured as found to new value as left.
LIMITED - Where an instrument fails calibration but is still functional in a limited manner.

The expanded uncertainty of measurement is stated as the standard uncertainty of measurement multiplied by the coverage factor k=2, which for a normal distribution corresponds to a coverage probability of approximately 95%, unless otherwise stated. This calibration report complies with ISO/IEC 17025:2017 and ANSI/NCSL Z540.3. Calibration cycles and resulting due dates were submitted/approved by the customer. Any number of factors may cause an instrument to drift out of tolerance before the next scheduled calibration. Recalibration cycles should be based on frequency of use, environmental conditions and customer's established systematic accuracy. All standards are traceable to SI through the National Institute of Standards and Technology (NIST) and/or recognized national or international standards laboratories. Services rendered include proper manufacturer's service instruction and are warranted for no less than thirty (30) days. The information on this report pertains only to the instrument identified. This may not be reproduced in part or in a whole without the prior written approval of the issuing MP Calibration Laboratory.

(CERT, Rev 7)

MICRO PRECISION

Tisco

Calibration Report of PRESSURE TRANSDUCER

Procedure Ref.:	MPC-PTD-001	Work Order No.:	QA-10042365
Calibration ID:	233531.0143	Serial Number:	233531.0143
Asset ID:	NONE	Model No.:	PA-35XHTC
Manufacturer:	KELLER	Calibration Date:	January 12, 2021

MEASUREMENT ACCURACY

Pressure Input	Current Output (Expected)	Lower Limit	As Found	As Left	Upper Limit	Result	Uncertainty (±)
0.000 bar	4.0000 mA	3.9920 mA	4.0002 mA	4.0002 mA	4.0080 mA	PASS	0.00023 mA
3.000 bar	4.0480 mA	4.0400 mA	4.0441 mA	4.0441 mA	4.0560 mA	PASS	0.00023 mA
6.000 bar	4.0960 mA	4.0880 mA	4.0913 mA	4.0913 mA	4.1040 mA	PASS	0.00023 mA
9.000 bar	4.1440 mA	4.1360 mA	4.1390 mA	4.1390 mA	4.1520 mA	PASS	0.00024 mA
12.000 bar	4.1920 mA	4.1840 mA	4.1863 mA	4.1863 mA	4.2000 mA	PASS	0.00024 mA
15.000 bar	4.2400 mA	4.2320 mA	4.2347 mA	4.2347 mA	4.2480 mA	PASS	0.00024 mA
12.000 bar	4.1920 mA	4.1840 mA	4.1885 mA	4.1885 mA	4.2000 mA	PASS	0.00024 mA
9.000 bar	4.1440 mA	4.1360 mA	4.1395 mA	4.1395 mA	4.1520 mA	PASS	0.00024 mA
6.000 bar	4.0960 mA	4.0880 mA	4.0916 mA	4.0916 mA	4.1040 mA	PASS	0.00023 mA
3.000 bar	4.0480 mA	4.0400 mA	4.0444 mA	4.0444 mA	4.0560 mA	PASS	0.00023 mA
0.000 bar	4.0000 mA	3.9920 mA	4.0006 mA	4.0006 mA	4.0080 mA	PASS	0.00023 mA

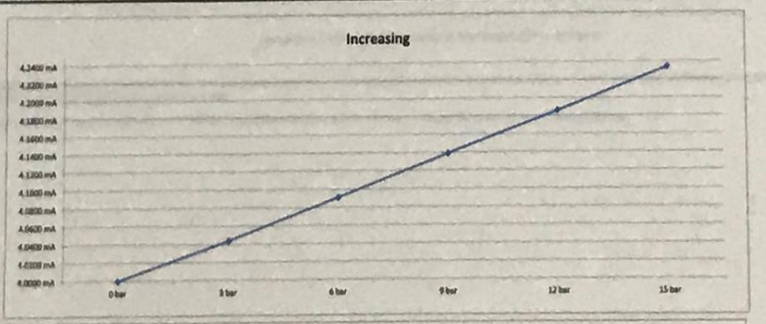

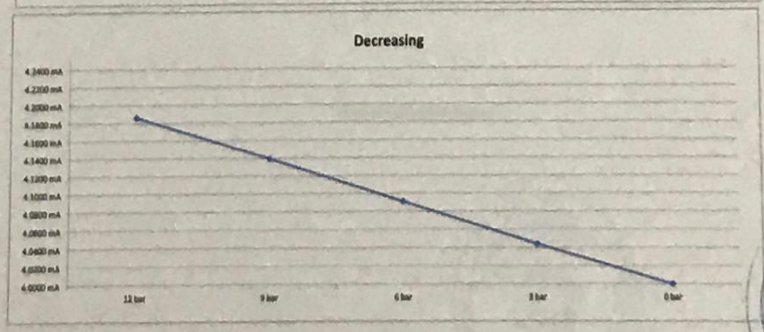

MICRO PRECISION

Tisco

Calibration Report of PRESSURE TRANSDUCER

Procedure Ref.:	MPC-PTD-001	Work Order No.:	QA-10042365
Calibration ID:	233531.0143	Serial Number:	233531.0143
Asset ID:	NONE	Model No.:	PA-35XHTC
Manufacturer:	KELLER	Calibration Date:	January 12, 2021

Statements of Pass or Fail Conformance

The uncertainty of measurement has been taken into account when determining compliance with specification.
All measurements and test results guard banded to ensure the probability of false-accept does not exceed 2% in compliance with ANSI/NCSL Z540.3-2006

The status of compliance with the acceptance criteria is reported as:

PASS	—	Compliant with specification.
PASS[Z]	—	The measured value is within acceptance limits. However, a portion of the expanded uncertainty of measurement at 95% exceeds the specified tolerance.
FAIL[Z]	—	The measured value is not within the acceptance limits. However, a portion of the expanded uncertainty of measurement at 95% is within the specified tolerance.
FAIL	—	Not compliant with specification.

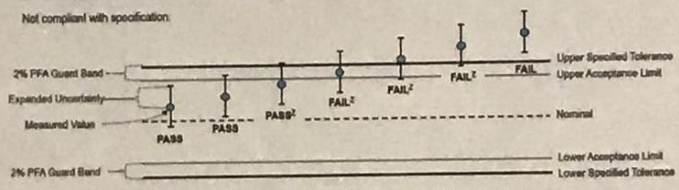

Acceptance limits for ≤ 2% probability of false accept (PFA) guard band

The expanded uncertainty of measurement is stated as the standard uncertainty of measurement multiplied by the coverage factor k = 2, which for a normal distribution corresponds to a coverage probability of approximately 95%, unless otherwise stated.

This calibration report complies with ISO/IEC 17025:2017 and ANSI/NCSL Z540.3-2006, Method 6 — Guard Bands Based on Test Uncertainty Ratio.

- End of Calibration Report -

OC-F08

Calibrate report

一、Technical parameters

Product Name: Fixed gas detector Model: OC-F08/O2

Power supply: 24V DC Range: 0-25%VOL

Output signal: RS485 / 4-20mA Accuracy: ±3%F.S

Product Code: OC102101112967838 Number: 1

二、Test environment

Ambient temperature: 25 ℃ Ambient humidity: 60 %RH

三、Test basis

Factory determined technical conditions

四、Test method and data

Gas detection	O2	Standard gas	O2
Standard gas concentration	10%VOL	Detection concentration	10.0 %VOL
Standard gas concentration	20.9%VOL	Detection concentration	20.9 %VOL
First level alarm	19.5%VOL	Secondary alarm	23%VOL
response time (T90)	17s	Detection time	1 min

五、Appearance inspection

The covering layer and name plate on the surface of instrument shell and parts shall be smooth and in good condition without defects such as spalling and scar, and the fasteners shall be complete.

六、Test results

Qualified

Check: QC 02 Approval: QC 02 Tester: QC PASS

Company: Henan Oceanus Import & Export Co., Ltd.

Date: January ,11, 2021

Calibration Chart

Substance	**Oxygen (O_2)**				
Enerac 700 Gas Analyzer (%O_2 vol)	21.5	21.0	20.5	20.0	19.5
OC-F08 Gas Detector (%O_2 vol)	21.5	21.0	20.5	20.0	19.5

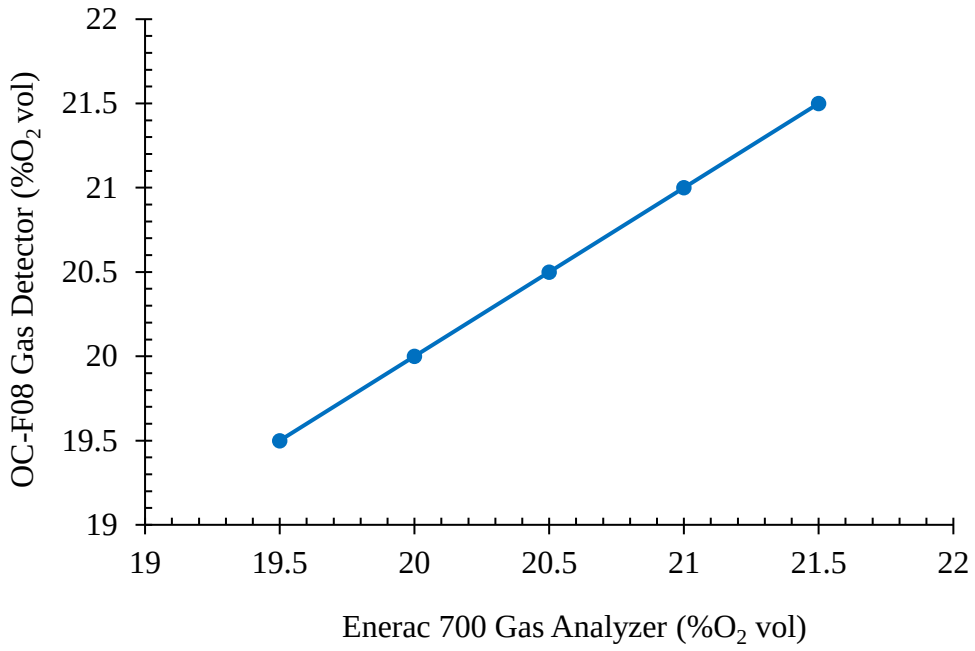

APPENDIX C: EQUIVALENCE RATIO CALCULATIONS

GTL

O_2 %	Moles O_2 (mol)	m_{air} (g)	V_{fuel} Injeced (mL)	m_{fuel} Injected (g)	m_{fuel} Evaporaed (g)	$(A/F)_a$	Φ
20.2	0.72	98.2	6.0	4.6	4.5	21.8	0.7
20.1	0.71	97.7	7.0	5.4	5.2	18.8	0.8
19.9	0.70	96.8	8.0	6.2	5.9	16.5	0.9
19.8	0.70	96.3	9.0	6.9	6.4	14.9	1.0
19.7	0.70	95.8	10.0	7.7	7.1	13.5	1.1
19.6	0.69	95.3	11.0	8.5	7.5	12.4	1.2
19.5	0.69	94.8	12.0	9.2	7.7	11.3	1.3

50/50 Diesel-GTL Blend

O_2 %	Moles O_2 (mol)	m_{air} (g)	V_{fuel} Injeced (mL)	m_{fuel} Injected (g)	m_{fuel} Evaporaed (g)	$(A/F)_a$	Φ
20.2	0.72	98.2	6.0	4.8	4.6	21.6	0.7
20.1	0.71	97.7	7.0	5.5	5.3	18.6	0.8
19.9	0.70	96.8	8.0	6.3	5.9	16.4	0.9
19.8	0.70	96.3	9.0	7.1	6.5	14.9	1.0
19.7	0.70	95.8	10.0	7.9	7.1	13.5	1.1
19.6	0.69	95.3	11.0	8.7	7.6	12.5	1.2
19.5	0.69	94.8	12.0	9.5	8.1	11.8	1.3

APPENDIX D: HOTWIRE ANEMOMETER CALIBRATION

Orthogonal Coordinates of the Measured Points in Centimeters:

O: (0,0)
1: (0.35,0)
2: (0.70,0)
3: (1.05,0)
4: (-0.35,0)
5: (-0.70,0)
6: (-1.05,0)
7: (0,0.35)
8: (0,0.70)
9: (0,1.05)
10: (0,-0.35)
11: (0,-0.70)
12: (0,-1.05)

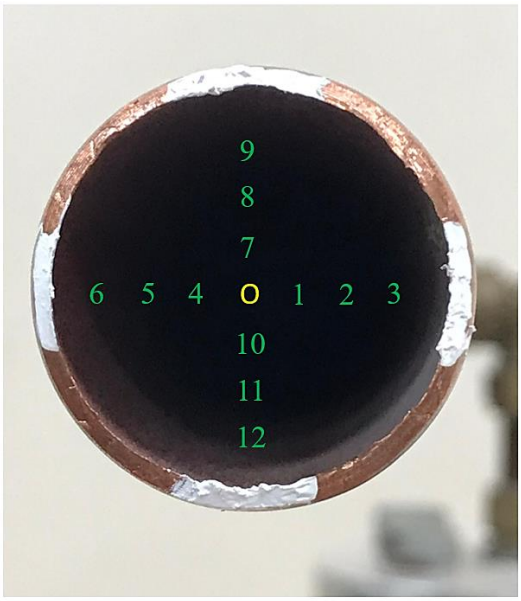

Average Voltage Readings (in Volts) at Each Point

Q m^3/h	**1**	**2**	**3**	**4**	**5**	**6**	**7**	**8**	**9**	**10**	**11**	**12**
3.00	1.54	1.52	1.49	1.54	1.52	1.49	1.54	1.52	1.49	1.54	1.52	1.49
4.00	1.61	1.59	1.56	1.61	1.59	1.56	1.61	1.59	1.56	1.61	1.59	1.56
5.00	1.66	1.64	1.61	1.66	1.64	1.61	1.66	1.64	1.61	1.66	1.64	1.61
6.00	1.71	1.69	1.66	1.71	1.69	1.66	1.71	1.69	1.66	1.71	1.69	1.66
7.00	1.77	1.74	1.66	1.77	1.74	1.66	1.77	1.74	1.66	1.77	1.74	1.66
8.00	1.83	1.79	1.74	1.83	1.79	1.74	1.83	1.79	1.74	1.83	1.79	1.74
9.00	1.91	1.86	1.79	1.91	1.86	1.79	1.91	1.86	1.79	1.91	1.86	1.79
10.00	2.01	1.94	1.85	2.01	1.94	1.85	2.01	1.94	1.85	2.01	1.94	1.85

APPENDIX E: MEASUREMENTS UNCERTAINITIES

Φ=0.7

u`(m/s)	S_t (cm/s)	B_{st} (cm/s)	Error %
0.50	70.98	0.65	0.92
1.00	103.16	1.28	1.24
1.50	149.03	2.00	1.34
2.00	202.31	3.07	1.52
2.50	295.90	5.67	1.92
3.00	389.57	8.21	2.11
Mean Error %			**1.51**

Φ=1.3

u`(m/s)	S_t (cm/s)	B_{st} (cm/s)	Error %
0.50	94.12	1.19	1.26
1.00	126.71	1.99	1.57
1.50	190.48	3.31	1.74
2.00	264.26	5.29	2.00
2.50	351.02	7.93	2.26
3.00	461.72	11.45	2.48
Mean Error %			**1.89**

APPENDIX F: LAMINAR FLAME SPEED RESULTS

Φ=0.7

	dr_i/dt (m/s)	r_i (m)	r_b (m)	T_u/T_i	S_l (cm/s)	S_l (cm/s) [10]	Ɛ (%)
1	0.457	1.356	8.243	1.065	47.78	49.20	0.86
2	0.456	1.355	8.226	1.066	47.67	49.20	0.89
3	0.457	1.356	8.243	1.066	47.80	49.20	0.74
M	0.457	1.356	8.237	1.066	47.75	49.20	0.83
σ=0.07cm/s				SEM= 0.04%			

Φ=0.8

	dr_i/dt (m/s)	r_i (m)	r_b (m)	T_u/T_i	S_l (cm/s)	S_l (cm/s) [10]	Ɛ (%)
1	0.618	1.577	10.015	1.065	58.44	59.81	1.05
2	0.616	1.575	9.994	1.066	58.32	59.81	0.85
3	0.616	1.575	9.994	1.066	58.50	59.81	0.85
M	0.617	1.576	10.001	1.066	58.42	59.81	0.91
σ=0.09cm/s				SEM= 0.53%			

Φ=0.9

	dr_i/dt (m/s)	r_i (m)	r_b (m)	T_u/T_i	S_l (cm/s)	S_l (cm/s) [10]	Ɛ (%)
1	0.682	1.656	10.553	1.065	65.12	67.12	1.45
2	0.681	1.655	10.545	1.066	65.03	67.12	1.48
3	0.681	1.655	10.545	1.066	65.71	67.12	1.48
M	0.681	1.655	10.548	1.066	65.29	67.12	1.47
σ=0.37cm/s				SEM= 0.21%			

Φ=1.0

	dr_i/dt (m/s)	r_i (m)	r_b (m)	T_u/T_i	S_l (cm/s)	S_l (cm/s) [10]	Ɛ (%)
1	0.760	1.749	11.129	1.065	72.04	73.58	0.63
2	0.764	1.742	11.100	1.066	72.31	73.58	0.99
3	0.763	1.742	11.100	1.066	72.21	73.58	0.86
M	0.763	1.745	11.110	1.066	72.19	73.58	0.82
σ=0.14cm/s				SEM= 0.08%			

Φ=1.1

	dr_i/dt (m/s)	r_i (m)	r_b (m)	T_u/T_i	S_l (cm/s)	S_l (cm/s) [10]	Ɛ (%)
1	0.843	1.842	11.638	1.065	82.21	83.19	0.03
2	0.841	1.840	11.627	1.066	82.09	83.19	0.12
3	0.843	1.842	11.638	1.066	82.01	83.19	0.15
M	0.842	1.841	11.634	1.066	82.10	83.19	0.10
σ=0.10cm/s				SEM= 0.06%			

Φ=1.2

	dr_i/dt (m/s)	r_i (m)	r_b (m)	T_u/T_i	S_l (cm/s)	S_l (cm/s) [10]	Ɛ (%)
1	0.835	1.834	11.594	1.065	80.03	81.63	0.85
2	0.833	1.832	11.583	1.066	80.10	81.63	0.70
3	0.833	1.832	11.583	1.066	80.15	81.63	0.70
M	0.834	1.832	11.587	1.066	80.09	81.63	0.75
σ=0.06cm/s				SEM= 0.04%			

Φ=1.3

	dr_i/dt (m/s)	**r_i (m)**	**r_b (m)**	**T_u/T_i**	**S_l (cm/s)**	**S_l (cm/s)** [10]	**Ɛ (%)**
1	0.814	1.810	11.469	1.065	79.44	80.52	0.78
2	0.818	1.814	11.492	1.066	79.34	80.52	0.12
3	0.820	1.817	11.504	1.066	79.64	80.52	0.16
M	0.817	1.814	11.488	1.066	79.47	80.52	0.35
σ=0.15cm/s				SEM= 0.09%			

APPENDIX G: TURBULENT FLAME SPEED RESULTS

(a) Diesel

				Φ= 0.7		
	u'=0.5m/s	u'=1.0m/s	u'=1.5m/s	u'=2.0m/s	u'=2.5m/s	u'=3.0m/s
r_m (cm)	7.60	7.09	6.62	6.20	5.63	5.09
S_t (cm/s)	70.98	103.16	149.03	202.31	280.22	375.73
				Φ= 0.8		
	u'=0.5m/s	u'=1.0m/s	u'=1.5m/s	u'=2.0m/s	u'=2.5m/s	u'=3.0m/s
r_m (cm)	7.51	7.05	6.56	6.15	5.58	5.05
S_t (cm/s)	79.18	108.90	160.32	218.91	299.64	401.44
				Φ= 0.9		
	u'=0.5m/s	u'=1.0m/s	u'=1.5m/s	u'=2.0m/s	u'=2.5m/s	u'=3.0m/s
r_m (cm)	7.44	7.00	6.51	6.09	5.53	5.01
S_t (cm/s)	87.07	116.23	171.67	237.21	322.10	424.15
				Φ= 1.0		
	u'=0.5m/s	u'=1.0m/s	u'=1.5m/s	u'=2.0m/s	u'=2.5m/s	u'=3.0m/s
r_m (cm)	7.38	6.96	6.46	6.03	5.49	4.97
S_t (cm/s)	93.79	122.68	183.75	255.66	340.79	449.74
				Φ= 1.1		
	u'=0.5m/s	u'=1.0m/s	u'=1.5m/s	u'=2.0m/s	u'=2.5m/s	u'=3.0m/s
r_m (cm)	7.36	6.92	6.42	5.99	5.45	4.93
S_t (cm/s)	95.65	128.84	194.04	271.60	361.91	478.78
				Φ= 1.2		
	u'=0.5m/s	u'=1.0m/s	u'=1.5m/s	u'=2.0m/s	u'=2.5m/s	u'=3.0m/s
r_m (cm)	7.37	6.93	6.42	6.00	5.45	4.94
S_t (cm/s)	94.90	127.76	192.84	267.88	359.12	470.09
				Φ= 1.3		
	u'=0.5m/s	u'=1.0m/s	u'=1.5m/s	u'=2.0m/s	u'=2.5m/s	u'=3.0m/s
r_m (cm)	7.38	6.93	6.43	6.01	5.46	4.95
S_t (cm/s)	94.12	126.71	190.48	264.26	353.67	465.87

(b) GTL						
				Φ=0.7		
	u'=0.5m/s	u'=1.0m/s	u'=1.5m/s	u'=2.0m/s	u'=2.5m/s	u'=3.0m/s
r_m (cm)	7.60	7.09	6.62	6.20	5.59	5.07
S_t (cm/s)	70.98	103.16	149.03	202.31	295.90	389.57
				Φ= 0.8		
	u'=0.5m/s	u'=1.0m/s	u'=1.5m/s	u'=2.0m/s	u'=2.5m/s	u'=3.0m/s
r_m (cm)	7.51	7.05	6.56	6.15	5.56	5.03
S_t (cm/s)	79.18	108.90	160.32	218.91	309.43	414.10
				Φ= 0.9		
	u'=0.5m/s	u'=1.0m/s	u'=1.5m/s	u'=2.0m/s	u'=2.5m/s	u'=3.0m/s
r_m (cm)	7.44	7.00	6.51	6.09	5.52	4.99
S_t (cm/s)	87.07	116.23	171.67	237.21	326.57	434.73
				Φ= 1.0		
	u'=0.5m/s	u'=1.0m/s	u'=1.5m/s	u'=2.0m/s	u'=2.5m/s	u'=3.0m/s
r_m (cm)	7.38	6.96	6.46	6.03	5.46	4.95
S_t (cm/s)	93.79	122.68	183.75	255.66	353.67	465.87
				Φ= 1.1		
	u'=0.5m/s	u'=1.0m/s	u'=1.5m/s	u'=2.0m/s	u'=2.5m/s	u'=3.0m/s
r_m (cm)	7.36	6.92	6.42	5.99	5.43	4.92
S_t (cm/s)	95.65	128.84	194.04	271.60	370.55	483.26
				Φ= 1.2		
	u'=0.5m/s	u'=1.0m/s	u'=1.5m/s	u'=2.0m/s	u'=2.5m/s	u'=3.0m/s
r_m (cm)	7.37	6.93	6.42	6.00	5.46	4.95
S_t (cm/s)	94.90	127.76	192.84	267.88	356.37	465.87
				Φ= 1.3		
	u'=0.5m/s	u'=1.0m/s	u'=1.5m/s	u'=2.0m/s	u'=2.5m/s	u'=3.0m/s
r_m (cm)	7.38	6.93	6.43	6.01	5.47	4.95
S_t (cm/s)	94.12	126.71	190.48	264.26	351.02	461.72

(c) 50/50 Diesel-GTL Blend						
				Φ=0.7		
	u'=0.5m/s	u'=1.0m/s	u'=1.5m/s	u'=2.0m/s	u'=2.5m/s	u'=3.0m/s
r_m (cm)	7.60	7.09	6.62	6.20	5.59	5.08
S_t (cm/s)	70.98	103.16	149.03	202.31	295.90	381.14
				Φ= 0.8		
	u'=0.5m/s	u'=1.0m/s	u'=1.5m/s	u'=2.0m/s	u'=2.5m/s	u'=3.0m/s
r_m (cm)	7.51	7.05	6.56	6.15	5.56	5.04
S_t (cm/s)	79.18	108.90	160.32	218.91	309.43	407.67
				Φ= 0.9		
	u'=0.5m/s	u'=1.0m/s	u'=1.5m/s	u'=2.0m/s	u'=2.5m/s	u'=3.0m/s
r_m (cm)	7.44	7.00	6.51	6.09	5.52	5.00
S_t (cm/s)	87.07	116.23	171.67	237.21	326.57	429.37
				Φ= 1.0		
	u'=0.5m/s	u'=1.0m/s	u'=1.5m/s	u'=2.0m/s	u'=2.5m/s	u'=3.0m/s
r_m (cm)	7.38	6.96	6.46	6.03	5.46	4.96
S_t (cm/s)	93.79	122.68	183.75	255.66	353.67	457.65
				Φ= 1.1		
	u'=0.5m/s	u'=1.0m/s	u'=1.5m/s	u'=2.0m/s	u'=2.5m/s	u'=3.0m/s
r_m (cm)	7.36	6.92	6.42	5.99	5.43	4.92
S_t (cm/s)	95.65	128.84	194.04	271.60	370.55	481.01
				Φ= 1.2		
	u'=0.5m/s	u'=1.0m/s	u'=1.5m/s	u'=2.0m/s	u'=2.5m/s	u'=3.0m/s
r_m (cm)	7.37	6.93	6.42	6.00	5.46	4.94
S_t (cm/s)	94.90	127.76	192.84	267.88	356.37	467.97
				Φ= 1.3		
	u'=0.5m/s	u'=1.0m/s	u'=1.5m/s	u'=2.0m/s	u'=2.5m/s	u'=3.0m/s
r_m (cm)	7.38	6.93	6.43	6.01	5.47	4.95
S_t (cm/s)	94.12	126.71	190.48	264.26	351.02	463.78